Impact of climate and tectonics on the morphodynamics of alluvial piedmonts, implications for sediment transfer and the stratigraphic record.

Thesis by
Luca Claude Malatesta

In Partial Fulfillment of the Requirements for the
degree of
Doctor of Philosophy

CALIFORNIA INSTITUTE OF TECHNOLOGY
Pasadena, California

2017
Defended September 29, 2016

Luca Claude Malatesta
ORCID: 0000-0003-0983-715X

ACKNOWLEDGEMENTS

This is arguably the most read part of the thesis. A crucial (and incomplete) list of names that explains why I am looking back at five fantastic years in Los Angeles.

I want to start by thanking my main advisor Jean-Philippe Avouac, and my co-advisor Mike Lamb, for all they taught me. Jean-Philippe is a remarkable advisor, and my voice is not necessary to confirm his scientific brilliance. Working with him has been a deeply inspiring experience. Often, after a breakthrough in a problem, I realized that all elements of the solution had been formulated by Jean-Philippe in a discussion years ago. The delay was simply the time I needed to catch up. As his student, I can say that he is someone who values the *happiness* of doing science and conveys it to the people around him fostering a very pleasant academic environment. I am thankful for the time he invested in our work and I am proud to have advanced his #1 hobby: tectonic geomorphology! Mike Lamb brought a new dimension to my understanding of the sedimentary realm by introducing me to sediment transport at the channel scale and I have been relying on this mechanic ever since. Mike Lamb's ability to see clear through a field problem and compartment it into a series of mechanistic modules, while in the field, is a great model to emulate. He is also simply a very good companion around a campfire and that matters in the West. I have a learned a great deal from Mike Lamb's group and I extend my gratitude to the brilliant students and postdocs Mike surrounds himself with: Jeff, Joel, Mathieu, Vamsi, Marissa, Mark, Austin, Alistair, Sam, and Roman. Lively group meetings helped me sharpen my thoughts like few other occasions.

I would to express my gratitude to the members of my thesis advisory committee, Jess Adkins, Woody Fischer and John Grotzinger for the time they invested in reading my work. Jess helped me in particular to quickly grasp the essential pieces of climate dynamics that I needed for my Central Asian work. It has been a real pleasure to work with Quentin Berger, Sebastian Breitenbach, Nathan Brown, and of course Jean-Arthur Olive during my thesis. They helped me improve my work with insights from their their own fields of expertise.

Heather, Lisa, Janice, Liz, Tony, Diane, Leticia, Julie, Mark and Marcia from the Division staff were immensely helpful I am grateful for their patience and help.

At and around Caltech, the list is long, may it be for their help during the long evenings of the first year, or for the company watching a mountain stage of the Tour of California in the San Gabriels: Jeff, Romain, Alison, François, Florent, Elizabeth, Joel, Brian, Sophie, Ted, Frank, Stephen, Kirsten, Adam, Daven, Kathy, Jason, Mathieu, Asaf.

I want to thank Kristel for letting me steal a few of her great friends and also being one, Jean-Arthur, Quentin and Romain, and through them Mélanie, Pénélope, Elsa. It is always such a pleasure to spend time with you all.

Séb Castelltort continues to be a great and inspiring 'background advisor', it is precious to know his door in Geneva is always open for great discussions. He helped me better frame the stratigraphic aspect of the thesis. I also want to thank Fréd Herman who was the first to push me in the direction of Caltech and put me in contact with Jean-Philippe.

10 years ago Zelda, Rafael, Peter and I were preparing together for the Basisprüfung, and they saw me through it, thank you that as well as for your friendship. Back home, there's a lot of people that I want to thank for making time at the last minute when I was on brief visits, the incredible Manu, Jamil, Myriam, Simon, Marius, and in Berlin Zoé and Sascha. It has been immensely resourceful to chat with them about all the fascinating things they are doing brilliantly.

One figure stands out in the last five years: Vicky. There are so many things I should thank her for, one thing for example: she taught me how to better read LA and embrace this fantastic city. Somehow Southern California is deeply intertwined with West Yorkshire for me. I am looking forward to the next stop.

And back to the literal home, I am forever grateful to my family for their support. I have my parents to thank for who and where I am now. I know California is quite far and my sister and my parents would have probably wanted to see me more often, just as I did. But knowing I could always rely on them is a chance I cherish. I am proud of my sister and always looking forward to see her.

ABSTRACT

Alluvial piedmonts encircle most of the Earth mountain ranges. The erosion product of these mountains must cross the piedmont domain before reaching the basins where they can enter the sedimentary record. The flux of sediment transfers environmental signals, e.g. tectonics and climate, from source to sink, their preservation is critical for the sedimentary record. Alluvial piedmonts are very reactive to external and internal forcing often incise by tens to hundreds of vertical meters over a few thousand years only to subsequently aggrade by roughly the same amount. In my thesis, I set to study the morphodynamics of alluvial piedmonts in two areas, Death Valley, California, and the Eastern Tian Shan.

In Death Valley I show that cycles of aggradation and incision repeatedly bury active fault scarps and that leads to the accumulation of tectonic slip until the next incision episode when a tall waterfall is released in the catchment. This process links the release of tectonic offset to climatic periods and it also accounts for many unexplained 10 to 30 m waterfalls in the Death Valley area.

In the Eastern Tian Shan, I establish that the northern alluvial piedmont, that is incised by 100 to 300 m in the Holocene, undergoes repeated cycles of aggradation and incision driven by fluctuations in Westerlies moisture and insolation at a 21 kyr period without the need for monsoonal moisture to drive the system. The varying extent of glacial overprint in the Eastern Tian Shan is responsible for the morphological contrast between the incised north and aggraded south piedmonts. I produce more terrace abandonment ages that show that all rivers of the northern piedmont incised since the last deglaciation but did so out of sync because of the geometry of the upstream glaciated valleys, and internal feedbacks with alluvial valley walls during river entrenchment. With new luminescence ages sampled in the stratigraphy I establish that sediments from the last 0.5 Myr are remobilized in the modern sediment flux by the alluvial incision. I develop a numerical tool that predicts locally the probability of sediment mixing based on the essential length- and timescales of the individual rivers of an alluvial piedmont.

PUBLISHED CONTENT AND CONTRIBUTIONS

Malatesta, Luca Claude, Jeffrey P Prancevic, and Jean-Philippe Avouac (2017). "Autogenic entrenchment patterns and terraces due to coupling with lateral erosion in incising alluvial channels". In: *Journal of Geophysical Research: Earth Surface* 122.1, pp. 335–355. DOI: 10.1002/2015JF003797.

L. C. M. was the lead designer, modeler, and writer for this study.

TABLE OF CONTENTS

LIST OF ILLUSTRATIONS

LIST OF TABLES

Chapter 1

INTRODUCTION

Understanding how the various spheres of the Earth System are connected and influence each other has been a major focus of the Earth Science community over the last few decades. Not long ago, the lithosphere and the atmosphere were studied in perfectly sealed off disciplines. As the community specialized in ever narrower niches, our entire approach also became simultaneously more holistic because we recognized the interdependence of all the components of the Earth system (e.g. Molnar and England, 1990; Bull, 1991). A critical aspect of the discussion the community holds is the way information about and from one subsystem, such as the atmosphere, can be transmitted to another one, like such as the lithosphere, and eventually recorded for us to read. A large part of this information transfer occurs at the surface of the Earth and is carried by a redistribution of mass along the sediment routing-system (e.g. Allen, 2008; Romans et al., 2015). The bulk mass that is produced and moved about can tell us about mountains that are no more, and geochemical signatures of these sediments provide us with information so that we can identify precisely when regional climatic patterns shift. Refining the increasingly detailed knowledge of the history of the planet requires an increasingly fine resolution of the sedimentary records. And as we delve into the finer and finer record, small disturbances to that record pose an ever larger problem. What good is it to have a yearly record of a sedimentary system without knowing the resolution capacity of the flux that enters it? A very important task of the surface process community today is to provide an understanding of the preservation or destruction of environmental signals by 'reactive' or 'buffering' landscapes and provide tools to decipher with confidence the stories held in the sediment record.

A large and crucial body of work has been done in the lowlands, the historical domain of sedimentology, where awesome rivers transport an immense amount of sediment and distribute them for posterity. But before reaching the lowlands, the bulk of the sediments are produced in, and transported away from, the highlands. Between the two lie alluvial piedmonts. Alluvial belts encircle

virtually all orogenies and the sediment flux that comes out of them — and the information it contains — have to cross the piedmonts. They are the necessary transit routes that I will discuss in this thesis.

A key element of piedmonts is that they do not only evolve in the horizontal with river migration and occasional avulsion but they also have the propensity to undergo fast and repeated variations in the vertical dimensions unseen elsewhere in the alluvial system. The capacity to aggrade and incise rapidly, much faster than tectonic rates, means that the dynamics of piedmonts can easily obscure tectonic signals. It also means that a cycle of aggradation and incision means a temporary storage of sediment on the alluvial piedmont and the potential remobilization of much older sediments (Allen, 2005). Alluvial piedmonts are particularly sensitive to climatic forcing and they not only react passively but they can play the role of an amplifier that can better transmit signals between the different components of the Earth system.

I propose to start with the study of a reasonably simple system, looking at the catchment-fan systems of the Death Valley Area. In this first chapter I will show how the burial of an active fault scarps leads to accumulation of tectonic slip and its sudden release in the form of a waterfall, that can retreat in the headwaters carrying the tectonic information of seismic slip. The crux of it is that if the alluvial fans of the piedmont react to climatic changes, as they most often do, then the tectonic signal released in the high range inherits a climatic component.

The second chapter focuses on the dynamics of incision of a river in an alluvial fan. In this theoretical work, I investigate the elementary feedbacks that lead to enhanced vertical incision over lateral erosion during the course of an entrenchment phase and how they affect the pace and geometry of incision. In this chapter we also discuss the how to make the best use of fill and fill-cut terraces to identify and quantify external forcing. This work is largely inspired by the field sites of the north piedmont of the Eastern Tian Shan which is the focus of the rest of the thesis manuscript.

In the third chapter, I explore the evolution of the deeply incised Tian Shan

piedmont since Mid-Pleistocene based on a large dataset of terrace abandonment ages that I complemented, and on new age constraints in the exposed stratigraphy of the alluvial fans. These burial ages open a new window into the history of the piedmont and extend the record far beyond the information held in terraces. We propose that the piedmont responded strongly to precessional cycles over the last 0.5 Myrs and repeatedly aggraded and incised over 100-300m because of the glacial reaction to changing Westerlies. With this knowledge I also establish that the flux of coarse sediment leaving the piedmont for the basin today contains a mixture of older sediments remobilized during incision as old as 400 ka.

For the fourth chapter, I step back and discuss how the imprint of alpine glaciers restricted to high mountains control the morphodynamics of the downstream piedmont. I show how the same climatic forcing can have opposite effects in the piedmont morphology depending on this imprint.

In the final chapter I lay down the foundation of a numerical tool that helps predict the amount of sediment mixing across a piedmont depending on its fundamental length- and timescales. This sediment transfer function can lead to better sampling strategies and improve the interpretation of the sediment record.

With this contribution I show that we can quantify the amount of mixing and buffering that occurs across a piedmont, and I sketch the outline of an approach that the sedimentology community will be able to use in the future. With a quantitative handle on the degree of mixing and buffering along the sediment routing system, the quality of paleoclimatic reconstructions and tectonic studies should improve. My approach was designed in the north Tian Shan but it was not designed for it: the reflection and the tools I propose here are adaptable to any sedimentary system.

References

Allen, Philip A (2005). “Striking a chord”. In: *Nature* 434.7036, pp. 961–961.

Allen, Philip A (2008). "From landscapes into geological history". In: *Nature* 451.7176, pp. 274–276.

Bull, W B (1991). *Geomorphic responses to climatic change*. New York: Oxford University Press.

Molnar, Peter and Philip C England (1990). "Late Cenozoic Uplift of Mountain-Ranges and Global Climate Change - Chicken or Egg". In: *Nature* 346.6279, pp. 29–34.

Romans, B W et al. (2015). "Environmental signal propagation in sedimentary systems across timescales". In: *Earth-Science Reviews* 153, pp. 7–29.

Chapter 2

FORMATION OF WATERFALLS DUE TO INTERMITTENT BURIAL OF ACTIVE FAULTS

with Michael P. Lamb[1]

In review at GSA Bulletin

Abstract

Waterfalls commonly exist near bounding faults of mountain ranges, where erosional bedrock catchments transition to depositional alluvial fans. We hypothesize that aggradation on alluvial fans can bury active faults, and that the faults accumulate slip in the subsurface to produce a bedrock scarp. Following entrenchment of the alluvial fan, the scarp can be exposed as a waterfall. To explore this hypothesis, we derive a geometric model for waterfall height which depends on alluvial fan length and the relative timescales of tectonic uplift, a forcing time for cycles of fan aggradation and entrenchment, and a response time for fan aggradation to respond to changes in sediment flux. We find that the model is consistent with observations at Gower Gulch, Death Valley, CA, where a man-made drainage capture event in 1941 caused rapid fan incision and exposed a waterfall at the canyon-fan transition. We also compare the model to 62 Pleistocene waterfalls in 18 catchments of the Death Valley area, and find that at least 15 of the waterfalls are best explained by the fault burial mechanism. Using field measurements of grain size and channel geometries, we show that the fault-burial mechanism can produce the observed waterfall heights, measuring 4 to 19 m, under a uniform climatic forcing requiring variations of 20% in precipitation during the Late Pleistocene. The fault burial mechanism, through the creation of upstream propagating waterfalls, may allow catchment-fan systems to experience frequent cycles of enhanced erosion in catchments and deposition on fans, that likely convolves tectonic and climatic signals.

[1]Division of Geological and Planetary Sciences, California Institute of Technology, Pasadena, CA 91125, USA

2.1 Introduction and motivation

Waterfalls and steep bedrock steps are important components of mountain river systems; they can serve as an agent to transfer tectonic, climatic, or autogenic signals upstream through a catchment (e.g. Howard, 1994; M. K. Clark et al., 2005; Wobus, Tucker, and R. S. Anderson, 2006; Berlin and R. S. Anderson, 2007; Whipple, DiBiase, and Crosby, 2013; DiBiase, Whipple, Lamb, et al., 2014). Retreating waterfalls and steps can produce fluvial terraces that are significant in tectonic and climatic studies (Crosby and Whipple, 2006; Finnegan and Balco, 2013; DiBiase, Whipple, Lamb, et al., 2014). Their migration forces a pulse of erosion by lowering the local base level of the adjacent hillslopes, and temporarily increases sediment delivery to the fluvial system (Humphrey and Heller, 1995; Carretier and Lucazeau, 2005; Gallen et al., 2011; Attal et al., 2015).

Several mechanisms and origins have been proposed to account for the formation of waterfalls in specific conditions. The relative eustatic forcing of sea cliffs results in knickpoints and waterfalls (Hayakawa and Matsukura, 2003; Bishop et al., 2005; Mackey et al., 2014). Large slumps can initiate waterfalls (Lamb, Howard, et al., 2007). The preexisting topography of deep glacial valleys with vertical walls creates spectacular waterfalls. Differential incision rates between trunk stream and tributary can also create waterfalls at their confluence (Hayakawa and Matsukura, 2003). Cutoffs in bedrock meanders are another way to produce waterfalls within a river system (Johnson and Finnegan, in review). Seismic slip with important throw can create waterfalls, like along the Tachia River in Taiwan following the 1999 Mw 7.6 Chi-Chi earthquake (Chen et al., 2002; Y. H. Lee et al., 2005; Huang, Pan, and Liao, 2013). Climatic forcing can also lead to the widespread creation of waterfalls (Crosby and Whipple, 2006). Waterfalls can develop at lithological boundaries with great changes in erodibility (Cook et al., 2009) or in vertically bedded substrates (Frankel, Pazzaglia, and Vaughn, 2007). Finally, steepening of bedrock reaches and the coalescence of small steps in bedrock river channels form autogenic waterfalls in upstream reaches (Sklar and Dietrich, 2004; Chatanantavet and Parker, 2009; Whipple, DiBiase, and Crosby, 2013).

Despite this work on waterfall mechanisms, many waterfalls exist without a

clear mechanism. For example, significant waterfalls are common near the outlet of fault-bounded mountain catchments in the Death Valley area in the southwest US (Figure 2.1, this study). Many of these waterfalls have heights too large to be explained by co-seismic throw and no clear lithological controls can account for their sizes. To help explain these anomalous waterfalls — building off ideas of Humphrey and Heller (1995), Carretier and Lucazeau (2005), and Pepin, Carretier, and Herail (2010) — Finnegan and Balco (2013) recently proposed a new mechanism to account for large waterfalls in the lower reaches of a catchment: the aggradation of an alluvial fan immediately downstream of an active dip-slip fault can bury the fault. It raises the relative base level of a catchment and tectonic slip can accumulate to that new level. If the fan incises again, it then exposes a waterfall that can retreat upstream. We call it the fault-burial mechanism. The transport-limited rivers flowing on alluvial fans are sensitive to environmental changes. Their slope scales inversely with water discharge (Gilbert and Murphy, 1914; Mackin, 1948; Hooke, 1968) and scales positively with the ratio of sediment flux over water discharge (Schumm, 1973; Leopold and Bull, 1979). This makes alluvial fans very dynamic landforms that can regularly aggrade and incise because of climatic forcing Poisson and Avouac (e.g. 2004) and D'Arcy, Roda Boluda, et al. (2014) or autogenic processes (Carretier and Lucazeau, 2005; Nicholas and Quine, 2007; Dijk, Postma, and Kleinhans, 2009; Reitz and Jerolmack, 2012). The fault-burial mechanism, which was also formulated by (DiBiase, Whipple, Lamb, et al., 2014) for the San Gabriel Mountains, has the potential to explain waterfalls in the Death Valley area and many more sites. This mechanism has not yet been formalized and tested with a model or focused fieldwork.

In this study, we test if the intermittent burial of active dip-slip fault scarps by cyclically aggrading and incising alluvial fans is a good mechanism to create waterfalls at the base of catchments. First we formalize mathematically the geometry of the fault-burial mechanism and use empirical laws to link waterfall heights with changes in water discharge that control fan slopes. Second, we take advantage of the engineered Gower Gulch catchment in Death Valley to test the relationship between waterfall height and water discharge variations in a controlled field site. Third, we apply the hypothesis to unexplained waterfalls of the Death Valley area where we compare the change in precipitation required to aggrade and incise the alluvial fans to bury and expose scarps as high as

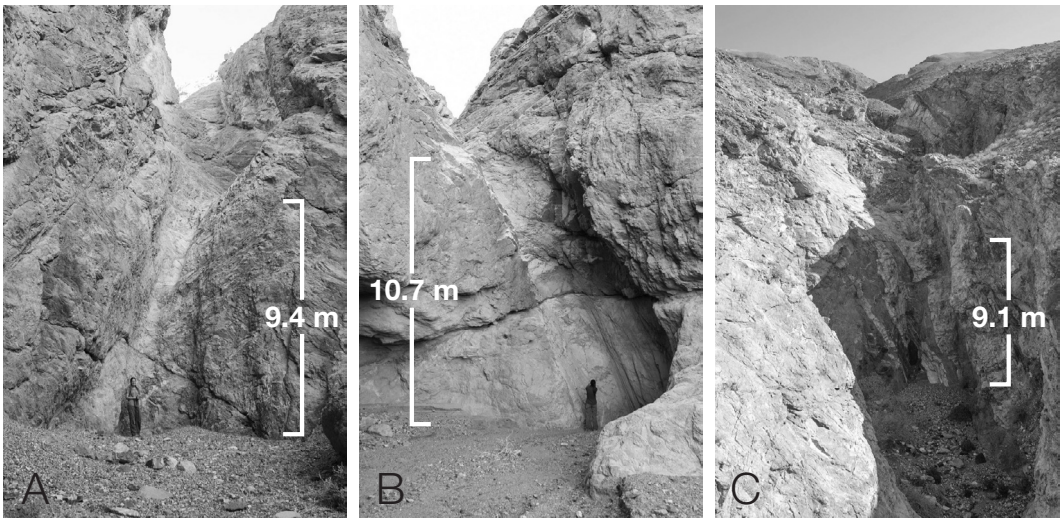

Figure 2.1: Field examples of waterfalls lying very close to the fan apex: in Death Valley's Black Mountains: A) Badwater and B) South Badwater 4; in Panamint Valley's eponymous mountains: C) South Park Canyon. See Figure 4 for location.

the surveyed waterfalls to the regional climatic record of wet and dry episodes in the Late Pleistocene.

2.2 Model for waterfall generation

Of the many landscapes that combine active faults and alluviation, we choose to conceptualize the fault-burial mechanism in coupled catchment-fan systems. Coupled catchment-fan systems are small, self-contained, complete sediment routing systems that are well studied as elemental landscapes to understand the fundamental dynamics ruling larger systems (Allen and Densmore, 2000; Densmore, Allen, and Simpson, 2007; Rohais, Bonnet, and Eschard, 2012). They can be summarized as the combination of a catchment draining an uplifting block and of a basin in relative subsidence where the sediments eroded from the catchment are entirely captured and form an alluvial fan. Essentially, sources and sinks of the sediment routing system are immediately adjacent and the transport path is relatively short. It has been argued that the evolution of downstream fans can influence upstream dynamics by varying at a relatively high frequency the base level of the upstream catchment (Humphrey and Heller, 1995; Carretier and Lucazeau, 2005; Pepin, Carretier, and Herail, 2010).

Here we investigate the mechanism of waterfall formation by shielding of the fault scarp driven by periodic changes in the alluvial channel-bed slope of a catchment-fan system, as proposed initially by Finnegan and Balco (2013). Our goal is to explore this idea as simply as possible using a 1-D model for the long-profile evolution of a catchment-fan system. In our conceptual model, a vertical dip-slip fault separates the uplifting and subsiding domains. We simplify the upstream end of the fan by assuming that a fluvial channel bridges the bedrock to alluvium transition, and we do not address channels dominated by debris flows. Elevation is fixed relative to base level and uplift U is uniform in the uplifting reach. We drive intermittent burial of the fault scarp through aggradation on the fan driven by changes in alluvial river-bed slope. For example, alluvial rivers can change their bed slope in response to changes in subsidence, grain size, channel width, water discharge, Q_w, and sediment supply, Q_s (Lane, 1937; Leopold and Maddock Jr, 1953; Lane, 1955; Knox, 1975; Bull, 1991). On small alluvial fans, channel slopes vary with these parameters but tend to remain only lightly concave up or linear across the fan (Bull, 1964; Densmore, Allen, and Simpson, 2007). Here, we model fan slopes as linear for simplicity.

Consider the simple geometry where the alluvial channel on the fan alternates between two linear slopes that hinge on the same base level so that the channel always ends at the same point (Figure 3.6). This type of fan geometry occurs, for example, if there is an axial channel along the toe of the fan that removes sediment there, or if fan aggradation is balanced by subsidence so that the toe of the fan is fixed. A forcing timescale, which could be allogenic or autogenic, would pace the alternation between steep and shallow channel configurations. A transition from low-slope (Figure 3.6 A) to steep-slope (Figure 3.6 B) configuration results in channel aggradation which drives a wedge of aggradation upstream of the fault scarp, burying the bedrock scarp (e.g. Frankel, Owen, et al., 2015). Erosion of the bedrock scarp at the canyon-fan transition stops as long as it is shielded under alluvium. The elevation of the now-buried bedrock bed immediately upstream of the scarp increases with repeated earthquakes, thinning the alluvial cover until bedrock is again exposed in the river bed at the scarp (Figure 3.6 C). When the fan transitions back to the low-slope configuration, the exposed fault scarp forms a waterfall (Figure 3.6 D). The waterfall then retreats upstream to propagate the base-level fall

through the catchment. The fault-burial mechanism allows tectonic slip to accumulate over several seismic cycles and results in waterfalls heights that can be multiple times larger than a coseismic throw.

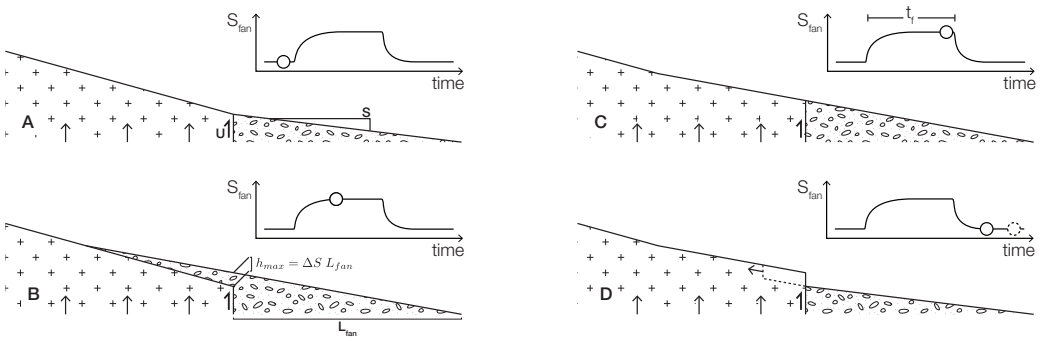

Figure 2.2: Illustration of the fault-burial mechanism in Regime I: a river flows from a steadily uplifting bedrock to the left on an alluvial fan. The inset plots show the evolution of the alluvial equilibrium slope, S_{fan}, over time as the system is disturbed by a phase of aggradation followed by a return to initial conditions. A: at equilibrium the alluvial fan grades into the bedrock channel at the scarp where a break in slope reflects the change from detachment-limited to transport-limited equilibriums. B: A change in equilibrium slope S_{fan} forces aggradation of the fan, and the bedrock channel backfills, effectively shielded from fluvial erosion until the alluvium is stripped. The maximum height of the future waterfall is set by the thickness of alluvium above the scarp. C: uplift brings the entire bedrock reach to the surface during the shielding period. D: when the fan incises to return to its initial shallow slope it exposes a waterfall at the location of the scarp. The tectonic displacement thus accumulated is released at once and retreats upstream in the drainage (dashed profile).

In this simple scenario the maximum height of the scarp, h_{max}, is the product of the change in equilibrium alluvial-bed slope, ΔS, and the length of the fan, L_{fan}, or:

$$h_{max} = \Delta S \; L_{fan}. \tag{2.1}$$

Here we assume that the alluvial fan has a stable length L_{fan} set by the fault slip rate following Allen and Densmore (2000). To model fans with radial profiles departing strongly from the linear slope assumption, the slope characterization in Equation 1 would need to be adjusted. Equation 2.1 is a maximum exposed scarp height because the timescale of forcing, t_f, during

which the fan is in a steep-slope configuration might be shorter than what is needed for the uplifting bedrock scarp to grow to its full potential h_{max}. The waterfall height might also be limited because a fan may adjust slowly in response to allogenic forcing (e.g. climate), and therefore not reach its equilibrium steep transport slope within the forcing timescale. These two scenarios highlight three important timescales for determining exposed scarp height by this mechanism. 1) The forcing timescale, t_f, sets for how long the fan stays in a steep equilibrium geometry, and is determined by external forcing like climate change or internal catchment-fan dynamics like a mass wasting event. 2) The sedimentary timescale, t_s, determines how long it takes for the alluvial channel to aggrade to the new higher elevation at the scarp. t_s is a function of the volume, V, necessary to aggrade to the new geometry and of the sediment flux from the catchment — the product of erosion rate, E, and drainage area, A — to fill this volume. However the pattern and rate of sediment deposition on the fan depends on [list what these are- patterns of downstream fining, subsidence, etc], so that in general: $t_s =\leq V/(E\ A)$. 3) The uplift timescale, t_u, is the time it takes for the fault scarp to be uplifted to the elevation of the new base level. The uplift timescale is simply the maximal height of aggradation at the scarp divided by the uplift rate:

$$t_u = \frac{h_{max}}{U}. \tag{2.2}$$

The relative durations of t_f, t_u, and t_s define three regimes of waterfall heights (Figure 2.3). In Regime I, the forcing timescale is the longest ($t_f > t_u$ & $t_f > t_s$), the scarp has enough time to aggrade and steepen to the new base level, and the scarp height reaches its maximum value given by Equation 2.1 (Figure 3.6). In Regime II, the uplift timescale is the longest ($t_u > t_f$ & $t_u > t_s$), the scarp does not grow fast enough to reach the new base level before the alluvial channel incises again, and the scarp height is limited to

$$h_{up} = U\ t_f = h_{max} \left(\frac{t_u}{t_f} \right)^{-1}. \tag{2.3}$$

In Regime III, the sedimentary timescale is the longest ($t_s > t_f$ & $t_s > t_u$), and the alluvial aggradation rate at the scarp limits the growth of the future waterfall to h_{sed}, which is the total alluvial thickness gained at the scarp at the end of the forcing period. Regime III does not have an analytical solution

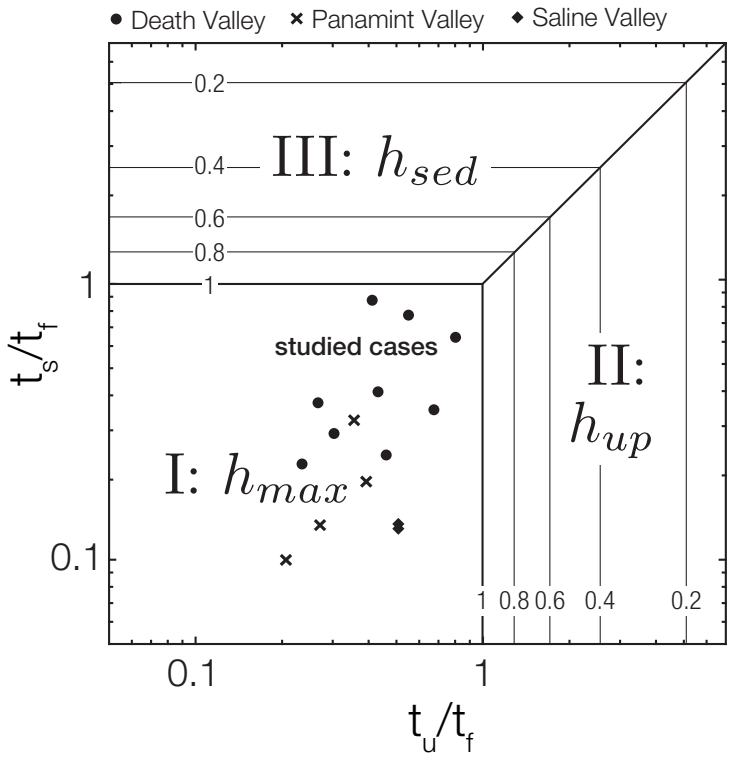

Figure 2.3: Three timescale regimes determine the effective height of the scarp: I) maximal height h_{max} , II) the total uplift reached during the shielding period, h_{up} , and III) the thickness of sediment aggradation, h_{sed} , at the scarp. The regimes depend on the relative durations of the forcing, sedimentary and uplift timescales (t_f, t_s, and t_u respectively). The contour lines mark waterfall heights normalized by h_{max}. The relative timescales of the sites of Saline, Panamint, and Death Valley are indicated with circles, crosses and diamonds respectively.

for scarp height because it requires modeling changes in river profile through time. However, by inspection of Figure 3 we see that Regimes II and III share a common boundary where $t_u = t_f$. Uplift and sediment-limited heights must be conformable along this boundary so that

$$h_{sed} = h_{max} \left(\frac{t_s}{t_f} \right)^{-1} . \tag{2.4}$$

We normalize Equations 2.3 and 2.4 by h_{max} to obtain three non-dimensional formulas that are function of the axes of the regime plot shown in Figure 2.3.

2.3 Model application to external forcing

The conceptual model we put forward can be explored in field cases where simple fan-catchment systems contain large unexplained waterfalls. After establishing the timescales t_f, t_u, and t_s, the model regime can be determined and the expected waterfall height defined. Changes in alluvial river slope following climate change are often attributed to the variations in water discharge and sediment flux (Gilbert and Murphy, 1914; Mackin, 1948; Hooke, 1968; Schumm, 1973; Leopold and Bull, 1979). In particular, an increase in the ratio of sediment supply to water discharge, Q_s/Q_w, is thought to cause an increase in the channel-bed slope on the alluvial fan and result in fan aggradation, whereas a decrease in Q_s/Q_w should drive fan entrenchment (S G Wells and A M Harvey, 1987; Adrian M Harvey, Wigand, and Stephen G Wells, 1999; DeLong, Pelletier, and Arnold, 2008; Rohais, Bonnet, and Eschard, 2012). Channel width, W, is also expected to change with changes in water discharge (Leopold and Maddock Jr, 1953). In addition climatic changes can affect sediment grain sizes, D, that are supplied to channels from hillsides and through the greater competency of higher discharge flows (Paola, Heller, and Angevine, 1992; D'Arcy, Whittaker, and Roda Boluda, 2016).

The waterfall height in regime I is set by the change in channel slope, ΔS, and the length of the fan, L_{fan} (Equation 2.1). L_{fan} can easily be measured on maps and satellite images. ΔS can be measured if the fan is presently at the shallow equilibrium configuration and the relict higher gradient configuration is preserved in the fan morphology. Otherwise, and more commonly, the shallow slope is buried and only the steep slope is observable in the field. The shallow slope can then be deduced with hydraulic resistance equations under the assumption of constant bankfull Shields stress $\tau_{\star bf}$ (Paola, Heller, and Angevine, 1992) as described below.

The geometry of a transport-limited alluvial channel is largely set by the hydraulic parameters of water discharge and sediment transport capacity, Qsc, as well as the sediment grain size (Parker, 1978). Conversely, we can retrieve hydraulic parameters from surveyed channel geometries using empirical equations. Water discharge is evaluated from measurements of channel width,

bankfull depth, h, flow velocity, u, following conservation of mass

$$Q_w = u\, h\, w. \tag{2.5}$$

Flow velocity, in turn, can be estimated using a version of the Manning-Strickler relation for the resistance of steady uniform flow as formulated by (Parker, 1991):

$$\frac{u}{u_\star} = 8.1 \left(\frac{h}{k_s}\right)^{1/6}, \tag{2.6}$$

in which $u_\star$ is the bed shear velocity and k_s is the bed roughness length scale. Bed load sediment transport capacity, Q_{sc}, is determined by an empirical law (Meyer-Peter and Müller, 1948; Wong and Parker, 2006), henceforth abbreviated ?MPM?:

$$\frac{Q_{sc}}{(RgD^3)^{1/2}} = 4.6\, W(\tau_{\star sf} - \tau_{\star c})^{8/5}, \tag{2.7}$$

where R is the submerged density of the sediment, $\tau_\star$ is the bankfull Shields number, and $\tau_{\star c}$ is the critical Shields number. Most self-formed alluvial rivers tend towards a certain value of the Shields stress at bankfull, which depends on the bed grain size (e.g. Paola, Heller, and Angevine, 1992; Parker et al., 2007; Trampush, Huzurbazar, and McElroy, 2014). The total bankfull Shields stress is partitioned between that due to skin friction and morphological form drag stress: $\tau_{\star T} = \tau_{\star sf} + \tau_{\star m}$ (Einstein and Barbarossa, 1952). The Shields number for morphologic form drag, $\tau_{\star m}$, accounts for the roughness of the stream bed and banks, and the skin friction component, $\tau_{\star sf}$, drives sediment transport. for For steady and uniform flow, the total bankfull Shields stress can be written as

$$\tau_{\star T} = \frac{hS}{RD}. \tag{2.8}$$

We combine Equations 2.5, 2.6, 2.7, and 2.8 to obtain an equation for the equilibrium slope as a function of sediment and water fluxes:

$$S = \left\{ \left[\left(\frac{Q_s}{4.6W(RgD^3)^{1/2}} \right)^{5/8} + \tau_{\star cT} \right] \frac{\tau_m}{\tau_T} RD \left[\frac{8.1 W g^{1/2}}{Q_w k_s^{1/6}} \right]^{3/5} \right\}^{10/7} \tag{2.9}$$

Equation 2.9 illustrates how alluvial slope is sensitivity to changes in Q_w, Q_s, W and D (Figure 4). Equation 8 can be combined with Equation 2.1 to calculate the maximum waterfall height, h_{max}, for given environmental changes that

produce a change in channel-bed slope. Depending on the relative magnitudes of timescales t_f, t_u, and t_s, the expected waterfall heights in the uplift or sedimentation limited regimes, h_{up} and h_{sed} , then can be found from Equations 2.3 and 2.4. On the other hand, if waterfall heights can readily be measured in the field, Equations 2.1 and 2.9 can be used to invert for changes in one of the controlling parameters: Q_w, Q_s, W or D that are needed to produce a waterfall of a known height by the fault burial mechanism. In the next section we develop this idea further to invert waterfall heights for paleo-river discharge.

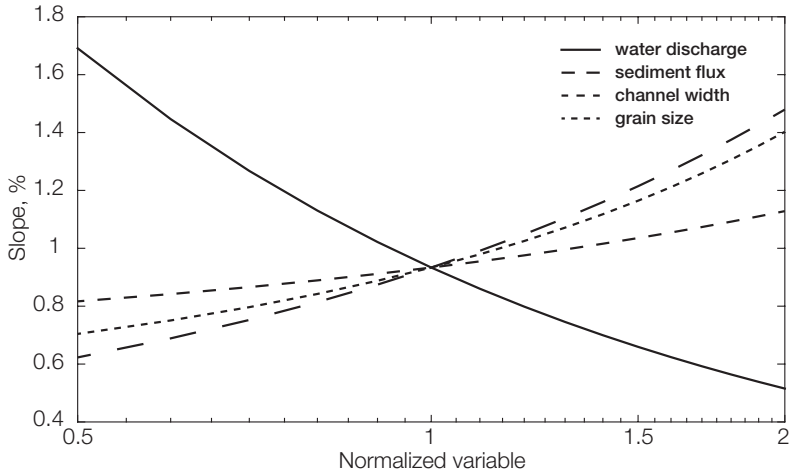

Figure 2.4: Effect of changes in water discharge (Q_w), sediment flux (Q_s), channel width (W) and grain size (D) on the equilibrium slope (S) of an alluvial river (Equation 2.9). Each of the four parameters is individually changed from half to double its reference value on the x-axis. At x=1, the reference values are $Q_w = 1$ [m^3/s], $Q_s = 0.005$ [m^3/s], $W = 10$ [m], and $D = 0.01$ [m].

Inverting waterfall heights for paleo-discharge

We cannot expect climate forcing to uniquely affect a single variable in a catchment-fan system. However, we argue that for small catchment-fan systems, it is reasonable to consider changes in water discharge as the first-order driver of channel slope variations on the alluvial fan while keeping other parameters, and in particular Q_s, fixed. It is partly justified if the catchments are near topographic equilibrium, such that sediment supply is in balance with tectonic uplift, and tectonic forcing has not changed in the Late Pleistocene, as is the case in the Death Valley area (Jayko, 2005; J. Lee et al., 2009; Frankel, Owen, et al., 2015). Climate change might also induce variations in hillslope

storage of sediment (Bull, 1991; Adrian M Harvey, Wigand, and Stephen G Wells, 1999; DeLong, Pelletier, and Arnold, 2008), but storage is expected to be small in steep, rapidly uplifting landscapes (Lamb, Scheingross, et al., 2011) typical of the semi-arid Southwestern US where we apply the model. Changes in channel bed slope can also be driven by variations in the size of sediments transported by the stream (Lane, 1937; Leopold and Maddock Jr, 1953), but the catchments of the study area drain similar bedrock types and possible drainage capture would not change the nature of the bedload (Jayko, 2005). We nevertheless recognize changes in sediment flux, grain size, and channel width are expected to scale positively with increased water discharge (Figure 2.4). These effects would partly offset the inferred change in channel slope caused by Q_w alone, and lead to smaller waterfalls by the fault-burial mechanism. Changes in river bed slopes can also result from autogenic mechanisms (Nicholas and Quine, 2007; Dijk, Postma, and Kleinhans, 2009; Reitz and Jerolmack, 2012), but the uniformity of the field sites we use — all are currently aggraded in a steep geometry (as discussed in Field Sites and Methods) — supports the argument of uniform external forcing. As we will show, our inferred water discharge changes inverted from measured waterfall heights are regionally consistent and are comparable to independent precipitation proxies.

Here we show how measurements of waterfall height, along with other field measurements, can be used to infer paleo-river bankfull discharge. If the change in river bankfull discharge is a result of climate change, then we would expect similar changes in other rivers across the field area. Assuming that the catchment is currently in a steep configuration, from field work we obtain the modern channel-bed slope S_{steep}, channel width W, and median bed grain size, D. By rearranging equations 2.5 and 2.6, the bankfull discharge for the steep configuration can be estimated from:

$$Q_{w\ Low} = 8.1W \left(\frac{\tau_\star RD}{S_{steep}}\right)^{11/6} \frac{gS_{steep}^{1/2}}{k_s^{1/3}}. \tag{2.10}$$

The higher bankfull water discharge can also be found from equations 2.5 and 2.6, except in this case the channel bed slope, $S_{shallow}$, is inferred from the waterfall height from equation 2.1, that is $S_{shallow} = S_{steep}?(h_{max}/L_{fan})$.

Thus, the high bankfull water discharge becomes:

$$Q_{w\,High} = 8.1W \left(\frac{\tau_\star RD}{S_{steep} - \frac{h_{max}}{L_{fan}}} \right)^{11/6} \frac{g \left(S_{steep} - \frac{h_{max}}{L_{fan}} \right)^{1/2}}{k_s^{1/3}}. \tag{2.11}$$

The two water discharge equations (2.10 and 2.11) for the modern steep and reconstructed shallow geometries can be used in a ratio of discharges that directly reflects the magnitude of the change in bankfull discharge necessary to produce a waterfall of height h_{max} in Regime I (Figure 2.3), assuming that no other parameters changes between the two configurations except bankfull water discharge:

$$\frac{Q_{w\,High}}{Q_{w\,Low}} = \left(1 - \frac{h_{max}}{S_{steep}\, L_{fan}} \right)^{-4/3}. \tag{2.12}$$

Equation 2.12 is a function of three parameters, S_{steep}, h_{max}, and L_{fan} that can all be measured in the field and from remote sensing data. To test the validity of the model, we verify Equation 2.12 with Gower Gulch, which experienced a known man-made changes in drainage area that produced a waterfall. Next we apply the model to reconstruct discharge changes during the Pleistocene based on surveyed waterfalls in the Death Valley area.

2.4 Field sites and methods

Field sites

We apply the alluvial fault-burial mechanism in field sites of Southern California (Figure 2.5). The three locations ? Saline, Panamint, and Death Valley ? lie in the southwestern corner of the Basin and Range province where the normal faults of horsts and grabens are linked by strike-slip faults that reflect the dextral shear component of the Walker Lane (Frankel, Glazner, et al., 2008). At a regional scale, we assume uniform Late Pleistocene climatic variability in the deserts of the southwest US. Neighboring fans have faced similar changes in hydraulic forcing proportional to changes in precipitation. In most of the catchments of these sites, waterfalls and very steep knickpoints interrupt the river profiles within 100 m of the alluvial fan apex. These steps have several times the height of coseismic throw on the range bounding fault (Klinger and Piety, 2001), and so cannot be explained as a result of single earthquakes.

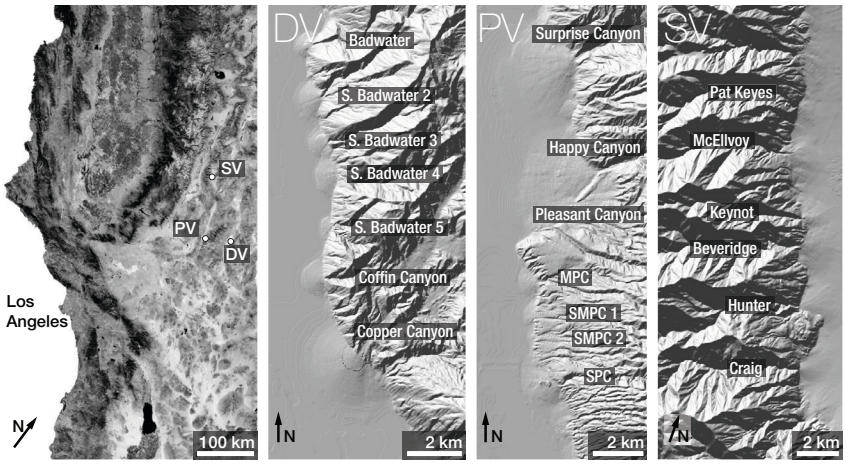

Figure 2.5: From left to right: Situation map of the field sites in Southern California with Panamint Valley (PV), Saline Valley (SV), and Death Valley (DV). Black Mountains in Death Valley. Panamint Mountains in Panamint Valley (MPC: Middle Park Canyon, SMPC1 & 2 South Middle Park Canyon 1 and 2, SPC: South Park Canyon). Inyo Mountains in Saline Valley.

In Saline Valley, the studied catchment-fan systems lie on the eastern slope of the Inyo Mountains and are separated from the valley floor by the normal and east dipping Eastern Inyo Fault (Figure 2.5 SV). The frontal fault marks the abrupt transition from the very steep catchments of the Inyo Mountains, culminating at 3384 m.a.s.l on Keynot Peak, to the flat valley floor (320 m.a.s.l.). The striking transition indicates that the Eastern Inyo Fault has consistently ruptured along the same surface scarp in the geological past. Excellent thermochronological work constrains the exhumation of the Inyo Mountains at the level of Saline Valley and sets the throw rate of the fault at 0.4-0.7 mm/yr since 2.8 Ma (J. Lee et al., 2009).

The second field site, in Panamint Valley, includes the catchments flowing west of the Panamint mountains and their respective alluvial fans (Figure 2.5 PV). The Panamint Valley Fault Zone, normal and west dipping, separates the Panamint mountains (culminating at Telescope Peak, 3367 m.a.s.l.) from the floor of the eponymous valley (315 m.a.s.l.) and is connected to the Eastern Inyo Fault by the right-lateral strike slip Hunter Mountain Fault (Burchfiel, Hodges, and Royden, 1987). Unlike the Eastern Inyo Fault, the Panamint Valley Fault Zone has a complex surface expression with several successive splay faults separating the basin from the mountain. As a consequence, alluvial fans

are often telescoped and abandoned by the changing location of the surface scarp (Numelin, Marone, and Kirby, 2007; Mason and Romans, 2015). Slip rate on the fault zone ranges from 0.1 to 2 mm/yr (Hart et al., 1989) with minimal slip rate of 0.34 mm/yr since 0.9 Ma around Ballarat, near our zone of study (Vogel et al., 2002).

The third field site lies along the Central Death Valley Fault Zone that runs at the foot of the Black Mountains, one valley east of the Panamint site (Figure 2.5 DV). The configuration of the Black Mountain catchment-fan systems on the east flank of Central Death Valley is similar to Saline Valley with a well-defined single fault trace marking the boundary between the steep catchments of the Black Mountains, peaking at Dante's view (1699 m.a.s.l.), and the flat bottom floor (85 m.b.s.l.) over which alluvial fans aggrade (Jennings, 1994). The west dipping Black Mountain Fault Zone has a normal motion and the Holocene slip rates are estimated between 1 and 3 mm/yr with average coseismic throw around 2.5 m (Klinger and Piety, 2001).

In Death Valley, we additionally use the alluvial fan of Gower Gulch (4 km south of the junction between Hwy 190 and Badwater Rd., 36° 24.6' N / 116° 50.5' W) as a controlled case study to test our hypothesis. In 1941, to protect settlements at Furnace Creek, the flows of the Furnace Creek catchment were diverted into the small mudstone catchment of Gower Gulch, effectively increasing its drainage area by a factor of about 75 (Snyder and Kammer, 2008) and routing igneous and metamorphic cobbles from the Amargosa Range through the original mudstone catchment. As a result of the increased water discharge, the alluvial fan of the enlarged catchment dramatically incised and exposed a 9.1 m waterfall at its apex, where the extensional Death Valley Fault Zone bounds the mountain (Figure 2.6).

The drainage areas of the studied catchments vary between 5 and 50 km^2 (see Table 2.2 for details), and they all share the same attributes of steep catchments (gaining on average 300 m for every horizontal km) with a high relief (1500 to 2500 m). All the alluvial fans but one (McElvoy in Saline Valley) are barely incised. They are in a steep configuration with linear profiles (Figure 2.6)corresponding to the contemporary interglacial aridity that followed the

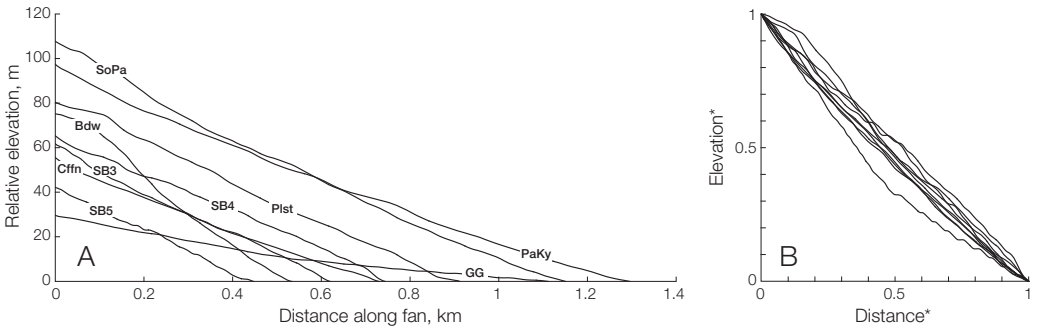

Figure 2.6: A: Radial profiles of the alluvial fans of the catchments used to test the fault-burial mechanism. The profiles are largely linear. The elevation is measured relative to the toe of the fan. The elevation is extracted from the 10 m ASTER GDEM v2 (a product of NASA and METI) using GeoMapApp (www.geomapapp.org). Canyon acronyms are GG: Gower Gulch; Bdw: Badwater; SB3, SB4 and SB5: South Badwater 3 to 5; Cffn: Coffin; Plst: Pleasant; SoPa: South Park; and PaKy: Pat Keyes. B: Stacked radial profiles normalized by their horizontal and vertical span to highlight their linear slopes.

Last Pluvial Maximum when we expect the fans to be incised by the greater water discharge.

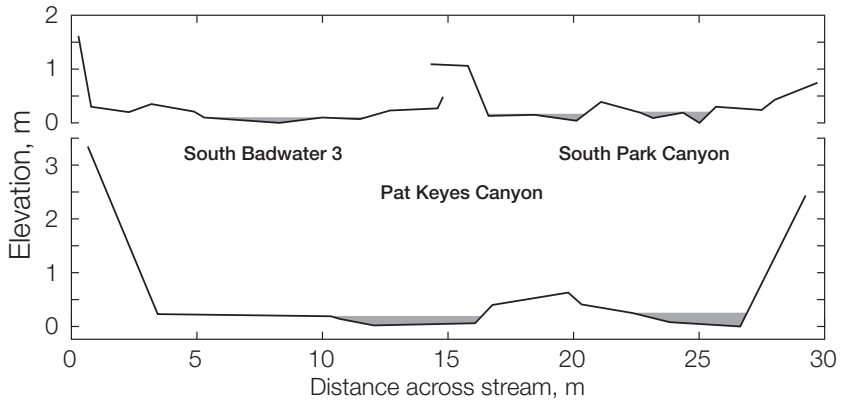

Figure 2.7: Cross-section of three of the surveyed rivers where we measured bankfull hydraulic geometry. The bankfull wetted area is represented in gray and is based on the elevation of the top of gravel bars.

The three sites experience a similar arid climate with a gradient in precipitation increasing with altitude from 0-4 cm/yr on the valley floor to 9-20 cm/yr at 1000 m.a.s.l. and above (Jayko, 2005). Rain is very infrequent and several

years of rainfall are often delivered during one intense short-lived event (Jayko, 2005). The recent climate history of the region saw an increased aridity after the moisture high of the Last Pluvial Maximum. At 20 ka, the region of Death Valley is estimated to experience about twice the amount of modern precipitation with an average temperature 5-6°C cooler than today according to paleo-lake levels (Ku et al., 1998; Lowenstein et al., 1999; Menking et al., 2004), pollen (Thompson, K. H. Anderson, and Bartlein, 1999), and oxygen isotope records (Quade, Forester, and Whelan, 2003).

Field methods and collected data

We have surveyed a total of 62 waterfalls in 18 catchments, listed in Table 2.1. We restrict the survey to the first three waterfalls within a few hundred meters upstream of the alluvial fan apex to avoid falls that could have significantly changed height as they retreated or that could be the result of coalescing steps during upstream propagation. The heights were measured from the surface of the plunge pool alluvium to the lip of the fall using a hand-held laser range under with 10 cm precision. On a few occasions, waterfalls and surrounding cliffs are impassable, limiting the survey to the first obstacle. Examples of surveyed waterfalls are shown in Figure 3.1.

We surveyed the geometry of the active channel at the fan apex in catchments selected for the analysis and a few other ones (Table 2.2). Sediment grain size values are based on the median value of the second semi-axis of 100 grains measured every 0.5 m along a survey measuring tape stretched in the along-stream direction across bars and thalweg. At a few sites, only 50 grains were measured. The geometry of alluvial reaches was recorded as a topographic profile across the channel and we used gravel bar tops as bankfull indicators to which we add the necessary water depth for sediment incipient motion. For mean bankfull depth, we use the hydraulic radius of the channel: the bankfull cross-sectional area of flow divided by the length of the wetted perimeter. The fluvial or debris-flow nature of the channels was determined by observing sorting and imbrication of clasts in the active channel and the incised channel walls, and morphology of depositional levees, lobes and snouts.

Active faults were identified from satellite imagery and topographic models

(Figure 2.5). We checked them against the significant faults map of the Southern California Earthquake Data Center (Jennings, 1994) and in the field. The many faults, active and inactive, traverse a fairly complex lithological assemblage ranging from Proterozoic metamorphics to Quaternary volcanics (Jennings, 1958) and demand close-up field inspection to identify the exact location of lithological contacts with respect to waterfalls. We used the 10m ASTER GDEM V2 (a product of NASA and METI) to survey the morphology of alluvial fans in Saline, Panamint and Death Valley. All the surveyed streams have slopes between 4 and 17%. To account for this, we choose a morphological drag of 40% ($\tau_m/\tau_T = 0.4$) of the total stress that corresponds to an average value for steep streams (Scheingross et al., 2013).

2.5 Results

Proof of concept with Gower Gulch

North of the Black Mountains in Death Valley, the Gower Gulch catchment (described above) allows us to test the approach at a site that experienced a known change in forcing (Figure 2.8). In 1941, there was an engineered channel diversion at the upstream part of the catchment which increased the drainage area 75 fold, forcing fan incision and exposing the fault scarp previously buried (Snyder and Kammer, 2008). In the incised active channel that is now relatively shallow in grade (3.7%), and coarse grained ($D_{50} = 16$ mm), has a bankfull discharge of $Q_w = 9.2$ m^3/s (Equation 2.5) and a bankfull Shields stress of $\tau_\star = 0.22$. We note that $\tau_\star$ is one order of magnitude greater than the critical Shields stress. It corresponds to the range of Shields stresses surveyed on other fans of the area in this study and to measurements by (Stock, Schmidt, and Miller, 2008)Stock et al. (2008) in the region. We postulate that a Shields stress well above the critical value for incipient motion could be a result of the flashy nature of these channels where all the transport happens during very short periods.

Unlike the active channel, there are no sediment bars in the steep (4.2%) abandoned channel that could help constrain bankfull depth. To remediate this, we use the same bankfull Shield stress calculated for the active channel, and calculated a bankfull depth of $h = 3$ cm using Equation 2.10, and obtain a water discharge of $Q_w = 0.2$ m^3/s. The measured bed grain sizes in the active channel ($D_{50} = 4.2$ mm), a factor of four finer than the active channel. We

find that the modern bankfull water discharge is 46 fold the pre-1941, and this is of the same order as the change in drainage area caused by the engineered diversion (75 fold).

At the Gower Gulch site, we can assess the validity of Equation 1 because we independently know the shallow and the steep slope configurations (3.7 and 4.2 % respectively) as well as the height of the waterfall (9.11 m). With Equation 2.1, we determine that the relevant length of the fan L_{fan} is 1.8 km. This value overshoots the fan length of 1.1 km measured from satellite imagery, but it remains a sufficient approximation. The slopes of alluvial fans are not perfectly straight and we expect discrepancies with our linear assumption (Figure 2.7).

The retreat of knickpoints through the Gower Gulch catchment after the change of hydraulic regime has been documented in Snyder and Kammer (2008). We observe additionally that the fault scarp waterfall lies 4 m in retreat of the fault plane. This corresponds to a retreat rate of more than 5 cm/yr.

Figure 2.8: Apex of the Gower Gulch fan. Gower Gulch lies 20 km to the north of Badwater in Figure 4. To the right, the picture is completed with an interpretation sketch: the abandoned steep alluvial fan surface is in medium gray, the incised channel in light gray, the dark gray plane indicates the waterfall and the upward arrows the fault plane.

Geology and geomorphology of field sites

For the case of Gower Gulch, the change in water discharge that exposed a waterfall was due to a change in drainage area under a similar climate. For

other Pleistocene waterfalls in the area, we assume that drainage area and other variables in Equations 2.1 and 2.9 were constant, and that waterfalls were exposed due to an entrenchment following a change in bankfull discharge associated with climate change. If the waterfalls in the field sites we study are the result of the fault-burial mechanism forced by climatic changes, then we expect inferred changes in bankfull discharge to be relatively uniform across all sites. First, based on our field observations we evaluate field sites for their application to the fault-burial mechanism.

The range-bounding fault in both Saline and Death Valley sites have an almost unique surface trace where slip accumulated over multiple cycles of fan aggradation and incision allowing the repetition of the fault-burial mechanism. On the contrary, complex surface faulting in Panamint Valley (Figure 2.5) is problematic. When the fault splays and creates a new surface rupture at each earthquake, cumulative tectonic displacement cannot build up on one single scarp and no waterfalls greater than the throw of a single earthquake would be created. We excluded catchments where field inspection indicate that multiple splay faults close to the waterfalls were recently active.

Our analysis is restricted to fluvially dominated fans for this study, and we exclude fans we observed to be dominated by debris flows from further analysis. In Saline Valley, five of the six sites we investigated have alluvial fans dominated by debris flow processes.

Close inspection in the field is a necessity to identify and exclude waterfalls that are controlled by lithological contacts or local faults. Lithological contrasts have the potential to allow the development of steep knickzones completely unrelated to the accumulation of tectonic throw on the front fault. For example, in Saline Valley's Craig Canyon three steep knickpoints higher than 5 m correspond to lumps of a granitic intrusion into a weaker gneissic marble. Elsewhere, in Panamint Valley's Surprise Canyon, two successive waterfalls of heights 2.4 and 3.4 m, coincide with faults crossing the bedrock channel subparallel to the waterfall plane. The faults are inactive but there is a systematic contrast of fracture density on either side of the slip plane. The hanging wall is typically densely fractured over a thickness of ca. 1 m away from the fault

plane while the footwall remains massive. This contrast conduces to a differential erodibility that explains the location of the waterfall. Many sites were discounted based on this criterion, in particular in Panamint Valley where the bedrock is heavily fractured by multiple faults. On two occasions, in the canyons of South Badwater 3 and 4, we combine successive waterfalls separated by a few meters into a total height.

Out of the 62 waterfalls we surveyed, 15 fit the three selection criteria for this study: stable fault trace, no lithological contacts, and fluvial regime (Table 2.3). The radial profiles of the fans are all largely linear.

Timescale regime of field sites

All the field sites that match the above conditions sit in Regime I where $t_f > t_u > t_s$ (Figure 2.3 and Table 2.3). We used a forcing timescale tf of half of the 23 kyr precession signal that dominates the recent climatic variability to represent the dry half of the cycle. We can therefor employ Equation 1 to describe the relationship between waterfall height and fan slopes. The forcing and uplift timescales necessary to establish the regime of a catchment are easily defined in the Death Valley area, with relatively fast fault slip rates and orbital climatic forcing. The sedimentary timescale is more difficult to establish because there exists no good dataset for all the catchments. Jayko (2005) provides estimates of denudation rates for the Panamint and Death Valley sites based on the volumes of alluvial fans assuming that they are built over the flat valley bottom. If the volume estimate is approximate, it has the advantage of constraining the coarse fraction of the sediment flux that builds the fan, while it underestimates the denudation rate that includes suspended and dissolved load. In Panamint, Jayko (2005) does not estimate an erosion rate for Pleasant Canyon. For lack of a better value, we average the rates calculated for the two neighboring catchments and obtain 0.11 mm/yr. For the Saline Valley field site, we use denudation rates estimated from ^{10}Be by Kirby (2013) who proposes rates of 0.7 to 1.2 mm/yr erosion in the steep lower reaches of the Inyo Mountains and 0.05 to 0.1 mm/yr in the gentler upstream catchment. About 40% of the Pat Keyes catchment is shallow and 60% is made of steep reaches. Using Kirby's rates, the average denudation rate in this catchment would be 0.6 mm/yr in this catchment (Kirby, 2013). 10Be denudation rates describe the entire sediment flux (dissolved, suspended,

and bedload). Fans are built with the coarse fraction of the flux. Without estimates of the different proportions of fluxes, we suppose that the coarse load represents half of the total load at the bottom of these steep catchments. We use then a rate of 0.3 mm/yr for the Saline Valley catchment. It is not a very precise estimate but in order to bring any sites in Regime III, the erosion rates would have to be at least one order of magnitude lower than in the slowly eroding part of the Inyo Mountains (Table 2.3).

Application to Pleistocene waterfalls

For each of the 15 unexplained waterfalls we reconstruct the ratio between higher paleo water discharge and modern discharge with Equation 10. We plot the results as a ratio of water discharges between shallow (Last Pluvial Maximum) and steep (modern) river profiles in Figure 9. The Gower Gulch catchment has a 46 fold increase in water discharge (in this case pre- and post-1941), while all the other waterfalls point at a mean value of 1.19±0.14 (one standard deviation). The waterfalls of Panamint and Saline Valley require a smaller change in water discharge ratio (1.07±0.02), while the waterfalls of Death Valley require larger changes in water discharge (1.26±0.13) and display a small positive scaling between discharge ratio and waterfall height. Nevertheless, the change in water discharge that is modeled is largely uniform across the sites.

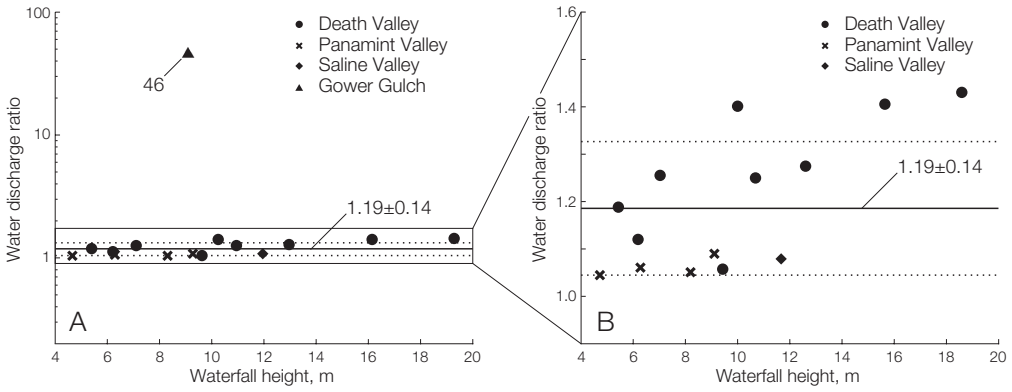

Figure 2.9: Plot of the ratio between the water discharge controlling the steep slope, calculated from the hydraulic geometry, and the water discharge reconstructed for the shallow slope. In A, the natural sites are compared with the case study of Gower Gulch. For the case of Gower Gulch, both water discharges derive from surveyed hydraulic geometries. In B, only the natural cases are plotted around the mean value and the 1-sigma confidence interval in a linear space.

2.6 Discussion

Comparison to climate proxies and uncertainties

Given the important uncertainties affecting estimates of past precipitation levels and of our own reconstructions of absolute water discharge, we cannot require a strict overlap to confirm the validity of the proposed model. Nonetheless we need to evaluate the compatibility of a regional increase of precipitation leading to a 1.19±0.14 rise in water discharge with the climate record. A sediment core in the Badwater Basin of Death Valley indicates significantly wetter conditions from 35 ka to 10 ka while Death Valley hosted the perennial Lake Manly (Lowenstein et al., 1999). A study of the LGM highstand of an endorheic lake in New Mexico, USA, suggests a doubled LGM precipitation rates in the southwestern US (Menking et al., 2004). Paleobotanical studies at Yucca Mountain, 85 km NNE of Badwater, propose from 1.3 to 1.4 or from 2.1 to 2.9 times larger precipitations at the LGM (Spaulding, 1985; Thompson, K. H. Anderson, and Bartlein, 1999, respectively). Finally, isotopic study of ostracode records in southern Nevada testifies of a wetter LGM as well (Quade, Forester, and Whelan, 2003). The requirement of a 1.19±0.14 greater water discharge for the low slope geometry is compatible with all the various climate reconstructions albeit on the lower end. Beside the general agreement between climate record and our reconstruction, the uniformity of the water discharge ratio across the field sites is more important and points at a unique external source of forcing.

Our method requires a series of assumptions that affect the absolute values of the water discharges that shaped the now buried shallower slope and thereby the ratio of high and low water discharges. However, all assumptions are identical in all field sites and any effect, skewing to greater or smaller values of Q_w, is equally applied in all our sites. This way we rely more on the relative uniformity of the Qw ratio than on its absolute value to link waterfalls and climatic variations. We sidestep the potentially problematic assumptions that we would face if our goal was to reconstruct the precise hydraulic history of a catchment.

The main uncertainty in our approach is that we only change the variable Q_w to keep the bankfull Shields stress constant with a changing slope and we ignore the co-evolution of Q_s, D, and W. The ratios of water discharges are

built keeping all other parameters constant. That results in a possible underestimate of the Q_w ratio since Q_s, D and W are expected to grow together with Q_w (Gilbert and Murphy, 1914; Leopold and Maddock Jr, 1953; Paola, Heller, and Angevine, 1992) but counteract its effect on slope (Figure 2.4).

Another potential source of error is the assumption that climatic cycles during the Late Pleistocene and Holocene were all identical. We reconstruct a single ratio of water discharges between the Last Pluvial Maximum and the modern from the surveyed waterfalls. But the waterfalls would have been created during earlier Pleistocene climatic fluctuations. At some sites we also use multiple successive waterfalls, which, by shielding and exposure, would be the products of successive climate cycles. We collapse all the different episodes onto a single value and ignore their variability. The scatter amongst the ratios presented in Figure 2.6 should be in part explained by the variability between climatic cycles.

Finally, autogenic dynamics such as landslides or drainage capture can trigger aggradation or incision of the studied alluvial fans, irrespective of climatic forcing. These internally forced events could increase the scatter between sites and/or produce waterfalls unrelated to climate forcing. Such autogenic variations in the modern are unlikely drivers in our study area as the uniformity among field sites testifies: all fans are currently aggraded in a steep geometry.

Further examples of fault-burial waterfalls

All the field sites of this study lie in a zone of fast active tectonics and are in Regime I, that is we expect waterfalls to reach the height h_{max} (Figure 2.3). For the shield-and expose mechanism to impact significantly the river system, h_{max} needs to be clearly taller than coseismic throw on the fault. If h_{max} is similar to the coseismic throw, alluvial shielding cannot accumulate displacement greater than the throw of a single event. Its only effect would merely be a delay of the release in the river system. In Death Valley, h_{max} goes up to 20 m (Figure 2.9) and largely exceeds the characteristic coseismic throw of ca. 2.5 m on the Black Mountain Fault (Klinger and Piety, 2001): alluvial shielding can release here the equivalent of two to eight earthquakes in the river system at once.

We expect Regime II in areas where the fault throw rates are not fast enough to bring the scarp to the surface. It is the case of Finnegan and Balco?s field site in the Santa Lucia Mountains of Central California (Finnegan and Balco, 2013). They proposed that Arroyo Seco?s alluvial fan aggradation and incision in Salinas Valley could shield and expose the scarp of the Reliz Canyon Fault to release a waterfall in the upstream catchment. However, with a very slow fault throw of 0.015 mm/yr (Rosenberg and J. C. Clark, 2005), cyclic aggradation-incision could only result in waterfalls of a height $h_{up} = U\ t_f = 0.2$ m with $t_f = 11.5$ kyr to represent the wet half of the dominant precession. This height would be a small fraction of h_{max} which is 30 m. according to the current incision of the stream (Finnegan and Balco, 2013). The Arroyo Secco would sit in Regime II ($t_u > t_f > t_s$). The small knickpoints could nevertheless retreat 12 km in the mudstone bedrock of the lower reach before stalling and accumulating on the crystalline core of the Santa Lucia Mountains where Finnegan and Balco (2013) document a large knickpoint that marks the upstream connection of the channel with 30 m high terraces.

In the Big Tujunga catchment of the San Gabriel Mountains in Southern California, where DiBiase, Whipple, Lamb, et al. (2014) proposed that tectonic deformation could accumulate under alluvium before being released as waterfall, the regime is difficult to identify. The extensive urbanization of the San Gabriel foothills mask the initial geometry of the alluvial fans and the shallow slope of the fan is currently buried. However we can reasonably assume that alluvial fans aggrade quickly at the base of the fast uplifting and eroding San Gabriel Mountains (DiBiase, Whipple, Heimsath, et al., 2010) and that the sedimentary timescale ts is short. With an uplift rate of around 1 mm/yr on the Sierra Madre Fault Zone (Lindvall and Rubin, 2008) and assuming a climate forcing timescale on a similar period as Death Valley (ca. 11.5 kyr), the interface between fan and scarp can then produce waterfalls equal to $h = U\ t_f = 11.5$ m. Waterfalls around that height or greater are common in the catchment (DiBiase, Whipple, Lamb, et al., 2014). Given the length of the fan, at least 7 km long today from the scarp to the Hansen Dam Flood Protection Basin, a change of slope of half a percent would result in a shielding thickness of 35 m at the scarp. The Big Tujunga Catchment would

then lie in Regime II.

Regime III requires a large alluvial fan that aggrades slowly together with a fast fault slip rate. These conditions go against the trend discussed in (Allen and Densmore, 2000) that sees the size of alluvial fans inversely correlated with fault slip rate and Regime III should rarely be met.

Role of exhumed waterfalls in fan-catchment autogenic feedbacks

Alluvial fans can undergo episodes of incision without external forcing caused by feedbacks between the fan and its catchment (Humphrey and Heller, 1995; Carretier and Lucazeau, 2005; Pepin, Carretier, and Herail, 2010), by changes from sheet to channelized flow (Nicholas and Quine, 2007; Dijk, Postma, and Kleinhans, 2009), or by channel avulsion (Reitz and Jerolmack, 2012). The fault-burial mechanism is potentially of great importance for the generation and sustainability of autogenic signals in a fan-catchment system that undergoes important autogenic incisional phases. As waterfalls retreat in a drainage basin, they force a local pulse of erosion by immediately lowering the hillslope base level (Gallen et al., 2011; Attal et al., 2015). In turn this erosion pulse will increase the ratio Q_s/Q_w and could lead to aggradation of the fan and renewed shielding of an active scarp until the erosion pulse initiated by the waterfall propagates through the entire catchment. This feedback is a potential driver to help sustain tintinnabulation of a fan-catchment system. The term tintinnabulation was employed by Humphrey and Heller (1995) to describe the dynamic state of a fan-catchment system where evolution of the one affects the other and finally reverberates as a dynamic equilibrium in the system. As a result the landscape is constantly reacting to new internal forcings that do not reflect changes in its environment.

Catchment reorganization by drainage capture will change the water discharge at the outlet and affect the equilibrium geometry of the alluvial fans lying at the outlet of the catchments. There are topographic evidences of important catchment reorganization in the Black Mountains, in particular with Coffin Canyon having captured 10% of Copper Canyon, thereby increasing its area by 80% (Jayko, 2005). Furthermore, avulsion in alluvial deposits mid-way in the catchment also has the potential to distribute discharge from a 10 km^2

sub-catchment to either Copper or Coffin Canyon. Such capture events can uncover a waterfall in a one-time event.

Implications for landscape evolution

The upstream migration of knickpoints equilibrates drainage systems to varying uplift rates and relative sea level falls (Howard, 1994). On the contrary, changes in precipitation rates affect the entire drainage simultaneously without knickpoint propagation (Bonnet and Crave, 2003). However, in the combined presence of an active fault and an alluvial fan, the fault-burial mechanism does create a knickpoint after an increase in precipitation that transmits both tectonic and climatic signals. Let us consider a coupled catchment-fan system in Regime I (Figure 2.10) forced by a cyclic climate with alternation of wet and dry phases and regular earthquakes that force base level fall (Figure 2.10 B). The alluvial fan aggrades in dry periods and incises during wet ones, alternatively burying and exposing the active fault scarp (Figure 2.10 C). Meanwhile, the fault ruptures repeatedly and coseismic waterfalls are released in the river in the absence of an alluvial shield represented in Figure 2.10 C (using the same representation introduced in Figure 2.10 A). When alluvial fill buries the scarp, tectonic slip accumulates until bedrock pierces through alluvium. In Figure 10, the fan-catchment system is in Regime I and tectonic throw reaches the new base-level during the period of shielding. At the end of this period, when the fan incises back to a shallow configuration and the total accumulated throw h_{max} is released as a large knickpoint in the river system (Figure 2.10 C). The climate-governed alluvial fan acts thus as a filter on the tectonic forcing, releasing seismic throw in rarer and bigger steps on a climatic beat (dotted vs. black line in Figure 2.10 D).

The processes controlling waterfall retreat are not yet understood and it is not clear whether and how waterfall retreat rate scales with waterfall height. Hayakawa and Matsukura (2003) propose that waterfall retreat rate scales negatively with waterfall height because the erosive force of the stream would be distributed over a greater area for larger waterfalls. In that case, releasing fewer, larger, and more slowly retreating waterfalls would augment the response time of a catchment. However, Whittaker and Boulton (2012) show that knickpoints retreat faster in regions of greater uplift. They propose that large amplitude tectonic perturbations result in shorter landscape response

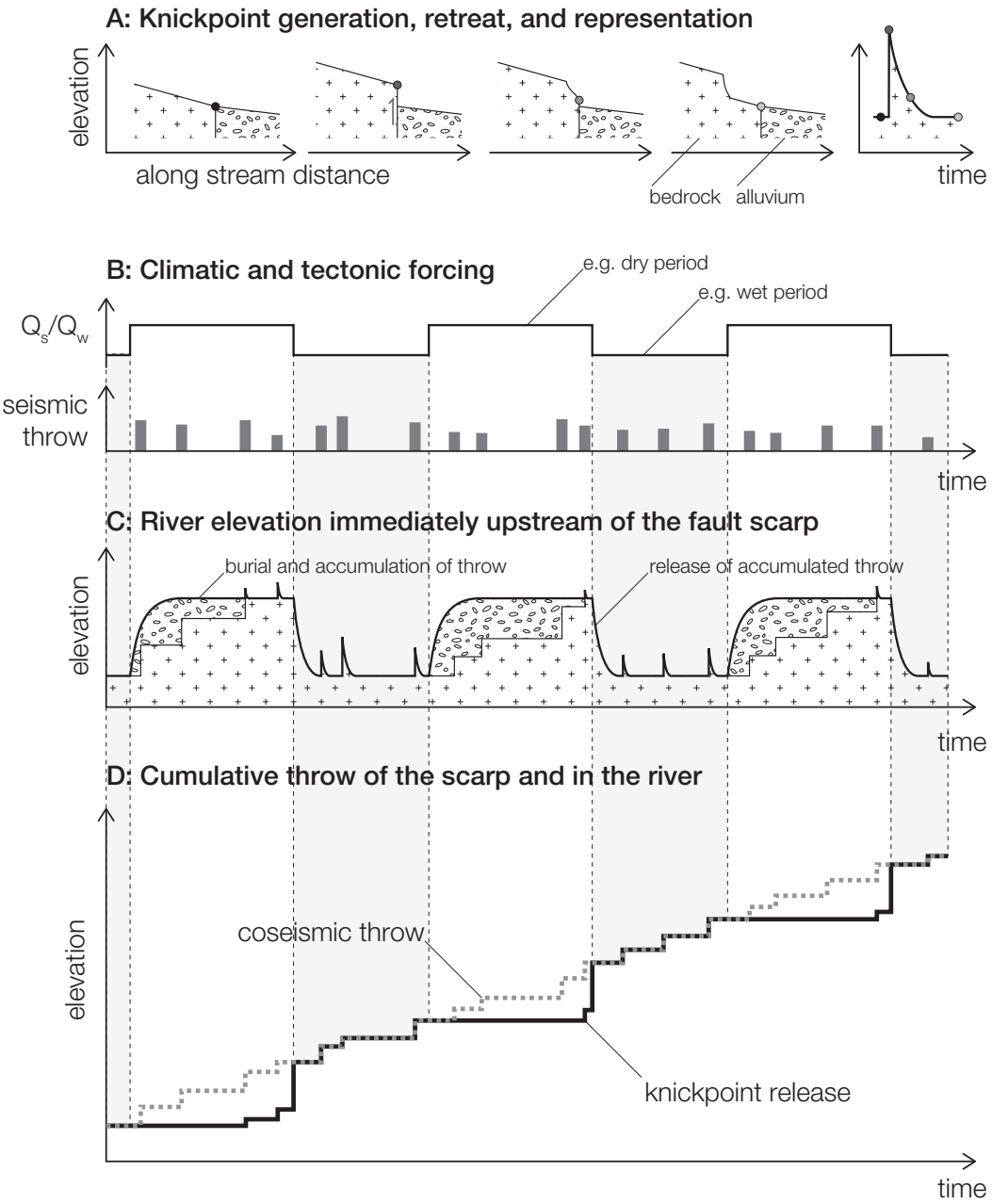

Figure 2.10: Effect of the regime I fault-burial mechanism on knickpoint release in the river system. A: The creation of a coseismic knickpoint and subsequent retreat upstream (1-4) can be represented as the elevation of the stream immediately upstream of the scarp (5). B: Let us consider a periodic climatic forcing expressed as the ratio between sediment flux and water discharge, and a tectonic forcing represented by the throw of earthquakes on the range-bounding fault. C: The elevation of the river bed immediately upstream of the fault scarp (using the representation introduced in A) shows how the tectonic and climatic forcing of B are translated into alluvial aggradation and uplift of the scarp. D: The cumulative release of waterfalls in the river system differs from the coseismic throw due to burial and incision.

times. Although waterfalls cannot be directly compared with the knickpoints of Whittaker and Boulton (2012), the relationship between faster retreat rates and greater disturbances along the river profile could hold for single waterfalls and very steep knickzones. Additionally, if all or part of the retreat of a waterfall results from the impact of sediments on canyon walls during free fall, then higher waterfalls should result in more energetic impacts and the retreat rate should scale positively with waterfall height (Lamb and Dietrich, 2009). Faster retreat rates for larger waterfalls would suggest that the discrete release of accumulated slip shortens the landscape reaction time and enhance its reactivity (Allen, 2005). As these knickpoints are exposed according to a climatic beat, they have the capacity to reduce the damping of climate-driven sediment fluxes (Armitage et al., 2013) and thereby improve the sensitivity of the sedimentary record to higher-frequency cycles in the purely denudational domain. In consequence, the fault-burial mechanism has the potential to extend the high-frequency fidelity of alluvial systems (Simpson and Castelltort, 2012) to the upstream detachment-limited reaches.

2.7 Conclusion

We demonstrate here that waterfalls can be created over an intermittently alluviated dip-slip fault. Burial of the fault scarp by sediments during periods of alluvial aggradation allows the accumulation of tectonic slip and its sudden release during subsequent incision. We establish three timescales controlling the generation of waterfalls: they are the forcing, uplift, and sedimentary timescales. The relative lengths of these timescales define three regimes in which waterfall height can be calculated with analytical solutions. The maximum height of a waterfall produced by fault burial depends on the length of the alluvial fan and its shallow and steep slopes.

We tested and validated the fault-burial mechanism against a fully constrained, man-made, alluvial fan incision driven by a 75-fold change in drainage area in Gower Gulch (Death Valley, CA) that led to the uncovering of a 9.1 m waterfall at the active fault scarp.

We showed that the fault-burial mechanism can relate otherwise unexplained waterfalls of 4 to 19 m in the Death Valley area to 20% variations in precip-

itations during the Late Pleistocene and Holocene. The wet-dry cycles led to the aggradation and incision necessary for fault burial.

The fault-burial mechanism is relevant wherever surface tectonic deformation is intermittently covered by sediments. Through the modulation of waterfall heights, the fault-burial mechanism can affect the response time of a landscape to downstream forcing by changing the retreat rate of knickpoints. Waterfalls created by climate driven aggradation and incision convolve tectonic and climatic signals.

Acknowledgment

We thank Austin Chadwick, Alistair Hayden, Marisa Palucis, and Victoria Stevens for support in the field; Mitch d'Arcy and Roman DiBiase for fruitful discussions. This work was supported by a Doc.Mobility Fellowship of the Swiss National Science Foundation (project number: P1SKP2 158716) for Malatesta, NSF grant #1147381 and ACS PRF grant #53204-ND8. Field work in the Death Valley National Park is registered as study # DEVA-00409 with permit # DEVA-2014-SCI-0040.

2.8 Tables

Table 2.1: List of the surveyed waterfalls in Saline, Panamint, and Death Valley with their location and the main characteristics of each site that determine their selection for the demonstration. The acronyms for catchments are Bdw: Badwater; SB: South Badwater; C: Canyon; M Park: Middle Park; SMP: South Middle Park. For the lcoation of the catchments, see Figure 2.5.

Catchment	**Waterfall #**	**Height [m]**	**UTM Quad**	**UTM E [m]**	**UTM N [m]**	**Channel**	**Fault Trace**	**WTF Cause**	**Selection**
Gower G	WTF 1	9.11	11S	514276	4029525	fluvial	unique	shield	yes
Bdw	WTF 1	9.44	11S	521618	4009049	fluvial	unique	shield	yes
SB3	WTF 1	12.6	11S	521132	4005658	fluvial	unique	shield	yes
SB3	WTF 2	2.03	11S	521201	4005646	fluvial	unique	shield	yes
SB3	WTF 3	4.16	11S	521244	4005641	fluvial	unique	shield	yes
SB3	WTF 4	25.98	11S	521300	4005687	fluvial	unique	coalescence?	no
SB4 (N)	WTF 1	4.39	11S	521627	4004662	debris flow	unique	shield	no
SB4	WTF 1	4.74	11S	521497	4004446	fluvial	unique	shield	no
SB4	WTF 2a	4.56	11S	521527	4004441	fluvial	unique	shield	yes
SB4	WTF 2b	5.55	11S	521527	4004441	fluvial	unique	shield	yes
SB4	WTF 2c	5.53	11S	521527	4004441	fluvial	unique	shield	yes
SB4	WTF 3a	2.97	11S	521527	4004441	fluvial	unique	shield	no
SB4	WTF 3b	3.34	11S	521527	4004441	fluvial	unique	shield	no
SB4	WTF 4	10.69	11S	521570	4004427	fluvial	unique	shield	yes
SB4	WTF 5	>20	11S	521624	4004403	fluvial	unique	shield	no
SB5 (N)	WTF 1	7.03	11S	521328	4002705	fluvial	unique	shield	yes
SB5 (S)	WTF 1	10.01	11S	521263	4002622	fluvial	unique	shield	yes
SB5 (S)	WTF 2	?	11S	521308	4002583	fluvial	unique	shield	no
SB5 (S)	WTF 3	5.43	11S	521335	4002573	fluvial	unique	shield	yes
Coffin C	WTF 1	18.6	11S	521070	4000915	fluvial	unique	shield	yes
Coffin C	WTF 1	-	-	-	-	fluvial	migrated	-	no
Surprise C	WTF 1	2.36	11S	484888	3996452	fluvial	multiple	fault	no
Surprise C	WTF 2	3.38	11S	485009	3996594	fluvial	multiple	fault	no
Surprise C	WTF 3	∼2.5	11S	485265	3996501	fluvial	multiple	fault	no
Happy C	WTF 1	2.9	11S	484386	3991702	fluvial	multiple	lithology	no
Happy C	WTF 2	6.92	11S	484462	3991760	fluvial	multiple	?	no
Happy C	WTF 3	4.09	11S	484594	3991794	fluvial	multiple	?	no
Happy C	WTF 4	1.62	11S	484663	3991834	fluvial	multiple	step-pool	no
Happy C	WTF 5	1.94	11S	484812	3991842	fluvial	multiple	step-pool	no
Pleasant C	WTF 1	8.19	11S	483161	3987841	fluvial	multiple	shield	no
M Park C	WTF 1	2.22	11S	482321	3987306	fluvial	multiple	fault	no
M Park C	WTF 2	3.23	11S	482477	3987317	fluvial	multiple	step-pool	no
M Park C	WTF 3	3.07	11S	482485	3987330	fluvial	multiple	step-pool	no
M Park C	WTF 4a	5.5	11S	482498	3987349	fluvial	multiple	step-pool	no
M Park C	WTF 4b	3.02	11S	482498	3987349	fluvial	multiple	step-pool	no
M Park C	WTF 5	4.96	11S	482511	3987369	fluvial	multiple	step-pool	no
SMPC (N)	WTF 1	2.12	11S	481404	3985107	fluvial	multiple	active fault	no
SMPC (E)	WTF 1	2.29	11S	482106	3984784	fluvial	multiple	step-pool	no
SMPC (E)	WTF 2	2.3	11S	482122	3984788	fluvial	multiple	step-pool	no
SMPC (E)	WTF 3	2.05	11S	482174	3984802	fluvial	multiple	step-pool	no
SMPC (S)	WTF 1	1.08	11S	482165	3984627	fluvial	multiple	step-pool	no
SMPC (S)	WTF 2	2.03	11S	482166	3984604	fluvial	multiple	step-pool	no
SMPC (S)	WTF 3	2.74	11S	482183	3984594	fluvial	multiple	step-pool	no
SMPC (S)	WTF 4	3.91	11S	482209	3984599	fluvial	multiple	step-pool	no
S Park C	WTF 1	9.11	11S	481887	3983493	fluvial	migrated	shield	yes
S Park C	WTF 2	4.73	11S	481978	3983504	fluvial	migrated	shield	yes

S Park C	WTF 3	6.28	11S	482096	3983500	fluvial	migrated	shield	yes
Pat Keyes	WTF 1	11.66	11S	419733	4070961	fluvial	unique	shield	yes
Pat Keyes	WTF 2	11.6	11S	419681	4070922	fluvial	unique	shield	yes
McEllvoy	WTF 1a	1	11S	419700	4068447	debris flow	unique	shield	no
McEllvoy	WTF 1b	8.31	11S	419700	4068447	debris flow	unique	shield	no
McEllvoy	WTF 2	2.59	11S	419621	4068485	debris flow	unique	shield	no
Beveridge	WTF 1	12.85	11S	422391	4064441	debris flow	unique	shield	no
Beveridge	WTF 2a	8.4	11S	422307	4064407	debris flow	unique	shield	no
Beveridge	WTF 2b	11.26	11S	422307	4064407	debris flow	unique	shield	no
Hunter C	WTF 1	6.12	11S	423932	4061926	debris flow	unique	lithology	no
Hunter C	WTF 2	10.23	11S	423932	4061926	debris flow	unique	lithology	no
Hunter C	WTF 3	∼5	11S	423881	4061904	debris flow	unique	lithology	no
Craig C	WTF 1a	3.14	11S	425396	4059038	debris flow	unique	lithology	no
Craig C	WTF 1b	2.97	11S	425396	4059038	debris flow	unique	lithology	no
Craig C	WTF 2	5.91	11S	424553	4058708	debris flow	unique	lithology	no
Craig C	WTF 3	11.29	11S	424553	4058708	debris flow	unique	lithology	no

Table 2.2: List of hydraulic parameters in all the surveyed catchments in Saline, Panamint and Death Valley. Grain sizes were measured by picking at least 100 clasts every 0.5 m on an along stream transect crossing thalweg and bars. Asterisks indicate reconstructed values. Daggers indicate grain size distributions based on less than 100 counts: GG active = 55, GG old = 50, SB3 = 50, SB4 = 75, SB5 = 75.

Catchment	**Fan length [m]**	**Watershed Area [km2]**	**channel width [m]**	**Slope [%]**	**D50 [mm]**	**D84 [mm]**	$\tau_\star$	**Rh**
Gower Gulch active channel	1300	439	30	3.7	16	59.5	0.22	0.15
Gower Gulch old channel	1300	5.8	6.1	4.2	4.7	9.9	0.22*	0.03*
Badwater	1770	5.2	9.2	13.1	18.7	41.9	0.14	0.036
S Badwater 3	850	3.9	6.5	8.9	7.4	77.3	0.16	0.024
S Badwater 4	950	6.1	4.8	7.3	5.2	11.3	0.19	0.025
S Badwater 5	560	1.9	13.6	8	4.7	9.9	0.22	0.023
Coffin Canyon	1000	11.1	6.4	7.9	9.3	22.6	0.2	0.043
Pleasant Canyon	2500	33	5.3	8.9	21	93	0.17	0.074
South Park Canyon	1250	8.3	6.8	11.7	19.3	58.1	0.1	0.03
Pat Keyes	1800	21.4	18.4	11	8.3	51.8	0.53	0.0678
McEllvoy	2300	23.3	11.6	10.3	44.4	157.1	-	-
Keynot	1500	10	19.3	15.3	29.2	142.3	-	-
Beveridge	2100	28.6	10.6	16.9	58	204	-	-
Hunter Canyon	2000	23.2	15.7	10.7	36	162.8	-	-
Craig Canyon	1700	22.6	14.4	9.5	60.5	275.1	-	-

Table 2.3: List of all the waterfalls selected for the demonstration in Saline, Panamint and Death Valley. Heights lumped by a square bracket are in close succession and considered as one. Erosion rates are extrapolated from (Kirby, 2013). The maximum t_s is calculated with the volume necessary to aggrade a fan opening at 90° to a height equivalent to h_{max} at the apex if there are no preexisting canyons.

Catchment	**Erosion Rate [mm/yr]**	**Uplift [mm/yr]**	**t_f [yr]**	**t_u [yr]**	**ts [yr]**	**Heights [m]**	**Steep slope**	**Shallow slope**	**Qw modern [m^3/s]**	**Qw past [m^3/s]**	**Qw past**
Gower Gulch, DV	-	-	-	-	-	9.11	0.042	0.037	9.2	0.2	46
Badwater, DV	0.15	2	11500	4720	9980	9.44	0.131	0.118	0.351	0.371	1.057
S Badwater 3, DV	0.07	2	11500	6300	8792	12.6	0.089	0.074	0.079	0.101	1.275
S Badwater 3, DV	0.07	2	11500	3095	4319	[2.03, 4.16]	0.089	0.082	0.079	0.089	1.121
S Badwater 4, DV	0.15	2	11500	7820	4027	[4.56, 5.55, 5.53]	0.073	0.057	0.104	0.146	1.406
S Badwater 4, DV	0.15	2	11500	5345	2752	10.69	0.073	0.062	0.104	0.13	1.25
S Badwater 5, DV	0.09	2	11500	5005	4720	10.01	0.08	0.062	0.29	0.406	1.401
S Badwater 5, DV	0.09	2	11500	2715	2560	5.43	0.08	0.07	0.29	0.344	1.188
S Badwater 5, DV	0.09	2	11500	3515	3315	7.03	0.08	0.067	0.29	0.364	1.256
Coffin Canyon, DV	0.06	2	11500	9300	7328	18.6	0.079	0.06	0.316	0.452	1.43
Pleasant Canyon, PV	0.11	0.34	11500	4555	3687	8.19	0.053	0.046	0.456	0.479	1.051
South Park Canyon, PV	0.2	0.34	11500	2365	2239	9.11	0.068	0.061	0.155	0.168	1.09
South Park Canyon, PV	0.2	0.34	11500	3140	1162	4.73	0.068	0.064	0.155	0.161	1.045
South Park Canyon, PV	0.2	0.34	11500	4095	1544	6.28	0.068	0.063	0.155	0.164	1.06
Pat Keyes, SV	0.3	0.6	11500	5830	1538	11.7	0.117	0.111	1.956	2.11	1.079
Pat Keyes, SV	0.3	0.6	11500	5800	1530	11.6	0.117	0.111	1.956	2.109	1.079

References

Allen, Philip A (2005). "Striking a chord". In: *Nature* 434.7036, pp. 961–961.

Allen, Philip A and Alexander L Densmore (2000). "Sediment flux from an uplifting fault block". In: *Basin Research* 12.3-4, pp. 367–380.

Armitage, John J et al. (2013). "Temporal buffering of climate-driven sediment flux cycles by transient catchment response". In: *Earth and Planetary Science Letters* 369, pp. 200–210.

Attal, M et al. (2015). "Impact of change in erosion rate and landscape steepness on hillslope and fluvial sediments grain size in the Feather River basin (Sierra Nevada, California)". In: *Earth Surface Dynamics* 3.1, pp. 201–222.

Berlin, Maureen M and Robert S Anderson (2007). "Modeling of knickpoint retreat on the Roan Plateau, western Colorado". In: *Journal of Geophysical Research: Earth Surface* 112.F3.

Bishop, Paul et al. (2005). "Knickpoint recession rate and catchment area: the case of uplifted rivers in Eastern Scotland". In: *Earth Surface Processes and Landforms* 30.6, pp. 767–778.

Bonnet, Stephane and A Crave (2003). "Landscape response to climate change: Insights from experimental modeling and implications for tectonic versus climatic uplift of topography". In: *Geology* 31.2, pp. 123–126.

Bull, W B (1964). "Geomorphology of segmented alluvial fans in western Fresno County, California". In: *U.S. Geological Survey Professional Paper* 352, pp. 89–129.

– (1991). *Geomorphic responses to climatic change*. New York: Oxford University Press.

Burchfiel, B C, K V Hodges, and L H Royden (1987). "Geology of Panamint Valley - Saline Valley Pull-Apart System, California: Palinspastic evidence for low-angle geometry of a Neogene Range-Bounding Fault". In: *Journal of Geophysical Research: Earth Surface* 92.B10, pp. 10422–10426.

Carretier, S and F Lucazeau (2005). "How does alluvial sedimentation at range fronts modify the erosional dynamics of mountain catchments?" In: *Basin Research* 17.3, pp. 361–381.

Chatanantavet, Phairot and Gary Parker (2009). "Physically based modeling of bedrock incision by abrasion, plucking, and macroabrasion". In: *Journal Of Geophysical Research* 114.F4.

Chen, Yue-Gau et al. (2002). "Geomorphic evidence for prior earthquakes: Lessons from the 1999 Chichi earthquake in central Taiwan". In: *Geology* 30.2, pp. 171–174.

Clark, M K et al. (2005). "The non-equilibrium landscape of the southern Sierra Nevada, California". In: *GSA Today* 15, pp. 4–10.

Cook, Kristen L. et al. (2009). "Rapid incision of the Colorado River in Glen Canyon - insights from channel profiles, local incision rates, and modeling of lithologic controls". In: *Earth Surface Processes and Landforms* 34.7, pp. 994–1010.

Crosby, B T and Kelin X. Whipple (2006). "Knickpoint initiation and distribution within fluvial networks: 236 waterfalls in the Waipaoa River, North Island, New Zealand". In: *Geomorphology* 82, pp. 16–38.

D'Arcy, Mitch, Duna C Roda Boluda, et al. (2014). "Dating alluvial fan surfaces in Owens Valley, California, using weathering fractures in boulders". In: *Earth Surface Processes and Landforms* 40.4, pp. 487–501.

D'Arcy, Mitch, Alexander C Whittaker, and Duna C Roda Boluda (2016). "Measuring alluvial fan sensitivity to past climate changes using a self-similarity approach to grain size fining, Death Valley, California". In: *Sedimentology*, n/a–n/a.

DeLong, Stephen B, Jon D Pelletier, and Lee J Arnold (2008). "Climate change triggered sedimentation and progressive tectonic uplift in a coupled piedmont–axial system: Cuyama Valley, California, USA". In: *Earth Surface Processes and Landforms* 33.7, pp. 1033–1046.

Densmore, Alexander L, Philip A Allen, and Guy Simpson (2007). "Development and response of a coupled catchment fan system under changing tectonic and climatic forcing". In: *Journal Of Geophysical Research* 112.F1.

DiBiase, Roman A, Kelin X. Whipple, Arjun M Heimsath, et al. (2010). "Landscape form and millennial erosion rates in the San Gabriel Mountains, CA". In: *Earth and Planetary Science Letters* 289.1-2, pp. 134–144.

DiBiase, Roman A, Kelin X. Whipple, Michael P Lamb, et al. (2014). "The role of waterfalls and knickzones in controlling the style and pace of landscape adjustment in the western San Gabriel Mountains, California". In: *Geological Society of America Bulletin* 127, pp. 539–559.

Dijk, Maurits van, George Postma, and Maarten G Kleinhans (2009). "Autocyclic behaviour of fan deltas: an analogue experimental study". In: *Sedimentology* 56.5, pp. 1569–1589.

Einstein, H A and N L Barbarossa (1952). "River Channel Roughness". In: *Transactions of the American Society of Civil Engineers* 117, pp. 1121–1132.

Finnegan, Noah J and Greg Balco (2013). "Sediment supply, base level, braiding, and bedrock river terrace formation: Arroyo Seco, California, USA". In: *Geological Society of America Bulletin* 125.7-8, pp. 1114–1124.

Frankel, Kurt L, Allen F Glazner, et al. (2008). "Active tectonics of the eastern California shear zone". In: *GSA Field Guide 11: Field Guide to Plutons, Volcanoes, Faults, Reefs, Dinosaurs, and Possible Glaciation in Selected Areas of Arizona, California, and Nevada*. Geological Society of America, pp. 43–81.

Frankel, Kurt L, Lewis A Owen, et al. (2015). "Timing and rates of Holocene normal faulting along the Black Mountains fault zone, Death Valley, USA". In: *Lithosphere* 8, pp. 3–22.

Frankel, Kurt L, Frank J Pazzaglia, and Jordan D Vaughn (2007). "Knickpoint evolution in a vertically bedded substrate, upstream-dipping terraces, and Atlantic slope bedrock channels". In: *Geological Society of America Bulletin* 119.3-4, pp. 476–486.

Gallen, Sean F et al. (2011). "Hillslope response to knickpoint migration in the Southern Appalachians: implications for the evolution of post-orogenic landscapes". In: *Earth Surface Processes and Landforms* 36.9, pp. 1254–1267.

Gilbert, Grove Karl and Edward Charles Murphy (1914). "The Transportation of Debris by Running Water". In: *U. S. Geological Survey Professional Paper* 86, pp. 1–263.

Hart, E W et al. (1989). Summary Report: Fault Evaluation Program, 1987-1988, Southwestern Basin and Range Region and Supplemental Areas. Tech. rep. 89-16. Pleasant Hill, CA: California Dept. of Conservation.

Harvey, Adrian M, Peter E Wigand, and Stephen G Wells (1999). "Response of alluvial fan systems to the late Pleistocene to Holocene climatic transition: contrasts between the margins of pluvial Lakes Lahontan and Mojave, Nevada and California, USA". In: *Catena* 36.4, pp. 255–281.

Hayakawa, Yuichi and Yukinori Matsukura (2003). "Recession rates of waterfalls in Boso Peninsula, Japan, and a predictive equation". In: *Earth Surface Processes and Landforms* 28.6, pp. 675–684.

Hooke, Roger LeB (1968). "Steady-state relationships on arid-region alluvial fans in closed basins". In: *American Journal Of Science* 266.8, pp. 609–629.

Howard, Alan D. (1994). "A detachment-limited model of drainage basin evolution". In: *Water Resources Research* 30.7, pp. 2261–2285.

Huang, Ming-Wan, Yii-Wen Pan, and Jyh-Jong Liao (2013). "A case of rapid rock riverbed incision in a coseismic uplift reach and its implications". In: *Geomorphology* 184.C, pp. 98–110.

Humphrey, Neil F and Paul L Heller (1995). "Natural Oscillations in Coupled Geomorphic Systems - an Alternative Origin for Cyclic Sedimentation". In: *Geology* 23.6, pp. 499–502.

Jayko, A S (2005). "Late Quaternary denudation, Death and Panamint Valleys, eastern California". In: *Earth-Science Reviews* 73.1-4, pp. 271–289.

Jennings, C W (1958). *Geologic map of California : Death Valley sheet*.

– (1994). *Fault activity map of California and adjacent areas with location and ages of recent volcanic eruptions*. California Geologic Data Map Series.

Kirby, Eric (2013). "Reading the signal of tectonics in landscape topography: challenges and opportunities". In: *EGU General Assembly Conference Abstracts*. Vienna.

Klinger, Ralph E and Lucille A Piety (2001). "Holocene faulting and slip rates along the Black Mountains fault zone near Mormon Point". In: *Quaternary and Late Pliocene Geology of the Death Valley Region: Recent Observations on Tectonics, Stratigraphy, and Lake Cycles (Guidebook for the 2001 Pacific Cell—Friends of the Pleistocene Fieldtrip)*. Ed. by Michael N Machette, Margo L Johnson, and Janet L Slate. United States Geological Service, pp. 1–11.

Knox, James C. (1975). "Concept of the graded stream". In: *Theories of Landform Development*. Ed. by Wilton N Melhorn and Ronald C Flemal. Theories of landform development, pp. 169–198.

Ku, Teh-Lung et al. (1998). "U-Series Chronology of Lacustrine Deposits in Death Valley, California". In: *Quaternary Research* 50.3, pp. 261–275.

Lamb, Michael P and William E Dietrich (2009). "The persistence of waterfalls in fractured rock". In: *Geological Society of America Bulletin* 121.7-8, pp. 1123–1134.

Lamb, Michael P, Alan D. Howard, et al. (2007). "Formation of amphitheater-headed valleys by waterfall erosion after large-scale slumping on Hawai'i". In: *Geological Society of America Bulletin* 119.7-8, pp. 805–822.

Lamb, Michael P, Joel S Scheingross, et al. (2011). "A model for fire-induced sediment yield by dry ravel in steep landscapes". In: *Journal Of Geophysical Research* 116.F3.

Lane, E W (1937). *Stable Channels in Erodible Material*. Tech. rep.

– (1955). "Design of stable channels". In: *Transactions of the American Society of Civil Engineers* 120, pp. 1234–1279.

Lee, Jeffrey et al. (2009). "Exhumation of the Inyo Mountains, California: Implications for the timing of extension along the western boundary of the Basin and Range Province and distribution of dextral fault slip rates across the eastern California shear zone". In: *Tectonics* 28.1, pp. 1–20.

Lee, Y H et al. (2005). "Structures Associated with the Northern End of the 1999 Chi-Chi Earthquake Rupture, Central Taiwan: Implications for Seismic-Hazard Assessment". In: *Bulletin of the Seismological Society of America* 95.2, pp. 471–485.

Leopold, L B and W B Bull (1979). "Base Level, Aggradation, and Grade". In: *Proceedings of the American Philosophical Society*, pp. 168–202.

Leopold, L B and Thomas Maddock Jr (1953). "The hydraulic geometry of stream channels and some physiographic implications". In: *U.S. Geological Survey Professional Paper* 252.

Lindvall, Scott C and Charles M Rubin (2008). *Slip Rate Studies Along The Sierra Madre-Cucamonga Fault System Using Geomorphic And Cosmogenic Surface Exposure Age Constraints:* tech. rep. 03HQGR0084.

Lowenstein, Tim K et al. (1999). "200 k.y. paleoclimate record from Death Valley salt core". In: *Geology* 27.1, pp. 3–6.

Mackey, Benjamin H et al. (2014). "Knickpoint formation, rapid propagation, and landscape response following coastal cliff retreat at the last interglacial sea-level highstand: Kaua'i, Hawai'i". In: *Geological Society of America Bulletin* 126.7-8, pp. 925–942.

Mackin, J H (1948). "Concept of the Graded River". In: *Geological Society of America Bulletin* 59.5, pp. 463–511.

Mason, Cody Curtis and B W Romans (2015). "Quantifying Sediment Supply in Stratigraphy Using Cosmogenic Nuclides: Insights From the Pleasant Canyon Complex, Panamint Mountains, California". In: *AAPG Annual Convention and Exhibition*. Boulder, CO.

Menking, Kirsten M et al. (2004). "Wetter or colder during the Last Glacial Maximum? Revisiting the pluvial lake question in southwestern North America". In: *Quaternary Research* 62.3, pp. 280–288.

Meyer-Peter, E and R Müller (1948). "*Formulas for bed-load transport*". In: *2nd Meeting of the International Association for Hydraulic Structures Research*. Stockholm: 2nd Meeting of the International Association for Hydraulic Structures Research, pp. 39–64.

Nicholas, Andrew P. and T A Quine (2007). "Modeling alluvial landform change in the absence of external environmental forcing". In: *Geology* 35.6, pp. 527–530.

Numelin, T, C Marone, and Eric Kirby (2007). "Frictional properties of natural fault gouge from a low-angle normal fault, Panamint Valley, California". In: *Tectonics* 26, pp. 1–14.

Paola, Chris, Paul L Heller, and Charles L Angevine (1992). "The large-scale dynamics of grain-size variation in alluvial basins, 1: Theory". In: *Basin Research* 4.2, pp. 73–90.

Parker, Gary (1978). "Self-formed straight rivers with equilibrium banks and mobile bed. Part 2. The gravel river". In: *Journal of Fluid Mechanics* 89.01, pp. 127–146.

– (1991). "Selective Sorting and Abrasion of River Gravel. 2. Applications". In: *Journal of Hydraulic Engineering* 117.2, pp. 150–171.

Parker, Gary et al. (2007). "Physical basis for quasi-universal relations describing bankfull hydraulic geometry of single-thread gravel bed rivers". In: *Journal Of Geophysical Research* 112.F4, F04005–21.

Pepin, E., S Carretier, and G. Herail (2010). "Erosion dynamics modelling in a coupled catchment-fan system with constant external forcing". In: *Geomorphology* 122, pp. 78–90.

Poisson, Blanche and Jean-Philippe Avouac (2004). "Holocene hydrological changes inferred from alluvial stream entrenchment in North Tian Shan (Northwestern China)". In: *Journal of Geology* 112.2, pp. 231–249.

Quade, Jay, Richard M Forester, and Joseph F Whelan (2003). "Late Quaternary paleohydrologic and paleotemperature change in southern Nevada". In: *Geological Society of America Special Paper* 368, pp. 165–188.

Reitz, Meredith D and Douglas J Jerolmack (2012). "Experimental alluvial fan evolution: Channel dynamics, slope controls, and shoreline growth". In: *Journal Of Geophysical Research* 117.F2, F02021–19.

Rohais, Sebastien, Stephane Bonnet, and Remi Eschard (2012). "Sedimentary record of tectonic and climatic erosional perturbations in an experimental coupled catchment-fan system". In: *Basin Research* 24.2, pp. 198–212.

Rosenberg, L I and J C Clark (2005). "Neotectonics of the Rinconada and Reliz Fault Zones, Salinas Valley, California". In: *GSA Cordilleran Section – 101st Annual Meeting*. San Jose, CA.

Scheingross, Joel S et al. (2013). "Influence of bed patchiness, slope, grain hiding, and form drag on gravel mobilization in very steep streams". In: *Journal of Geophysical Research: Earth Surface* 118.2, pp. 982–1001.

Schumm, Stanley Alfred (1973). "Geomorphic thresholds and complex response of drainage systems". In: *Fluvial Geomorphology*. Ed. by M Morisawa. Fluvial geomorphology, pp. 299–310.

Simpson, Guy and Sébastien Castelltort (2012). "Model shows that rivers transmit high-frequency climate cycles to the sedimentary record". In: *Geology* 40, pp. 1–4.

Sklar, Leonard S and William E Dietrich (2004). "A mechanistic model for river incision into bedrock by saltating bed load". In: *Water Resources Research* 40.6, pp. 1–21.

Snyder, Noah P and Lisa L Kammer (2008). "Dynamic adjustments in channel width in response to a forced diversion: Gower Gulch, Death Valley National Park, California". In: *Geology* 36.2, pp. 187–190.

Spaulding, W G (1985). *Vegetation and climates of the last 45,000 years in the vicinity of the Nevada Test Site, south-central Nevada*. Tech. rep. professional paper 1329. USGS.

Stock, J D, K M Schmidt, and David M Miller (2008). "Controls on alluvial fan long-profiles". In: *Geological Society of America Bulletin* 120.5-6, pp. 619–640.

Thompson, Robert S, Katherine H Anderson, and Patrick J Bartlein (1999). *Quantitative Paleoclimatic Reconstructions From Late Pleistocene Plant Macrofossils of the Yucca Mountain Region*. Tech. rep. Open-File Report 99-338. USGS.

Trampush, S M, S Huzurbazar, and B McElroy (2014). "Empirical assessment of theory for bankfull characteristics of alluvial channels". In: *Water Resources Research* 50.12, pp. 9211–9220.

Vogel, Marylin Browning et al. (2002). "Quaternary Exhumation Rate Central Panamint Range, California from U-Pb Zircon Ages". In: *GSA 2002 Denver Annual Meeting*. Denver, CO.

Wells, S G and A M Harvey (1987). "Sedimentologic and geomorphic variations in storm-generated alluvial fans, Howgill Fells, northwest England". In: *Geological Society of America Bulletin* 98, pp. 182–198.

Whipple, Kelin X., Roman A DiBiase, and B T Crosby (2013). "9.28 Bedrock Rivers". In: *Treatise on Geomorphology*. Elsevier, pp. 550–573.

Whittaker, Alexander C and Sarah J Boulton (2012). "Tectonic and climatic controls on knickpoint retreat rates and landscape response times". In: *Journal Of Geophysical Research* 117.F2, F02024–19.

Wobus, C W, G E Tucker, and Robert S Anderson (2006). "Self-formed bedrock channels". In: *Geophysical Research Letters* 33.L18408, pp. 1–6.

Wong, Miguel and Gary Parker (2006). "Reanalysis and correction of bed-load relation of Meyer-Peter and Muller using their own database". In: *Journal of Hydraulic Engineering* 132.11, pp. 1159–1168.

Chapter 3

AUTOGENIC ENTRENCHMENT PATTERNS AND TERRACES DUE TO COUPLING WITH LATERAL EROSION IN INCISING ALLUVIAL CHANNELS

with Jeff P. Prancevic[1,2] and Jean-Philippe Avouac[2]

Published in JGR Earth Surface, 2017, vol. 122, pp. 335-355, DOI:10.1002/2015JF003797

Abstract

The abandonment of terraces in incising alluvial rivers can be used to infer tectonic and climatic histories. A river incising into alluvium erodes both vertically and laterally as it abandons fill-cut terraces. We argue that the input of sediment from the valley walls during entrenchment can alter the incision dynamics of a stream by promoting vertical incision over lateral erosion. Using a numerical model, we investigate how valley wall feedbacks may affect incision rates and terrace abandonment as the channel becomes progressively more entrenched in its valley. We postulate that erosion of taller valley walls delivers large pulses of sediment to the incising channel, potentially overwhelming the local sediment transport capacity. Based on field observations, we propose that these pulses of sediment can form talus piles that shield the valley wall from subsequent erosion and potentially force progressive channel narrowing. Our model results show that this positive feedback mechanism can result in enhanced vertical incision relative to 1-D predictions that ignore lateral erosion. We explore a wide parameter space of channel characteristics and find that incision is most significantly enhanced when sediment transport rates are low relative to the typical volume of material collapsed from the valley walls. The model also shows that the youngest terraces are selectively eroded away when river vertical incision slows down. The systematic erosion of the youngest terraces is as important as the initial formation of terraces for estimating the history of river incision and interpreting its relation to climatic forcing and

[1]Department of Environmental Systems Science, ETH Zurich, Zurich, Switzerland

[2]Division of Geological and Planetary Sciences, California Institute of Technology, Pasadena, CA 91125, USA

tectonic factors. Consequently, the effect of autogenic lateral sediment input needs to be taken into account in the interpretation of complex-response terraces.

3.1 Introduction

Fluvial terraces provide records of past river geometries and can therefore be used to quantify spatial and/or temporal changes in rates of vertical incision and lateral erosion of the river. River incision and terrace abandonment can be driven by climate and tectonics, and it is typically assumed that if one of these forcings can be constrained the terrace record may be used to reconstruct the other. Fluvial terraces are defined morphologically as a near-flat surface flanking a river, but their types vary depending on their genesis: strath terraces are cut into bedrock, fill terraces mark the culmination of an episode of alluvial deposition followed by subsequent incision, and fill-cut terraces are carved into these deposits as a river both incises and migrates laterally, leaving flights of terraces (Bucher, 1932; Howard, 1959; W. B. Bull, 1991; Frank J Pazzaglia, 2013). All terrace types have been used for tectonic and climatic reconstructions, although both fill and fill-cut terraces (also called complex-response terraces) are less frequently employed (W. B. Bull, 1991; Frank J Pazzaglia, 2013). For example, river terraces have been used to reconstruct past climatic conditions in Central China (Porter and Zhisheng, 1992), along the Rio Grande Rift in New Mexico (Reneau, 2000), in the American Great Plains (Arbogast and Johnson, 1994), in the Peruvian Andes (Steffen, Schlunegger, and Preusser, 2010; Bekaddour et al., 2014), or along the Thames in England (Maddy, D. Bridgland, and Westaway, 2001). In other studies, tectonic histories have been reconstructed from the terrace record in Central Anatolia (Schildgen et al., 2011), in the Apennines (Picotti and Frank J Pazzaglia, 2008), in the Sub-Himalaya (Lavé and Avouac, 2000), or across Cascadia in the northwest United States (Frank J Pazzaglia and Brandon, 2001). Finally, careful examination of a single fluvial terrace record may even yield simultaneous histories of tectonics and climate, as was done in the Spanish Pyrenees (Jones, Frostick, and Astin, 1999), on the South Island of New Zealand (W. L. Bull and Knuepfer, 1987), in the Olympic Peninsula of the northwest United States (Wegmann and F J Pazzaglia, 2002), northwestern China (Poisson and Avouac, 2004) or in northwest Europe (D. R. Bridgland, 2000).

It is often difficult to disentangle tectonic and climatic forcing in the fluvial record. This is exemplified by the conflicting interpretation of the extensive fill-cut and strath terrace record in the northern piedmont of the Chinese Tian Shan. Some authors interpret these terraces mostly as recorders of Quaternary climate change (Molnar et al., 1994; Poisson and Avouac, 2004; Lu, Burbank, and Y. Li, 2010), while others attribute them to changing tectonic forcing (Gong, S.-H. Li, and B. Li, 2014; Wei, Arrowsmith, and He, 2015). Whether terraces are systematically linked to any discrete forcing events, as for example modeled by Hancock and Anderson (2002), has a long history of debate: field studies (Womack and Schumm, 1977), numerical models (N. J. Finnegan and Dietrich, 2011; Limaye and Lamb, 2014; Limaye and Lamb, 2016) and experimental analogues (Gardner, 1983) have shown that internal dynamics during phases of incision can lead to autogenic strath and fill-cut terrace abandonment. Using the terrace record to infer past environmental forcing thus requires identifying the effect of autogenic processes first. Recent debate has also emerged regarding the sensitivity of incision rates to the timescale of analysis (N. J. Finnegan, Schumer, and S. Finnegan, 2014; Gallen et al., 2015). N. J. Finnegan, Schumer, and S. Finnegan (2014) argue that there is a systematic bias towards faster erosion rates when measuring terraces separated by shorter time intervals. They describe the bias with a negative powerlaw dependence of incision rates on time intervals and suggest that it is the result of episodic hiatuses in erosion. In contrast, Gallen et al. (2015) propose that the temporal dependence results from a methodological bias that can be avoided by measuring incision rates between terraces, rather than using the modern streambed as the datum for incision given that streambed elevation is an unsteady reference frame. These two recent studies are based on long-term records of strath terraces, but do not consider complex-response terraces and the effect of autogenic processes on incision rates inferred from the terrace record.

While the fluvial terrace record is three-dimensional, theories of alluvial river morphodynamics tend to be one-dimensional (e.g. Schumm, 1973; Leopold and W. B. Bull, 1979; Parker, 2015). Consequently, the information held in the terrace record about changes in channel width and lateral river migration is generally ignored. Here, we investigate whether the record of vertical incision rates in complex-response terraces can be affected by lateral feedbacks inher-

ent to transport-limited streams. We focus on the influence of these feedbacks on the evolution of a single continuous phase of river incision in an alluvial substrate over thousands to tens of thousands of years. We assume a fixed base level and that incision is instead forced by an upstream change in the sediment transport capacity of the stream. As the channel incises vertically, we also allow the channel to migrate laterally and entrain sediment from valley walls. We specifically test how the contribution of sediment from valley walls affects the creation, preservation, and eventual destruction of terraces. We use a numerical model to illustrate the incision scenario and examine the internal processes leading to changes in the vertical incision rate that could be misinterpreted as externally forced. We investigate a wide range of river parameters to constrain the conditions where we expect lateral dynamics to have the greatest impact on vertical incision of the river.

3.2 Scenario of alluvial incision

Dynamics and processes controlling incision

Removal of material from the bed or banks of a transport-limited river is determined by the local excess sediment transport capacity that is greater than the local sediment supply. This is in contrast to a detachment-limited river, where sediment transport capacity is not met by the material supplied and the bed and banks are eroded at a pace limited by the bedrock erodibility. This difference makes transport-limited channels particularly sensitive to sediment inputs and the geometry of entrenchment: 1) high banks limit lateral migration and promote vertical incision (Nicholas and Quine, 2007), and 2) sediments delivered to the channel by bank erosion affect the transport budget of the stream (Schumm and Hadley, 1957; Patton and Schumm, 1975; Schumm, Harvey, and Watson, 1984; G. A. Meyer, Wells, and Jull, 1995; Gran et al., 2013). In entrenched systems, these effects should be more pronounced. When a channel reaches the edge of its floodplain by migrating laterally, it abuts the valley wall, which is likely much taller than the river bank. When sediments derived from these valley walls are not immediately transported away, they form a talus pile, shielding the wall from subsequent erosion until their removal and potentially constraining channel width (Figure 3.1).

In any alluvial channel with excess transport capacity, the channel will in-

Figure 3.1: Talus piles shield the base of the alluvial valley walls in a tributary of the Anji Hai River, piedmont of the northeastern Tian Shan, Xinjiang Region, China (43°58'42"N/85°06'37"E).

cise its bed. However, alluvial channels are rarely static in their planform geometry, and vertical incision during a flood event may be distributed over a broader region than a single channel width as the channel moves laterally during the event. The resulting net vertical incision of the channel is thereby inversely proportional to the lateral migration. Large lateral migration results in a reduced net vertical incision (Figure 3.2 A), while a channel with limited lateral migration will have a greater net vertical incision (Figure 3.2 B). Lateral migration is set by the competition between the stress applied to the bank (or valley wall) and the pushback of valley wall collapse. The product of collapse events could overwhelm local sediment transport capacity and force aggradation of the entire channel following the scenario put forward by Schumm, Harvey, and Watson (1984, section 6.3) and revisited in Schumm and Rea, 1995. However, for the bank or valley wall sediments to overwhelm the entire cross section, the channel must be narrow. Most of the time, we expect that lateral inputs of sediment from the bank or valley wall will be mobilized by the shear stress acting on that portion of the channel, while flowing water in the rest of the channel will continue incising its bed (Figure 3.2 B).

As a consequence, bed erosion is distributed over a progressively smaller area and net vertical incision increases as valley walls and banks get higher.

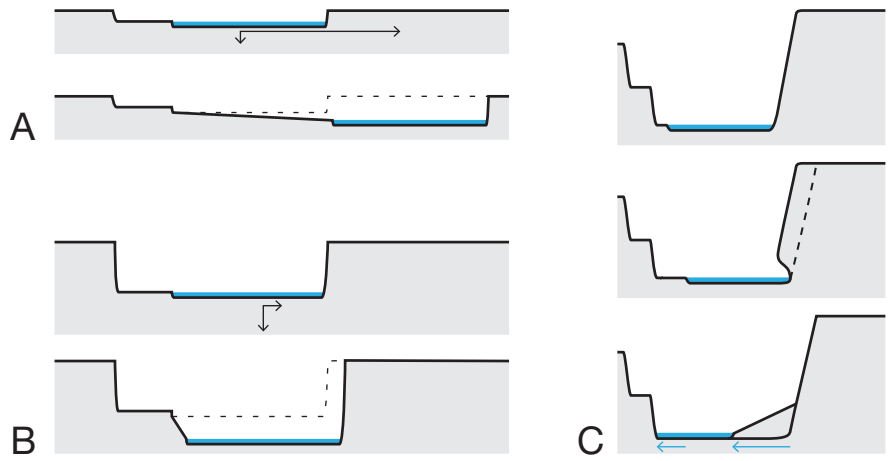

Figure 3.2: Processes in entrenching transport-limited rivers can promote vertical incision. In B, valley walls are taller than in A and limit lateral migration resulting in greater net vertical incision. C: bank undercut followed by a collapse that overwhelms the instantaneous sediment transport capacity results in a talus deposit pushing the river back and reducing its width. The narrower channel is deeper and its sediment transport capacity per unit width becomes larger.

When valley walls are high, talus piles encroach on the floodplain and can affect the river hydraulic geometry. The fluvial erosion of valley walls and terrace risers proceeds by undercutting and cliff collapse, delivering sediment to the channel (Schumm, Harvey, and Watson, 1984). When a tall wall collapses, the volume of sediment it yields exceeds the immediate transport capacity of the portion of the river abutting the valley wall and a talus forms (Figure 3.2 C and Figure 3.1). Runoff from the terrace tread and scarp diffusion will also contribute sediments and potential talus deposits. The talus has two main effects, it shields the valley wall from fluvial erosion and it is a source of recruitable sediments. Schumm's work focused on the second aspect whereby the erodibility contrast between bank and talus material is important and the sudden availability of much more easily recruitable talus material consumes the excess transport capacity, hampering vertical incision (Schumm, Mosley, and Weaver, 1987). It should also be noted that this requires talus material to be distributed over the whole channel width before inhibiting the entrain-

ment of bed material entirely. Alternatively, when the difference in erodibility between bed and talus is small, and/or the material is not distributed across the entire channel width, then local entrainment of bed material can proceed. In this case, the effect of the talus is to shield the valley wall until its complete removal, thus temporarily limiting lateral migration while permitting vertical incision. In addition, when the floodplain is only marginally larger than the channel, the deflection caused by a talus deposit can constrain and reduce the channel width (Figure 3.2 C). Once narrowed, the channel will have a greater water depth and the shear stress at its base will increase. For the narrowing of relatively wide channels, the increase in shear stress outweighs the loss of active channel width, resulting in a larger local sediment transport capacity. The resulting enhanced vertical incision rate leads to higher valley walls that, by further collapse, can further constrain the geometry of the channel. However, if the channel continues to narrow below an optimal width, the reduction in active bed area over which sediment is transported outweighs the gain in transport capacity per unit width due to the increase in shear stress. Under such narrow channel geometries, vertical incision rates will be reduced or even reverse if the transport capacity drops below the sediment supply rate. Meanwhile, stresses acting on the banks are large compared to wide channel geometries and erosion of the banks may proceed. As a result, this configuration is likely to be unstable and the channel will revert to a wider geometry with greater transport capacity.

In this wall feedback process, there are two thresholds marking a significant enhancement in vertical incision of the stream. One threshold is the critical height of the valley wall, above which the material collapsing by undercut overwhelms the local sediment transport capacity of the river, leading to generation of talus piles. Above that height, lateral erosion is self-limiting and vertical incision should be favored. The other threshold is reached when the alluvial floodplain is narrowed to a width equivalent to that of the channel. In that situation, new talus deposits of any size will result in a narrowing of the channel and likely an increase of its sediment transport capacity.

Conceptual incision model

Following a period in which an alluvial river is in equilibrium with its sediment supply, vertical incision is initialized when an external forcing either reduces the river's sediment load or increases its water discharge (Schumm, 1973; Leopold and W. B. Bull, 1979). As the channel entrains material from its bed, it also easily erodes the shallow banks and freely migrates laterally (Figure 3.3 A). Vertical incision and lateral erosion continue and the random lateral migration of the stream forms fill-cut terraces (W. B. Bull, 1991) (Figure 3.3 B). These fill-cut terraces result from the combination of external forcing (increased transport capacity) and autogenic dynamics (lateral migration). Progressively, the height of the valley walls increases, the lateral erosion rate of the river against the walls is reduced by the increasing amount of sediment they yield, and the vertical erosion is distributed across a smaller area, increasing net vertical incision (Nicholas and Quine, 2007). As incision continues, the episodic collapse of the ever-higher walls through undercut and run-off erosion produces so much sediment that it exceeds the immediate sediment transport capacity at the channel margins and talus piles start accumulating at the toes of the cliffs (Figure 3.3 C). The rivers of the north Tian Shan piedmont, flowing on a poorly consolidated fanglomerate (Avouac et al., 1993), illustrate this behavior well (Figure 3.1). Preceding the onset of incision 10-12 kyrs ago, the rivers migrated over an expansive and steep floodplain over 2 km wide. This floodplain has since reduced to a modern width of 200-300 m, matching the bankfull width of the channel after up to 300 m of channel entrenchment and reduction of its slope by a factor of almost two (Poisson and Avouac, 2004). The existing talus deposits reduce the width of the floodplain, forcing the channel to narrow instead of widen with the shallowing slope (N. J. Finnegan, Roe, et al., 2005).

A narrower channel increases water depth, shear stress at the channel bed, and hence sediment transport capacity. In the case of an incising alluvial river, ongoing vertical incision with respect to a fixed base level is necessarily accompanied by a decrease in slope. In a 1-D conceptualization, this reduction in slope would reduce the sediment transport capacity of the channel and slow the incision rate. Narrowing the river channel by lateral inputs of talus material can offset this decrease in transport capacity, and a high incision rate may be maintained or even increase as a result. The channel is trapped in a positive

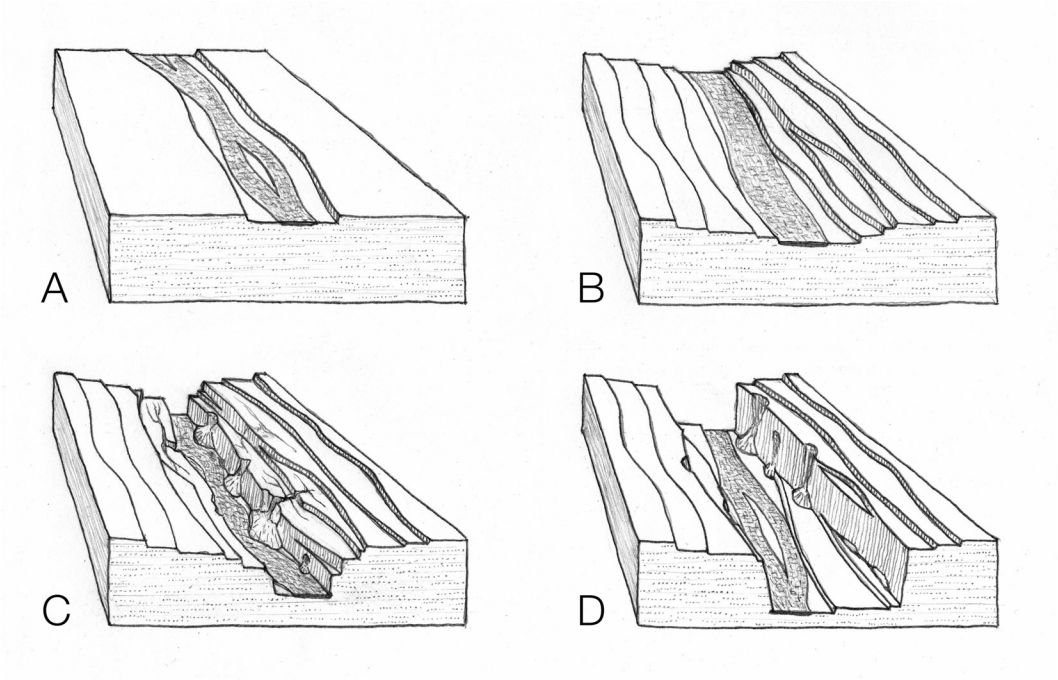

Figure 3.3: Scenario for the abandonment of fill-cut terraces by the entrenchment of a transport-limited river with fixed base level in an easily erodible sedimentary substrate triggered by a change in water or sediment flux from upstream: A) at the onset of incision, short alluvial banks with relatively low resistance allow the river to easily migrate laterally; B) migration and incision of the river result in the abandonment of autogenic fill-cut terraces; C) taller banks slow down lateral erosion and talus deposits force narrowing of the channel. As a result, vertical incision accelerates and the stream carves a canyon; D) after reaching a longitudinal profile close to being in equilibrium with the new upstream fluxes of water and sediment, vertical incision slows down and the river starts to migrate laterally again and to erode the youngest terraces.

feedback loop in which increasing vertical incision leads to ever higher banks constraining the channel even more, reducing its width, which forces a greater vertical incision and so forth. The loop is broken when the stream gradient is so shallow that excess basal shear stress is entirely dedicated to move the sediment flux from upstream, preventing further vertical incision and shallowing. In summary, instead of a continuous slowdown of vertical incision expected from a decrease in channel slope as the river profile nears its equilibrium for a 1-D analysis, we expect here a sustained vertical incision rate and even in some cases an apparent acceleration of vertical incision rates unrelated to any external forcing but, rather, caused by lateral inputs of sediment from valley

walls that narrow the channel and increase the shear stress over the bed. Such an acceleration could be misinterpreted as resulting from some environmental change.

Finally, when the river is near its longitudinal equilibrium and can no longer incise vertically, it will still occasionally erode the valley walls and widen its floodplain (Figure 3.3 D). As a result, the youngest fill-cut terraces are destroyed first while the oldest terraces have a higher probability of preservation. A similar preservation bias toward older strath terraces has been demonstrated in the numerical modeling of Limaye and Lamb (2016). Our model is aimed at constraining the timing and magnitude of these processes governing terrace creation and preservation.

This study fundamentally differs from knickpoint experiments in flumes where entrenchment in alluvial substrate follows from a base level drop at the downstream boundary condition of the setup (e.g. the early work of Brush Jr. and M. Gordon Wolman, 1960; Begin, D. F. Meyer, and Schumm, 1981; Schumm, Harvey, and Watson, 1984). In contrast, we use a fixed base level and the disturbance to the stream is hydraulic, as the sediment transport capacity suddenly increases at the upstream boundary of the model. The relevant landform for this case is a river flowing across a piedmont over a large alluvial fan or a bajada that incises its bed after a change in climate, and not an alluvial river forced by its base level. One of the key differences resides in the evolution of the sediment flux during the experiment: in a knickpoint setup, the stream is subject to an increase in sediment flux after passage of the knickpoint. But in the case of a stream that incises from a steep to a shallower gradient, the sediment flux gradually decreases as the river nears equilibrium. The work of Schumm, Mosley, and Weaver (1987, Ch. 6), G. A. Meyer, Wells, and Jull (1995) or Gran et al. (2013) describes entrenched channels after the passage of a knickpoint and their reaction to lateral sediment input due to channel migration and erosion of confining alluvial walls. This is relevant for the post-incision evolution of the channels we model.

Entrenchment index

A rich incisional history is recorded in the cross-sectional geometry of an entire flight of terraces. However, no standard metrics exist for quantifying the different geometries a valley cross section can take as a result of its incisional history. To cast this two dimensional geometry into a single scalar parameter, we define an entrenchment index, i_E. i_E is inspired by the idea of a hypsometric curve but with valley width replacing elevation. The eroded area between the channel bed and the top of the highest terrace is cumulatively measured from bottom to top, $A(z)$ with $z = [z_{base} \dots z_{top}]$. The integral of $A(z)$ is then normalized by the total area of the cross section, A_t, and by the maximum elevation difference $z_{top} - z_{base}$ (Figure 3.4 A-B). The normalized integral of the cumulative function is then multiplied by two so that its maximum value ($i_E = 1$) represents a perfect rectangular geometry (Figure 3.4 A) and smaller values represent increasingly more funnel-shaped geometries (Figure 3.4 B):

$$i_E = \frac{2}{A_t \left(z_{top} - z_{base}\right)} \int_{z=z_{base}}^{z_{top}} A(z)dz \tag{3.1}$$

The entrenchment index allows us to quantify the geometric evolution of the valley. i_E is very sensitive in minimally incised valleys because small topographic changes are very important relative to the total vertical incision. The entrenchment index is best used in geometries where width and depth are of the same order of magnitude. For example, in the scenario envisioned in Figure 3.3, entrenchment starts with a value $i_E = 1$ (Figure 3.4 C I). The index i_E decreases with the development of stepped terraces (Figure 3.4 C II). When the river starts to carve an entrenched canyon, the wall feedbacks engage, and i_E drops (Figure 3.4 C III). Eventually, as the equilibrium gradient is reached, ongoing lateral erosion progressively erases the youngest terraces from the record, leading to an increase in i_E (Figure 3.4 C IV).

3.3 Model

Setup

In the next three sections we test the entrenchment scenario (Figure 3.3) and the influence of the feedback mechanisms described above. We employ a simple numerical model that formalizes the essential physical mechanisms at work in a set of geometric rules. We opt for a geometric model instead of a physical one so that we can use an equal and balanced geometric abstraction of phys-

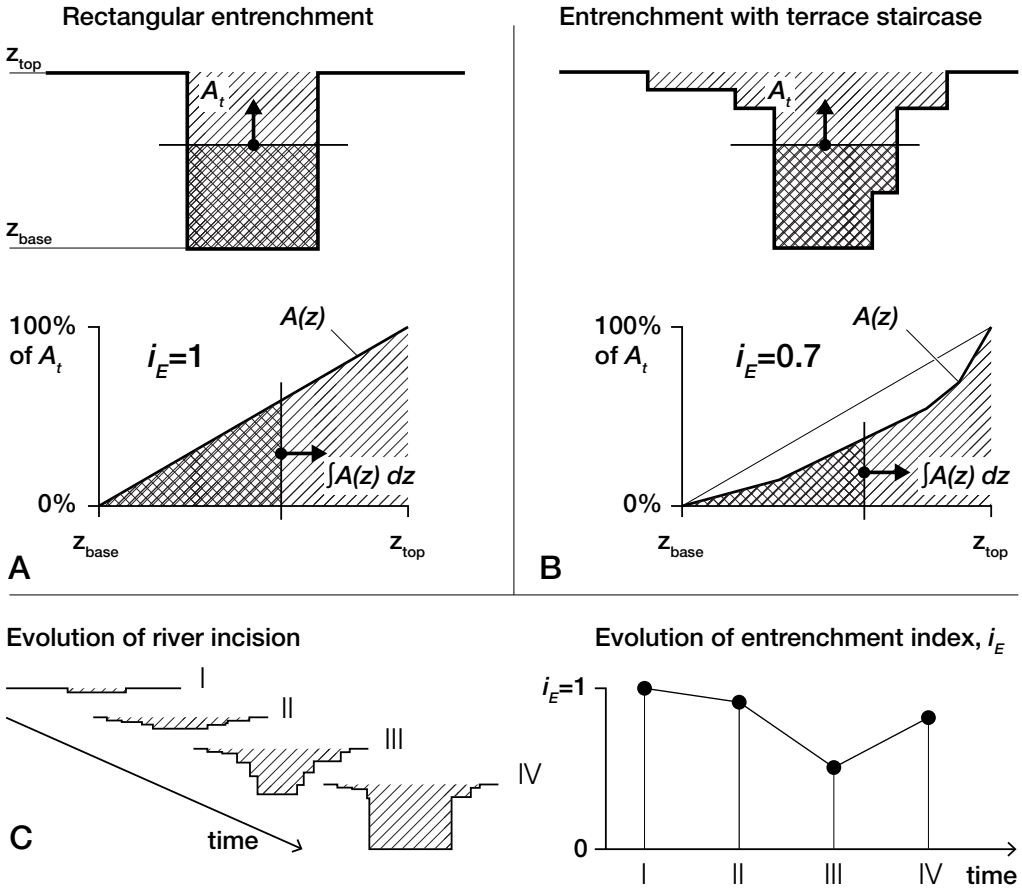

Figure 3.4: Illustration of the entrenchment index i_E, for a rectangular canyon in A (top) and for a stepped canyon in B (top). i_E is calculated with Equation 3.1 from the normalized integral of the cumulative function recording canyon area from base to top as represented by the arrow marking the cumulative measure, $A(z)$ (cross-hatched), of the entire area, A_t (hatched, A and B bottom). C: scenario of valley entrenchment similar to Figure 3.3 and evolution of the respective i_E values.

ical laws for all the components of the model. State-of-the-art physical laws for the different processes involved in the model have widely different levels of sophistication and coupling them would result in a model of heterogeneous complexity and only as good as its most rudimentary component. The use of geometric rules, also makes the modeling computationally inexpensive. Every time step is an erosive bankfull event, corresponding to a characteristic flood. The code is designed to model the continuous incision of a channel in a gravel-sized sedimentary substrate. The width of the channel can only narrow in reaction to lateral constraints during entrenchment. We do not seek to model the long-term evolution of the channel which would include widening after it reaches its near-equilibrium shallower slope and erodes its lateral constraints. The model is non-dimensional but we parametrize it so that dimensionalization to field values result in vertical incision rates on the order of mm/yr to cm/yr.

The model setup is a series of river cross sections. Sections are linked through their thalweg elevations that define the local stream gradient. The channel migrates sideways independently in each cross section. Sediment erosion and transport are expressed as surface area in the spatial dimension of the cross sections. Steep alluvial rivers are often braided, but during bankfull episodes, only one or a few strands will channelize the bulk of the water in a braided floodplain, the smaller, shallower, channels do not play a significant role in shaping the floodplain geometry (M G Wolman and Miller, 1960). We consider one single channel and not multiple strands for the sake of simplicity. During a bankfull event, a stream can incise its bed and move across its floodplain. In reality, the lateral motion depends on various fluvial processes such as braid avulsion, channel curvature, and bed morphology, and is not straightforward to predict. We use a random-walk model to attribute a lateral distance to be travelled by the channel during each bankfull event and to reflect the stochasticity of lateral migration. The lateral migration distance x_{lat} is chosen by a random selection from a normal distribution centered around a factor of channel width, and is independently generated for each cross section. The direction of migration has equal chances to be left or right, regardless of proximity to valley walls or migration history.

The topographic nodes of each cross section are divided into four categories: 1) river channel, 2) floodplain, that is all nodes lower than a prescribed threshold height, above the thalweg, h_{FP}, 3) talus deposited after bank collapse, and 4) terraces, that is abandoned floodplain at heights $\geq h_{FP}$. The substrate is equally erodible in these four categories and the product of erosion is directly added to the sediment flux. In the floodplain nodes, pure lateral displacement has no cost for the sediment budget: in the absence of vertical incision, the product of horizontal erosion is not added to the sediment flux, but is moved to the lateral fill of the trailing bank.

The erosion that occurs during the bankfull event is set by hydraulic geometry and incoming fluxes of sediment and water. In a transport-limited river, the rate of bed erosion or deposition is defined by the downstream divergence of total bedload sediment flux, $Q_s = Wq_s$, where W is channel width and q_s is bedload flux per unit width (Exner, 1925; Paola and Voller, 2005). q_s is determined by the non-dimensional shear stress (Shields stress) acting on the bed: $\tau^* = \frac{\tau_b}{(\rho_s - \rho_w)gD}$, where τ_b is basal shear stress, ρ_s is sediment density, ρ_w is water density, D is the characteristic grain size, and g is gravity (Shields, 1936). In steady, uniform flow, the basal shear stress is defined as $\tau_b = \rho_w ghS$, where h is water depth and S is slope. Furthermore, continuity requires that $h = Q_w u^{-1} W^{-1}$, where Q_w is water discharge, and u is flow velocity. Flow velocity is typically calculated using a flow resistance equation that depends on slope, grain size, hydraulic radius ($R = \frac{hW}{2h+W}$), and/or flow depth. q_s is then a function of the geometric terms (channel slope and width), material terms (grain size and density), and of the hydraulic terms (water discharge, velocity, and flow depth).

Different empirical equations for sediment transport have been proposed to predict q_s in gravel streams (e.g. Meyer-Peter and Müller, 1948; Rickenmann, 2001; Wong and Parker, 2006). They generally rely on the concept of excess Shields stress: $q_s = f(\tau^* - \tau_c^*)$, where τ_c^* is the threshold Shields stress for incipient motion of bed material. Combining such equations to predict sediment flux yields an expression that is non-linear and exhibits threshold behavior (i.e., $q_s = 8(\tau^* - \tau_c^*)^{3/2}$). In order to solve this system of equations we must iteratively solve for q_s by converging to a valid combination of u and h. This

must be done for each combination of W and S. In order to simplify our calculation of sediment transport we used simple expressions to match the behavior of this system of equations. Sediment grain size, which is not explicitly considered, is implicitly assumed constant along the downstream dimension of the model and through the modeling period. Similarly, there is no explicit water discharge in the model and consequently no flow depth or velocity. Instead we assume that contributions of the hydraulic terms to the bedload flux are only a function of slope and width. The model focuses only on variations in these geometric terms, that is channel slope and width, to control changes in sediment flux during each model run and across the model space. The range of sediment transport we model is that of a condition largely exceeding the threshold of transport and we assume a linear slope dependency, ignoring the threshold behavior. The resulting sediment flux equation takes the form

$$Q_s = k_A k_w \frac{S}{S_i} Q_{s_i}, \text{ with} \tag{3.2}$$

$$k_w = k_{norm} \frac{W^v}{(W_o \frac{u-v}{v} + W)^u}, \tag{3.3}$$

which mimics the empirical equations of Meyer-Peter and Müller (1948), Rickenmann (2001) and Wong and Parker (2006) as discussed below. Equation 3.2 predicts bed load transport relative to initial values of channel slope, S_i, and transport capacity, Q_{s_i}. The sediment flux is modulated with the erosivity coefficient, k_A, that accounts for the flow characteristics and its duration, as well as the size of the bedload which are not explicit in the geometric model. The width function $k_w(W)$ specifies how the sediment transport rate changes as a function of width. For a given water discharge, a narrower channel results in a larger water depth, an increased basal shear stress and a greater sediment transport flux per unit width. But if the section over which sediment is transported is too narrow, the total sediment flux Q_s decreases. The optimal width, W_o, offers the maximum total sediment transport capacity and k_w is a function that takes the form of a gamma distribution (Eq. 3.3). k_{norm} is a normalization coefficient that sets $k_w = 1$ when $W = W_o$. The coefficients $u = 0.9$ and $v = 0.6$ in Eq. 3.3 are kept constant. They are chosen so that the width dependency of Eq. 3.2 fits the trends predicted by the empirical equations of Meyer-Peter and Müller (1948), Rickenmann (2001) and Wong and Parker (2006). The evolution of the sediment transport law (Eq. 3.2) as a function

of the two geometric parameters slope and width is shown in Figure 3.5 along with the empirical laws of Meyer-Peter and Müller (1948), Rickenmann (2001) and Wong and Parker (2006) for comparison. The sediment transport law we employ is calibrated against values of channel slope ranging from 0.1% to 2%, channel width from 1 to 1000 m, grain size of 1 cm, and water discharge of 1000 m^3/s.

Our approach purposefully reduces the complexity of fluvial sediment transport to changes only in slope and width during runs. Equations 3.2 and 3.3 linearly scale with changes in hydrology represented by the erosivity coefficient k_A. In the empirical equations used for comparison in Figure 3.5, changes in hydraulic parameters modify the curvature of the functions and we ignore these effects here to focus on the geometric terms. As a consequence, the model we build here has only a qualitative predictive power and the magnitude of the dynamics we model can vary under different hydraulic conditions. The model is not designed for the investigation of the long term post-incisional evolution of the channel in large part due to the absence of mechanisms to widen the channel and aggrade the floodplain. The post-incisional evolution of the scenario, after the end of the model run, should however be similar to flume experiments (Schumm, Mosley, and Weaver, 1987) and field observations (G. A. Meyer, Wells, and Jull, 1995; Gran et al., 2013) that describe deposition of alluvium on the floodplain and widening of the stream under the influx of sediment from the eroding valley walls.

In a 1-D model, deposition would never occur under this incisional regime. However, because we prescribe stochastic lateral migration of the channel, the total amount of vertical and lateral erosion can vary from one time step to another, in turn, leading to local variations in slope that may induce deposition. Nevertheless, the primary way for sediment supply to exceed transport capacity is by lateral supply of sediment from the valley walls. We did not model sediment deposition caused by divergence of flux between cross section. In such cases, sediment was assumed to bypass cross sections where sediment supply exceeded transport capacity. This is not physically correct, but is not expected to substantially affect the findings because such instances were rare in this rapidly incising channel.

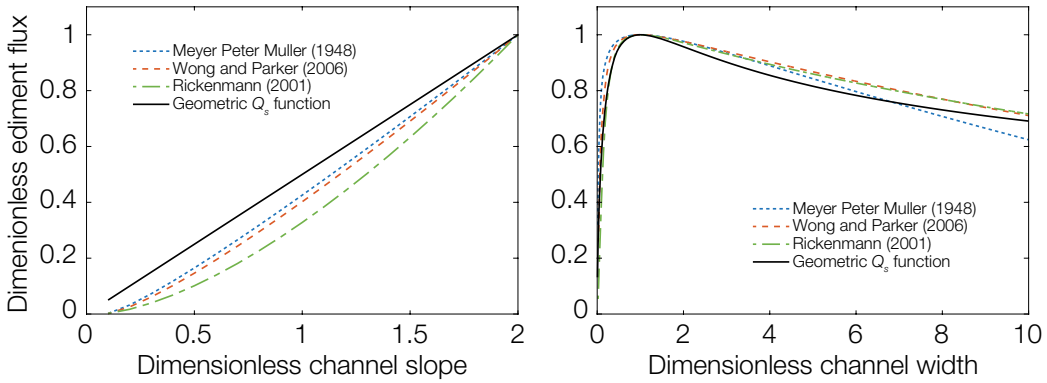

Figure 3.5: Comparison of the geometric sediment transport law (Eq. 3.2) as a function of changes in slope and width with the empirical equations of Meyer-Peter and Müller (1948), Rickenmann (2001), and Wong and Parker (2006). Sediment flux is normalized by the maximum transport capacity and width is normalized by the optimal width for sediment transport (20, 46, and 33 m for the laws of Meyer-Peter and Müller (1948), Rickenmann (2001), and Wong and Parker (2006) respectively). The three empirical equations are calculated for a large river with a fixed width of 150 m when slope varies (left), and a fixed slope of 1% when width varies (right), grain size of 1 cm, and water discharge of 1000 m^3/s using the flow resistance equation of Bathurst (1985).

For our incision scenario with lateral valley wall inputs (Figure 3.3), the expected changes in geometric parameters are shallowing of the stream gradient and potential narrowing of the width relative to the initial values, S_i and W_i. All cross sections start with the same initial values of width (W_i) and slope (S_i) and the first cross section of the model is fed with a sediment input from upstream, $Q_{s_{in}}$. At equilibrium, the model will have a transport capacity matching the incoming $Q_{s_{in}}$ in all cross sections. To promote erosion, we use a value of $Q_{s_{in}}$ that is four times smaller than the initial transport capacity of each cross section, Q_{s_i}. The erosion E at every time step is expressed in the model space as a surface area. E results from the divergence of sediment flux from one cross section to another:

$$E = \frac{\partial Q_s}{\partial x} \tag{3.4}$$

where x is the downstream distance between cross sections and sediment flux is a function of geometric conditions (W, S) per Equations 2 and 3.

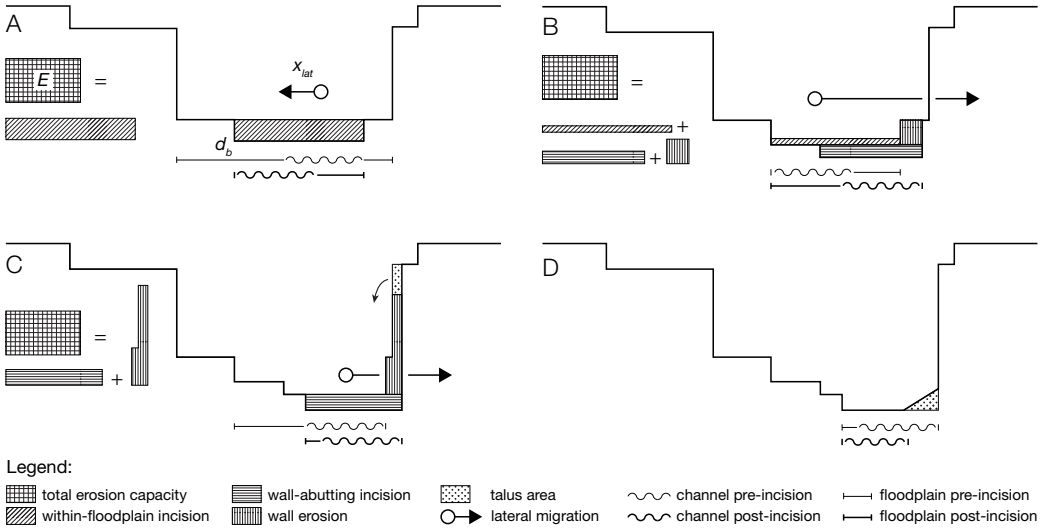

Figure 3.6: Step by step illustration of the model evolution. A) At the first step, lateral migration x_{lat} is a small jog to the left and the channel is confined within the floodplain. The area to be eroded E is represented by the cross-hatched rectangle to the left and is distributed under the channel migration path. B) At the second time step, the lateral migration is a larger step to the right. The channel incises the floodplain until meeting the valley wall. Then erosion is partitioned between terrace erosion and bed incision. The bank is short and the product of erosion by successive undercutting can be immediately evacuated. C) Lateral motion continues to the right. The channel now undercuts a taller cliff and it cannot immediately remove the entire product of cliff erosion from undercutting. D) The rest of the material (stippled pattern) is deposited as a talus pile at the base of the cliff and forces the channel to narrow.

In a given cross section, the lateral distance travelled by the stream, x_{lat}, sets the section across which the eroded area E is distributed. Figure 3.6 shows how erosion is formalized in the geometric model in three successive time steps. When the stream is confined within the floodplain, x_{lat} is smaller than the distance between the valley wall bounding the floodplain and the river on its migrating side, d_b (Figure 3.6 A). In this case, the entire erosion capacity E is distributed evenly across the lateral path to reflect vertical incision under the channel bed and erosion of the channel bank such that the depth of vertical incision is

$$I_1 = \frac{E}{x_{lat} + W}, \quad \text{for } x_{lat} < d_b \tag{3.5}$$

When the prescribed lateral displacement is greater than the distance to the valley wall, $x_{lat} > d_b$ (Figure 3.6 B), the stream moves against the edge of the floodplain and starts eroding the terrace riser. Vertical incision during migration across the floodplain remains I_1. The ratio d_b/x_{lat} partitions the total erosion E into floodplain-confined E_1 and terrace-abutting E_2 and E_3, bed and wall erosion, respectively, such that

$$E = \underbrace{E\frac{d_b}{x_{lat}}}_{E_1} + \underbrace{\lambda\, E\left(1 - \frac{d_b}{x_{lat}}\right)}_{E_2} + \underbrace{(1-\lambda)\, E\left(1 - \frac{d_b}{x_{lat}}\right)}_{E_3}, \quad \text{for } x_{lat} > d_b \quad (3.6)$$

The factor λ, between 0 and 1, sets the proportion of sediment transport capacity available for vertical incision of the bed when the river is simultaneously horizontally eroding a valley wall ($\lambda = 1$ prescribing only bed incision and $\lambda = 0$ prescribing only wall erosion). We choose here a value of $\lambda = 0.7$ for all runs, which means that when the channel erodes a valley wall, 30% of its transport capacity is dedicated to undercutting the wall and removing material that collapses into the river. We do not explore different values of λ, but future investigation is warranted as the partitioning of vertical and lateral erosion is an important parameter for valley wall feedback. The horizontal distance eroded into the wall depends on the lateral erosion budget of the stream and the mean height of the valley wall. In the model, the mean height is defined over a distance calculated iteratively until the eroded area corresponds to E_3. However, the lateral distance eroded into valley walls is always smaller than the distance that the stream would have traversed across its floodplain had it not encountered any obstacles.

Because the sediment of the valley wall will likely have some cohesive strength, we assume that erosion of the valley wall does not occur continuously as the river undermines this sediment. Instead, sediment is assumed to collapse into the river in pulses when lateral erosion has sufficiently undercut the valley wall. That critical depth of undercut for wall collapse is parametrized as x_{ucut} in the model. For short valley walls, we assume that x_{ucut} is limited by the tensile strength of the cantilevered block of sediment and scales with the height of the valley wall (e.g., Kogure et al., 2006). Crudely, we prescribe the critical depth of undercut to equal a fraction of valley wall height for short walls

($x_{ucut} = 0.2H$). Once valley walls exceed some critical height that is determined by its cohesive strength, we assume that this local cohesive strength sets the maximum undercut depth $x_{ucut,max}$, which becomes the critical value for failure.

Lateral erosion thus occurs stepwise during the flood event in cycles of undercut and collapse. Lateral erosion proceeds by increments equal to x_{ucut} until the eroded area meets or exceeds E_3. The eroded area in excess of E_3 is then deposited as talus at the foot of the cliff (Figure 3.6 C). The talus can constrain the channel in its floodplain and effectively reduce its width (Figure 3.6 D). We assume that channel width tends unidirectionally towards W_o for a maximum transport capacity at a given slope (Lavé, 1997). There is no mechanism for channel widening or floodplain aggradation in the model and the channel cannot narrow below the optimal width W_o to avoid scenarios warranting widening. For the same reason, once a constraining talus pile is cleared from the floodplain, the channel does not revert back to its former width. In reality we expect transient phases of aggradation to restore full transport capacity when $W < W_o$. To keep the model simple we ignore this transient effect.

Vertical incision occurs at a slower rate when eroding a cliff because part of the transport capacity is dedicated to sediments yielded by the wall. But the channel, limited by the pace of valley wall erosion, stays in the same location, resulting in a deeper wall-abutting vertical incision I_2:

$$I_2 = \lambda \frac{E}{W + x_{bank}} \left(1 - \frac{d_b}{x_{lat}}\right) \tag{3.7}$$

Our model can be reduced to one dimension by setting $x_{lat} = 0$, to compare the effects of lateral dynamics on vertical incision rates with the predictions of widely used 1-D frameworks (Parker, 2015). The reduced model is obtained by switching off lateral movement of the channel, thereby preventing any interaction with the banks, and keeping the channel width constant. The 1-D comparison is not used to investigate terrace formation per se, but rather as a reference for quantifying incision rate in the absence of autogenic enhancement due to lateral inputs of talus. This comparison allows us to better understand

response to external forcing versus autogenic processes as further discussed in section 3.5.

Parameter exploration

The model explores the impact of five parameters that represent the main elements controlling river incision: 1) the erosive potential of the bankfull event, represented by the erosivity coefficient k_A, 2) the maximum depth of undercut before bank collapse $x_{ucut,max}$, 3) the initial width of the river W_i, 4) the lateral mobility of the channel in the floodplain x_{lat}, and 5) the height of the floodplain relief h_{FP} (Table 3.1). The parameters can express the combined effect of different convolved factors. The range of values of these parameters is inspired by the rivers of the north Tian Shan. The dimensionalization of the runs with meters for length units and years for timestep units results in river segments that are 30 km long, with an initial slope of 2% and incising at rates of mm/yr to cm/yr over 2000 to 8000 years, similar to the rivers of the north Tian Shan. We systematically investigate the effect of the parameters on vertical incision patterns.

The erosivity coefficient k_A is a proxy for the intensity and the duration of a bankfull event. If the storms are very powerful and erode significantly during each flood, k_A is large. On the contrary, for the case of a river where bankfull events have a moderate magnitude and where erosion occurs by smaller increments, k_A is smaller.

The maximum undercut depth that a bank or a wall can support before failure is a proxy for its strength. As described in the previous section, the critical undercut depth for collapse scales directly with the height of the wall as a function of tensile strength ($x_{ucut} = 0.2H$) until a maximum undercut value, $x_{ucut,max}$, is reached for tall cliffs (set by cohesive strength), at which point cliff collapses occur. A small value represents a weak lithology, e.g. loose sand, while a large value reflects stronger material, e.g. cemented conglomerate, capable of supporting a significant undercut at its base. Larger undercut depths result in larger talus piles.

The initial width of the river depends on the local history of the stream and its

condition at the onset of incision as inherited from the latest phase of aggradation or sediment bypass. This initial condition governs the susceptibility of the channel to subsequent evolution. An initially wide channel has the opportunity to narrow significantly and modify its hydraulic geometry.

The parameter x_{lat} sets the cross-stream distance covered by the migrating channel if it does not encounter any obstacles: that is, if it remains within the floodplain and does not erode valley walls. If the channel erodes valley walls, then the migration distance is limited by the erosion capacity of the stream. The random walk underlying x_{lat} is designed to represent the distribution of stresses within a cross section that may lead to lateral migration. In addition, the mean of the distribution of x_{lat} reflects the resistance of the floodplain to lateral erosion and the duration of the bankfull event, with large migration corresponding to high erodibility and/or long events.

A surface abandoned by the channel becomes a terrace when it rises above the prescribed topographic relief of the floodplain: h_{FP}. In the model, that transition determines when the undercut of valley walls (i.e. terrace risers) engages. The relief of a floodplain is expected to scale with the flow depth of a bankfull event and the size of the sediments.

Simulation procedure

We tested 40 sets of parameters in 360 simulations to assess the sensitivity of the model to the various parameters. Each of the five parameters k_A, x_{lat}, h_{FP}, $x_{ucut,max}$, and W_i is varied systematically while the others are held constant (Table 3.2). In addition, we ran three sets of simulations where variables covary to illustrate the end member cases. We monitor the model evolution by recording vertical incision at every cross section and geometry of entrenchment (with i_E, Figure 3.4). Simulations are run nine times with each parameter configuration to account for the variability due to the random walk controlling lateral migration (Figure 3.7).

3.4 Results

To illustrate the model setup and the breadth of dynamics it captures, we present two end-member simulations in Figure 3.8 (runs 19 and 18 in Table

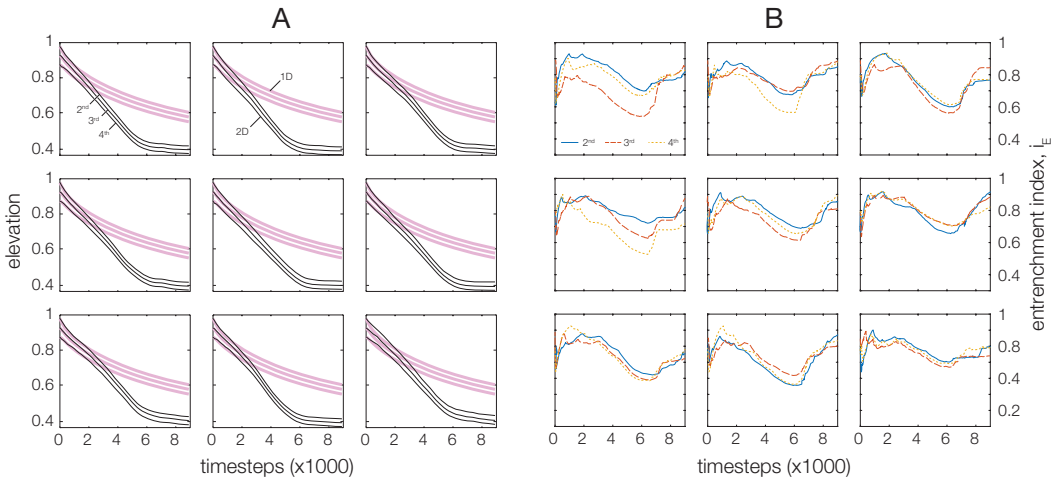

Figure 3.7: Nine repeated simulations of run 19 (Table 3.2) with identical parameters that illustrate the inherent variability of the geometric code. A) Time evolution of the elevation of the second, third and fourth cross section from upstream in black. The y-axis is normalized by the maximum height of the cross-section. The pink lines show, for reference, the same runs without lateral migration, effectively 1-D simulations. B) Evolution of the entrenchment index for the same three cross sections during the model run time.

3.2) and Figure 3.9 (run 18). The left side of Figure 3.8, A-D, is a simulation with relatively weak hydraulic parameters: reduced erosivity k_A, low floodplain relief h_{FP}, and small characteristic lateral migration x_{lat}. The result is an extensive series of abandoned terraces in the deeply incised upper reach that turns into a wide floodplain downstream as the channel nears base level (Figure 3.8 A). The great number of terraces (illustrated by the time-evolution of the second cross section from upstream in Figure 3.8 B) is the product of the channel's inability to efficiently erode its banks due to low k_A (low discharge) and low x_{lat} (short bankfull events). The limited transport capacity of bankfull events means that the thresholds for talus deposition and channel narrowing are reached early on. It leads to an acceleration of the vertical incision rate that departs starkly from the monotonic slowdown of vertical incision observed if the same experiment is run with $x_{lat} = 0$, effectively a 1-D simulation (Figure 3.8 C). The longitudinal profile evolution of the same run is shown in Figure 3.9. The narrowing of the channel and its floodplain and the abandonment of stable terraces have a characteristic geometric signature captured by the entrenchment index i_E in the second cross section from upstream (Figure 3.8 D). i_E decreases as the funnel shape of the cross sections

is accentuated by enhanced vertical incision and increasingly reduced lateral erosion until the gradient reaches near equilibrium (stabilization of the channel elevation in Figure 3.8 C). The vertical incision slows down to zero while lateral migration of the channel continues and eventually erodes valley walls and terraces (youngest first). i_E then increases again towards one, the value characteristic of a perfectly rectangular cross section.

The right side of Figure 3.8, A'-D', illustrates the opposite end-member scenario where the hydraulic parameters are relatively strong: large erosivity k_A, significant floodplain relief h_{FP}, and long characteristic lateral migration x_{lat}. The high sediment transport capacity can easily remove material collapsed form the valley walls. The few abandoned terraces are eroded quickly and have a short lifetime because the river erodes the terrace risers easily, sustaining a wide floodplain and little reduction in channel width (Figure 3.8 A' and B'). While the vertical incision pattern of this simulation resembles that of the 1-D reduction (Figure 3.8 C'), we note that vertical incision in the 2D model initially lags the 1-D case and later overtakes it when the slight channel narrowing that does occur provides additional transport capacity to reach a shallower equilibrium slope, i.e. lower elevation. In this case the thresholds that lead to deposition of talus piles and narrowing of the channel that results in enhanced vertical incision are not met.

Every parameter set has a characteristic geometry with some degree of variability unique to each run. The inherent scatter of every run is illustrated in Figure 3.10 where the entrenchment index i_E is quantified at the end of the main phase of vertical incision before lateral erosion widens the floodplain again and where i_E is minimized (see Figure 3.8 C and D). Each vertical cluster in Figure 3.10 is composed of i_E measured at the second, third and fourth cross sections from upstream in the 9 repeat runs for a total of 27 points. We omit i_E at the first cross section to avoid boundary effects, and limit the measurements to the upstream reach to compare cross sections with similar total vertical incision. The broad scatter of results along the y-axis, reflects the variability of results within one parameter set. The autogenically-dominated behaviour exemplified in Figure 3.8 A-D is primarily controlled by a reduced k_A (Figure 3.10 A) while the parameters u_{cut} and W_i have a weak effect on

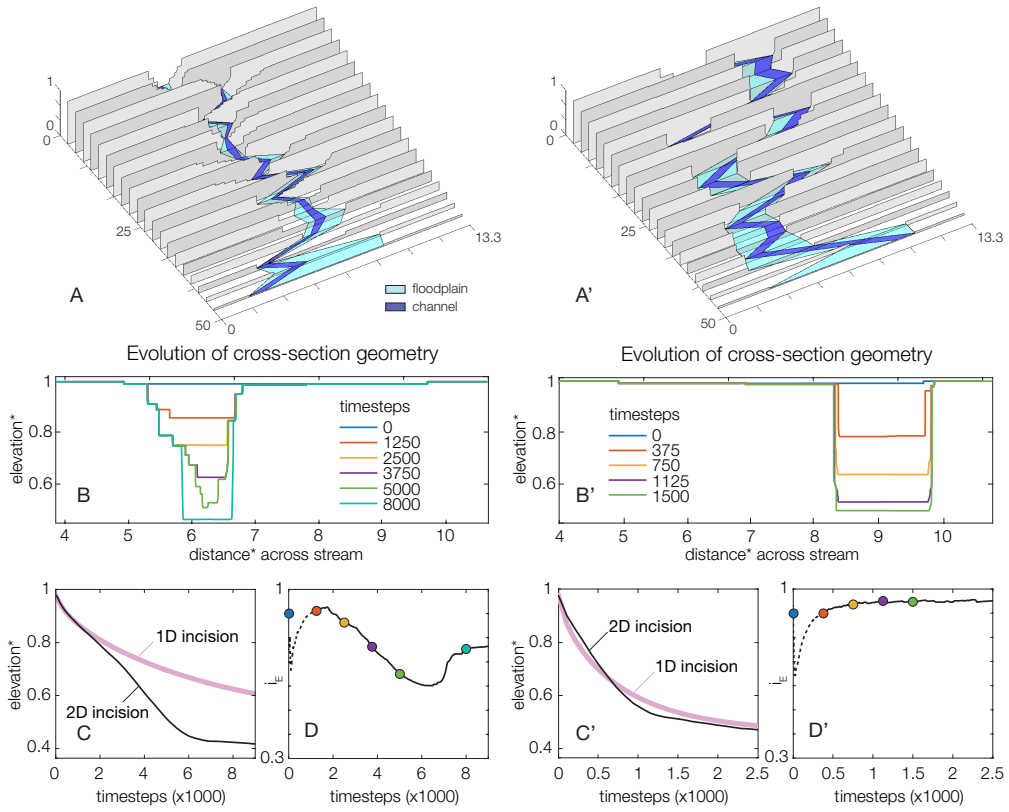

Figure 3.8: Two simulations capturing the end member behavior of the model with respectively low (A to D) and high (A' to D') intensity bankfull events represented by low or high erosivity of the bankfull flood k_A, floodplain relief h_{FP}, and channel migration x_{lat} (run 19 and 18 in Table 3.2). A & A': Geometry of the model when the channel gradient is near equilibrium after slowdown of the incision rate (at time steps 7000 and 1500 respectively). The three axes are normalized by the total height of the model in the z dimension. B & B': Evolution of the second cross section from upstream through time, starting with the initial geometry at t=0. C & C': Elevation of the channel in the second cross section through time in black; the pink line represents the same experiment without lateral migration of the channel, effectively a 1-D simulation. D & D': Evolution of the entrenchment index i_E through time for the second cross section. The initial drop due to shallow incision in a floodplain flanked by short walls is ignored and marked by a dotted line.

i_E. A small maximum undercut depth u_{cut} limits the potential growth of talus piles and has a weak effect on i_E as well, largely within the scatter of results. A narrower initial width W_i increases the potential for fast vertical incision rates at an early stage because it is closer to the optimal transport width (Figure 3.5). Additionally, as the lateral migration of the channel scales with

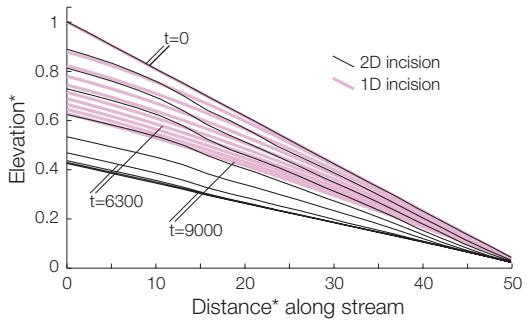

Figure 3.9: Longitudinal profile evolution of run 19 (Figure 3.8 A-D and Table 3.2) from t=0 to t=9000 with one profile every 900 time steps. The black lines show the model with lateral migration and the pink lines represent a 1-D model with lateral migration switched off. The x- and y-axes are normalized by the maximum height of the model.

channel width in the model, a smaller initial width will result in more frequent vertical incision episodes and the river will entrench faster (Figure 3.10 C). Characteristic lateral migration x_{lat} and floodplain relief h_{FP} do not affect i_E. A large x_{lat} value can delay the initial entrenchment because the channel tends to sweep long lateral distances and rarely focus its incision vertically.

3.5 Discussion

Our simulations show that even in the simple case of a river entrenching into its former fill under constant forcing, the vertical incision history can differ significantly from what a 1-D model would predict. Interactions between valley wall erosion, vertical incision and channel width evolution, as captured in our model, can lead to enhanced vertical incision, compared to the 1-D channel evolution (Figures 3.7-3.9). However, our model explores only one simple scenario and ignores several processes that are ongoing in fill-cut terrace environments. For example our model ignores hillslope and cliff erosion not driven by fluvial action: terraces shielded from fluvial undercutting do not degrade. In nature we expect hillslope processes to degrade and eventually erase abandoned surfaces.

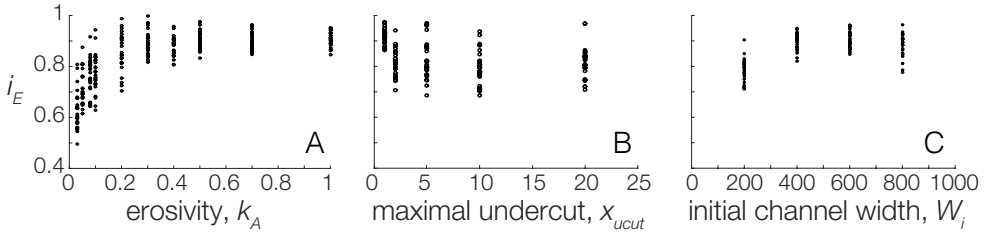

Figure 3.10: Sensitivity test of the model by systematic variation of one parameter and its effect on the minimum entrenchment index (captured at the end of the main incision phase, before its recovery by lateral erosion, see Figure 3.8 C and D). Every cluster on the x-axis is made of 27 points. In A, test of the erosivity parameter k_A [unitless]; in B, of the maximum undercut depth $x_{ucut,max}$ [L]; and in C, of the initial channel width W_i [L].

Comparison with earlier studies

Two studies in particular, by Schumm, Mosley, and Weaver (1987, Ch. 6) and G. A. Meyer, Wells, and Jull (1995), have investigated similar fluvial geometries where a river is bound by tall valley walls of alluvium. There are fundamental differences between the forcings they considered and ours, but this earlier work sheds light on the evolution of the river after it reaches near longitudinal equilibrium and that we only partly investigate with our model.

The post-incisional dynamics of the present scenario should correspond to the observations of Schumm, Mosley, and Weaver (1987, Ch. 6). In their flume experiments, the changing boundary condition is a drop in base level that forces fast localized incision by a migrating knickpoint. As the knickpoint migrates upstream, an increase in sediment flux overwhelms the sediment transport capacity downstream and shuts off vertical incision, promoting downstream widening of the valley. This is analogous to the valley widening that occurs in our model after the river has adjusted to its new equilibrium slope and vertical incision has stalled. In a flume experiment related by Schumm, Mosley, and Weaver (1987, Ch. 6, p. 206), the channel reacts to a change in base level with rapid initial incision, followed by widening of the channel and floodplain to adjust to the increased sediment flux. Unfortunately, slope changes are not precisely tracked in these experiments and it is hard to identify trade-offs between the two essential geometric adjustments of the channel that are slope and width. In our study, the changing boundary condition is an increased sed-

iment transport capacity that leads to progressive adjustment of the channel slope from steep to shallow gradient. It is accompanied by a constantly decreasing sediment flux at the outlet: from the strong flux caused by the rapid initial erosion, to a smaller flux equal to the input from the upstream boundary condition of the model after erosion has ceased and the stream reached a new equilibrium.

G. A. Meyer, Wells, and Jull (1995, p. 1227-1228) suggest that during valley widening, "the threshold of critical power for channel incision is not exceeded" meanwhile "a consistent supply of sediment from distal fan erosion would permit construction of a broad floodplain and inhibit degradation in the lower valley." Like the flume experiments of Schumm, Mosley, and Weaver (1987, Ch. 6), this is a case of a channel subject to an increasing sediment flux. The river adapts its transport capacity to an increasing load and does so by widening the channel and the floodplain. This situation would again be relevant for the period that follows the entrenchment phase we model, that is when the channel ceases to incise with respect to its base level and widening of the valley continues. During the window of vertical incision that is the focus here, the sediment flux in the channel decreases with the sediment transport capacity as it relaxes from its oversteepened initial geometry to a shallower slope.

Effects of parameters

The erosivity coefficient k_A appears to be the key parameter determining if the positive entrenchment feedbacks can be initiated. k_A is a proxy for the total sediment transport capacity of a bankfull event, that is its magnitude and/or duration. Ultimately, it is the capacity of the river to evacuate material collapsed from the valley walls that determines if and when lateral feedbacks can enhance entrenchment and lead to channel narrowing.

The characteristic lateral migration of the channel has little effect on the evolution of entrenchment. This is due to the fact that, initially, even a limited lateral motion will cause the channel to interact with the valley walls. Furthermore, it is the probability of very small migration distances that matters most. In this case, the increase in wall height is maximal and subsequent lat-

eral erosion is that much harder. Finally, the initial width matters in that it sets the potential for stream narrowing and thereby the possible increase in sediment transport capacity relative to the initial geometry.

To synthesize the numerical exercise, we collapse the simulation results to show i_E as a function of a common non-dimensional parameter k_{ND}. The key component controlling lateral feedbacks is the relationship between the volume of material produced by the eroding valley walls and the capacity of the river to remove this material. When the former exceeds the latter, significant talus deposits start shielding the banks and constraining the channel. To reflect this first-order relation, we define $k_{ND} = k_A W_{in}/x_{ucut,max}$, so that the erosivity coefficient [dimensionless] and the width [length] across which sediment is transported are balanced by the value of the maximum undercut [length], a parameter for the volume of material shed from the valley walls. The other control on that volume is the height of the walls but this value varies with time and cannot be treated as a model parameter. We show in Figure 3.11 how k_{ND} captures, albeit crudely, the sensitivity of entrenchment geometry to the parameters. The entrenchment is enhanced for smaller values of k_{ND}, reflecting the increasing importance of talus deposits.

Rate of vertical incision

We compare each simulation with a 1-D counterpart that is identical except for the absence of channel lateral migration (Figure 3.7 A). The channel lateral dynamics affect vertical incision rates in two ways. First, the initial rate is slower than in 1-D as a result of the lateral migration that consumes sediment transport capacity otherwise budgeted for vertical incision. Second, if significant channel narrowing occurs, the increased sediment transport capacity perpetuates a rapid vertical incision rate compared to the 1-D case. The equilibrium slope of the narrower channel is shallower and the stream incises deeper into the substrate. The magnitude of the two effects vary with different parameters but they are almost always observable. Accelerated vertical incision rates also mean that deeper strata of the underlying substrate can be eroded and remobilized in the modern sediment flux relatively fast. Recycling of old sediments in modern fluxes has consequences for the study of signals in sediment routing systems (e.g. Romans et al., 2015).

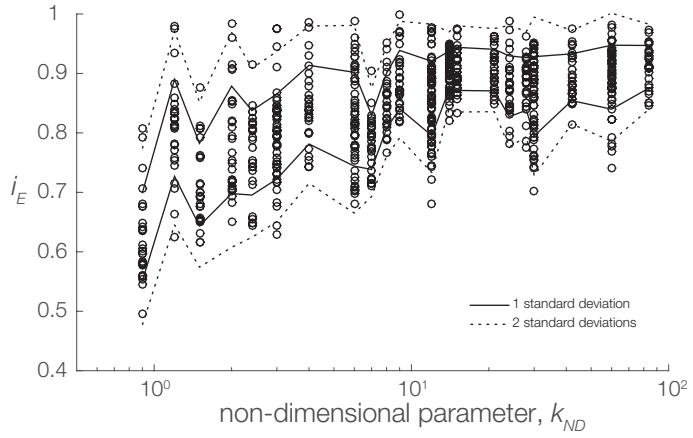

Figure 3.11: Minimum entrenchment index (captured at the end of the main incision phase, before its recovery by lateral erosion, see 3.8 C and D) as a function of the non-dimensional parameter $k_{ND} = k_A W_i / x_{ucut,max}$ where k_A is the erosivity parameter, W_i is the initial channel width, and $x_{ucut,max}$ is the maximum undercut necessary for the collapse of tall cliffs for each of the runs listed in Table 3.2 (open circles). One and two standard deviations are drawn to indicate the trend that is partly obscured by the model stochasticity.

The initial vertical incision rate slows down with greater lateral migration because much of the erosional capacity is consumed laterally (cf. Figures 3.8 C and C'). This situation is favored when the initial channel is wide and has a small vertical incision capacity per unit width.

Our model suggests that incising alluvial rivers are constrained by valley walls and can narrow during entrenchment. The reduction in transport capacity that follows from a shallowing slope is counter-balanced by the increased water depth if the channel narrows. As a result, the vertical incision history of the river departs from the monotonic relaxation expected from the 1-D perspective (Figure 3.8 C-C').

The numerical experiments illustrate the importance of the thresholds for talus deposition and channel narrowing. Autogenically-accelerated vertical incision occurs when both are passed. Two quantities are in play: 1) the amount of material that can be removed from the channel during a bankfull event, which is set by the local divergence in sediment transport capacity, and 2) the volume

of material that collapses from the valley walls into the channel and forms a talus pile after the budget for lateral erosion (E_3) has been consumed. The collapsed material is a function of the wall height and the critical undercut depth leading to failure — depending on the cohesion of the valley wall — and is independent from the hydraulic conditions. Under conditions of relatively low-intensity bankfull events (small k_A, x_{lat} and h_{FP}) the channel finds itself more sensitive to bank collapse because small floods are only capable of removing a small portion of the collapsed material and the rest forms a talus. As a consequence, the importance of lateral feedbacks grows with reduced flood erosion capacity. In the low erosivity parameter space, channel width is thus reduced early, when the stream gradient is far from equilibrium. And so the enhanced erosion capacity due to channel narrowing impacts the system while its incision potential is still large. In this case, the decrease in transport capacity due to the shallowing slope is outweighed by the channel narrowing (Figure 3.5 and 3.9) and vertical incision can accelerate (Figure 3.8 C). On the contrary, in the parameter space of larger erosion rates, the channel only starts narrowing when the cliffs are high and the stream gradient already close to equilibrium, leaving little incision potential. There is then no opportunity to accelerate vertical incision and the valley geometry remains rectangular (Figure 3.8 C').

The local conditions of an entrenching alluvial river will define the magnitude of autogenic modifications of the vertical incision rate. From the vertical incision history provided by a fill-cut terrace record, it is necessary to first identify possible autogenic effects before attempting a quantitative interpretation of the external forcing. In the case of an observed acceleration in the vertical incision rate of a site, even qualitative interpretations of the situation first require assessing the origin of that signal, and how much of it, can be accounted for by autogenic dynamics.

Terrace record

Here, we discuss how our results may best be applied to actual records of complex-response terraces under climatic and tectonic forcings, including the possible bias introduced by incision transience and selective preservation of terraces.

The terrace record is often used as a direct proxy for external forcing. Usually researchers focus on strath terraces to stay clear of the autogenic patterns that can dominate fill and fill-cut terrace records (Schumm, 1973; W. B. Bull, 1991). It can happen, however, that both strath and fill-cut terraces share the same tread such as in the northern piedmont of the Chinese Tian Shan (Molnar et al., 1994) and the Himalayan piedmont (Lavé and Avouac, 2000), blurring the local relevance of discriminating strath versus fill-cut terraces. Furthermore, complex-response terraces hold information that their strath counterparts often miss. They often quickly succeed each other, offering a high-resolution temporal record which does not document a series of discrete forcing events but the history of the river elevation at punctual times during one episode of entrenchment. That is when the channel moves away from one side of the floodplain and continues incising long enough for the abandoned floodplain to become a terrace. In addition to their susceptibility to autogenic dynamics, fill and fill-cut terraces respond to and record external high-frequency forcings. Indeed, Poisson and Avouac, 2004 invert a fill-cut record to retrieve Holocene hydraulic forcing in Central Asia. Identifying and removing the incision effects of autogenic dynamics should permit the interpretation of high-resolution external forcings in a fill-cut record.

Our study shows that when autogenic feedbacks play a strong role, the entrenchment pattern recorded by the distribution of abandoned fill-cut terraces differs starkly from the actual forcing if one was to invert the vertical incision rate directly (Figure 3.8 C). To illustrate this point, we discuss here a thought experiment with a full terrace record comprised of allogenic fill terraces and autogenic fill-cut terraces sketched in Figure 3.12 after two cycles of incision and aggradation in a landscape in net uplift, such as a piedmont fold-and-thrust belt. Figure 3.12 is an illustration of the concepts discussed here and not a rigorous model prediction. We argue that differences in terrace generation and destruction may be deduced from entrenchment geometries and terrace ages.

Terraces are transient landforms. If fill-cut terraces are often created as a result of stochastic circumstances during an incisional phase, they will almost be surely destroyed later. Lateral erosion continues occasionally and trims the

terrace risers of the valley walls as the channel keeps migrating in its floodplain after the river reaches its equilibrium grade. It is noteworthy that a straight-flowing river (on average) has an equal chance of eroding either valley wall at any time by the random change in lateral migration of the stream while a river migrating unilaterally will preserve an entire terrace record in its wake. Younger terraces are eroded first as they border the channel and do so quickly because their height (and volume) is relatively low. This is illustrated in the short lifespan of terraces abandoned late in the incision cycle of Figure 3.12 B. For long-term preservation, terraces first need to survive their infancy close to the river channel where the risk of erosion is highest. In the scenario where autogenic dynamics are important (illustrated by run 19 in Figure 3.8 A-D and Figure 3.9) we observe that the older fill-cut terraces tend to be wider and this, together with their greater height, means that they take longer to be entirely eroded. The larger resistance to erosion and the lesser risk of burial make the complex-response terraces that are abandoned shortly after a transition from aggradation to incision more likely to be preserved, a bias also observed in strath terraces (Limaye and Lamb, 2016). Consequently, the terrace record may be strongly affected by the degree of selective degradation that occurs. In Figure 3.12, the terrace record at time t_3 has been reworked relative to the record at time t_2, with the youngest terraces eroded. Classically, the youngest preserved terraces at t_3 in Figure 3.12 could be interpreted as markers of a discrete external event that forced a sudden entrenchment. But they could as well be the youngest remaining fill-cut terraces of a partially eroded record and bear no information about any punctual forcing event such as in the scenario of Figure 3.12. An entrenched river flanked by only high terraces may hint at a partial record where younger terraces have already been eroded. In contrast, in an uplifting alluvial setting, the vertical incision rate derived from comparison of the elevations and ages of fill terraces is likely to be free of the shorter-term cycles of incision and aggradation, often climatically driven and potentially autogenically biased, and should be the closest reflection of the local tectonic uplift. Sometimes the stratigraphic architecture of terraces is unclear or masked and fill terraces cannot be unambiguously identified. In this case, selecting terraces separated by the period of the relevant higher-frequency forcing (e.g. 21 kyr orbital cycles) skips the fast incision rates driven by them and samples the river at the same relative position in the cycle, presumably at a terrace-carving high stand. That record, spaced by

the period of short-term forcing, is likely to reflect the long-term incision rate of the river (e.g. driven by tectonic uplift).

To assess the history of a field site with complex-response terraces, both the preserved terrace record and the potential for already eroded terraces need to be assessed. And so, while the preserved record is a straightforward observation, the likelihood of missing terraces can be indirectly estimated by establishing how much vertical incision has slowed down and lateral erosion picked up. For example, without stratigraphic context, the terrace record at time t_3 suggests an increase in the incision rate since abandonment of the highest terrace (Figure 3.12 E, solid line). However, consideration of the real incision history (Figure 3.12 E, dashed line) shows that the incision rate is actually decelerating at t_3. If a decelerating incision can be established, the likelihood that a series of younger terraces has been eroded is greater than if fast ongoing incision is documented. In the case of decreasing incision rates, a valley combining perched terraces above a canyon with vertical walls (e.g. Figure 3.3 D and Figure 3.12 at t_3) is less likely to be diagnostic of an external driver forcing the excavation of the canyon after the abandonment of the terraces, but rather of a formerly stepped canyon where the youngest terraces all have been eroded by the increased lateral erosion of a river that almost ceased to incise vertically.

This simple thought experiment with complex-response terraces is reminiscent of the ongoing debate about the timescale dependency of vertical incision rates derived from the record of strath terraces (N. J. Finnegan, Schumer, and S. Finnegan, 2014; Gallen et al., 2015). The potentially opposing interpretations of the two groups of authors is reflected in the evolution of the record of complex-response terraces in Figure 3.12 C, D and E. We see in our work that the preferential destruction of younger terraces may have an important influence on the incision history derived from them. N. J. Finnegan, Schumer, and S. Finnegan (2014) consider the entire terrace record and observe that faster rates are systematically obtained on shorter timescales. A similar trend in the entire record is visible in Figure 3.12, where terraces abandoned in quick succession (fill-cut) capture high-frequency climate forcing and yield higher incision rates than terraces farther apart. Contrary to strath terraces

that are preserved over longer timescales, fill-cut terraces abandoned during the youngest episode of rapid vertical incision will be progressively truncated starting with the youngest terraces when the incision phase reaches its end. When terraces in close temporal succession are clipped off the record by erosion or burial, so are the fastest vertical incision rates. Consequently, with time, the terrace record is systematically altered and information about high-frequency forcing is lost (Figure 3.12 C - E). But the fill terraces, always separated by a full climatic episode, have the best chance of preservation among complex response terraces and record the same instant of the cycle: the onset of incision at the river 'highstand'. Gallen et al. (2015) argue that deriving vertical incision rates from terrace to terrace, excluding the elevation of the stream, removes the bias of the transient faster rates caused by the unsteady river datum. In their model, strath terraces are abandoned at the 'highstand' of the river incision-aggradation cycle and since any other position of the river in the cycle is lower than the 'highstand', the incision rate from the youngest terrace to the river is faster than from terrace to terrace. This is the case here as well: we obtain the long-term incision rate of the river from the fill terraces that record the river 'highstand' position in the climate cycles and by excluding the climate forcing recorded by the successive fill-cut terraces.

Diachronous terraces

In our model, terraces are not explicitly linked from one cross section to the other. In nature however, fill-cut terraces can often be tracked over tens of kilometers without interruption. In the model, the similar geometry of neighboring cross sections (Figure 3.8 A and A') is due to the dependency of incision on the channel slope which is estimated from the thalweg elevation at successive sections. This dependency synchronizes entrenchment from one section to the other. But as cross sections lie relatively far apart, changes in slope are moderate and unlikely to drive abandonment of terraces at the exact same relative elevation in neighboring profiles over a short time. The model is designed to treat every bankfull event as a single erosional time step. It requires a minimum distance between the cross sections set by the potential differential in vertical incision between two successive cross sections at any time step to prevent runaway breaks in slope and warrant numerical stability. In cases of very low erosion capacity, that distance can be reduced significantly, and

terraces can then be traced from one cross section to the other. These more coherent terraces are nevertheless diachronous with an age gradient from old to young moving upstream. Identifying the direction of surface younging of a diachronous terrace could be a telling sign for its autogenic or allogenic nature. For example, in alluvial fans external forcing (tectonics and climate) tends to drive changes from the apex downstream because it is the outlet of the catchment and often the location of an active fault, while autogenic signals appear within the fan and ripple upstream.

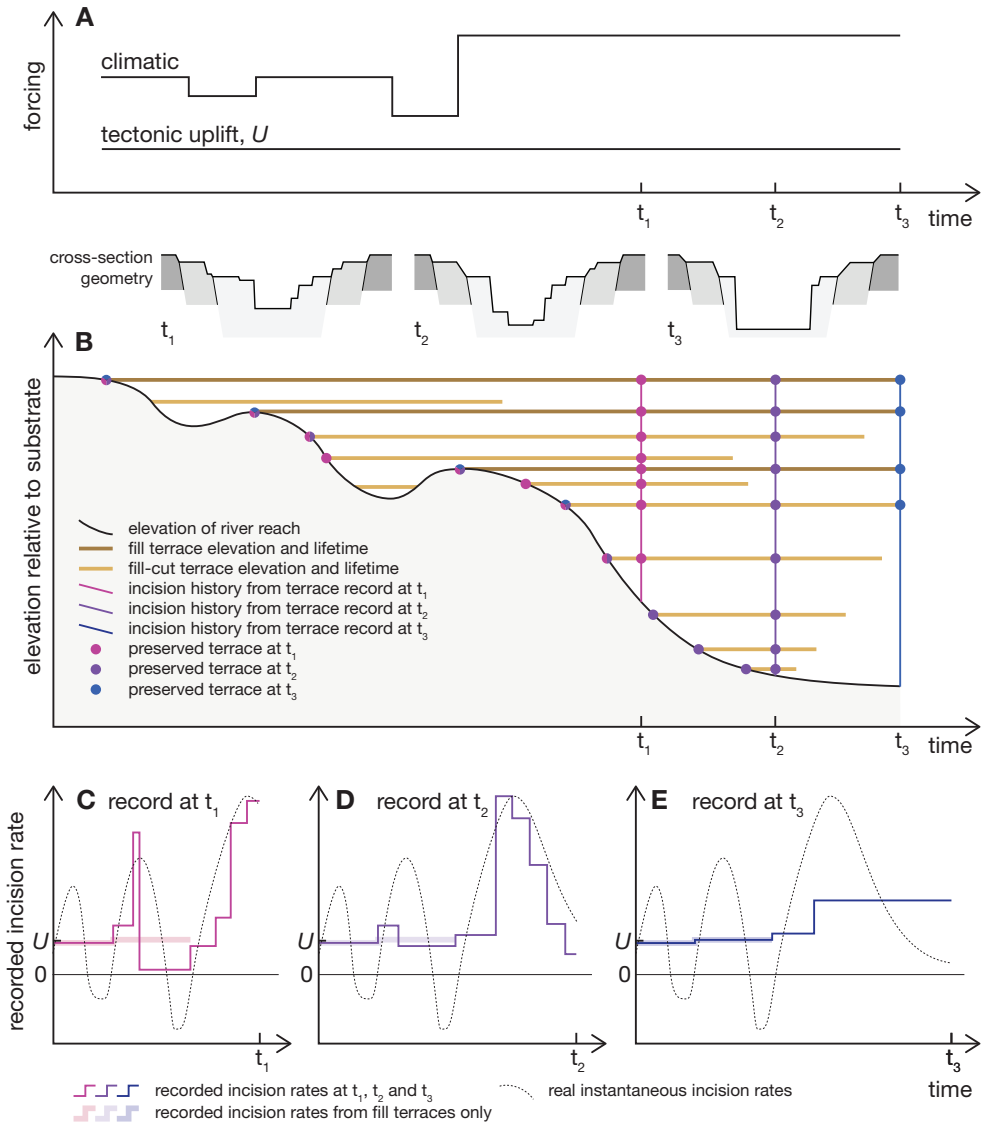

Figure 3.12: Illustration of the model dynamics in a thought experiment of an alluvial river under the cyclic climatic forcing and constant tectonic uplift indicated in panel A. The incision and aggradation of one location along the stream in response to the forcing are shown with a black line in panel B, relative to the elevation of the material in which it incises or aggrades. The cross-sectional geometry of the valley and its stratigraphy at t_1, t_2 and t_3 are sketched above. The occasional complex-response terraces that record incision are shown as horizontal lines in panel B with their elevation on the y-axis, and lifetime on the x-axis. The terrace records at three different times t_1, t_2 and t_3 (panels C, D and E) illustrate how reconstructed incision rates (thin lines) can deviate from the real rate (dashed line) and how fill terraces (thick lines) under a similar climatic forcing can reflect uplift rate. The three time steps broadly mark the evolution of the model in Figure 3.3 B, C and D.

3.6 Conclusion

Vertical incision of a transport-limited stream is prone to interactions between the channel and the valley walls. The volume of sediment collapsing from valley walls scales with their heights. Consequently, as wall heights increase, the collapsed material becomes more likely to overwhelm the local instantaneous transport capacity of the channel and form talus piles that shield banks and walls. These talus piles have the potential to constrain channel width and enhance vertical incision. This internal mechanism has a geometric signature which can be tracked with the entrenchment index i_E that quantifies the cross-sectional shape of an incised valley. We make the point that autogenically-enhanced entrenchment and systematic erosion of younger terraces may be mistaken for an external forcing when interpreting cross-sectional valley geometry. Our model results suggest that this enhanced vertical incision is most pronounced in rivers with low erosivity.

Our numerical simulations also show that after a phase of vertical incision, the terrace record is progressively truncated by lateral erosion of the river starting with the youngest deposits. In a channel reaching the end of an incision phase, youngest terraces have likely been systematically eroded and the truncated record can erroneously indicate an apparent external forcing.

While this work is focused on transport-limited channels and fill-cut terraces, the dynamics resulting from the coupling of vertical and lateral erosion are probably also relevant to strath terraces that formed alongside or underneath their alluvial equivalents and potentially survived them. The interpretation of a fill-cut terrace record in terms of paleo-hydraulic conditions should take into consideration the effect of the valley wall feedback processes explored in this contribution.

Acknowledgments

This manuscript has greatly benefited from the remarkably thorough and precise comments of the editor John Buffington and from insightful and engaging reviews from Frank Pazzaglia and an anonymous reviewer. This study is partly supported by a PRF New Direction grant of the American Chemical

Society (grant number: PRF #53814-ND8), a Doc.Mobility fellowship of the Swiss National Foundation (project number: P1SKP2_158716) for Malatesta, NSF grant EAR-1349115 (to Michael Lamb) for Prancevic, and the donors of the American Chemical Society Petroleum Research Fund (to Michael Lamb). The source code of the model is publicly available on the web platform of the Community Surface Dynamics Modeling System (csdms.colorado.edu).

Table 3.1: List of model parameters and their field equivalents.

Symbol	**Name**	**Natural equivalent or driving process**
k_A	Erosivity coefficient	Magnitude of bankfull event
$x_{ucut,max}$	Maximum undercut forcing cliff collapse	Strength of the bank material
W_i	Initial width of the channel	Width of bankfull channel at incision onset
x_{lat}	Lateral channel migration	Rate of channel migration across floodplain
h_{FP}	Floodplain relief	Height of bankfull stage above thalweg

Table 3.2: List of simulations and parameters. Every parameter set is run 9 times. W_i: initial channel width; x_{lat}: mean and one standard deviation lateral movement as a function of channel width W; k_A: Erosivity parameter; $x_{ucut,max}$: maximum undercut depth necessary for cliff collapse; h_{FP}: floodplain relief. The units of length are arbitrary.

Run	W_i [L]	x_{lat} [L]	k_A [1]	$x_{ucut,max}$ [L]	$h_{FP}[L]$
1	600	4W-3W	0.7	20	2
2	200	4W-3W	0.7	20	2
3	400	4W-3W	0.7	20	2
4	800	4W-3W	0.7	20	2
5	600	0.5W-0.5W	0.7	20	2
6	600	2W-2W	0.7	20	2
7	600	6W-4W	0.7	20	2
8	600	4W-3W	0.1	20	2
9	600	4W-3W	0.4	20	2
10	600	4W-3W	1	20	2
11	600	4W-3W	0.7	5	2
12	600	4W-3W	0.7	10	2
13	600	4W-3W	0.7	30	2
14	600	4W-3W	0.7	20	0.5
15	600	4W-3W	0.7	20	1
16	600	4W-3W	0.7	20	4
17	600	0.5W-0.5W	0.1	20	0.5
18	600	6W-4W	1	20	4
19	600	2W-2W	0.1	20	1
20	600	4W-3W	0.2	20	2
21	600	4W-3W	0.3	20	2
22	600	4W-3W	0.5	20	2
23	600	4W-3W	0.05	20	2
24	600	4W-3W	0.08	20	2
25	600	4W-3W	0.03	20	2
26	600	0.5W-0.5W	0.1	20	2
27	600	2W-2W	0.1	20	2
28	600	6W-4W	0.1	20	2
29	600	4W-3W	0.1	20	2
30	600	4W-3W	0.1	5	2
31	600	4W-3W	0.1	10	2
32	600	4W-3W	0.1	30	2
33	600	4W-3W	0.1	50	2
34	600	4W-3W	0.1	1	2
35	600	4W-3W	0.1	2	2
36	600	4W-3W	0.2	5	2
37	600	4W-3W	0.2	10	2
38	600	4W-3W	0.2	15	2
39	600	4W-3W	0.2	30	2
40	600	4W-3W	0.2	2	2

References

Arbogast, Alan F and William C Johnson (1994). "Climatic Implications of the Late Quaternary Alluvial Record of a Small Drainage Basin in the Central Great Plains". In: *Quaternary Research* 41.3, pp. 298–305.

Avouac, Jean-Philippe et al. (1993). "Active Thrusting and Folding Along the Northern Tien Shan and Late Cenozoic Rotation of the Tarim Relative to Dzungaria and Kazakhstan". In: *Journal Of Geophysical Research* 98.B4, pp. 6755–6804.

Bathurst, J C (1985). "Flow Resistance Estimation in Mountain Rivers". In: *Journal of Hydraulic Engineering* 111.4, pp. 625–643.

Begin, Ze'ev B., David F Meyer, and Stanley Alfred Schumm (1981). "Development of longitudinal profiles of alluvial channels in response to base-level lowering". In: *Earth Surface Processes and Landforms* 6.1, pp. 49–68.

Bekaddour, Toufik et al. (2014). "Paleo erosion rates and climate shifts recorded by Quaternary cut-and-fill sequences in the Pisco valley, central Peru". In: *Earth and Planetary Science Letters* 390.C, pp. 103–115.

Bridgland, D R (2000). "River terrace systems in north-west Europe: an archive of environmental change, uplift and early human occupation". In: *Quaternary Science Reviews* 19.13, pp. 1293–1303.

Brush Jr., Lucien M. and M. Gordon Wolman (1960). "Knickpoint behavior in noncohesive material: a laboratory study". In: *Geological Society of America Bulletin* 71.1, pp. 59–74.

Bucher, W H (1932). ""Strath" as a geomorphic term". In: *Science* 75.1935, pp. 130–131.

Bull, W B (1991). *Geomorphic responses to climatic change*. New York: Oxford University Press.

Bull, William L and Peter L K Knuepfer (1987). "Adjustments by the Charwell River, New Zealand, to uplift and climatic changes". In: *Geomorphology* 1.1, pp. 15–32.

Exner, Felix Maria von (1925). "Über die Wechselwirkung zwischen Wasser und Geschiebe in Flüssen". In: *Sitzungsberichte der Akademie der Wissenschaften in Wien mathematisch-naturwissenschaftlichen Klasse. Abteilung 2a*, pp. 165–203.

Finnegan, Noah J and William E Dietrich (2011). "Episodic bedrock strath terrace formation due to meander migration and cutoff". In: *Geology* 39.2, pp. 143–146.

Finnegan, Noah J, Gerard H Roe, et al. (2005). "Controls on the channel width of rivers: Implications for modeling fluvial incision of bedrock". In: *Geology* 33.3, pp. 229–232.

Finnegan, Noah J, Rina Schumer, and Seth Finnegan (2014). "A signature of transience in bedrock river incision rates over timescales of 10^4--10^7 years". In: *Nature* 505.7483, pp. 391–394.

Gallen, Sean F et al. (2015). "The dynamic reference frame of rivers and apparent transience in incision rates". In: *Geology* 43.7, pp. 623–626.

Gardner, Thomas W (1983). "Experimental study of knickpoint and longitudinal profile evolution in cohesive, homogeneous material". In: *Geological Society of America Bulletin* 94.5, pp. 664–672.

Gong, Zhijun, Sheng-Hua Li, and Bo Li (2014). "The evolution of a terrace sequence along the Manas River in the northern foreland basin of Tian Shan, China, as inferred from optical dating ". In: *Geomorphology* 213.C, pp. 201–212.

Gran, Karen B et al. (2013). "Landscape evolution, valley excavation, and terrace development following abrupt postglacial base-level fall". In: *Geological Society of America Bulletin* 125.11-12, pp. 1851–1864.

Hancock, Gregory R and Robert S Anderson (2002). "Numerical modeling of fluvial strath-terrace formation in response to oscillating climate". In: *Geological Society of America Bulletin* 114.9, pp. 1131–1142.

Howard, Arthur David (1959). "Numerical Systems of Terrace Nomenclature - a Critique". In: *The Journal of Geology* 67.2, pp. 239–243.

Jones, Stuart J, Lynne E Frostick, and Timothy R Astin (1999). "Climatic and tectonic controls on fluvial incision and aggradation in the Spanish Pyrenees". In: *Journal Of The Geological Society* 156.4, pp. 761–769.

Kogure, Tetsuya et al. (2006). "Effect of the development of notches and tension cracks on instability of limestone coastal cliffs in the Ryukyus, Japan". In: *Geomorphology* 80.3-4, pp. 236–244.

Lavé, Jérôme (1997). "Tectonique et érosion: l'apport de la dynamique fluviale à l'étude sismotectonique de l'Himalaya du Népal central ". PhD thesis. University Paris VII.

Lavé, Jérôme and Jean-Philippe Avouac (2000). "Active folding of fluvial terraces across the Siwaliks Hills, Himalayas of central Nepal". In: *Journal Of Geophysical Research* 105.B3, pp. 5735–5770.

Leopold, L B and W B Bull (1979). "Base Level, Aggradation, and Grade". In: *Proceedings of the American Philosophical Society*, pp. 168–202.

Limaye, A and Michael P Lamb (2014). "Numerical simulations of bedrock valley evolution by meandering rivers with variable bank material". In: *Journal of Geophysical Research: Earth Surface* 119.4, pp. 927–950.

Limaye, A and Michael P Lamb (2016). "Numerical model predictions of autogenic fluvial terraces and comparison to climate change expectations". In: *Journal of Geophysical Research: Earth Surface*, –n/a.

Lu, Honghua, Douglas West Burbank, and Youli Li (2010). "Alluvial sequence in the north piedmont of the Chinese Tian Shan over the past 550 kyr and its relationship to climate change". In: *Palaeogeography Palaeoclimatology Palaeoecology* 285.3-4, pp. 343–353.

Maddy, Darrel, David Bridgland, and Rob Westaway (2001). "Uplift-driven valley incision and climate-controlled river terrace development in the Thames Valley, UK". In: *Quaternary International* 79.1, pp. 23–36.

Meyer, Grant A, Stephen G Wells, and A. J. Timothy Jull (1995). "Fire and alluvial chronology in Yellowstone National Park: Climatic and intrinsic controls on Holocene geomorphic processes". In: *Geological Society of America Bulletin* 107.10, pp. 1211–1230.

Meyer-Peter, E and R Müller (1948). "*Formulas for bed-load transport*". In: *2nd Meeting of the International Association for Hydraulic Structures Research*. Stockholm: 2nd Meeting of the International Association for Hydraulic Structures Research, pp. 39–64.

Molnar, Peter et al. (1994). "Quaternary climate-change and the formation of river terraces across growing anticlines on the north flank of the Tien-Shan, China". In: *Journal of Geology* 102.5, pp. 583–602.

Nicholas, Andrew P. and T A Quine (2007). "Modeling alluvial landform change in the absence of external environmental forcing". In: *Geology* 35.6, pp. 527–530.

Paola, Chris and V R Voller (2005). "A generalized Exner equation for sediment mass balance". In: *Journal Of Geophysical Research* 110, pp. 1–8.

Parker, Gary (2015). *1D Sediment Transport Morphodynamics With Applications to Rivers and Turbidity Currents*. University of Illinois: http://hydrolab.illinois.edu/people/parkerg.

Patton, Peter C and Stanley Alfred Schumm (1975). "Gully Erosion, Northwestern Colorado: A Threshold Phenomenon". In: *Geology* 3.2, pp. 88–90.

Pazzaglia, Frank J (2013). "9.23 Fluvial Terraces". In: *Treatise of Geomorphology*. Ed. by E Wohl. Elsevier, pp. 379–412.

Pazzaglia, Frank J and Mark T Brandon (2001). "A fluvial record of long-term steady-state uplift and erosion across the Cascadia forearc high, western Washington State". In: *American Journal Of Science* 301.4-5, pp. 385–431.

Picotti, Vincenzo and Frank J Pazzaglia (2008). "A new active tectonic model for the construction of the Northern Apennines mountain front near Bologna (Italy)". In: *Journal Of Geophysical Research* 113, pp. 1–24.

Poisson, Blanche and Jean-Philippe Avouac (2004). "Holocene hydrological changes inferred from alluvial stream entrenchment in North Tian Shan (Northwestern China)". In: *Journal of Geology* 112.2, pp. 231–249.

Porter, SC and A Zhisheng (1992). "Cyclic Quaternary alluviation and terracing in a nonglaciated drainage basin on the north flank of the Qinling Shan, central China". In: *Quaternary Research* 38, pp. 157–169.

Reneau, S L (2000). "Stream incision and terrace development in Frijoles Canyon, Bandelier National Monument, New Mexico, and the influence of lithology and climate". In: *Geomorphology* 32.1-2, pp. 171–193.

Rickenmann, D (2001). "Comparison of bed load transport in torrents and gravel bed streams". In: *Water Resources Research* 37.12, pp. 3295–3305.

Romans, B W et al. (2015). "Environmental signal propagation in sedimentary systems across timescales". In: *Earth-Science Reviews* 153, pp. 7–29.

Schildgen, T F et al. (2011). "Multi-phased uplift of the southern margin of the Central Anatolian plateau, Turkey: A record of tectonic and upper mantle processes". In: *Earth and Planetary Science Letters* 317-318.C, pp. 85–95.

Schumm, Stanley Alfred (1973). "Geomorphic thresholds and complex response of drainage systems". In: *Fluvial Geomorphology*. Ed. by M Morisawa. Fluvial geomorphology, pp. 299–310.

Schumm, Stanley Alfred and Richard Frederick Hadley (1957). "Arroyos and the semiarid cycle of erosion [Wyoming and New Mexico]". In: *American Journal Of Science* 255.3, pp. 161–174.

Schumm, Stanley Alfred, Michael D Harvey, and Chester C Watson (1984). *Incised channels: morphology, dynamics, and control*. Littleton, Colorado: Water Resources Publications.

Schumm, Stanley Alfred, M P Mosley, and W Weaver (1987). *Experimental fluvial geomorphology*. New York, NY: John Wiley and Sons Inc.

Schumm, Stanley Alfred and David K Rea (1995). "Sediment Yield From Disturbed Earth Systems". In: *Geology* 23.5, pp. 391–394.

Shields, Albert (1936). "Anwendung der Ähnlichkeitsmechanik und der Turbulenzforschung auf die Geschiebebewegung ". PhD thesis. Berlin: Preussische Versuchsanstalt für Wasserbau und Schiffbau.

Steffen, Damian, Fritz Schlunegger, and Frank Preusser (2010). "Late Pleistocene fans and terraces in the Majes valley, southern Peru, and their relation to climatic variations". In: *International Journal Of Earth Sciences* 99.8, pp. 1975–1989.

Wegmann, Karl W and F J Pazzaglia (2002). "Holocene strath terraces, climate change, and active tectonics: The Clearwater River basin, Olympic Peninsula, Washington State". In: *Geological Society of America Bulletin* 114.6, pp. 731–744.

Wei, Zhanyu, J Ramon Arrowsmith, and Honglin He (2015). "Evaluating fluvial terrace riser degradation using LiDAR-derived topography: An example from the northern Tian Shan, China". In: *Journal of Asian Earth Sciences* 105.C, pp. 430–442.

Wolman, M G and J P Miller (1960). "Magnitude and Frequency of Forces in Geomorphic Processes". In: *The Journal of Geology* 68.1, pp. 54–74.

Womack, W R and Stanley Alfred Schumm (1977). "Terraces of Douglas Creek, northwestern Colorado: An example of episodic erosion". In: *Geology* 5.2, pp. 72–76.

Wong, Miguel and Gary Parker (2006). "Reanalysis and correction of bed-load relation of Meyer-Peter and Muller using their own database". In: *Journal of Hydraulic Engineering* 132.11, pp. 1159–1168.

Chapter 4

REPEATED CYCLES OF PIEDMONT AGGRADATION AND INCISION DRIVEN BY CLIMATE VARIABILITY DURING GLACIAL PERIODS IN THE TIAN SHAN

with Jean-Philippe Avouac[1], Nathan Brown[2], Sebastian Breitenbach[3], Jiawei Pan[4], Marie-Luce Chevalier[4], Edward Rhodes[5][2], Dimitri Saint-Carlier[6], Wenjing Zhang [4], Julien Charreau[6], Jérôme Lavé[6], Pierre-Henri Blard[6]

In review at Basin Research

4.1 Abstract

Accurate interpretation of clastic sedimentary records hinges on a detailed understanding of the timescale and mode of sediment transport from source to sink. A forcing signal, whether of tectonic or climatic origin, can be accurately recorded in the stratigraphy if it is transported quickly without being mixed with older sediments, or it can be entirely shredded by slow transport and mixing. Both can happen in alluvial piedmonts, which are critical components of the sediment-routing system. To quantify their effects, we study alluvial aggradation and reincision in the north piedmont of the Eastern Tian Shan. We compiled chronologic data from the literature and complemented them with 20 new luminescence ages and one cosmogenic age of terrace abandonment and alluvial aggradation. The piedmont deeply incised and aggraded many times per 100 kyr over the last 0.5 Myrs. Aggradation is driven by an increased sediment flux at the warmer and wetter deglaciation that flushes

[1]Division of Geological and Planetary Sciences, California Institute of Technology, Pasadena, CA 91125, USA

[2]Department of Earth, Planetary, and Space Sciences, University of California Los Angeles, CA 90095, CA

[3]Institute of Geology, Mineralogy & Geophysics, Ruhr-Universität Bochum, 44780 Bochum, Germany

[4]Institute of Geology, Chinese Academy of Geological Sciences, Beijing 100037, China

[5]Department of Geography, The University of Sheffield, S10 2TN Sheffield, UK

[6]Centre de Recherches Pétrographiques et Géochimiques, Vandoeuvre-lès-Nancy, 54500 France

glacial sediment accumulated in the high range onto the piedmont. Fluvial incision starts when sediment flux from the high range drops after bulk evacuation is completed resulting in incision rates as fast as 9 cm/yr in canyons as deep as 330 m. The precise timing of incision does not reflect climate forcing but the time it takes to evacuate sediments flushed out during deglaciation. A significant fraction of sediments evacuated from the high range is temporarily deposited on the piedmont before a later incision phase can deliver it to the basin. We quantitatively constrain the effect of the alluvial piedmont on the sediment flux: 1) the delivery of coarse sediments to the basin is delayed by at least 7 to 14 kyrs between the first evacuation from the mountain and later re-erosion and basinward transport; 2) the output flux of coarse sediments from the piedmont contains a significant amount of recycled material that was deposited on the piedmont as early as the Middle Pleistocene. The arrival of the gravel front into the proximal basin is delayed relative to the fine-grained load and both are separated by a hiatus. Variations in temperature and moisture delivered by the Westerlies are the likely cause of repeated aggradation and incision of the north piedmont.

4.2 Introduction

Most mountain ranges on Earth are bounded by alluvial piedmonts. The piedmonts are the first long term accommodation zones for the sediments leaving the mountains. They also temporarily trap part of the sediment flux through episodes of aggradation and subsequent incision, controlling the spatial and temporal delivery of sediments from the bedrock source to the foreland basin sink (e.g. Paola, Heller, and Angevine, 1992; Métivier, 2002; Allen, 2008; Allen, Armitage, et al., 2013). Alluvial piedmonts can take a wide range of geometries depending on the tectonic setting. The simplest configuration is that of isolated alluvial fans separating hanging- and footwall across a normal fault like in Death Valley, California (Allen and Densmore, 2000). Convergent tectonics results in more complicated structures where thrusts and folds capture sediments in piggyback basins and older deposits are thrusted at the surface to be eroded and remobilised (e.g. Puigdefàbregas and Souquet, 1986). The sedimentary outflux from a piedmont to the basin is a mixture of fresh input from the mountain and of recycled older piedmont deposits that depends on the pattern and timing of alluvial aggradation and incision.

Alluvial piedmonts are built by transport-limited rivers — from wide sheet flow to narrow entrenched channels (Bull, 1977; Parker, Paola, Whipple, and Mohrig, 1998; Parker, Paola, Whipple, Mohrig, et al., 1998; Nicholas and Quine, 2007; Pepin, Carretier, and Herail, 2010) — that distribute the coarse sediment load on alluvial fans and primarily react to changes in the fluxes of water and sediment. Alluvial piedmonts are relatively steep and the rivers crossing them deliver their suspended and dissolved load directly to the basin, while the bedload of the piedmont rivers, coarse sand to cobbles, build the bulk of the fan morphology (Paola, Heller, and Angevine, 1992; Smith and Ferguson, 1996; Allen, Armitage, et al., 2013). However, the bedload is only a fraction of the total (solid and dissolved) sediment flux of a river. The bedload fraction tends to decrease down river and amounts to 30-50% of the solid load in sand bedded streams (Turowski, Rickenmann, and Dadson, 2010). Along the Eastern Tian Shan river Urumqi, more than 80% of the total load is transported dissolved or in suspension in the high range(Liu et al., 2011). Alluvial slopes scale inversely with water discharge (Gilbert and Murphy, 1914; Mackin, 1948; Hooke, 1968), and positively with the ratio of sediment flux over water discharge Q_s/Q_w (Schumm, 1973; Leopold and Bull, 1979). This makes alluvial fans particularly sensitive to climatic forcing (Bull, 1991; Molnar, E. T. Brown, et al., 1994; Tucker and Slingerland, 1997; Rohais, Bonnet, and Eschard, 2012; D'Arcy and Whittaker, 2014).

Both tectonics and climate affect the Earth surface, and the environmental signals they cause are transferred along the sediment-routing system. Mixing or buffering along the way can affect signal preservation (Allen, 1997; Romans et al., 2015). Models suggest that, despite buffering along the way, high-frequency signals can be preserved in the sedimentary record (Simpson and Castelltort, 2012), or be entirely shredded by sediment transport processes (Jerolmack and Paola, 2010). There is however a lack of field studies that quantitatively constrain these effects at timescales of 10's to 100's kyrs. A first step in this direction is to characterise the aggradation and incision cycles that modify environmental signals across piedmonts at a particular field location. How rapid and how large are these cycles? And how do they relate to climate and tectonic forcing?

To address questions related to the intricate links between tectonics, climate, hydrology, and geomorphology, we investigate the northern piedmont of the Eastern Tian Shan. The piedmont is formed by alluvial fans coalesced in bajadas and deformed in a fold-and-thrust belt (Avouac, Tapponnier, et al., 1993). The coalesced Late Pleistocene fans of the north piedmont have been deeply incised after the last deglaciation and provide an excellent opportunity to study a reasonably simple system that evolved in the Late Quaternary. First, we present the geological setting of the Eastern Tian Shan in Section 4.3 and describe the study sites in Section 4.4. We then discuss new luminescence ages that constrain the chronology of terrace abandonment and stratigraphic accumulation in Section 4.5. This new dataset is combined with previously published age constraints to describe the morphological evolution of the piedmont in Section 4.6. In Section 4.7, we compare our observations to theoretical considerations, extend the morpho-sedimentary history of the north piedmont to the Middle Pleistocene and discuss implications regarding the stratigraphic record.

4.3 Geological setting of the north piedmont of the Eastern Tian Shan

The Tian Shan range initially formed around two late Paleozoic sutures (Windley et al., 1990). Throughout the Mesozoic and early Cenozoic, a reduction in the persistent mountain relief and occasional reactivations of the range is documented by thermochronology and decreasing sediment fluxes into the adjacent basins: the Tarim to the south and the Junggar to the north (Windley et al., 1990; Hendrix, Graham, et al., 1992; T A Dumitru et al., 2001; Jolivet, Heilbronn, et al., 2013). At ca. 24 Ma, the India-Eurasia collision reactivated Central Asian tectonics and mountain building along the Tian Shan Paleozoic suture by rigid block rotation north of the Himalayas (Avouac and Tapponnier, 1993; Sobel and T A Dumitru, 1997). In the Oligocene, large volumes of coarse clastic deposits atop an unconformity in the Tarim and Junggar basins document the renewed mountain building that ensued (Windley et al., 1990; Métivier and Gaudemer, 1997). North-south compression resulted in the development of dominant east striking reverse faults and large southeast striking right-lateral strike-slip faults (Tapponnier and Molnar, 1979). Shortening is distributed across the southern and northern fold-and-thrust belts

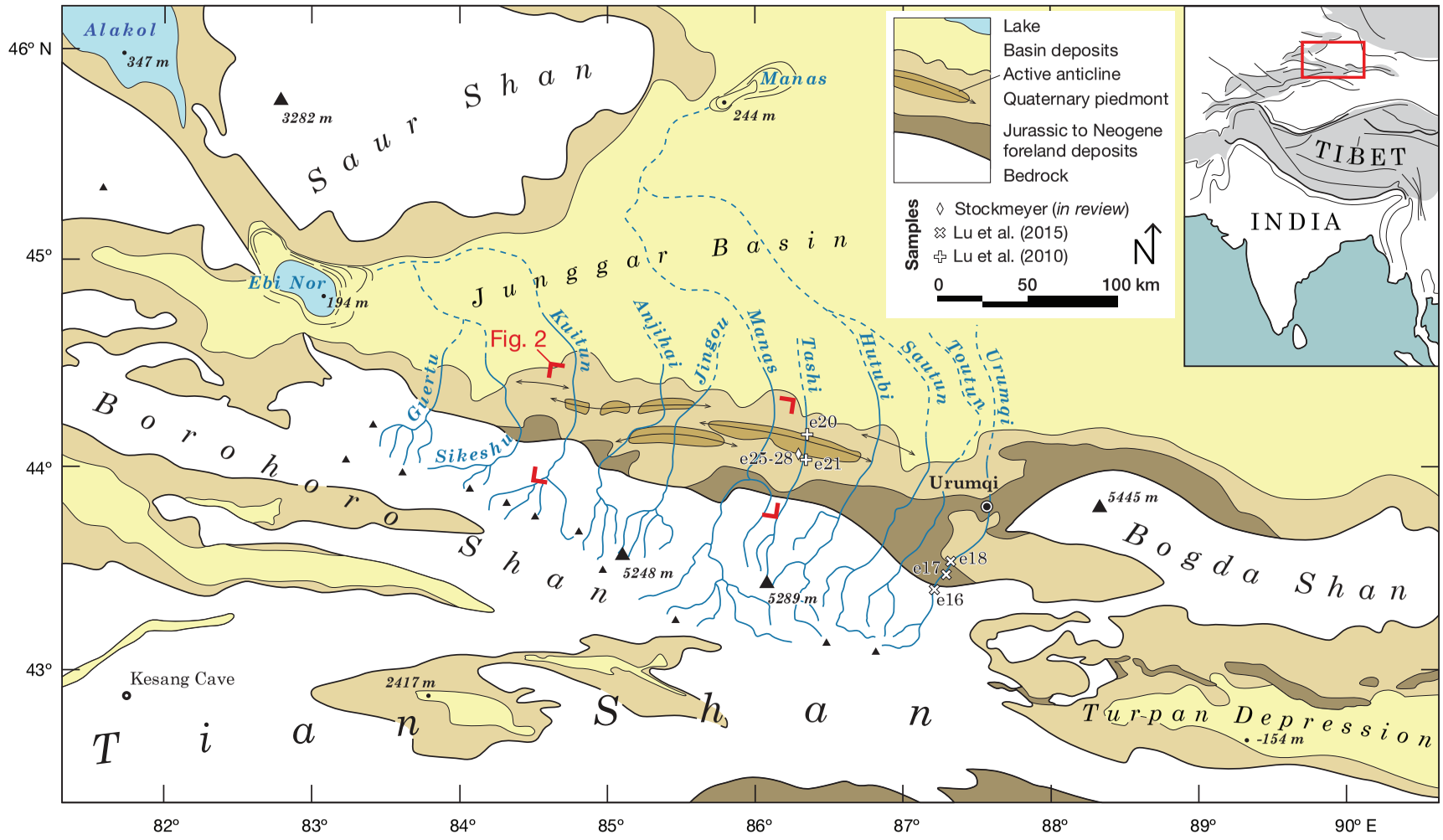

Figure 4.1: Location map of the foreland and basin deposits and main rivers on the north side of the Eastern Tian Shan. The lakes Ebi Nor and Manas (dry) are the low points of the endorheic Junggar Basin. The sample labels (e#) refer to the compilation list of Supplementary Table 3.

that were activated at ca. 24 Ma (Hendrix, T. Dumitru, and Graham, 1994; T A Dumitru et al., 2001) and within the deforming inner mountain basins (Thompson et al., 2002; B. H. Fu et al., 2003; Jolivet, Dominguez, et al., 2010; Saint-Carlier et al., 2016). Along the northern piedmont (Figure 4.1), several parallel rows of east-southeast striking anticlines deform foreland sediments deposited since the Jurassic and absorb about 3 mm/yr of shortening (Avouac, Tapponnier, et al., 1993; Molnar, E. T. Brown, et al., 1994; Burchfiel et al., 1999, Stockmeyer et al., *in review*). Structural sections and seismic profiles suggest that the thrust faults in the piedmont splay from a single detachment, characterised by ramps and flats, which roots southwards beneath the high range (Avouac, Tapponnier, et al., 1993; Burchfiel et al., 1999; C.-Y. Wang et al., 2004; Dengfa et al., 2005; Stockmeyer, Shaw, and Guan, 2014; Shuwei Guan et al., 2016).

The piedmont deposits consist of Mesozoic and Cenozoic clastic sedimentary layers, and form a ca. 50 km wide thrust belt drowned in Quaternary alluvium, which separates the basin from the high range (Avouac, Tapponnier, et al., 1993; Honghua Lu, Burbank, Y. Li, and Yunming Liu, 2010). The total relief of the piedmont is on the order of 800 to 1000 m over a distance of 25 to 45 km. Magnetostratigraphic studies show that local rates of sediment accumulation have been relatively steady at about 0.2 mm/yr over the last 10 Myr (Charreau, Y. Chen, Gilder, Dominguez, et al., 2005; Charreau, Y. Chen, Gilder, Barrier, et al., 2009; Honghua Lu, Burbank, Y. Li, and Yunming Liu, 2010; Honghua Lu, W. Zhang, et al., 2013). Erosion rate in the high range has been estimated between 0.1 and 1 mm/yr in the last 9 Myr with an excursion to 2-2.5 mm/yr at the onset of Quaternary glaciations according to cosmogenic isotope measurements in exposed piedmont deposits (Charreau, Blard, et al., 2011; Puchol et al., 2016). Guerit et al. (2016) estimated erosion rates at 0.135 mm/yr for the last 300 kyrs from the mass balance of 10 alluvial fans in the northern piedmont of the Eastern Tian Shan. These authors also suggest that the dry Central Asian climate is responsible for the imbalance between the very low erosion rates and the important uplift rate in a mountain range accommodating nearly half of the India-Eurasia convergence.

The north piedmont is largely drowned under a bajada of Pleistocene alluvial

fans (Avouac, Tapponnier, et al., 1993). The main rivers flowing northwards out of the range have deeply incised the piedmont since the last deglaciation ($\sim$ 20-15 ka) and older prominent terraces, uplifted by the anticlines, suggest that episodes of aggradation and incision occurred repeatedly (Molnar, E. T. Brown, et al., 1994). The evolution of the piedmont is driven by the punctual evacuation of large volumes of glacial sediment from the upper half of the catchments: first, the alluvial fans aggrade and steepen under the increased sediment flux; then they become dramatically incised when the upstream reservoir is depleted and sediment-starved water flows on the oversteepened piedmont (Poisson and Avouac, 2004). The Holocene incision rates of 10 to 30 mm/yr are one order of magnitude faster than the uplift of anticlines in the fold-and-thrust-belt (Molnar, E. T. Brown, et al., 1994; Poisson and Avouac, 2004; Honghua Lu, Burbank, and Y. Li, 2010; Gong, S.-H. Li, and B. Li, 2014). More than 200 m of Holocene incision and important narrowing of the active floodplain carved several Holocene terraces that provide a detailed entrenchment history (e.g. 10 along the Kuitun River, 18 along the neighboring Anjihai River, Figure 4.2). The gravel previously deposited at the range front is now remobilised by incision and transported farther downstream, feeding the lower fans, located ca. 30 km downstream from the range front (Figure 4.3, see also Jolivet, Barrier, et al., 2014; Guerit et al., 2016). East of the Kuitun River, most of the rivers first cross folded and thrusted Jurassic to Neogene foreland deposits before reaching the Pleistocene series. The deformation front defined by the Dushanzi, Huergosi, Manas and Tugulu anticlines exposes Paleogene to Pleistocene foreland deposits that are actively eroded (Figure 4.3). After leaving the mountain and before entering the alluvial piedmont, the rivers east of the Anjihai cross a wider swath of deformed and largely bevelled Jurassic to Neogene foreland deposits (Avouac, Tapponnier, et al., 1993; C. Li, Guo, and Dupont-Nivet, 2010).

4.4 Geometry of alluvial terraces and sediment characteristics

Our study focuses on the neighbouring rivers Kuitun, Anjihai, Jingou, and Manas (Figure 4.3). Like all rivers of the north piedmont, they are characterised by very wide fill terraces (2-3 km) incised by deep canyons at the bottom of which a braided river flows in a narrower, 100's m wide floodplain. The fill-cut terraces of the alluvial fill become strath terraces as they cross anticlines

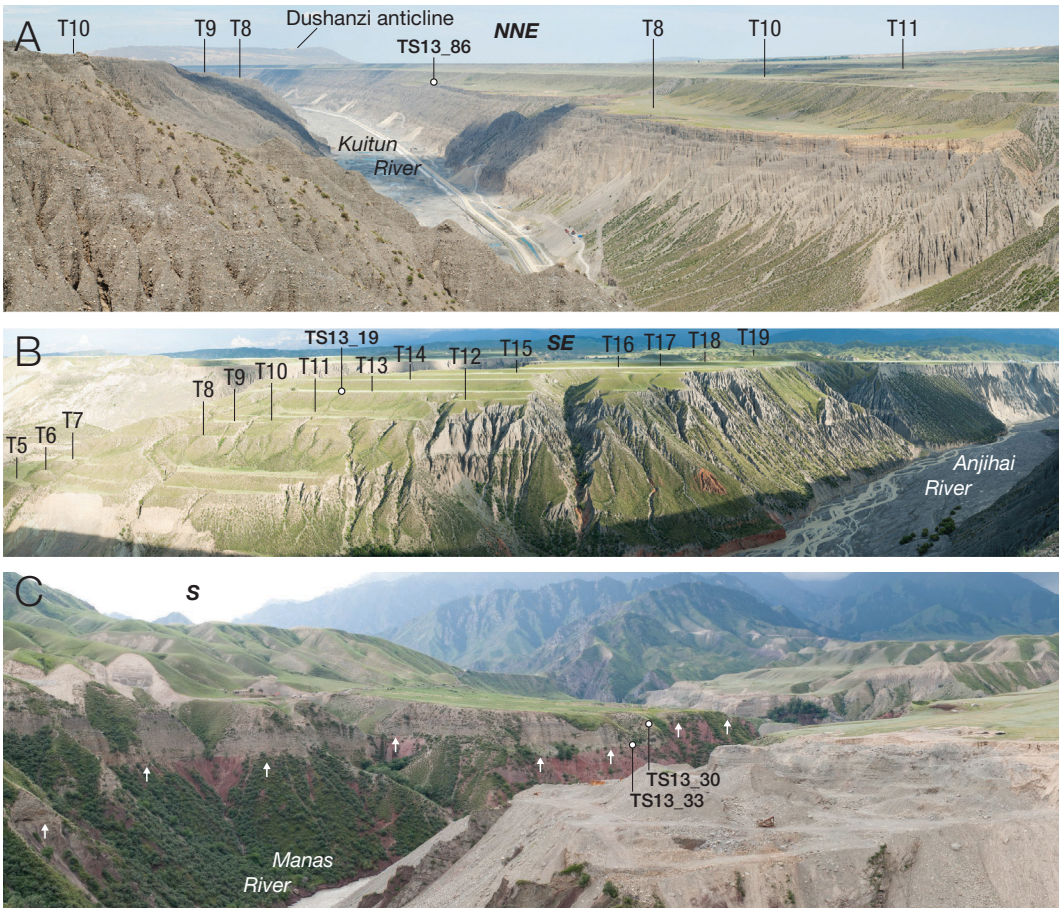

Figure 4.2: Field pictures of the piedmont rivers, see Figure 4.3 for location of the point of view. A: Kuitun River, picture from the left wall at the apex looking north, where local incision is 330 m. The Dushanzi anticline is visible in the background. B: Terrace flight along the Anjihai, looking to the southeast with the high range visible on the right. The river flows from right to left and is incised 240 m in Pleistocene conglomerate (grey and beige) and in tilted Neogene clastic series (red and rust). C: Strath terraces of the upper Manas River looking south, the tilted Jurassic series is red. In the foreground, a gravel pit illustrates the thickness of the alluvial fill above the strath. The different levels of the strath are visible along the cliff (white arrows).

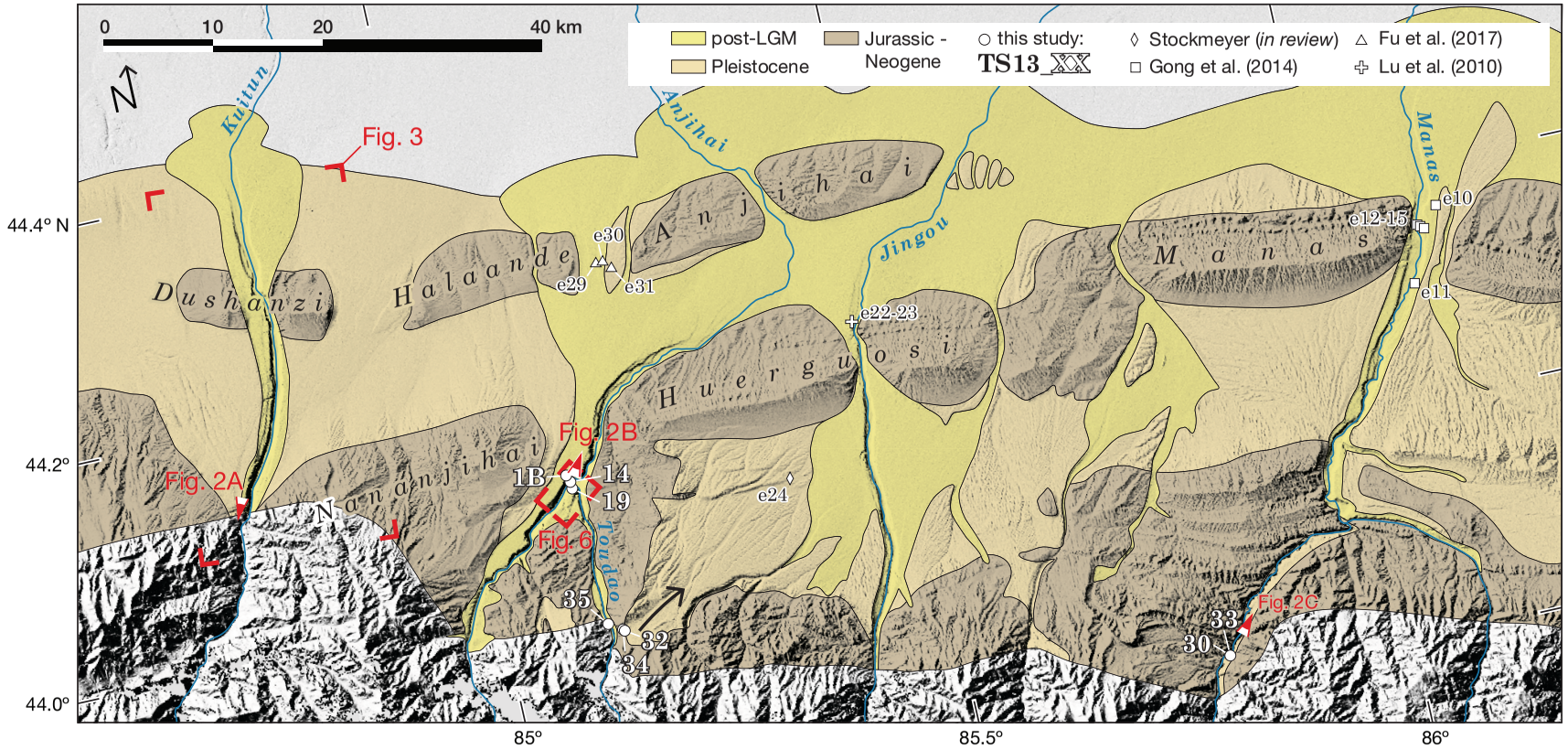

Figure 4.3: Map of the north piedmont of the Eastern Tian Shan from the Kuitun to the Manas Rivers. Hillshade and elevation from ASTER GDEM v2 (a product of NASA and METI). Samples from this study are marked by two characters in white (last two characters from their field codes, see Table 4.1). The black sample labels starting with 'e' are from third party authors (Supplementary Table 3). Samples for the Kuitun River are shown in Figures 4.4 and 4.7.

and bedrock benches. Both types record the same incisional event and the discrimination between them is considered irrelevant here. The morphological similarities point to a synchronised evolution of all the rivers. The Kuitun River presents a simple geometry where the apex of the fan lies at the front of the range and the channel flows straight northwards into the Junggar basin, crossing the active Dushanzi anticline on the way. Across the anticline, a migrating bend of the locally narrowed channel left a series of 9 Holocene terraces (Figures 4.4 and 4.5). The Kuitun is entrenched 330 m at the apex (Figure 4.2 A). The Anjihai River flows out of the mountain range to the northeast and crosses the Huerguosi and the Anjihai anticlines (Figure 4.3). Upstream of the Huergosi anticline, the river is entrenched in Pleistocene deposits that fill paleo-valleys separated by epigenic canyons cut in steeply dipping Jurassic and Cretaceous foreland deposits (Guerit et al., 2016). A flight of 19 terraces is preserved where the Toudao River flows into the Anjihai River immediately upstream of the Huerguosi anticline (Figures 4.2, 4.3, 4.6). Downstream from the Huerguosi anticline, the Anjihai River flows eastwards to cross the Anjihai anticline near the Jingou River instead of following a more direct northern course through a windgap. The Jingou River crosses the same two anticlines as the Anjihai River, but is not incised in Mesozoic sediments and instead flows directly on Pleistocene deposits like the Kuitun River. As it exits the high range, the Jingou River is incised 185 m in a wide alluvial surface converging towards it. The western edge of that surface marks a sharp transition to the Toudao catchment (Figure 4.3). The Jingou River outlet lies 400 m lower relative to the Anjihai River, and needs only 850 m instead of 1250 m of elevation drop to reach the basin. The Manas River leaves the high range to traverse steeply dipping Jurassic and Cretaceous foreland deposits (Figures 4.2 and 4.3). It then flows over Pleistocene deposits and crosses the Manas and Tugulu anticlines at their junction. These anticlines are the structural prolongation of the Huerguosi anticline but they are the frontal structure at the level of the Manas River.

We used remote sensing data and our field observations to map the various terraces in the study area. We used high-resolution satellite imagery from Landsat, Digital Globe, and Spot freely available on Google Earth and Bing Maps. The topographic data from ASTER GDEM2 (NASA and METI) and SRTM 1 arc second (NASA, USGS, DLR, ASI, NGIA) provides a good regional

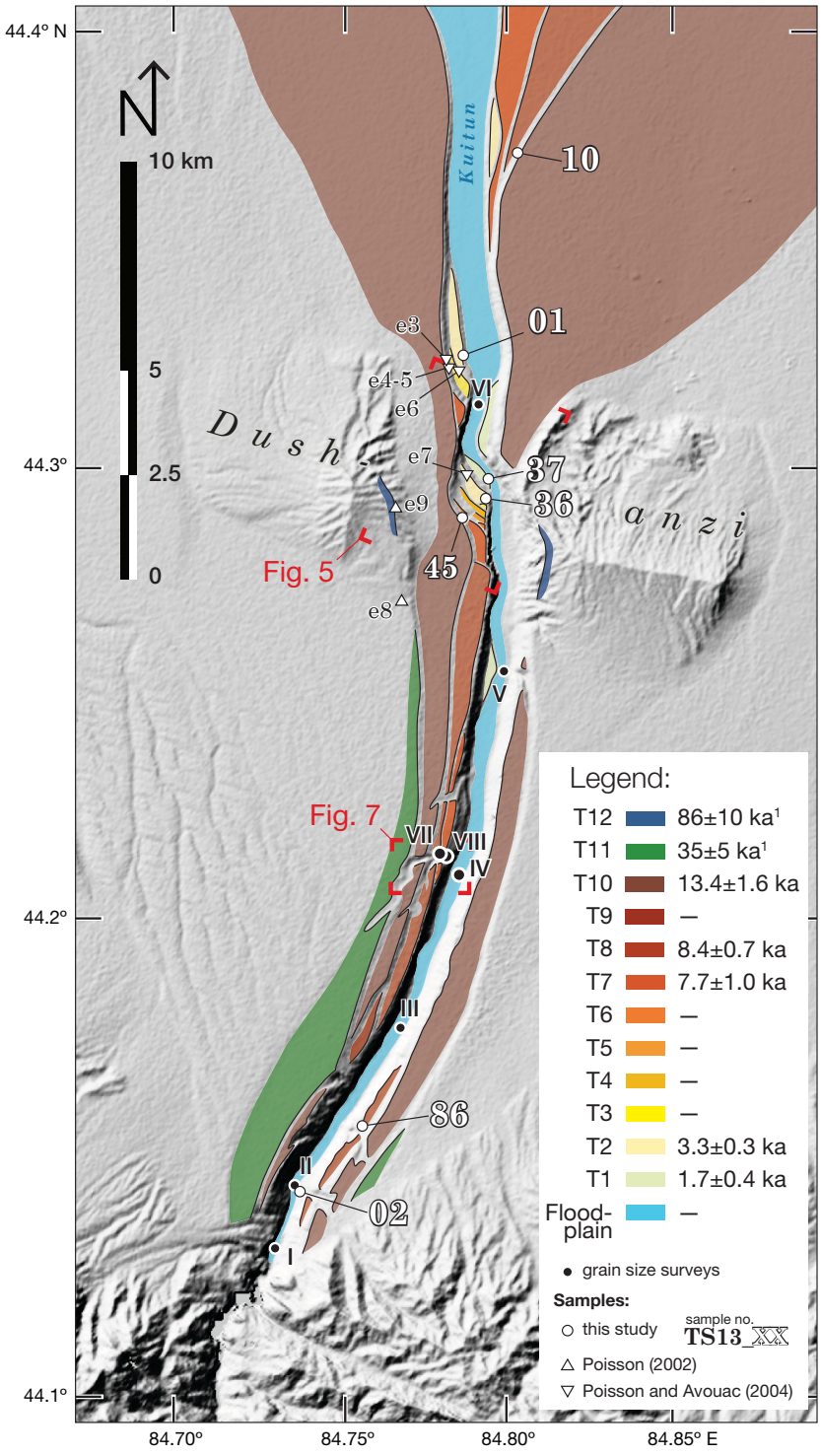

Figure 4.4: Map of the Kuitun River flowing across its alluvial fan and location of samples (XX and e#) and grain size surveys (I to VI). Hillshade from SRTM v2 data. Third party samples: 1) Poisson and Avouac (2004); 2) Poisson (2002).

dataset for the north piedmont of the Chinese Tian Shan. To compensate for their insufficient resolution at the scale of individual terraces, we surveyed two terrace flights along the Kuitun and the Anjihai Rivers at very high resolution with a terrestrial LiDAR scanner (RIEGL Laser Measurement Systems, Austria) during the 2013 field expedition. The LiDAR instrument is managed by the Key Laboratory of Continental Tectonics and Dynamics, Institute of Geology of the Chinese Academy of Geological Sciences in Beijing. The terrestrial LiDAR dataset provides a very high quality documentation of the geometry of the terraces and entrenchment of the modern rivers. Two areas were surveyed: seven point clouds cover the Kuitun River terrace series in the heart of the anticline and resolve 9 Holocene terraces (Figure 4.5); five point clouds cover a terrace series along the Anjihai River where 19 terraces document river incision (18 are captured by the LiDAR, Figure 4.6). The point clouds cover a radius of 1.2 km each and are subsampled at 0.5 m for entire scenes and 0.1 m for zones of interest such as floodplain roughness. We assembled them in one single dataset for each location using the open source software *Cloud Compare* (version 2.7, GPL software, 2016, retrieved from http://www.cloudcompare.org) and analyze them with the software *Quick Terrain Modeler* from *Applied Imagery.*

Along the Kuitun River, we surveyed the distribution of grain sizes in the river bed (6 sites, Figure 4.4 and 4.7) as well as in a steep and short tributary canyon (Swallows' Canyon) of the Kuitun River representing the valley walls (2 sites, Figure 4.7). Swallows' Canyon offer exposures normal to the stream direction but without reliably identifiable cross-cutting relationships in the stratigraphy, because the boundaries between conglomeratic packages can not be traced for more than tens of meters. Grain sizes were surveyed on the surface of alluvial bars next to the active river channel. Sampling was performed by defining an area of roughly 20 by 20 meters in which the surveyors would walk at random and, at each step, pick and measure the second axes of at least 100 sediment grains that their finger would first hit when reaching for the ground without looking. The eight surveys along the Kuitun River reveal a quick decrease in the 84^{th} percentile fraction (D_{84}) past the apex of the fan from 87 and 119 mm to ca. 50 mm (Supplementary Figure 2). Meanwhile the median grain size D_{50} remains constant along 30 km of the river with a mean value of 30.5 mm. The two samples in the tributary Swallows' Canyon have a D_{50} of 38 and 39

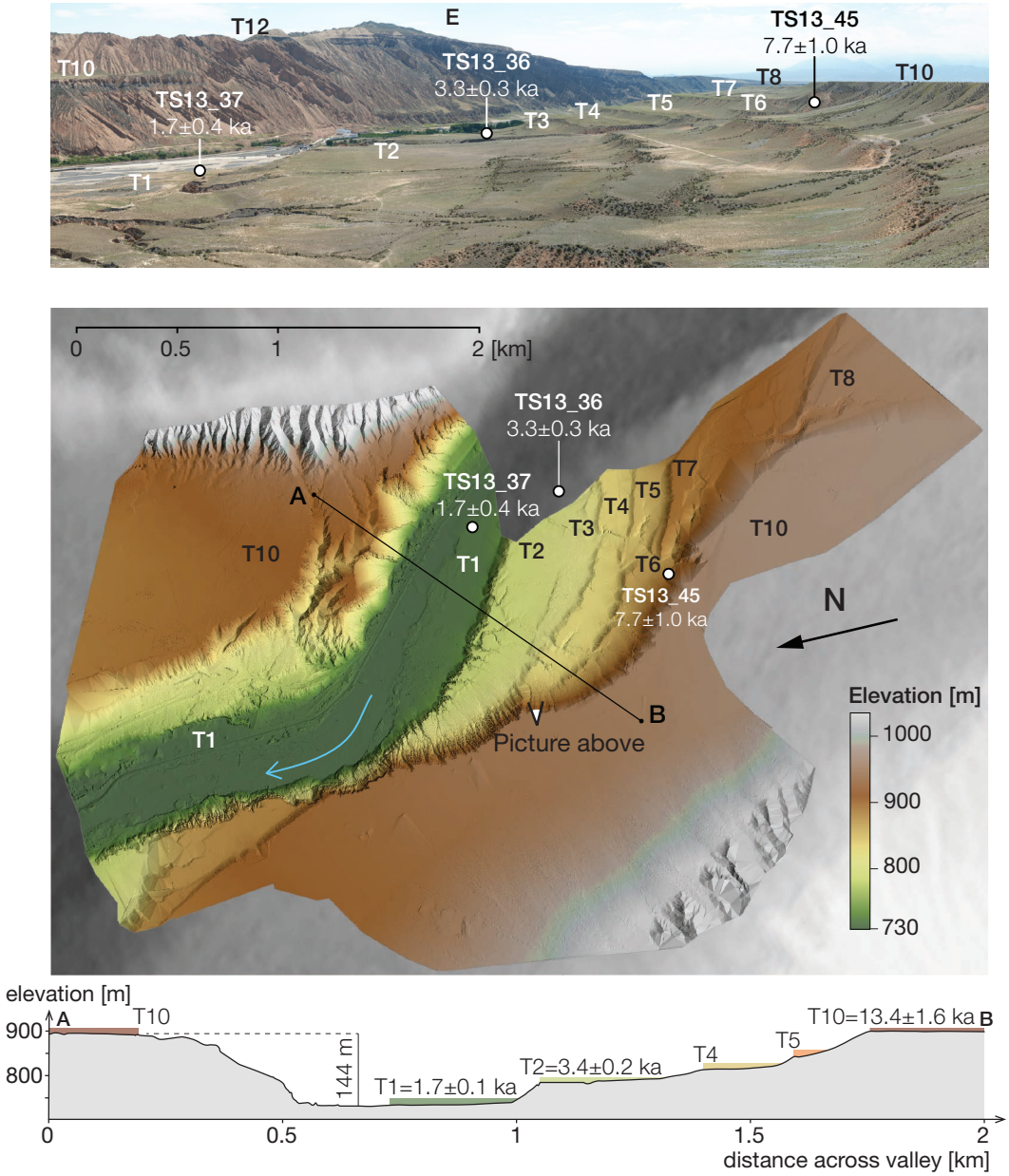

Figure 4.5: Terrace flight of the Kuitun River in the Dushanzi anticline. Top: photo taken looking south south-east, with the Kuitun River flowing from right to left, the oldest dated terrace uplifted by the anticline is visible in the background. The high range lies to the right. Center: terrestrial LiDAR map of the terrace flight. Bottom: profile across the valley from the LiDAR data.

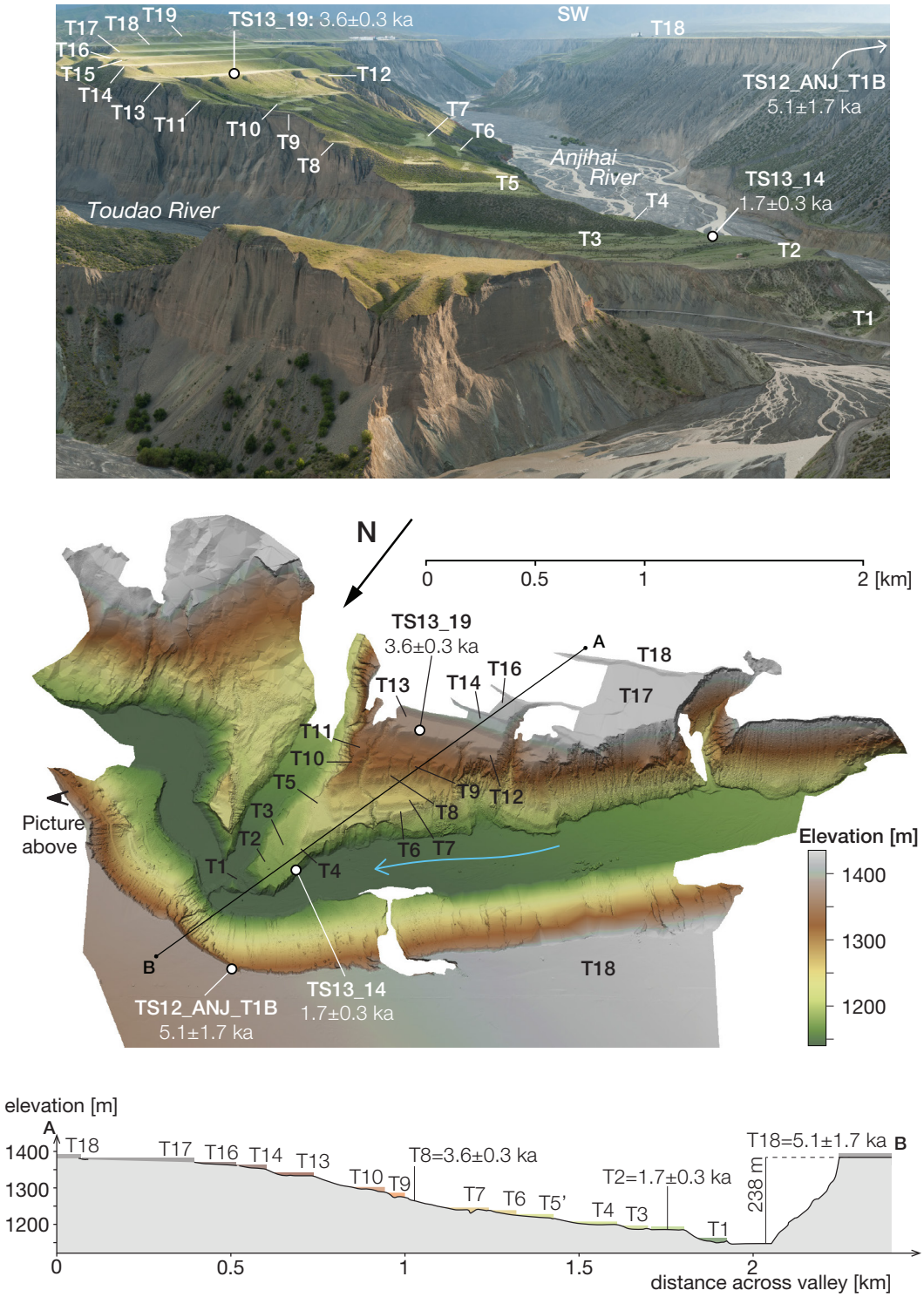

Figure 4.6: Terrace flight of the Anjihai River at the junction with its tributary the Toudao River. Top: photo taken looking southwest, the Anjihai River is on the right and flows toward the camera, the Toudao River flows from the left. Tilted Neogene series (grey) outcrop at the base of the conglomerate cliff (brown). Center: terrestrial LiDAR map of the terrace flight. Bottom: profile across the valley from the LiDAR data.

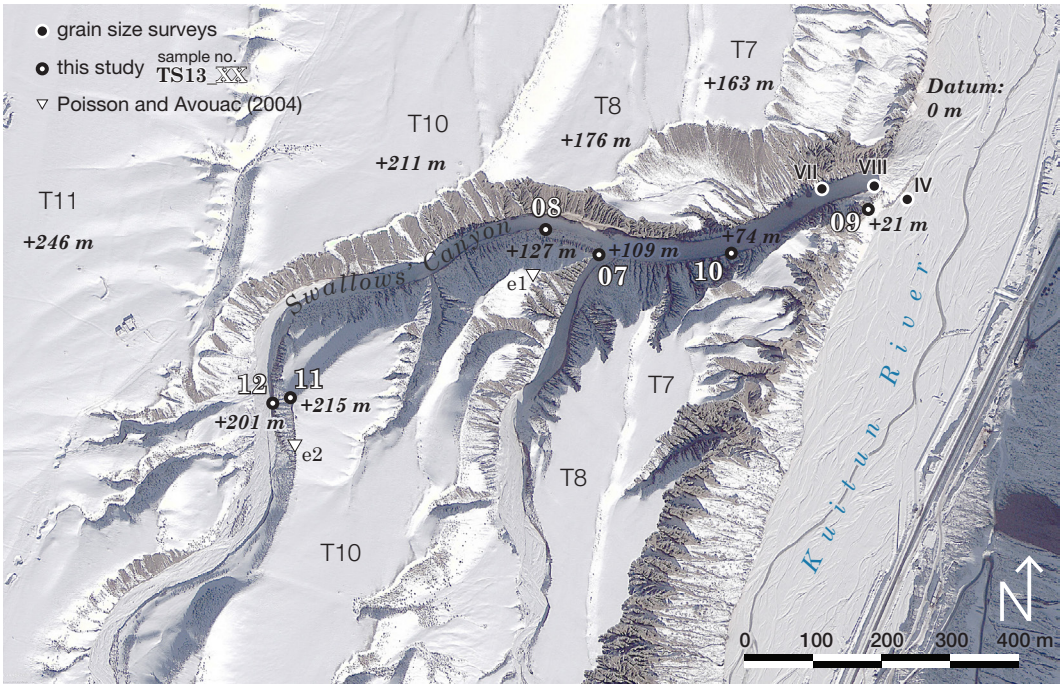

Figure 4.7: Map of Swallows' Canyon with location samples and grain size surveys. DigitalGlobe image (23.12.2012) accessed from Google Earth.

mm, with D_{84} of 70 and 78 mm.

4.5 Chronological constraints

We compiled all the chronological constraints available from the literature (Poisson, 2002; Poisson and Avouac, 2004; Honghua Lu, Burbank, and Y. Li, 2010; Gong, S.-H. Li, and B. Li, 2014; Lu et al., 2014, Stockmeyer et al. *in review*) and complemented them with our own data based on luminescence dating (supplementary Table A.3). The locations of the complete dataset assembled for this study is indicated in Figures 4.1, 4.3, 4.4, and 4.7 and the Supplementary Table A.3. Location and results for the new samples are listed in Table 4.1 and detailed descriptions of the sampling sites and the luminescence results are given in the supplemental material.

Luminescence dating

Defects in the crystal lattice of quartz and felspar grains can trap excited electrons in higher energy states. These traps are emptied when the crystal is exposed to light (bleaching). In the dark, during burial, these traps progressively fill up with electrons excited by the incoming ambient radiation from

nearby radionuclides. The time elapsed since the last sunlight exposure can be measured in a laboratory by releasing and measuring the trapped electrons (Huntley, Godfrey-Smith, and Thewalt, 1985; Aitken, 1998; E. J. Rhodes, 2011). The luminescence analysis was performed at the UCLA laboratory.

Sampling approach

We sampled material for post-IR Infrared Stimulated Luminescence (post-IR IRSL) dating to constrain 1) the timing of terrace abandonment by sampling the loess cover and/or the topmost alluvial deposits of terrace treads and 2) the timing of aggradation by sampling in the fan stratigraphy. The dataset consists of 7 samples for post-IR IRSL dates constraining terrace abandonment ages and 13 post-IR IRSL dates documenting alluvial aggradation ages. The samples were collected on terraces and in the banks of the Kuitun, Anjihai, and Manas Rivers. The alluvial fans are mostly built by gravels to cobbles and the fine grained material necessary for post-IR IRSL measurement is scarce. We targeted rare silt-to-sand lenses deeper than $\sim$ 30 cm and thicker than $\sim$ 5 cm to be sampled with an aluminium tube. The loess samples are the simplest to obtain by hammering the tube into the base of the horizon, immediately above the top gravel of the alluvial fill. The loess deposition ages provide a minimum abandonment age for the respective terrace. This arid region is poor in organic material and we could not find any charcoal or other material for radiocarbon dating. Detailed descriptions of the sample settings and analytical results can be found in the supplemental material.

Equivalent dose determination

The preparation and measurement of the samples followed standard procedures for single-grain post-infrared infrared-stimulated luminescence (IRSL) dating which are described in detail in the supplementary material. However, the equivalent dose values for some older fluvial samples cannot be interpreted using standard approaches because of the between-grain scatter. We develop a framework presented in detail hereafter to interpret such samples.

We use a single-grain post-IR IRSL method to determine the equivalent dose (D_e) since deposition. This technique has only recently been developed (Buylaert et al., 2009; Thiel et al., 2011), and few studies have applied the tech-

nique to single grains within fluvial deposits (Nian, Bailey, and Zhou, 2012; Trauerstein et al., 2014; N. D. Brown et al., 2015). This study explores the applicability of this promising method in a region where organic material is sparse and the quartz content has been measured to be as low as $0.05 - 1\%$ by weight.

With the exception of sample J0649, all measured samples yielded at least 5 single-grain results, with an average of 57 ± 33 grains out of 200 measured responding per sample. The distributions of D_e values fall into three categories: Types A, B, and C. Type A samples exhibited the simplest but least-common distribution: a single, well-bleached population, adequately described using the Central Age Model of Galbraith et al., 1999. Three samples fell into this category (see the 'Distribution type' column within Supplementary Table A.2). The other two distribution types exhibited more variance than would be expected within the defined sources of error. In other words, the overdispersion parameter was greater than would be expected for a well-bleached population (well-bleached samples exhibit an overdispersion of about 20 ± 9 % for multi-grain quartz OSL (Optically Stimulated Luminescence), though variability is high and the parameter should be quantified for a given site; Arnold and Roberts, 2009). This situation arises when multiple dose populations are mixed together (e.g., bank collapse during fluvial transport, bioturbation), when a sediment is not exposed to sunlight for enough time (i.e., partial bleaching), or due to problematic luminescence responses (thermal transfer, first-cycle sensitivity changes; Neudorf, Roberts, and Jacobs, 2012).

Of those distributions with high overdispersion, two types of D_e distributions were found. In Type B samples (12 of the 22 samples), the D_e values varied as a function of grain brightness and by considering only the brightest grains, the overdispersion could be reduced to reasonable values. This effect is shown for sample J0654 in Figure 4.8 a and b. To determine the D_e values for Type B samples, the brightest subset of grains were chosen to minimise the overdispersion, and then the Central Age Model (Galbraith et al., 1999) was applied.

While the reason for this relationship between grain sensitivity and overdispersion is unknown, it seems that the variation in internal potassium content between grains is the likely reason. Smedley et al. (2012) have recently demonstrated the exponential increase of feldspar grain brightness as a function of

K-content and Reimann et al. (2012) have shown that the brightest subset (e.g., 30%) of individual K-feldspar grains give post-IR IRSL ages concordant with independent age controls. This is borne out in the only Type B sample with radiocarbon age controls, J0646, which has a post-IR IRSL age of 3.3 ± 0.3 ka, indistinguishable from ^{14}C samples C-T5-1 (3.33 ± 0.04 kyr BP) and C-T5-2 (3.4 ± 0.2 kyr BP) (Poisson and Avouac, 2004).

Type C samples (5 out of 22) retained high overdispersion even when only the brightest grains were considered. The source of inter-grain variability was therefore considered to reflect incomplete bleaching. Two routines were used to evaluate Type C D_e values. The Minimum Age Model (3 variables, MAM-3; Galbraith et al., 1999) was used, assuming an overdispersion of 25% (an average value from Type A and B samples). A Discrete Minimum Model (DMM) was also used (Fuchs and Lang, 2001; E. J. Rhodes, 2015) wherein first dim grains were rejected, and then older grains were rejected until an overdispersion threshold of 25% was reached. The results from these methods compare well, in most cases overlapping at 1σ (Supplementary Figure A.1).

Cosmogenic dating

We infer the ages of abandonment of the terrace T18 along the Anjihai river from a depth distribution of cosmogenic isotope concentrations (Gosse and Phillips, 2001; Dunai, 2010). We sampled 3 granite cobbles from the surface and collected 4 samples of sand and small pebbles from different depths in a fresh open gravel quarry (supplementary Figure A.27). To invert the depth profile we modified the formulation of Lal (1991) that describes the change in ^{10}Be concentration as a function of depth to account for the deposition of loess and/or soil after the terrace abandonment (Braucher, Merchel, et al., 2011; Guralnik et al., 2011). The exposure age was then derived from a Monte Carlo inversion procedure which tests thousands of parameter combinations to find the best fitting solution by minimizing the difference between the model and the data (Braucher, Del Castillo, et al., 2009; Hidy et al., 2010; Saint-Carlier et al., 2016). The detail of the methods, the associated parameters and the sample treatment and analyses are provided in the online repository. Results of the cosmogenic analyses are reported in supplementary Table A.3. The cosmogenic depth profile shows the expected exponential decrease and its inversion constrain the mean exposure time of the terraces to 5.1 ± 1.7 ka (supplementary Figure A.27).

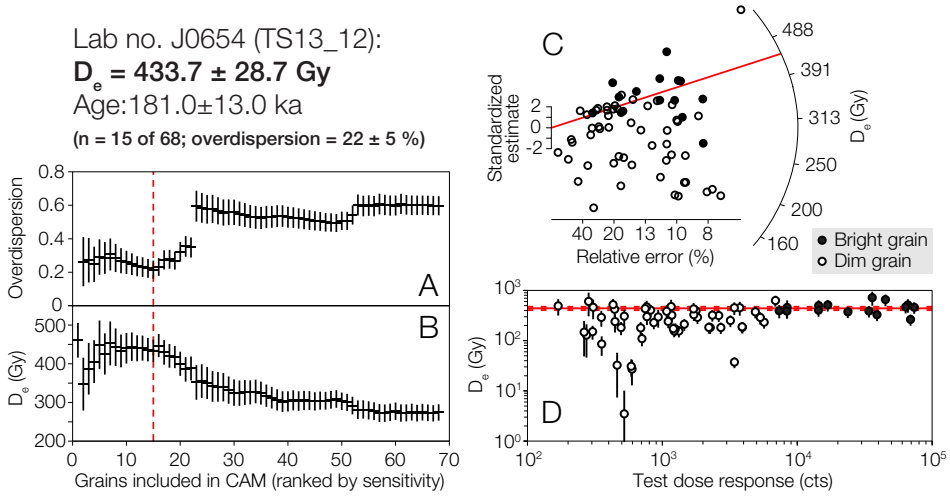

Figure 4.8: The relationship between grain brightness (i.e. sensitivity) and equivalent dose is shown for sample J0654. A: By incrementally increasing the number of grains included in the Central Age Model, the overdispersion reaches a minimum when the brightest 15 grains are included. B: The effect of adding the next-dimmest grain to the calculation of D_e is illustrated. C: A radial plot of all single-grain D_e values shows the wide range in apparent burial doses. By selecting only the brightest 15, however (shown as filled circles), a finite depositional age is apparent, with an overdispersion within the expected range (20 ± 9%, Arnold and Roberts, 2009) for a well-bleached population: 22%. D: The D_e values of individual grains are plotted against their response to a test dose of 35 Gy. The mean and standard deviation (1σ) of the population is shown as a solid and two dashed lines, respectively.

Results for the Kuitun River

Sampling in the Kuitun River followed two objectives: complementing the published dataset of Holocene terrace abandonment ages, and opening up a new dimension of the record with depositional ages of strata exposed in the canyon. Three samples were collected from the flight of terraces in the core of the Dushanzi anticline (Figures 4.2 and 4.5). Two other samples constrain abandonment of the terraces upstream of the anticline: on T10 at the top of Swallows' Canyon, in which the stratigraphic section was surveyed, and on T8 close to the apex (Figure 4.4 and 4.7). A summary of the samples collected along the Kuitun River is presented in Figure 4.9.

The samples of the strath terraces of the Dushanzi anticlines were sampled on T7, T2, and T1, which respectively lie 123 m, 52 m, and 3 m above the thalweg (Figure 4.5). The abandonment age of T7 is determined at 7.7 ± 1.0 ka by

Table 4.1: Results of post-IR IRSL luminescence (pIRIR) and Cosmogenic (TCN) dating of terraces and stratigraphy with location details. The River acronyms are KTN (Kuitun), AJH (Anjihai), TDO (Toudao), and MNS (Manas). Targets are either terraces (T#) or stratigraphy (S). The relative height* is the elevation of the sample above the river divided by the height of the fill terrace marking the onset of incision. If an incision episode is only documented by a single terrace, it is assumed to be a fill terrace with elevation 1.

Field code	**River**	**Target and Method**	**Height***	**Latitude (°N)**	**Longitude (°E)**	**Elevation (m.a.s.l.)**	**Age (ka)**
TS13_37	KTN	T1 (pIRIR)	0.02	44.296	84.789	734	1.7±0.4
TS13_36	KTN	T2 (pIRIR)	0.32	44.292	84.787	809	3.3±0.3
TS13_45	KTN	T7 (pIRIR)	0.76	44.288	84.782	865	7.7±1.0
TS13_86	KTN	T8 (pIRIR)	0.65	44.29	84.79	1169	8.4±0.7
TS13_11	KTN	T10 (pIRIR)	1.00	44.212	84.767	1118	13.4±1.6
TS13_02	KTN	S (pIRIR)	0.05	44.141	84.735	976	286.1±40.9
TS13_09	KTN	S (pIRIR)	0.09	44.215	84.781	924	316.9±24.3
TS13_01	KTN	S (pIRIR)	0.10	44.326	84.779	705	116.8±8.1
TS13_10	KTN	S (pIRIR)	0.30	44.214	84.777	977	396.5±36.7
TS13_07	KTN	S (pIRIR)	0.44	44.215	84.774	1012	193.4±28.0
TS13_08	KTN	S (pIRIR)	0.52	44.215	84.773	1030	48.9±3.6
TS13_03	KTN	S (pIRIR)	0.67	44.369	84.793	680	18.3±2.6
TS13_12	KTN	S (pIRIR)	0.82	44.212	84.767	1104	181.0±13.0
TS13_14	AJH	T3 (pIRIR)	0.16	44.101	85.098	1198	1.7±0.3
TS13_19	AJH	T13 (pIRIR)	0.88	44.093	85.099	1377	3.6±0.3
TS12-ANJ-T1B	AJH	T18 (TCN)	1.00	44.105	85.097	1424	5.1±1.7
TS13_35	TDO	T- (pIRIR)	1.00	43.979	85.107	1783	37.4±6.4
TS13_32	TDO	T- (pIRIR)	1.00	43.973	85.126	2063	111.0±7.0
TS13_34	TDO	T- (pIRIR)	1.00	43.974	85.126	2064	236.1±26.3
TS13_30	MNS	T- (pIRIR)	0.95	43.849	85.801	1189	81.3±9.0
TS13_33	MNS	T- (pIRIR)	0.80	43.849	85.801	1158	198.1±20.5

the sample TS13_45 taken in the middle of a 0.3 m thick silt horizon capping the 1.5 m thick cobble conglomerate that lies on the strath of T7. The silt horizon is buried by a layer of colluvium. On T2, we collected a tube 20 cm above the contact between the ca. 4 m thick alluvial cobble deposit covering the strath and the 3.2 m fluvially reworked loess and fine sand layer that caps it. This sample gives a minimum abandonment age for T2 at 3.3 ± 0.3 ka that corresponds to the age of two charcoal samples from T2 radiocarbon-dated by Poisson and Avouac (2004) at 3.33 ± 0.04 ka and 3.4 ± 0.2 ka (C-T5-1 and C-T5-2). The final sample (TS13_37) was collected on T1 5 cm above the fluvial fill in 0.8 m of clayey fine sand to silt with few granules. The fluvial fill is 3.2 m thick and lies on the bedrock strath of T1 that is only 1.6 m above the river. The minimum age of abandonment of the lowest terrace T1 is 1.7 ± 0.4 ka. This luminescence age corresponds to the maximum age constraint from a

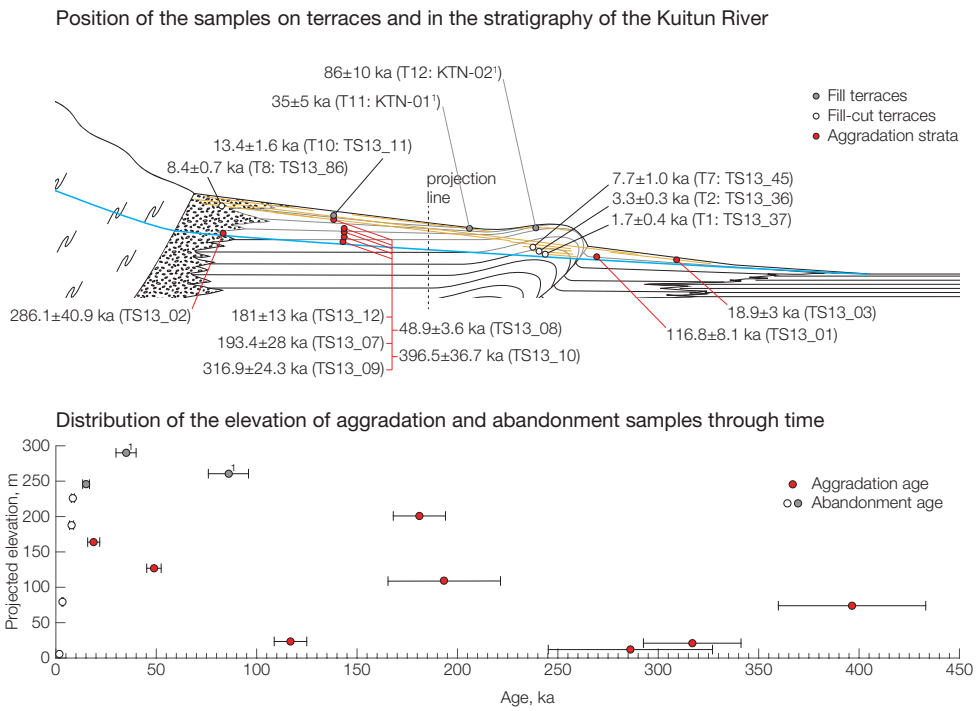

Figure 4.9: Samples collected along the Kuitun River. Top: position of all the samples in a sketch of the river system. Bottom: elevation of the samples above the river. To compare the samples with each other, all samples are projected on a central vertical transect where T10, the mot recent fill terrace, lies 245 m above the river and by multiplying that height by the fraction of the local height of T10 they lie at. All data from this study except for 1) Poisson (2002).

charcoal taken from the same reworked loess cap and dated at 1.71 ± 0.04 ka by Yang, A. Li, and Hunag (2013). The new dates for the Kuitun River terraces, and in particular the confirmation of the relatively old age of the most recent very low terrace suggest that the river started incising around 13 ka and that incision rates increased up to at least 30 mm/yr at the anticline until 1.7 ka when the river almost entirely ceased to incise vertically (Figure 4.10).

At the top of Swallows' Canyon we collected TS13_11 in a silt lens at the base of the colluvium wedge that caps the alluvial tread of terrace T10. The resulting abandonment age is 13.4 ± 1.6 ka which is somewhat older than the sample KTN-09 taken below the same colluvial cover 100 m farther south and measured at 10 ± 2 ka by Poisson and Avouac (2004). TS13_86 is sampled on

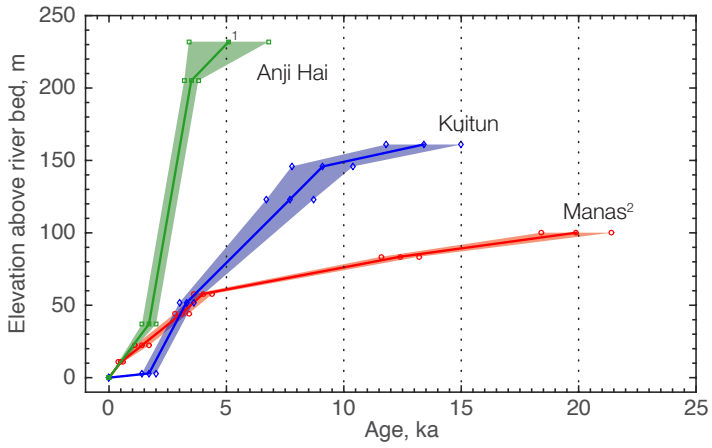

Figure 4.10: Age and elevation above the river of the terraces documenting the youngest incision in the Kuitun, Anji Hai, and Manas River. The samples in each river are from the same reach and no correction is applied to their height. Source of the marked samples: 1) Saint-Carlier (2015), 2) Gong, S.-H. Li, and B. Li (2015), all other samples from the present study.

T8 in a silt horizon 20 cm above the fluvial deposit of the terrace and below a wedge of colluvium. It yields an age of 9.1 ± 1.3 ka. Terrace T8 is found on either sides of the river and can be followed to the anticline.

Five out of eight samples documenting the aggradation time frame of the canyon walls were taken in the steep tributary Swallows' Canyon that exposes 246 m of stratigraphy and drains the river's left terraces T7 to T10 (Figure 4.7). The stratigraphy exposed in Swallows' Canyon is a series of subhorizontal layers made of rounded pebble to cobble conglomerate that are either matrix or clast supported. Rare silt to sand cross-bedded lenses of thickness 5 to 30 cm are wedged within the conglomerate. The location of the samples reflects a more opportunistic approach than a systematic sampling as silt to fine sand lenses suitable for luminescence dating are few and far between. In Swallows' Canyon, the five samples TS13_09, TS13_10, TS13_07, TS13_08, and TS13_12 are found at elevations of 21, 74, 109, 127, and 201 m above the thalweg and increasing distance from the left edge of the floodplain of 30, 230, 480, 590, and 930 m respectively (supplementary Figure A.11). TS13_09 is sampled in a 15 cm thick lens of silt to medium sand. TS13_10 is taken from a 10-15 cm thick lens of silt to fine sand. TS13_07 is sampled in a 20 cm thick lens of silt to fine sand. TS13_08 is sampled in a 5 cm thin lens of silt

that held few grains of the target size (175-200 μm) and only 4/5 grains were used. Finally TS13_12 is sampled in a 10-15 cm thick lens of silt to medium sand. The ages we obtained from bottom to top are respectively 316.9 ± 24.3 ka, 396.5 ± 36.7 ka, 193.4 ± 28.0 ka, 48.9 ± 3.6 ka, and 181.0 ± 13.0 ka.

At the fan apex, the sample TS13_02 was taken in the river's right wall, 15 m above the thalweg where the total depth of the canyon is 308 m. The tube was collected in a 1.5 m thick fluvial silt to fine sand horizon wedged between pebble to boulder conglomerates. The age of this layer is 286.1 ± 40.9 ka. The first of the two downstream samples, TS13_01, was taken in a 0.5 m thick short lens of fluvial silt to fine sand and gives an age of 116.8 ± 8.1 ka. The lens lay 10 m above the thalweg, in the river's left wall, where the canyon is 105 m deep, 420 m north of the frontal thrust. The last sample, TS13_03, was taken in a terrace riser on the river's right at an elevation of 40 m above the river for a total incision of 60 m. The target was a thin lens of silt which yielded an age of 18.9 ± 3.0 ka.

Results for the Anjihai River

Along the Anjihai River, we focused the dating effort on a flight of 18 Holocene terraces (Figure 4.6). The terraces (T1 to T18) are preserved at the junction of the Anjihai and the Toudao Rivers. The flow direction of both streams directs erosion away from the terrace flight, promoting the preservation of the flight in its wake, similarly to the Dushanzi anticline one where the Kuitun migrates unidirectionally. The total incision at the location of the terrace flight is 238 m. The pace of incision is documented by the TCN profile TS12_ANJ-T1B on the highest terrace T18 and by two post-IR IRSL ages sampled on the terrace flight: TS13_19 on T13 and TS13_14 on T1. Luminescence targets are scarce on these terraces due to very thin loess cover and important bioturbation of the treads. The abandonment age of T18 is 5.1 ± 1.7 ka (TS12_ANJ-T1B) and fits the timing of abandonment of the same surface at the windgap between the Halaande and the Anjihai Anticlines to the north (Figure 4.3) measured by X. Fu et al. (2017) with OSL and post-IR IRSL dating of the top of the fluvial deposits and the bottom of the loess cover between 5.3 ± 0.3 – 4.1 ± 0.2 ka (AJH-03, AJH-05 in top of alluvial deposit) and 3.7 ± 0.2 – 3.5 ± 0.2 ka (AJH-04, AJH-02 in loess cover). The two post-IR IRSL samples we obtained for T13 and T1 yield ages of 3.6 ± 0.3 ka and 1.7 ± 0.3 ka respectively. The

terraces document a local incision rate peaking at 93^{+47}_{-23} mm/yr between ca. 3.6 and 1.7 ka. Since the abandonment of the youngest terrace 37 m above the riverbed, the incision rate decreased to 22 ± 4 mm/yr (Figure 4.10).

Upstream from the terrace flight, the Toudao River is incised through Jurassic foreland deposits after leaving the mountain range. Interestingly, one can easily identify the Jurassic series in satellite images using coal mines as markers. The incised floodplain is flanked by a terrace that seemingly projects into the highest terrace of the flight downstream. The terrace surface is however partly covered by colluvium derived from the valley flanks. We collected a sample (TS13_35) in a silt horizon 5 to 10 cm above the cobble conglomerate that fills the valley and at the base of ca. 10 m of fine grained colluvium. The sampled layer had only few grains of the target size (175-200 μm) and only 6/7 grains were used. The sample constrains the minimum age of abandonment of fluvial aggradation at 37.4 ± 6.4 ka. This corresponds to the same age of abandonment as the OSL sample KTN-01 on the Kuitun terrace T11 at 35 ± 5 ka (Figure 4.4; Poisson, 2002).

We collected two samples overlooking the Toudao River at the edge of a gently sloping pasture draining into the neighbouring Jingou River and away from the mountain outlet of the Toudao River (Figure 4.3). The Toudao River itself flows more than 250 m below the edge of the pasture. The road outcrop of these samples exposes 10 to 20 m of coarse sand to cobble sized fluvial deposits with few thin lenses of silt to medium sand where the pasture is cut by the Toudao Valley (supplementary Figure A.21). The fluvial deposits cover a strath cut into Jurassic foreland deposits. The lower of the two samples (TS13_34) is taken in a 10 cm thick silt lens, at the base of a 3 to 4 m thick massive fluvial conglomerate and 2.5 m above the bedrock strath. It yields an age of 236.1 ± 26.3 ka. The second sample (TS13_32) is taken in the first silt lens above the massive fluvial cobble conglomerate and below a few thinner pebble conglomerate horizons. It lies 3 to 4 m higher in the stratigraphy, about 60 m further to the southeast and has an age of 111.0 ± 7.0 ka.

Results for the Manas River

The samples from the Manas River are taken from a wide strath terrace cut into north dipping Jurassic and Cretaceous foreland deposits directly at the exit of the high range (Figures 4.2 and 4.3). The surface of the strath exposed along the canyon has multiple levels indicating different episodes of cutting (Figure 4.2). The sample pair (TS13_33 and TS13_30) constrains the deposition and abandonment of a section of the alluvium on the wide strath terrace. The alluvium cover is made of a ca. 10 m thick clast-supported conglomerate ranging from boulder to pebble from base to top. The conglomerate is covered by a discontinuous layer of silt to fine sand with a maximum thickness of 20 cm. The fine grained layer is capped by ca. 1.5 m of angular to subangular cobble to pebble colluvium and soil. TS13_33 was collected 2.5 m above the strath in a pocket of silt wedged between boulders. The aggradation age of the base of that cobble conglomerate is 198.1 ± 20.5 ka and the age of the cap above the conglomerate is 81.3 ± 9.0 ka (supplementary Figure A.24).

4.6 Morphological evolution of the piedmont

The observations and data assembled here allow a reconstruction of late Quaternary piedmont evolution The anticlines of the fold-and-thrust belt in the northern piedmont are truncated in several places (Figure 4.3). Most of these gaps are canyons occupied by the active rivers that are incised not only in the anticlines, but also in the Quaternary alluvial fans upstream and downstream of the anticlines. Others are windgaps that lie flush with abandoned fan surfaces only offset by several meters high fault scarps at the deformation front (Avouac, Tapponnier, et al., 1993; Gong, S.-H. Li, and B. Li, 2015). These windgaps were cut by the piedmont rivers following different courses in the past. In order to maintain the gaps, the rivers have had to occupy them frequently and not let the growing anticline build an unsurpassable barrier that would have deflected them. The rivers presumably shift location when the fans are fully aggraded and their channels migrate freely. The presence of multiple gaps across the anticlines thus testifies of repeated episodes of aggradation and incision.

Kuitun River

We can establish a detailed record of the Holocene incision in the Kuitun River thanks to the nine Holocene terraces preserved in the Dushanzi Anticline. Upstream from the anticline, the river flows on a straight path and there, the youngest preserved terrace is T7 (TS13_45 at 7.7 ± 1 ka). The new ages complete the incision history of the Kuitun River and reveal that the river largely ceased to incise at 1.7 ka (TS13_37, Figure 4.10). The fluvial incision rate at the anticline since 1.7 ka cannot be precisely calculated because the exact elevation of the bedrock strath in the middle of the channel is unknown. The abandoned strath lay 1.6 m above the water edge in June 2013 and the water was at least 1 m deep from visual inspection giving an incision rate of at least 1.5 mm/yr since 1.7 ka. This rate of incision corresponds well to a newly estimated Holocene uplift rate of the anticline of $1.49^{+0.20}_{-0.16}$ mm/yr. The rate is calculated from the 20 m of vertical offset recorded by the deformation of T10 (Poisson and Avouac, 2004) and our new age for T10 of 13.4 ± 1.6 ka (TS13_11) instead of 10 ± 2 ka corresponding to a Holocene uplift rate of ca. 2 mm/yr (Poisson and Avouac, 2004). Without knowing the age of the lowest terrace in the anticline (1.7 ka at 5 m above the channel, sample TS13_37) the rectangular entrenchment geometry of the rectilinear canyon gives the impression that the river is still incising at a very high rate. However, when vertical incision stalls, like the Kuitun River since 1.7 ka, ongoing lateral erosion erodes the valley walls and systematically destroys the youngest terraces, carving a rectangular cross-section (Malatesta, Prancevic, and Avouac, 2017). The rectangular valley cross-section is the signature of a river that stopped incising vertically, rather than a fast ongoing incision that started with the abandonment of T8 and T7 as previously thought (Poisson and Avouac, 2004).

The new deposition ages in the stratigraphy of the Kuitun fan, together with the abandonment ages of the terraces, open a window to the aggradation and incision history of the river. The combination of abandonment and aggradation ages of this fluvial system indicates repeated episodes of aggradation and incision over the last 450 kyrs. While the fill-terraces constrain the maximum elevation reached by the river, the aggradation samples only provide a minimum depth for river incision, i.e. the river had first to incise to this level, before depositing material at this level. To compare the relative elevations of these samples taken at various positions along the stream, where the canyon

depths range from 60 to 308 m (Figure 4.9, top), we project each elevation above the river to a central section where T10 is 246 m above the river (Figure 4.9, bottom) and assume that the river rapidly incises and aggrades around a pivot at the fan toe without being deformed by subsidence. The elevation of the 86 ± 10 ka terrace T12 is restored to its initial position by removing the accumulated uplift ($1.49^{+0.20}_{-0.16}$ mm/yr) that perched it 150 m above T10 since abandonment. Between the terrace T10 that marks the onset of the youngest incision and the next older terrace (T11 at 35±10 ka, KTN-01), we document a phase of aggradation one third down the existing canyon at 18.9 ± 3 ka (TS13_03). Similarly, terraces T11 and T12 (called F_K and Q_3 by Poisson and Avouac, 2004) are separated by a phase of aggradation documented at 48.9 ± 3.6 ka (TS13_08). Three successive incisional episodes separated by aggradation phases can be thus identified in the last 100 kyrs. No well defined terraces older than T12 have been found that could place the maximum elevation of the river at earlier stages. This could mark a long term shift of the depocenter downstream of the active fault and the abandonment of the upstream Pleistocene surfaces as proposed by Guerit et al. (2016). Alternatively, the aggradation phase between T11 and T10 in the Kuitun River could simply have been not as large as previous ones. In the neighboring Anjihai and Jingou Rivers on the contrary, the surface of the piedmont has been largely reworked since the Last Glacial Maximum (LGM, Figure 4.3). If the average aggradation rate in the piggy-back basin is 0.7 mm/yr since 4 Ma (Charreau, Avouac, et al., 2008), it would continue to largely exceed the relative uplift of the thrust's hanging wall (3 mm/yr of basinward motion of a block with a surface slope of 2% results in 0.06 mm/yr of uplift) and the future episodes of aggradation are likely to resurface the entire fan again.

We can continue the same exercise without the maximum elevation provided by fill terrace abandonment. Nine tenth down the existing canyons, we document an aggradation phase at 112.4 ± 45.8 ka (TS13_01) that would have been shortly followed by terrace T12 on top of the canyon. Before that, two additional ages in Swallows' Canyon indicate a period of aggradation between three and one fifth down the canyon at 193.4 ± 28 ka and 181.0 ± 13.0 ka (TS13_07 and TS13_12). A phase of incision had to follow it to bring the river down to the level of TS13_01. Interestingly, the two samples around 180 ka lie stratigraphically below and above TS13_08 at 48.9 ± 3.6 ka. As these

are 110 and 340 m away from the river, the age inversion is a likely sign of truncation of the strata by an incision phase between the two ages (supplementary Figure A.11). Three additional ages collected near the level of the modern Kuitun River (TS13_02, TS13_09, and TS13_10) indicate aggradation phases between 286.1 ± 40.9 and 396.5 ± 36.7 ka. These ages lie near the methodological limit of luminescence dating and the fading correction results in very large uncertainties (see methods). We are not able to identify distinct phases of aggradation with these older samples, but they indicate that the sediment remobilized by Holocene incision contained material deposited between the latest aggradation phase between ca. 15 and 20 ka and the Middle Pleistocene, a time span representing 5 glacial periods.

The grain sizes in the active channel of the Kuitun River largely reflect those of the valley walls. The only significant trend in the channel grain size is a rapid loss of very coarse material near the apex (Supplementary Figure A.2). The bedrock channel upstream from the apex is not gravel bedded and holds cobbles and boulders, but we were not able to access and survey it. We have not surveyed sediment grain size at the dated horizons, but we sampled the bed of the tributary canyon and a small fan collecting sediment at the foot of a chute in the canyon wall. These surveys integrate sources across the stratigraphic stack above the sampling site. The similarity between the walls and the stream bed as well as the drop in D_{84} away from the apex are clear signs that the bedload consists overwhelmingly of material currently eroded from the fan. Given how grain size on alluvial fans can co-evolve with changing climate (D'Arcy, Whittaker, and Roda Boluda, 2016), it would be informative to survey the D_{50} at each dated horizon.

Anjihai River

The Anjihai River started incising its modern canyon, flowing to the northeast, during the mid-Holocene (Figure 4.3). The northeast course does not provide a faster drop in elevation than if the river flew straight north through the now abandoned windgap. On the contrary, the north course would provide the path of steepest descent. It is therefore unlikely that the Anji-Hai River was captured by a smaller stream offering a quicker drop in elevation to the east. The river was probably aggrading and migrating across the entire fan surface until the mid-Holocene when it started incising as it was flowing on

the eastern flank of the fan, becoming stuck in that course.

The samples documenting aggradation of fluvial conglomerate on the bedrock strath, now located 250 m above the Toudao River (TS13_32 and TS13_34) testify of a former northeast path of the smaller river that must have bevelled the foreland deposits and flowed toward the Jingou River over what is now a gently sloping pasture (highlighted by an arrow in Figure 4.3). The beveling of the foreland must have occurred prior to 236.1 ± 26.3 ka and the river abandoned that course to flow northwards after 111.0 ± 7.0 ka. The modern northward course is the steepest descent for this river and the change of path could be the result of a capture from the main trunk of the Anjihai River after erosion through the Jurassic foreland deposits.

Manas River

The large strath of the Manas River, right after leaving the high range, has been cut in tilted Jurassic and Cretaceous series. The sample collected in conglomerate 2.5 m above the strath constrains the minimum age of strath creation at 198.1 ± 20.5 ka (TS13_33). The last time the river aggraded high enough to resurface the tread of the terrace is at 81.3 ± 9.0 ka (TS13_30).

4.7 Pleistocene climate and aggradation-incision cycles

In this section we combine our observations constraining the geomorphic evolution of the piedmont and the Late Quaternary climate in Eastern Central Asia.

Pleistocene climate

The Junggar Basin and the piedmont are semi-arid and most precipitation is derived from the Westerlies and falls in early summer; the rest falls as snow in the high-range during fall and winter (H. Cheng et al., 2012; Sorg et al., 2012). The hydrograph of the rivers is dominated by the melt season with peak discharges between June and August (Poisson, 2002; Liu et al., 2011). Past climate dynamics in the region have been reconstructed from caves in the Tian Shan (H. Cheng et al., 2012; Hai Cheng, Spötl, et al., 2016, see Figure 4.1 for location), from sedimentary and pollen studies in Lake Manas (Figure 4.1; Jelinowska et al., 1995; T. E. Rhodes et al., 1996; Fan, S.-H. Li, and Y.-G. Chen, 2012), from lake level reconstructions of Ebi Nor Lake (Figure

4.1; Poisson, 2002) and of lakes in Northwest China (Liu et al., 2011). The larger scale climate dynamics are captured by speleothem records, of the main moisture source in the Eastern Mediterranean (Bar-Matthews, Ayalon, and Kaufman, 1997), carried to Central Asia by the Westerlies, and of a potential second southern source from the East Asian (EASM; Y. J. Wang et al., 2001; Y. Wang et al., 2008) and the Indian Summer Monsoons (ISM; Kathayat et al., 2016).

It has been proposed that the monsoon might occasionally encroach into Central Asia, e.g. during the Holocene Thermal Optimum (ca. 10-4 ka; Gasse et al., 1991; H. Cheng et al., 2012). Monsoonal moisture could reach the Tian Shan during interglacials if the ISM is strong enough to cross the Tibetan Plateau (Gasse et al., 1991) and/or if the EASM extends deep inland from the east (H. Cheng et al., 2012). Increased insolation during interglacials allows the EASM to reach deeper into Central Asia, due to a northward shifted Intertropical Convergence Zone (ITCZ) and associated monsoonal circulation (Schneider, Bischoff, and Haug, 2014). Conversely, a southward-shifted ITCZ during glacial periods prevents significant incursion of the ISM and EASM into Central Asia. The Westerlies, bringing recycled moisture from the Atlantic realm, are repositioned at glacial-interglacial time scales and seem antiphased to the EASM (Nagashima et al., 2011). A more northern mean position is found during periods of high insolation and weak Siberian High, whereas during times of low insolation, a more southerly position of the Westerlies leads to deeper intrusion of moisture into Central Asia, as found in various archives (Vandenberghe et al., 2006; F.-H. Chen et al., 2010; Nagashima et al., 2011; An et al., 2012). Insolation changes could drive North Atlantic sea ice dynamics, which in turn would affect the mean latitudinal position of the Westerlies (Bakke et al., 2009). Lower insolation could result in more extensive sea ice cover in the North Atlantic, southward repositioning of the Westerlies and a stronger glacial Siberian High, which prevents intrusion of the Westerlies north of the Pamiro-Alai-Tian Shan mountain chains. Instead, the Westerlies would be deflected southward, enhancing moisture availability in western Central Asia.

The causal link between solar forcing, Westerlies and Asian monsoon, sug-

gests that the Central Asian moisture budget is strongly affected by underlying forcings and seasonality in precipitation. Combined enhanced winter (Westerlies-derived) and higher summer (monsoonal) precipitation would be expected during intervals of highest insolation, whereas during periods of low insolation total annual precipitation would be minimized. When insolation and/or glaciation conditions are in an intermediate stage, either the Westerlies, or the southern monsoons might govern the annual moisture budget. Thus, there appears to be an optimum period for each of the two moisture sources, related to insolation state of glaciation and Siberian High intensity (Wolff et al., 2016; Cai et al., 2017). This is important for the interpretation of our dataset, as higher winter snowfall allowed glacier buildup during glacial periods, while summer rainfall would allow sediment evacuation.

Variations in both temperature and precipitation affect sedimentary dynamics on the piedmont by modifying sediment and water fluxes. Cooler temperatures, together with higher precipitation support extensive glaciation, enhanced glacial erosion, and accumulation of loose sediment in the high mountain (Molnar and England, 1990; P. Z. Zhang, Molnar, and Downs, 2001; Herman et al., 2013). Wetter conditions under a cool climate also result in larger and faster flowing glaciers, greater erosion and production of sediments (Oerlemans and Fortuin, 1992; Brozovic, Burbank, and Meigs, 1997). But any increase in water discharge during spring and summer improves the fluvial evacuation of glacial sediments from the high range to the basin (Gilbert and Murphy, 1914). Cold and dry periods, conditions inferred for stadial periods in Central Asia, would result in glacial erosion in the high range, but little hydraulic power to transport and evacuate these sediments.

River incision and climate since 30 ka

With the new dates presented here and the terrace ages reported by Poisson (2002), Poisson and Avouac (2004), Honghua Lu, Burbank, and Y. Li (2010), Gong, S.-H. Li, and B. Li (2014), Lu et al. (2014), and Stockmeyer (*in review*), we can constrain recent fluvial incision by the four rivers Kuitun, Anjihai, Jingou and Manas in unprecedented detail. Entrenchment of the rivers Kuitun, Anjihai, and Manas are each measured in the same terrace flight (Figure 4.3). The Jingou record, however, is a composite from different reaches along the

river. To compare the relative incision of the four rivers with each other, we normalise the elevation of the terraces by the local height of the fill terrace that marks the onset of incision (Figure 4.11 A). It was known that all rivers had incised rapidly during the Holocene, but insufficiently detailed sampling gave the impression of an apparent synchronous incision (Avouac, Tapponnier, et al., 1993; Molnar, E. T. Brown, et al., 1994). Here we show that the onset of incision and its slowdown were not synchronous across the piedmont. The onset of incision varies by ca. 8 kyrs with the Kuitun River starting at 13 ka and the Anjihai River at 5 ka. The Kuitun River has stopped incising at 2 ka, with the incision rate measured in the anticline today matching that of its uplift. The Manas River, on the other hand, appears to not have slowed down yet, suggesting that the equilibrium profile is still far from reached. Collectively, the four rivers indicate individual transitions from aggradation to incision around the early Holocene and an acceleration of incision rates between 5 and 3 ka.

A detailed climate record from diverse archives allows us to compare the fluvial dynamics discussed above with moisture budget around the Junggar Basin since the LGM. The local lakes Manas (now almost dry) and Ebi Nor (now at low stand) provide proxy data for the moisture budget in their catchments (Figure 4.1). Sedimentological and palynological data from a sediment core of Lake Manas indicate a period of increased effective moisture starting at 10 ka after a very arid period and finishing at 1 ka with two dry episodes at 5 and 3 ka (Figure 4.11 B; T. E. Rhodes et al., 1996). The lake level reconstruction for Ebi Nor provided by Poisson (2002) shows a very similar trend with the lake reaching a high stand at the onset of the Holocene and decreasing to the current low level after 5 ka. Additionally, data from four NW China lakes for the last 18 kyrs by Yu, Harrison, and Xue (2001) provide a larger scale proxy for Central Asian moisture (Figure 4.11 B). The lacustrine data show a period of increased moisture around 15 to 5 ka, followed by increased aridity leading to today's dry conditions. The high stand of the lakes reflect the contemporary increase in moisture of the Mid-Holocene Thermal Optimum with a lag of a few kyr, because high evaporation rates prevented high lake levels at the peak of the Thermal Optimum (T. E. Rhodes et al., 1996; Hai Cheng, Spötl, et al., 2016; Cai et al., 2017). The association of warm and wet conditions stands in contrast to the dry and cold climate characterizing the glacial maxima in

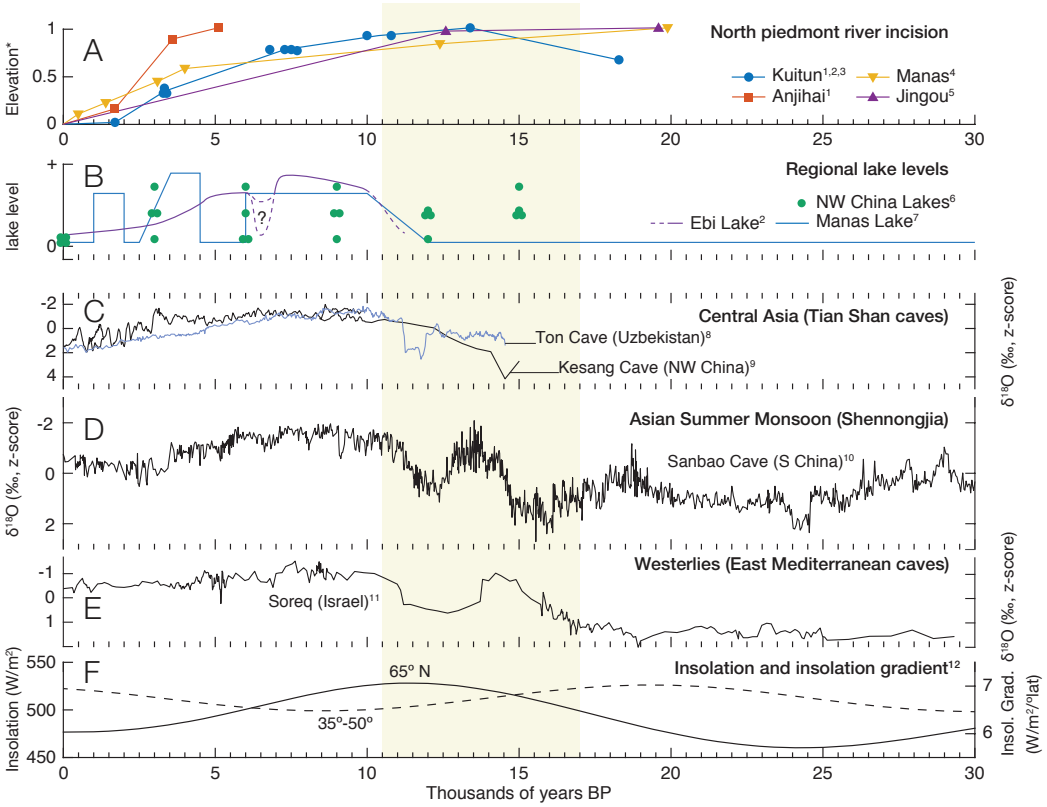

Figure 4.11: Evolution of climate and incision four surveyed rivers of the north piedmont in the last 30 kyrs. Rivers incise as the region becomes warmer and more humid, yet the onset and pattern of incision is different for each of them, suggesting that it is not directly driven by the contemporary climate change. The yellow band highlights the last deglaciation. A: youngest incision phase in four rivers of the piedmont and the last documented aggradation for the Kuitun River; 1) this study; 2) Poisson (2002); 3) Poisson and Avouac (2004); 4) Gong, S.-H. Li, and B. Li (2014); 5) Honghua Lu, Burbank, and Y. Li (2010). B: Regional lake levels; 6) Yu, Harrison, and Xue (2001); 7) T. E. Rhodes et al. (1996). C: δ^{18}O values for the Central Asian record of the Kesang and Ton Caves; see Figure 4.1 for location of Kesang; 8) H. Cheng et al. (2012); 9) Hai Cheng, Spötl, et al. (2016). D: δ^{18}O for the Asian Summer Monsoon; 10) Hai Cheng, Edwards, et al. (2016). E: δ^{18}O values for the Westerlies; 11) Bar-Matthews, Ayalon, and Kaufman (1997). F: insolation at 65°N and insolation gradients between 35°N and 50°N; 12) Berger (1978).

Central Asia (H. Cheng et al., 2012). Finally, in the modern dry and warm conditions, glaciers are mostly confined to cirques. The post-LGM increase in temperature is also recorded by the speleothem δ^{18}O record from Kesang Cave (Figure 4.1; H. Cheng et al., 2012; Cai et al., 2017). At the same time, lower δ^{18}O values in the Soreq Cave record suggest increased rainfall at the source of Westerlies moisture (Bar-Matthews, Ayalon, and Kaufman, 1997).

The "incised" state of fans with a semi-glaciated catchment reflects a climatic forcing but the onset and the pattern of incision cannot be used to time the forcing because it depends on the local timescale of sediment evacuation from the high range. Furthermore, the vertical incision response of a river to a drop in input Q_s/Q_w can be delayed by the initial consumption of excess transport capacity for horizontal erosion. The terraces abandoned in the early Holocene are typically 2-3 km wide, indicating that the rivers were initially spending most of their excess transport capacity in lateral erosion. During entrenchment, feedbacks with the valley walls can accelerate the incision rate by limiting lateral migration of the channel and promoting vertical incision (Malatesta, Prancevic, and Avouac, 2017).

The evolution of the rivers in the context of climatic forcing since 30 ka is outlined below (Figure 4.11 C-F). The phase of sediment evacuation and fan aggradation corresponds to the deglaciation period, when the extensive glaciers of the LGM started to retreat under increasingly warmer and wetter conditions, exposing moraine material to greater water discharge that could evacuate them out of the mountain and onto the piedmont. The last deglaciation is highlighted with the shaded yellow rectangle in Figure 4.11. The changes in insolation of the precessional cycles are reflected in the δ^{18}O trends in proxies of regional moisture sources: the Westerlies, the Asian Summer Monsoon, and finally the local records of the Kesang and the Ton Caves (Figure 4.11 C-D-E). The input Q_s/Q_w at the apex of the piedmont fans drops after evacuation of the bulk of the sediment readily available in the high range, causing subsequent incision of the oversteepened alluvial slopes. The onset of incision varies in each catchment as it depends on the size of the respective reservoirs of loose sediments upstream and the speed of evacuation. Molnar, E. T. Brown, et al. (1994) already suggested that the glacial geometry could modulate the local

effects of Pleistocene climate changes in the piedmont. This can be the case for the total incision in the fan which depends on the difference between steep and shallow alluvial slopes. A greater sediment flux, which is expected to vary locally, results in a steeper slope that is prone to deeper subsequent incision.

Aggradation and incision since 450 ka.

We can precisely constrain fluvial incision since the LGM thanks to numerous fill-cut terraces. The task is more arduous for previous incision phases. The preservation of fill terraces is incomplete and the samples in the stratigraphy are too few to establish a precise stratigraphic model for the piedmont. We can inform the sparse data with what we know about the last 30 kyrs to propose a history of aggradation and incision since 450 ka. The correlation between insolation and isotopic composition of regional climate systems is repeated in the longer 450 kyr record (Figure 4.12 C-D). We use yellow shading in Figure 4.12 to mark stadial-interstadial transitions, when Central Asian climate transitions from cold and dry, to warmer and wetter. Following our interpretation for the dynamics that led to the current incision (Figure 4.11), we expect aggradation of the piedmont during deglaciation and rising insolation. Incision follows when the upstream sediment reservoir is emptied and water discharge still relatively large. We do not expect all past incision onsets to be preserved because any aggradation episode higher than the previous one will bury the previous terrace treads and overprint the record. However the multitude of ages in different rivers and the presence of active anticlines that can uplift and safeguard straths allow the identification of several contemporary incision episodes across the rivers that support the relationship proposed for the youngest incision phase. The entire dataset is shown in Figure 4.12 A, with normalized elevation as in Figure 4.11 A. The compilation of ages with all the references and coordinates can be found in the supplementary Table A.3.

Most notably, terraces on the Kuitun, Jingou, Manas, and Hutubi Rivers mark an onset of incision coinciding with the 85 ka insolation peak (Marine Isotope Stage 5a). Along the Manas River this interval marks the last time that the tread at the outlet of the high-range was flooded and reworked, suggesting a particularly high episode of aggradation (TS13_33, Figure 4.3). Multiple terraces of the Kuitun, Anjihai, and Jingou Rivers match the weaker insolation

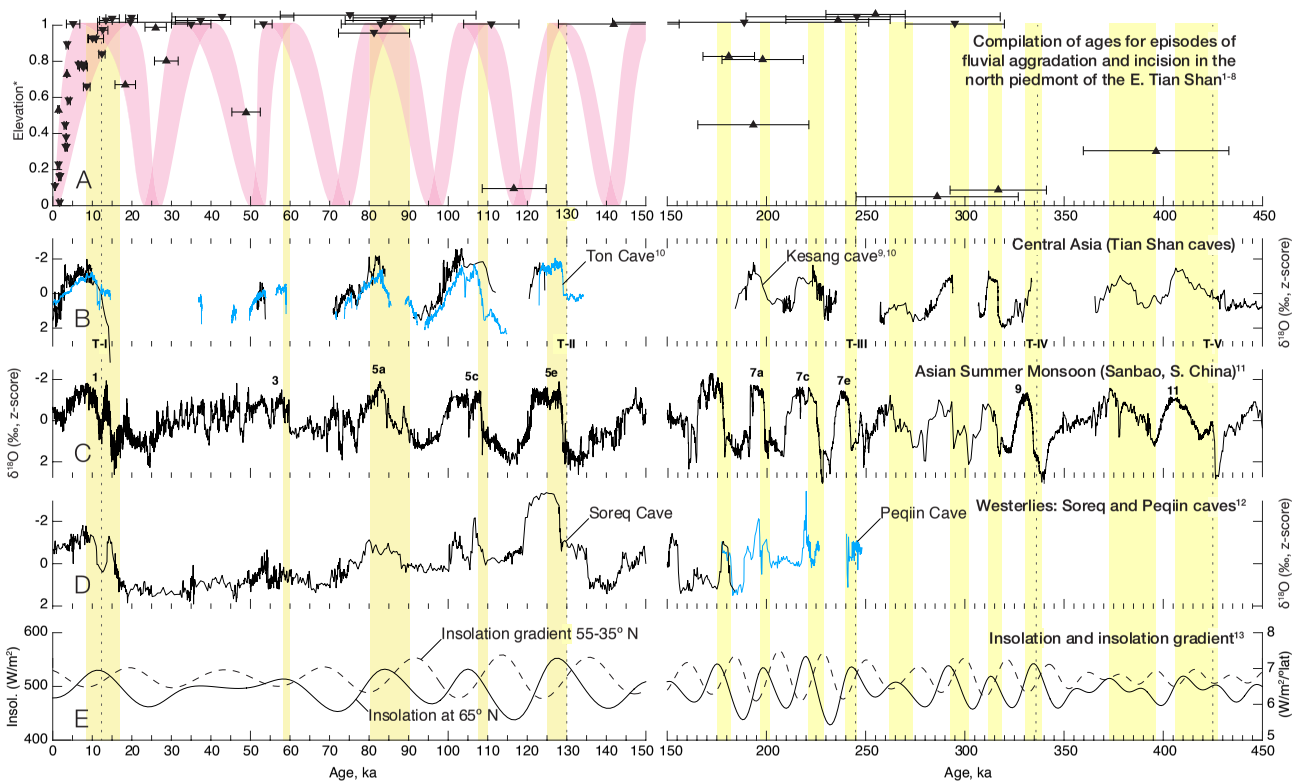

Figure 4.12: Ages of the alluvial system with climate data since 450 ka. Clusters of abandoned terraces separated by aggradation episodes suggest fast and repeated cycles of aggradation and incision over the last 150 kyrs (suggested by the magenta tracks) and probably since 450 ka at least. Yellow bands highlight stadial-interstadial transitions. A: terrace abandonment ages and stratigraphy aggradation ages in rivers of the Tian Shan north piedmont (detailed age compilation in Supplementary Table A.3); 1) this study; 2) Poisson (2002); 3) Poisson and Avouac (2004); 4) Honghua Lu, Burbank, and Y. Li (2010), 5) Lu et al. (2014); 6) Gong, S.-H. Li, and B. Li (2015); 7) X. Fu et al. (2017); 8) Stockmeier et al. (*in review*). B: Climate sources: 1: δ^{18}O values for the Central Asian record of the Kesang and Ton Caves; 9) H. Cheng et al. (2012); 10) Hai Cheng, Spötl, et al. (2016). C: δ^{18}O for the Asian Summer Monsoon; 10) Hai Cheng, Edwards, et al. (2016). D: δ^{18}O values for the Westerlies; 11) Bar-Matthews, Ayalon, and Kaufman (1997). E: insolation at 65°N and insolation gradients between 35°N and 50°N; 12) Berger (1978).

peak at 35 ka. Older ages have errors that span several insolation cycles and cannot be reliably attributed to one or the other. We note however a cluster of terrace ages near the interglacial before last, around 240 ka (MIS 7e). This is congruent with the causal chain of insolation driving North Atlantic sea ice extent (Bakke et al., 2009), in turn affecting the latitude of the Westerlies (Brauer et al., 2008), and modulating moisture delivery to Central Asia.

Based on the spacing of uplifted terraces on the active anticlines of the fold-and-thrust belt, Molnar, E. T. Brown, et al. (1994) proposed that major phases of incision in the piedmont occurred at a 100 kyr frequency. Instead of the slow and continuous fan aggradation during the glacial periods suggested by Molnar, E. T. Brown, et al. (1994) and Poisson and Avouac (2004), we find repeated episodes of aggradation and incision, possibly timed by the 21 kyr precession cycle during the glacial period. Possibly, incision is deepest during interglacials if sufficient monsoonal moisture reaches eastern Central Asia, as for example during MIS 11 when higher effective moisture availability allowed speleothem growth in todays arid Gobi desert (Vaks et al., 2013). Still, the monsoon is not a necessary component to drive the morpho-sedimentary evolution of the piedmont, which appears to vary greatly under the solely Westerlies regime of the glacial periods. Interestingly, this would occur with only subtle changes in climate in this hyper-continental region, highlighting the glaciers importance in modulating sediment flux and exacerbating the morphological impact of climatic variations.

Stratigraphic perspective

The cycles of aggradation and incision in the piedmont delay the progradation of the coarse sediment load. They also change the composition of that flux as fluvial incision injects older material in the modern sediment flux. We describe here how this affects the downstream stratigraphy of the basin in a simple configuration. Figure 4.13 A shows the progression of the sediment flux in the basin as a Wheeler-type diagram tracking the fine and the coarse load of a unique pulse. Final sediment deposition is marked by the shaded area. The transient presence of bypass material en route to the basin is indicated with a thinner outline and no shading. The coarse material is first deposited on the upper fan before being remobilised by the subsequent incision. Down-

stream of the zone of initial aggradation, the sediment flux contains recycled older sediments. The coarse bedload material progresses more slowly than the suspended and dissolved loads that essentially move together with the water. The difference in progression rate of the two loads leads to a hiatus between the two where they overlap. By swapping time for stratigraphic height, we build the basin and the foreland stratigraphy in Figure 4.13 B, assuming repetition of the same cycle. At the transition zone, the fine load that very quickly prograded into the basin is interfingered with the gravel front. Here, the sediments from the same initial pulse, a deglaciation in the case of the north Tian Shan, are separated by a hiatus equal to the time necessary for the gravel front to cross the piedmont, while originating in the same initial pulse (Figure 4.13 C). In the northern piedmont, the hiatus is 6 to 15 kyrs long depending on the onset of incision. In the immensely larger Indus drainage, Clift and Giosan (2014) estimate a similar lag of 7 to 14 kyrs. If both systems are characterised by a similar lag despite the difference in length scale, the transport timescale of the coarse load should be primarily dependent on the periodicity of forcing. Moreover, in the Kuitun River, the sediment composition downstream of the initial aggradation zone includes significant quantities of older recycled material ranging from the Middle Pleistocene to present.

Incision episodes in alluvial piedmonts can quickly mobilise a significant volume of sediment and impact the downstream stratigraphy, such that while the mountain range itself can act as a low pass filter damping environmental signals created by high-frequency climatic forcing (Castelltort and Van Den Driessche, 2003; Armitage, Dunkley Jones, et al., 2013), alluvial piedmonts can amplify and record these signals by rapid reaction as documented here. High-frequency environmental signals sourced in alluvial piedmonts can be transferred along the alluvial domain (Simpson and Castelltort, 2012). However, they have a potentially limited downstream impact because they are carried by coarse grained sediments and are likely to only influence the gravel front, having little relevance for the stratigraphy farther downstream (Paola, Heller, and Angevine, 1992; Armitage, Burgess, et al., 2016). Furthermore, a reserve of coarse sediments that can be mobilised when water discharge increases will tend to stabilize the position of the gravel front position by balancing the Q_s/Q_w ratio as suggested by Armitage, Burgess, et al. (2016).

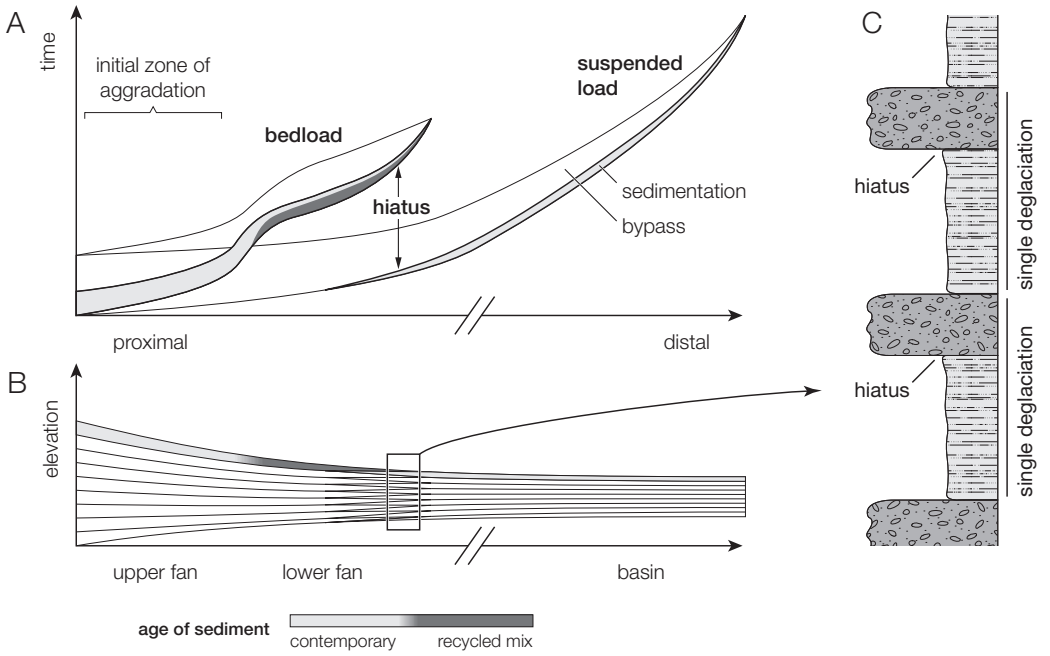

Figure 4.13: A: Propagation of the bedload and suspended load of a sediment pulse in a time vs. distance space (Wheeler-type diagram). The suspended load is immediately delivered to the basin. The bedload moves slowly, in two phases, first deposited directly in front of the high range and then remobilized by incision and transported to the foot of the piedmont (current situation in the north piedmont). The darker shade indicates bedload deposit with recycled material. B: collapse of the time vs. distance in spatial dimensions, assuming a repeated identical pulses. C: the two deposits overlap at the transition basin-piedmont, and a hiatus of 6 to 15 kyrs separates the coarse and the fine sediment deposits initially produced by the same forcing.

4.8 Conclusion

This study extends the chronological constrains on the morpho-sedimentary evolution of the north piedmont of the Eastern Tian Shan with new ages of terrace abandonment and of strata exposed in the canyon walls of the entrenched Kuitun River.

We have shown that variations in temperature and moisture delivered by the Westerlies is the likeliest cause of repeated aggradation and incision of the north piedmont. Glacial erosion and river transport in the high range modulate the ratio of sediment flux and water discharge to the piedmont and exacerbate the morphological reaction of the piedmont. Aggradation of the

piedmont accompanies the retreat of glaciers during periods of increasing insolation and greater precipitation. Subsequent fast incision occurs after the upstream sediment reservoir is depleted and its timing does not directly depend on a direct external forcing.

Cycles of aggradation and incision in the north piedmont delay the flux of coarse material en route to the basin by 6 to to 15 kyrs. The temporary deposition of the coarse sediment load separates it from the finer load that is directly delivered to the basin. As a consequence, a depositional hiatus between the fine and coarse fractions of the same sediment pulse is expected where both facies overlap. In the Kuitun River, incision in the piedmont remobilises a mixture of sediments from the Middle Pleistocene to today and injects it in the modern sediment routing system.

Acknowledgment

The authors thank Sébastien Castelltort for his sedimentary insights. Stimulating discussions with Laure Guérit were most useful to design our work. Jess Adkins provided precious advice regarding the climatic considerations. We thank Stéphane Dominguez for his help collecting the sample TS12-ANJ-T1B. This study was supported by a PRF New Direction grant of the American Chemical Society (grant number: PRF #53814-ND8) and a Doc.Mobility fellowship of the Swiss National Foundation (project number: P1SKP2_158716) for L. C. Malatesta. This study received funding from the European Union's Horizon 2020 Research and Innovation program under the Marie Sklodowska-Curie grant agreement No 691037 to S.F.M. Breitenbach.

References

Aitken, M J (1998). *An introduction to optical dating : the dating of Quaternary sediments by the use of photon-stimulated luminescence*. Oxford University Press.

Allen, Philip A (1997). *Earth Surface Processes*. Wiley-Blackwell.

– (2008). "Time scales of tectonic landscapes and their sediment routing systems". In: *Geological Society, London, Special Publications* 296.1, pp. 7–28.

Allen, Philip A, John J Armitage, et al. (2013). "The Qs problem: Sediment volumetric balance of proximal foreland basin systems - Allen - 2013 - Sedimentology - Wiley Online Library". In: *Sedimentology* 60, pp. 102–130.

Allen, Philip A and Alexander L Densmore (2000). "Sediment flux from an uplifting fault block". In: *Basin Research* 12.3-4, pp. 367–380.

An, Zhisheng et al. (2012). "Interplay between the Westerlies and Asian monsoon recorded in Lake Qinghai sediments since 32 ka". In: *Scientific Reports* 2, pp. 1–7.

Armitage, John J, Peter A Burgess, et al. (2016). "Deciphering the origin of cyclical gravel front and shoreline progradation and retrogradation in the stratigraphic record". In: *Basin Research*, pp. 1–21.

Armitage, John J, Tom Dunkley Jones, et al. (2013). "Temporal buffering of climate-driven sediment flux cycles by transient catchment response". In: *Earth and Planetary Science Letters* 369, pp. 200–210.

Arnold, L J and R G Roberts (2009). "Stochastic modelling of multi-grain equivalent dose (D_e) distributions: Implications for OSL dating of sediment mixtures". In: *Quaternary Geochronology* 4.3, pp. 204–230.

Avouac, Jean-Philippe and P Tapponnier (1993). "Kinematic model of active deformation in Central-Asia". In: *Geophysical Research Letters* 20.10, pp. 895–898.

Avouac, Jean-Philippe, P Tapponnier, et al. (1993). "Active Thrusting and Folding Along the Northern Tien Shan and Late Cenozoic Rotation of the Tarim Relative to Dzungaria and Kazakhstan". In: *Journal Of Geophysical Research* 98.B4, pp. 6755–6804.

Bakke, Jostein et al. (2009). "Rapid oceanic and atmospheric changes during the Younger Dryas cold period". In: *Nature Geoscience* 2.3, pp. 1–4.

Bar-Matthews, Miryam, Avner Ayalon, and Aaron Kaufman (1997). "Late Quaternary Paleoclimate in the Eastern Mediterranean Region from Stable Isotope Analysis of Speleothems at Soreq Cave, Israel". In: *Quaternary Research* 47.2, pp. 155–168.

Berger, André L (1978). "Long-term variations of caloric insolation resulting from the earth's orbital elements". In: *Quaternary Research* 9.2, pp. 139–167.

Braucher, R, P Del Castillo, et al. (2009). "Determination of both exposure time and denudation rate from an in situ-produced 10Be depth profile: A mathematical proof of uniqueness. Model sensitivity and applications to natural cases". In: *Quaternary Geochronology* 4.1, pp. 56–67.

Braucher, R, S Merchel, et al. (2011). "Production of cosmogenic radionuclides at great depth: A multi element approach". In: *Earth and Planetary Science Letters* 309.1–2, pp. 1–9.

Brauer, Achim et al. (2008). "An abrupt wind shift in western Europe at the onset of the Younger Dryas cold period". In: *Nature Geoscience* 1.8, pp. 520–523.

Brown, Nathan D et al. (2015). "Single-grain post-IR IRSL signals of K-feldspars from alluvial fan deposits in Baja California Sur, Mexico". In: *Quaternary International* 362, pp. 132–138.

Brozovic, Nicholas, Douglas West Burbank, and A J Meigs (1997). "Climatic limits on landscape development in the northwestern Himalaya". In: *Science* 276.5312, pp. 571–574.

Bull, W B (1977). "The alluvial-fan environment". In: *Progress in Physical Geography* 1.2, pp. 222–270.

– (1991). *Geomorphic responses to climatic change*. New York: Oxford University Press.

Burchfiel, B C et al. (1999). "Crustal shortening on the margins of the Tien Shan, Xinjiang, China". In: *International Geology Review* 41.8, pp. 665–700.

Buylaert, Jan-Pieter et al. (2009). "Testing the potential of an elevated temperature IRSL signal from K-feldspar". In: *Radiation Measurements* 44.5-6, pp. 560–565.

Cai, Yanjun et al. (2017). "Holocene moisture changes in western China, Central Asia, inferred from stalagmites". In: *Quaternary Science Reviews* 158, pp. 15–28.

Castelltort, Sébastien and Jean Van Den Driessche (2003). "How plausible are high-frequency sediment supply-driven cycles in the stratigraphic record?" In: *Sedimentary Geology* 157, pp. 3–13.

Charreau, Julien, Jean-Philippe Avouac, et al. (2008). "Miocene to present kinematics of fault-bend folding across the Huerguosi anticline, northern Tianshan (China), derived from structural, seismic, and magnetostratigraphic data". In: *Geology* 36.11, pp. 871–874.

Charreau, Julien, P H Blard, et al. (2011). "Paleo-erosion rates in Central Asia since 9Ma: A transient increase at the onset of Quaternary glaciations?" In: *Earth and Planetary Science Letters* 304.1-2, pp. 1–8.

Charreau, Julien, Yan Chen, Stuart Gilder, Laurie Barrier, et al. (2009). "Neogene uplift of the Tian Shan Mountains observed in the magnetic record of the Jingou River section (northwest China)". In: *Tectonics* 28.TC2008, pp. 1–22.

Charreau, Julien, Yan Chen, Stuart Gilder, Stephane Dominguez, et al. (2005). "Magnetostratigraphy and rock magnetism of the Neogene Kuitun He section (northwest China): implications for Late Cenozoic uplift of the Tianshan mountains". In: *Earth and Planetary Science Letters* 230.1-2, pp. 177–192.

Chen, Fa-Hu et al. (2010). "Moisture changes over the last millennium in arid central Asia: a review, synthesis and comparison with monsoon region". In: *Quaternary Science Reviews* 29.7-8, pp. 1055–1068.

Cheng, Hai, R. Lawrence Edwards, et al. (2016). "The Asian monsoon over the past 640,000 years and ice age terminations". In: *Nature* 534.7609, pp. 640–646.

Cheng, Hai, Christoph Spötl, et al. (2016). "Climate variations of Central Asia on orbital to millennial timescales". In: *Scientific Reports*, pp. 1–11.

Cheng, H. et al. (2012). "The climatic cyclicity in semiarid-arid central Asia over the past 500,000 years". In: *Geophysical Research Letters* 39.L01705, pp. 1–5.

Clift, P D and L Giosan (2014). "Sediment fluxes and buffering in the post-glacial Indus Basin". In: *Basin Research* 26.3, pp. 369–386.

D'Arcy, Mitch and Alexander C Whittaker (2014). "Geomorphic constraints on landscape sensitivity to climate in tectonically active areas". In: *Geomorphology* 204, pp. 366–381.

D'Arcy, Mitch, Alexander C Whittaker, and Duna C Roda Boluda (2016). "Measuring alluvial fan sensitivity to past climate changes using a self-similarity approach to grain size fining, Death Valley, California". In: *Sedimentology*, n/a–n/a.

Dengfa, H et al. (2005). *Guide book for the field trip in south and north Tianshan foreland basin, Xinjiang Uygur Autonomous Region, China*. International Conference on Theory and Application of Fault-Related Folding in Foreland Basins. Research Institute of Petroleum Exploration and Development, PetroChina.

Dumitru, T A et al. (2001). "Uplift, exhumation, and deformation in the Chinese Tian Shan". In: *Geological Society of America Memoir: Paleozoic and Mesozoic tectonic evolution of central Asia: From continental assembly to intercontinental deformation* 194, pp. 71–99.

Dunai, Tibor J (2010). *Cosmogenic Nuclides*. principles, concepts and applications in the earth surface sciences. Cambridge University Press.

Fan, Anchuan, Sheng-Hua Li, and Yue-Gau Chen (2012). "Late pleistocene evolution of Lake Manas in western China with constraints of OSL ages of lacustrine sediments". In: *Quaternary Geochronology* 10.C, pp. 143–149.

Fu, B H et al. (2003). "Quaternary folding of the eastern Tian Shan, northwest China". In: *Tectonophysics* 369.1-2, pp. 79–101.

Fu, Xiao et al. (2017). "A fluvial terrace record of late Quaternary folding rate of the Anjihai anticline in the northern piedmont of Tian Shan, China". In: *Geomorphology* 278, pp. 91–104.

Fuchs, M and A Lang (2001). "OSL dating of coarse-grain fluvial quartz using single-aliquot protocols on sediments from NE Peloponnese, Greece". In: *Quaternary Science Reviews* 20.5-9, pp. 783–787.

Galbraith, R F et al. (1999). "Optical dating of single and multiple grains of quartz from Jinmium rock shelter, northern Australia: Part I, experimental design and statistical models". In: *Archaeometry* 41.2, pp. 339–364.

Gasse, F et al. (1991). "A 13,000-year climate record from western Tibet". In: *Nature* 353.6346, pp. 742–745.

Gilbert, Grove Karl and Edward Charles Murphy (1914). "The Transportation of Debris by Running Water". In: *U. S. Geological Survey Professional Paper* 86, pp. 1–263.

Gong, Zhijun, Sheng-Hua Li, and Bo Li (2014). "The evolution of a terrace sequence along the Manas River in the northern foreland basin of Tian Shan, China, as inferred from optical dating ". In: *Geomorphology* 213.C, pp. 201–212.

– (2015). "Late Quaternary faulting on the Manas and Hutubi reverse faults in the northern foreland basin of Tian Shan, China". In: *Earth and Planetary Science Letters* 424.C, pp. 212–225.

Gosse, John C and FM Phillips (2001). "Terrestrial in situ cosmogenic nuclides: theory and application". In: *Quaternary Science Reviews* 20.14, pp. 1475–1560.

Guan, Shuwei et al. (2016). "Structural inversion, imbricate wedging, and out-of-sequence thrusting in the southern Junggar fold-and-thrust belt, northern Tian Shan, China". In: *AAPG Bulletin*.

Guerit, Laure et al. (2016). "Denudation intensity and control in the Chinese Tian Shan: new constraints from mass balance on catchment-alluvial fan systems". In: *Earth Surface Processes and Landforms* 41.8, pp. 1088–1106.

Guralnik, Benny et al. (2011). "Constraining the evolution of river terraces with integrated OSL and cosmogenic nuclide data". In: *Quaternary Geochronology* 6.1, pp. 22–32.

Hendrix, M S, TA Dumitru, and Stephan A Graham (1994). "Late Oligocene-early Miocene unroofing in the Chinese Tian-Shan: An early effect of the India-Asia collision". In: *Geology* 22.6, pp. 487–490.

Hendrix, M S, Stephan A Graham, et al. (1992). "Sedimentary Record and Climatic Implications of Recurrent Deformation in the Tian-Shan - Evidence From Mesozoic Strata of the North Tarim, South Junggar, and Turpan Basins, Northwest China". In: *Geological Society of America Bulletin* 104.1, pp. 53–79.

Herman, Frederic et al. (2013). "Worldwide acceleration of mountain erosion under a cooling climate". In: *Nature* 504.7480, pp. 423–426.

Hidy, Alan J et al. (2010). "A geologically constrained Monte Carlo approach to modeling exposure ages from profiles of cosmogenic nuclides: An example from Lees Ferry, Arizona". In: *Geochemistry Geophysics Geosystems* 11.

Hooke, Roger LeB (1968). "Steady-state relationships on arid-region alluvial fans in closed basins". In: *American Journal Of Science* 266.8, pp. 609–629.

Huntley, D J, D I Godfrey-Smith, and M L W Thewalt (1985). "Optical Dating of Sediments". In: *Nature* 313.5998, pp. 105–107.

Jelinowska, A et al. (1995). "Mineral Magnetic Record of Environment in Late Pleistocene and Holocene Sediments, Lake Manas, Xinjiang, China". In: *Geophysical Research Letters* 22.8, pp. 953–956.

Jerolmack, Douglas J and Chris Paola (2010). "Shredding of environmental signals by sediment transport". In: *Geophysical Research Letters* 37.19, pp. 1–5.

Jolivet, Marc, Laurie Barrier, et al. (2014). "Unbalanced sediment budgets in the catchment–alluvial fan system of the Kuitun River (northern Tian Shan, China): implications for mass-balance estimates, denudation and sedimentation rates in orogenic systems". In: *Geomorphology* 214, pp. 168–182.

Jolivet, Marc, Stephane Dominguez, et al. (2010). "Mesozoic and Cenozoic tectonic history of the central Chinese Tian Shan: Reactivated tectonic structures and active deformation". In: *Tectonics* 29.6, n/a–n/a.

Jolivet, Marc, G Heilbronn, et al. (2013). "Reconstructing the Late Palaeozoic — Mesozoic topographic evolution of the Chinese Tian Shan: available data and remaining uncertainties". In: *Advances in Geosciences* 37, pp. 7–18.

Kathayat, Gayatri et al. (2016). "Indian monsoon variability on millennial-orbital timescales". In: *Scientific Reports* 6, pp. 24374–8.

Lal, Devendra (1991). "Cosmic-Ray Labeling of Erosion Surfaces - Insitu Nuclide Production-Rates and Erosion Models". In: *Earth and Planetary Science Letters* 104, pp. 424–439.

Leopold, L B and W B Bull (1979). "Base Level, Aggradation, and Grade". In: *Proceedings of the American Philosophical Society*, pp. 168–202.

Li, ChuanXin, ZhaoJie Guo, and Guillaume Dupont-Nivet (2010). "Late Cenozoic tectonic deformation across the northern foreland of the Chinese Tian Shan". In: *Journal of Asian Earth Sciences* 42.5, pp. 1–8.

Liu, Y et al. (2011). "Erosion rates deduced from seasonal mass balance along the upper Urumqi River in Tianshan". In: *Solid Earth* 2.2, pp. 283–301.

Lu, Honghua, Douglas West Burbank, and Youli Li (2010). "Alluvial sequence in the north piedmont of the Chinese Tian Shan over the past 550 kyr and its relationship to climate change". In: *Palaeogeography Palaeoclimatology Palaeoecology* 285.3-4, pp. 343–353.

Lu, Honghua, Douglas West Burbank, Youli Li, and Yunming Liu (2010). "Late Cenozoic structural and stratigraphic evolution of the northern Chinese Tian Shan foreland". In: *Basin Research* 22.3, pp. 249–269.

Lu, Honghua, Weiguo Zhang, et al. (2013). "Rock magnetic properties and paleoenvironmental implications of an 8-Ma Late Cenozoic terrigenous succession from the northern Tian Shan foreland basin, northwestern China". In: *Global and Planetary Change* 111, pp. 43–56.

Lu, H et al. (2014). "Late Quaternary alluvial sequence and uplift-driven incision of the Urumqi River in the north front of the Tian Shan, northwestern China". In: *Geomorphology* 219, pp. 141–151.

Mackin, J H (1948). "Concept of the Graded River". In: *Geological Society of America Bulletin* 59.5, pp. 463–511.

Malatesta, Luca Claude, Jeffrey P Prancevic, and Jean-Philippe Avouac (2017). "Autogenic entrenchment patterns and terraces due to coupling with lateral erosion in incising alluvial channels". In: *Journal of Geophysical Research: Earth Surface* 122.1, pp. 335–355. DOI: 10.1002/2015JF003797.

Métivier, Francois (2002). "On the use of sedimentation rates in deciphering global change". In: *Geophysical Research Letters* 29.15.

Métivier, Francois and Yves Gaudemer (1997). "Mass transfer between eastern Tien Shan and adjacent basins (central Asia): Constraints on regional tectonics and topography". In: *Geophysical Journal International* 128.1, pp. 1–17.

Molnar, Peter, Erik Thorson Brown, et al. (1994). "Quaternary climate-change and the formation of river terraces across growing anticlines on the north flank of the Tien-Shan, China". In: *Journal of Geology* 102.5, pp. 583–602.

Molnar, Peter and Philip C England (1990). "Late Cenozoic Uplift of Mountain-Ranges and Global Climate Change - Chicken or Egg". In: *Nature* 346.6279, pp. 29–34.

Nagashima, Kana et al. (2011). "Millennial-scale oscillations of the westerly jet path during the last glacial period". In: *Journal of Asian Earth Sciences* 40.6, pp. 1214–1220.

Neudorf, C M, R G Roberts, and Z Jacobs (2012). "Sources of overdispersion in a K-rich feldpar sample from north-central India: Insights from D_e, K content and IRSL age distributions for individual grains". In: *Radiation Measurements* 47.9, pp. 696–702.

Nian, Xiaomei, Richard M Bailey, and Liping Zhou (2012). "Investigations of the post-IR IRSL protocol applied to single K-feldspar grains from fluvial sediment samples". In: *Radiation Measurements* 47, pp. 703–709.

Nicholas, Andrew P. and T A Quine (2007). "Modeling alluvial landform change in the absence of external environmental forcing". In: *Geology* 35.6, pp. 527–530.

Oerlemans, J and J. P. F. Fortuin (1992). "Sensitivity of Glaciers and Small Ice Caps to Greenhouse Warming". In: *Science* 258.5079, pp. 115–117.

Paola, Chris, Paul L Heller, and Charles L Angevine (1992). "The large-scale dynamics of grain-size variation in alluvial basins, 1: Theory". In: *Basin Research* 4.2, pp. 73–90.

Parker, Gary, Chris Paola, Kelin X. Whipple, and David Mohrig (1998). "Alluvial Fans Formed by Channelized Fluvial and Sheet Flow. I: Theory". In: *Journal of Hydraulic Engineering* 124.10, p. 985.

Parker, Gary, Chris Paola, Kelin X. Whipple, David Mohrig, et al. (1998). "Alluvial Fans Formed by Channelized Fluvial and Sheet Flow. II: Application". In: *Journal of Hydraulic Engineering* 124.10, p. 996.

Pepin, E., S Carretier, and G. Herail (2010). "Erosion dynamics modelling in a coupled catchment-fan system with constant external forcing". In: *Geomorphology* 122, pp. 78–90.

Poisson, Blanche (2002). "Impact du climat et de la tectonique sur l'évolution géomorphologique d'un piémont: exemple du piémont Nord du Tian Shan depuis la fin du Pléistocène ". PhD thesis. Université Paris XI.

Poisson, Blanche and Jean-Philippe Avouac (2004). "Holocene hydrological changes inferred from alluvial stream entrenchment in North Tian Shan (Northwestern China)". In: *Journal of Geology* 112.2, pp. 231–249.

Puchol, Nicolas et al. (2016). "Limited impact of Quaternary glaciations on denudation rates in Central Asia". In: *Geological Society of America Bulletin*, B31475.1–21.

Puigdefàbregas, Cayo and P Souquet (1986). "Tecto-sedimentary cycles and depositional sequences of the Mesozoic and Tertiary from the Pyrenees". In: *Tectonophysics* 129.1-4, pp. 173–203.

Reimann, Tony et al. (2012). "Single-grain dating of young sediments using the pIRIR signal from feldspar". In: *Quaternary Geochronology* 11, pp. 28–41.

Rhodes, Edward J (2011). "Optically Stimulated Luminescence Dating of Sediments over the Past 200,000 Years". In: *Annual Review Of Earth And Planetary Sciences* 39.1, pp. 461–488.

– (2015). "Dating sediments using potassium feldspar single-grain IRSL: initial methodological considerations". In: *Quaternary International* 362, pp. 14–22.

Rhodes, Thomas E et al. (1996). "A Late Pleistocene-Holocene lacustrine record from Lake Manas, Zunggar (northern Xinjiang, western China)". In: *Palaeogeography Palaeoclimatology Palaeoecology* 120.1-2, pp. 105–121.

Rohais, Sebastien, Stephane Bonnet, and Remi Eschard (2012). "Sedimentary record of tectonic and climatic erosional perturbations in an experimental coupled catchment-fan system". In: *Basin Research* 24.2, pp. 198–212.

Romans, B W et al. (2015). "Environmental signal propagation in sedimentary systems across timescales". In: *Earth-Science Reviews* 153, pp. 7–29.

Saint-Carlier, Dimitri (2015). "Evolution tectonique du Tianshan oriental du Néogène à l'actuel". PhD thesis. Nancy: Université de Lorraine.

Saint-Carlier, Dimitri et al. (2016). "Major temporal variations in shortening rate absorbed along a large active fold of the southeastern Tianshan piedmont (China)". In: *Earth and Planetary Science Letters* 434, pp. 333–348.

Schneider, Tapio, Tobias Bischoff, and Gerald H Haug (2014). "Migrations and dynamics of the intertropical convergence zone". In: *Nature* 513.7516, pp. 45–53.

Schumm, Stanley Alfred (1973). "Geomorphic thresholds and complex response of drainage systems". In: *Fluvial Geomorphology*. Ed. by M Morisawa. Fluvial geomorphology, pp. 299–310.

Simpson, Guy and Sébastien Castelltort (2012). "Model shows that rivers transmit high-frequency climate cycles to the sedimentary record". In: *Geology* 40, pp. 1–4.

Smedley, R K et al. (2012). "Determining the K-content of single-grains of feldspar for luminescence dating". In: *Radiation Measurements* 47.9, pp. 790–796.

Smith, GH Sambrook and R I Ferguson (1996). "The gravel-sand transition: flume study of channel response to reduced slope". In: *Geomorphology* 16, pp. 147–159.

Sobel, E R and T A Dumitru (1997). "Thrusting and exhumation around the margins of the western Tarim basin during the India-Asia collision". In: *Journal Of Geophysical Research* 102.B3, pp. 5043–5063.

Sorg, Annina et al. (2012). "Climate change impacts on glaciers and runoff in Tien Shan (Central Asia)". In: *Nature Climate Change* 2.10, pp. 725–731.

Stockmeyer, J M, J H Shaw, and S Guan (2014). "Seismic Hazards of Multi-segment Thrust-Fault Ruptures: Insights from the 1906 Mw 7.4-8.2 Manas, China, Earthquake". In: *Seismological Research Letters* 85.4, pp. 801–808.

Tapponnier, P and Peter Molnar (1979). "Active faulting and Cenozoic tectonics of the Tien Shan, Mongolia and Baykal regions". In: *Journal Of Geophysical Research* 84.NB7, pp. 3425–3459.

Thiel, Christine et al. (2011). "Luminescence dating of the Stratzing loess profile (Austria) - Testing the potential of an elevated temperature post-IR IRSL protocol". In: *Quaternary International* 234.1-2, pp. 23–31.

Thompson, S C et al. (2002). "Late Quaternary slip rates across the central Tien Shan, Kyrgyzstan, central Asia". In: *Journal Of Geophysical Research* 107.10.1029.

Trauerstein, Mareike et al. (2014). "Small aliquot and single grain IRSL and post-IR IRSL dating of fluvial and alluvial sediments from the Pativilca valley, Peru". In: *Quaternary Geochronology* 22, pp. 163–174.

Tucker, G E and R Slingerland (1997). "Drainage basin responses to climate change". In: *Water Resources Research* 33.8, pp. 2031–2047.

Turowski, Jens M., Dieter Rickenmann, and Simon J Dadson (2010). "The partitioning of the total sediment load of a river into suspended load and bedload: a review of empirical data". In: *Sedimentology* 57.4, pp. 1126–1146.

Vaks, A et al. (2013). "Speleothems Reveal 500,000-Year History of Siberian Permafrost". In: *Science* 340.6129, pp. 183–186.

Vandenberghe, Jef et al. (2006). "Penetration of Atlantic westerly winds into Central and East Asia". In: *Quaternary Science Reviews* 25, pp. 2380–2389.

Wang, Chun-Yong et al. (2004). "Crustal structure of the northern margin of the eastern Tien Shan, China, and its tectonic implications for the 1906 M 7.7 Manas earthquake". In: *Earth and Planetary Science Letters* 223.1-2, pp. 187–202.

Wang, Y J et al. (2001). "A High-Resolution Absolute-Dated Late Pleistocene Monsoon Record from Hulu Cave, China". In: *Science* 294.5550, pp. 2345–2348.

Wang, Yongjin et al. (2008). "Millennial- and orbital-scale changes in the East Asian monsoon over the past 224,000 years". In: *Nature* 451.7182, pp. 1090–1093.

Windley, B F et al. (1990). "Paleozoic accretion and Cenozoic redeformation of the Chinese Tien Shan Range, central Asia". In: *Geology* 18.2, pp. 128–131.

Wolff, Christian et al. (2016). "Precipitation evolution of Central Asia during the last 5000 years". In: *The Holocene* 27.1, pp. 142–154.

Yang, Xiao-Ping, An Li, and WeiLiang Hunag (2013). "Uplift differential of active fold zones during the late Quaternary, northern piedmonts of the Tianshan Mountains, China". In: *Science China Earth Sciences* 56.794, pp. 1–12.

Yu, G, S P Harrison, and B Xue (2001). *Lake status records from China: Data Base Documentation*. Tech. rep. 4. Jena, Germany: Max Planck Institute für Biogeochemie.

Zhang, P. Z., Peter Molnar, and W R Downs (2001). "Increased sedimentation rates and grain sizes 2-4 Myr ago due to the influence of climate change on erosion rates". In: *Nature* 410.6831, pp. 891–897.

Chapter 5

CONTRASTED RIVER INCISION IN NORTH AND SOUTH TIAN SHAN PIEDMONTS DUE TO DIFFERENT GLACIAL OVERPRINT OF HIGH RANGE TOPOGRAPHY

with Jean-Philippe Avouac[1]

in review at Geology

5.1 Abstract

Incision of rivers and the terraces they abandon are widely used to investigate external forcing by climate and tectonics. In the Eastern Tian Shan, rivers in the north and south piedmonts are respectively deeply incised (mean: 124 m) or barely, if at all (mean: 17 m), incised despite virtually identical tectonic and climatic conditions. We attribute the contrast in incision to a difference in maximum glacial extent in the catchments. Whereas the upper halves of the valleys in the northern range are formerly glaciated, wide, U-shaped valleys, the southern catchments are dominated by fluvial erosion. The glaciated valleys act as capacitors that accumulate and release glacial sediment onto the piedmont where the resulting change in sediment flux, Q_s, forces important aggradation and incision of the piedmont. The fluvial valleys do not accumulate sediment and changes in water discharge Q_w primarily control the slope of the river crossing the piedmont. Today, incision in the north follows a drop in Q_s after the upstream reservoir was depleted while aggradation in the south is due to aridity and low Q_w. The same climatic forcing can have strikingly different morphological expressions depending on the characteristics of sediment transfer upstream.

5.2 Introduction

In Central Asia, the morphologic contrast between the north and south alluvial piedmonts of the Eastern Tian Shan (Xinjiang, China, Figure 5.1), is both striking and puzzling. Under the same climate and the same tectonic regime,

[1]Division of Geological and Planetary Sciences, California Institute of Technology, Pasadena, CA 91125, USA

the northern rivers are deeply entrenched by up to 300 m in the piedmont (Figure 5.2 A), while the southern rivers are shallowly entrenched, if at all (Figure 5.2 B and C). No explanation reconciling their stark differences has yet been proposed.

Paleoclimatic studies indicate that the two piedmonts share a very similar climate history. They both lie within a climatic domain dominated by the Westerlies, where colder temperatures are accompanied by aridity and warmer conditions associated with a modest increase in moisture (Yu, Harrison, and Xue, 2001; Jelinowska et al., 1995; Rhodes et al., 1996; Qin, Shi, and Ge Yu, 1998; Cheng et al., 2016). In Central Asia, the period from the deglaciation to the early Holocene is characterized by much wetter conditions than today (Rhodes et al., 1996; Yu, Harrison, and Xue, 2001) and in northwest China, aridification has steadily increased since 7 ka (Qin, Shi, and Ge Yu, 1998; Yu, Harrison, and Xue, 2001; Cai et al., 2017). Aridity seems indeed to prevail during minimums of insolation at the precessional cycle, like today or at the Last Glacial Maximum (Cheng et al., 2016). The north piedmont is marked by several cycles of aggradation and incision over the last 150 kyrs that suggest that the sedimentary system responds strongly to climate variability during glacial periods (Chapter 4).

The tectonic structures on either flanks of the Eastern Tian Shan present a near mirror image, with two E-W striking fold-and-thrust belts that accommodate most of the total shortening across the Tian Shan with ca. 4.5 mm/yr each (Avouac et al., 1993; Yin et al., 1998; Burchfiel et al., 1999; Heermance et al., 2007; Yang, J. Li, and Wang, 2008).

While climate and tectonic conditions are virtually identical in the north and south of the Eastern Tian Shan, glacial extent differs. The Tian Shan glaciations are moderate and alpine glaciers are restricted to the mountain areas (Koppes et al., 2008; Zech, 2012; Stroeven et al., 2013; Lifton et al., 2014). In the Eastern Tian Shan, the maximum glacial footprint decreases dramatically east of 81ï£¡E as the elevation of the highest peaks drops from 7000 masl to 4000 masl (Figure 5.1, Stroeven et al., 2013). In the Borohoro Shan, the northern subrange with 5000 masl peaks (Figure 5.1), glaciers occupied the upper

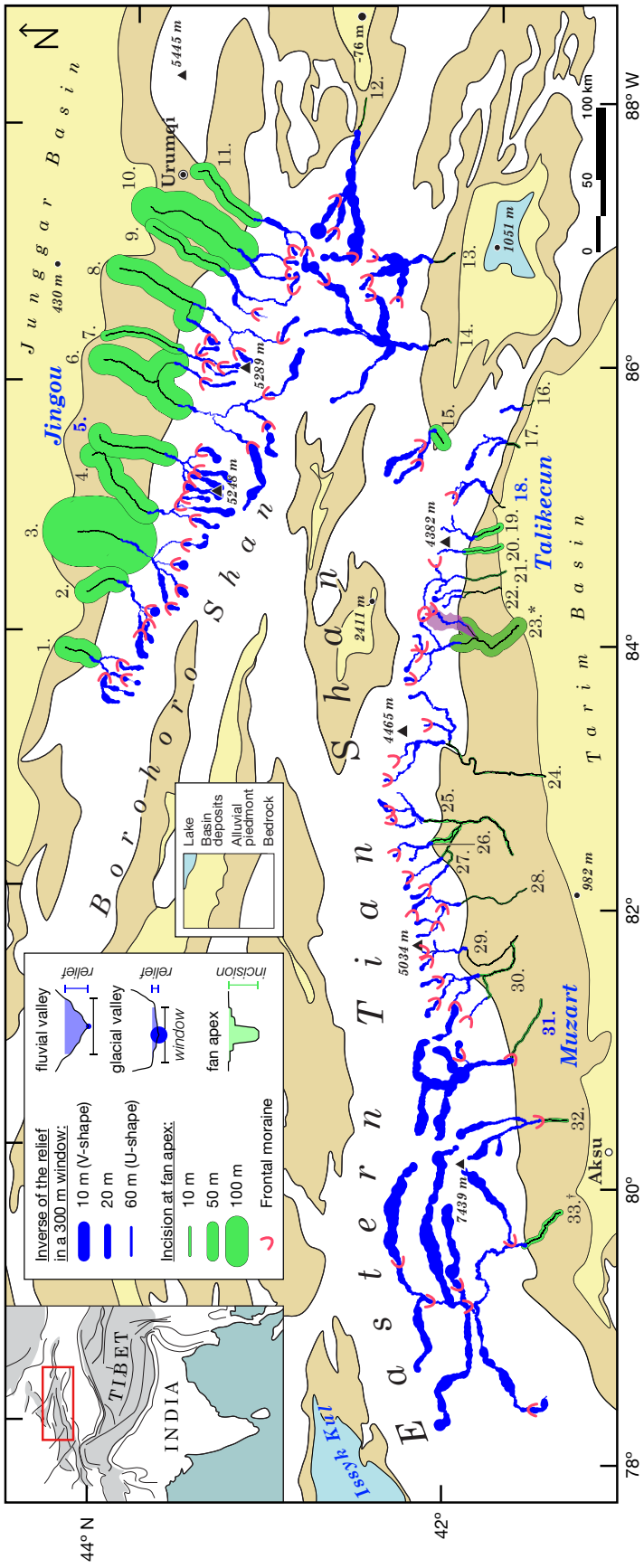

Figure 5.1: Map of the Eastern Tian. The depth of river incision at the apex of the Quaternary fan is marked by the width of the green outline. The width of the dark blue track scales inversely with the relief in a 300 m radius window along the mountain valleys so that wide tracks mark wide valleys (U-shaped). The pink shading in catchment 23 is a recently captured branch. See supplementary material for river names.

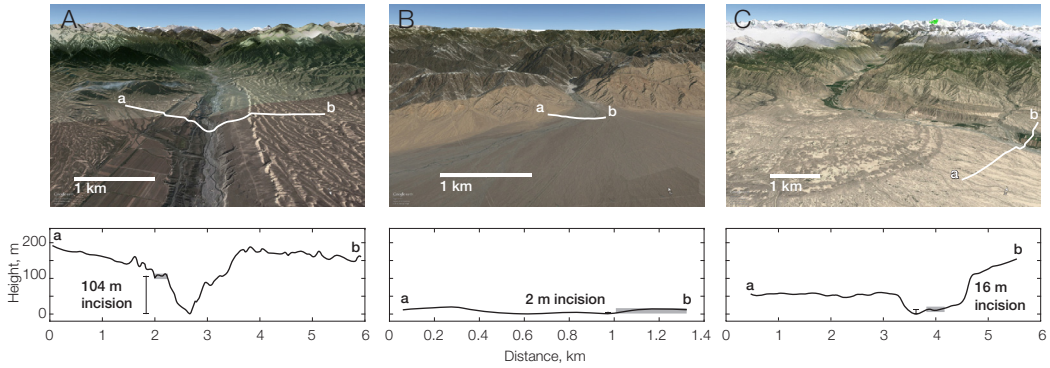

Figure 5.2: Outlets of three representative rivers in the Eastern Tian Shan from Google Earth and cross sections near the fan apex from ASTER GDEM V2 data. Incision is measured with respect to the youngest fill terrace. A: outlet of the Jingou River looking south. B: outlet of the entirely fluvial Talikecun Valley. C: outlet of the Muzart River looking north. Note the concentric frontal moraines on the fan in the foreground.

half of the mountain valleys were much larger than at the same longitude in the south (Stroeven et al., 2013; Yingkui Li et al., 2014; Lifton et al., 2014).

The northern piedmont records climatic changes and primarily reacts to changes in sediment flux from the high range: aggrading when glacial sediments are flushed out of the mountain, and incising after their evacuation when clear water enters the piedmont (Avouac et al., 1993; Molnar et al., 1994; Poisson and Avouac, 2004, Chapter 4). We argue here that the north-south contrast of river entrenchment in the piedmont is due to differences in the maximum glacial extent (e.g. confined to cirques or absent, occupying the upper valley, or going past the mountain front). Alpine glaciers carve wide, shallow U-shaped valleys and their extent sets how much, if any, loose sediment can be stored in the high range and how fast it can be evacuated. If glacial extent is not uniform across the range, the piedmont of the same mountain can be subject to variable and diachronous changes in sediment fluxes causing rivers to incise to different depths and to vary out of sync.

5.3 Piedmont and catchment morphology

We compare incision of 33 piedmont rivers in the Eastern Tian Shan (11 in the north, 22 in the south) to the glacial overprint of their upper reach. Depth

of incision was measured at the apex of the Quaternary alluvial fans. Figure 5.3 shows these measurements with the rivers ordered clockwise from north to southwest (depths are listed in Table 5.1). The northern rivers are entrenched by an average of 124 m and the southern rivers by 17 m only. The north piedmont rivers started to incise diachronously after evacuation of the upstream sediment between 13 and 5 ka (Poisson and Avouac, 2004; Lu, Burbank, and Youli Li, 2010; Gong, S.-H. Li, and B. Li, 2014, Chapter 4). The south piedmont is generally fully aggraded and the rivers distribute sediment on active fans immediately downstream of the range front and bevel active anticlines (Heermance et al., 2007; Bufe, Paola, and Burbank, 2016).

All the northern catchments were glaciated but these glaciers stayed in the upper half of the catchments and carved wide U-shaped valleys there (Figure 5.1). The profile of the Jingou River is representative of the semi-glaciated catchments: the upper reach is a broad and shallow alluvial valley with a braided river; and downstream of a break-in-slope, the lower valley is steeper, concave, with a bedrock gorge (Figure 5.4 A). The frontal moraine indicates that, at its maximum extent, the glacier overspilled from the carved upper valley.

The southern catchments are mostly fluvial, often with small cirque glaciers that never extended far downstream (red bows in Figure 5.1). Their profiles look similar to that of the Talikecun River (Figure 5.4 B): the bedrock river has an uninterrupted profile and is slightly concave up before flowing on the aggraded alluvial piedmont (Figure 5.2 B).

The three catchments in the southwestern quadrant of Figure 5.1 drain the highest peaks of the Tian Shan ($>$ 7000 masl) and were extensively glaciated. For two of them, the Muzart and the Tailan (no. 31 and 32), large frontal moraines have been abandoned on the alluvial piedmont (Figure 5.2 C). The alluvial bed of the glacial valley extends uninterrupted upstream from the fan (Figure 5.4 C, top plot). The Kaylan catchment (no. 33) is much larger than any other. It is constituted of several wide glacial valleys parallel to the E-W strike of the range and separated by a narrow gorge from the alluvial piedmont (Figure 5.1).

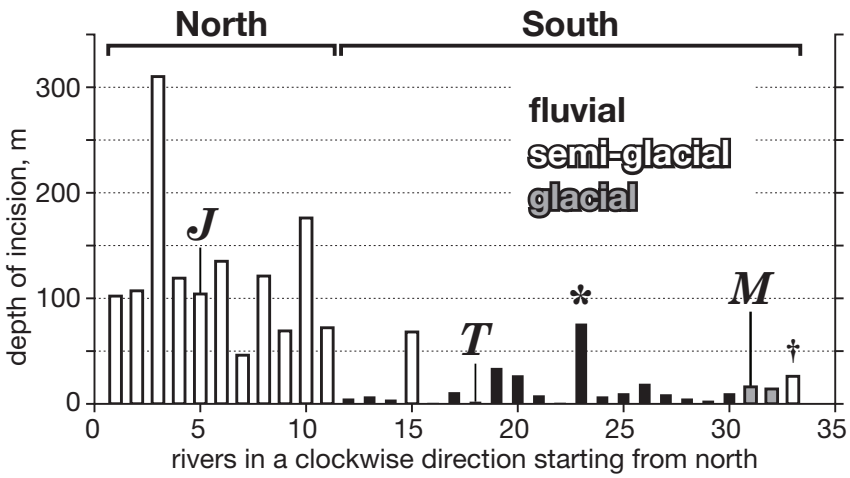

Figure 5.3: Incision at the apex of the Quaternary alluvial fan of the studied rivers (see supplementary material for values). The rivers are arranged in sequential clockwise order starting from the north to the southwest. Rivers are grouped into: 1) fluvially dominated catchments (black); 2) semi-glacial catchments with U-shaped upper valleys, and V-shaped lower valleys (white with black outline); 3) fully glacial catchments with U-shaped valleys reaching the piedmont (gray with black outline). The asterisk marks catchment 23 where a capture recently occurred (see pink shading in Figure 5.1). The dagger marks catchment 33 that is presumably still evacuating glacial sediments and has not started to incise yet. Labels J, T and M point to the Jingou, Talikecun and Muzart rivers respectively.

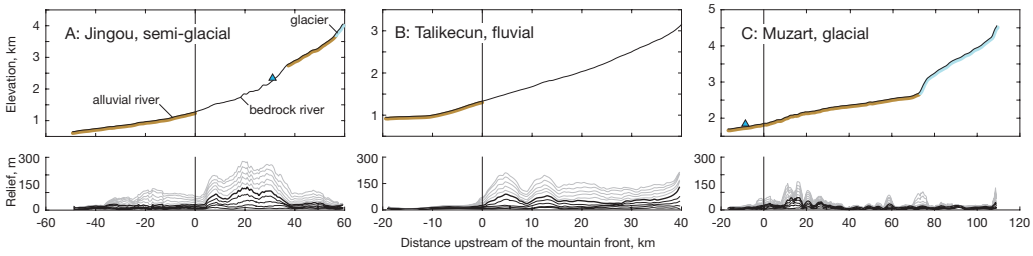

Figure 5.4: Evolution of relief along stream in three representative rivers of the Eastern Tian Shan. Top: longitudinal profile of the river with alluvial reaches highlighted in dark gray, bedrock with hatching, glaciers in light gray. Km 0 indicates the fan apex. Triangles mark frontal moraines. Bottom: relief along stream in windows of radii 60 to 600 m in 60 m increments. A: the upper half of the catchment of the Jingou bears the mark of important glacial. High relief in windows <300 m indicate V-shaped valleys, and low relief mark U-shaped ones. B: the fluvial Talikecun Valley has a relatively high and uniform relief along stream. C: the Muzart Valley was entirely glaciated with a wide low-relief cross-section throughout.

5.4 Glacial overprint and classification of the catchments

The degree of incision of the 33 rivers falls neatly in two categories along the extent of their glaciation: semi-glaciated, and either fluvial or fully glaciated respectively (Figure 5.3). Incision of the piedmont coincides with catchments where the upper valley has a wide alluviated floor carved by glaciers and the lower valley is a narrow gorge. To precisely relate piedmont incision to the extent of glaciation, we characterize the degree of glacial overprint of a valley by measuring local relief. This metrics is necessary because frontal moraines do not always constrain the lower limit of the alluviated glacial valley. To capture the fluvial or glacial geometry of the valley, we measure the relief along the valley bottom in windows of 60 to 600 m in 60 m increments. On average, the bottom of the glacial valleys is about 300 to 350 m wide in the Tian Shan and the relief rises past these window sizes. The along stream relief of the three case examples is shown in Figure 5.4. When the valley flanks rise continuously on either side of the river (V-shape), the relief increases progressively with the window size (e.g. middle reach of the Jingou or mountain reach of the Talikecun, Figure 5.4). In a flat bottom valley (U-shape), relief does not significantly increase until the size of the window matches that of the floodplain. Past this point, the sampling window captures the rising valley walls and relief increases (e.g. upper reach of the Jingou River, Figure 4). Note that for the Muzart, the valley floor is ca. 1.1 km wide and the relief remains very low at a 600 m radius (figure 5.4 C). We center the sampling windows in the middle of the valley to avoid immediately capturing the valley walls where the river flows on the edge of a wide floodplain. River incision in the piedmont is measured at the apex of the Quaternary fan using its surface as the upper datum. All topographic measurements are made with ASTER GDEM V2 from METI and NASA. The analysis is automated and the matlab code is available on the CSDMS repository.

To render the relief along the valleys in map view, we plot the 300 m window relief in Figure 5.1 (with a hillshade background in supplementary Figure B.1). The size of the markers is inversely proportional to the relief, so that a wide blue track represents a wide valley. The relief measurement is only plotted for the mountain valleys. The map resulting from the automated process reflects the same distribution of glaciation in the Eastern Tian Shan as the hand drawn map of Stroeven et al. (2013). Differences between the two is explained by

the respective methods: we survey the geometry of the valley while Stroeven et al. (2013) base their interpretation on apparent surface features such as hummocky terrain or glacial lineations. It should be noted that a low relief is not diagnostic of glacial erosion per se, the three eastern catchments 12, 13 and 14, display very low relief in the fluvial domain well below the uppermost moraines (Figure 5.1). The weaker lithology of these catchments can partly explain the low profile (C. Li, Guo, and Dupont-Nivet, 2010). But more importantly, the catchments lie at the eastern edge of the Tian Shan range where the shortening rate, and thereby uplift rate, are smaller and more recent than further west (Yang, J. Li, and Wang, 2008). There are two incised outliers in the compilation: the Kaerta catchment, and the Kaylan catchment. The Kaerta catchment (no. 23, marked with an asterisk in Figure 5.3) is an outlier with 76 m of incision in a fluvially dominated system. However, it appears that the east fork has been recently captured by the main river (42.12°N / 84.08°E, purple highlight in Figure 5.1). The change in water discharge over sediment flux caused by that extension is likely to have caused local incision. In the large Kaylan catchment (no. 33, marked with a dagger in Figure 5.3), the glaciers flowing from the highest peaks of the range did not extend to the piedmont outlet. This configuration places the Kaylan system in the semi-glacial category, yet its piedmont is only incised by 26 m. It is likely that the evacuation of sediment is not complete given the very large volume stored in the huge upper valleys and incision has yet to happen.

5.5 Conceptual model

The rivers that build alluvial fans primarily respond to changes in environmental forcing by adapting their slopes. The equilibrium gradient of an alluvial river scales positively with the ratio of sediment flux (Q_s) over water discharge (Q_w), so that a higher Q_s/Q_w leads to a steeper equilibrium slope (Gilbert and Murphy, 1914; Mackin, 1948).

In a catchment dominated by fluvial processes, climate variability primarily translates to changes in Q_w. So that the Holocene aridification would translate into a transition from incised to aggraded channels (Figure 5.5 A & B).

Catchments that have large glaciated valleys in their upper reach follow the dy-

namics proposed by Poisson and Avouac (2004). Sediments eroded by glaciers during the dry glacial maxima accumulate in the upper reach. The sediments are evacuated later during deglaciation, when moisture picks up and increases the sediment transport capacity of the rivers and thereby the ratio Q_s/Q_w at the outlet of the high range, causing piedmont rivers to aggrade and steepen (Figure 5.5 A & C *1*). Fan incision follows when the reservoir of readily available loose sediment is depleted and Q_s/Q_w drops again (Figure 5.5 A & C *2*).

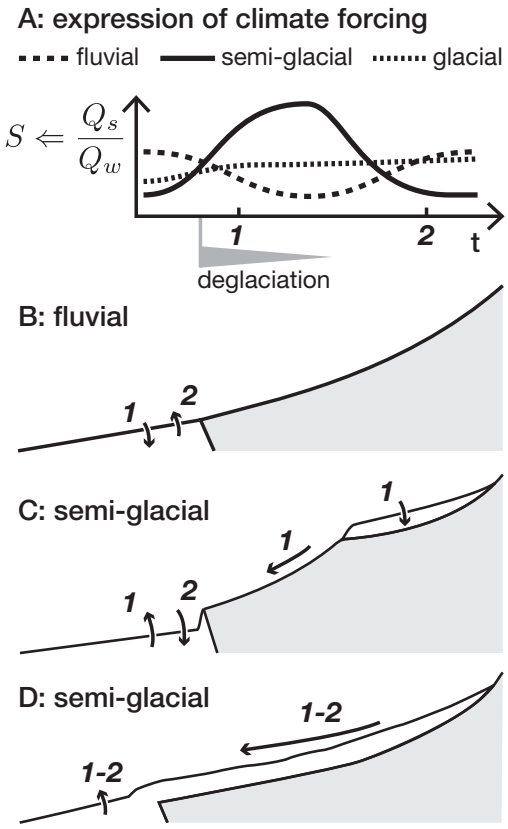

Figure 5.5: Model for the morphological contrast between south and north piedmont of the Eastern Tian Shan since the last glacial maximum. A: ratio of sediment flux over water discharge (Q_s/Q_w) to the piedmont since LGM. B: in a fully fluvial catchment, the fan incises during the wetter Holocene Optimum (*1*) and aggrades during aridification (*2*). C: in a semi-glaciated valley, Q_s/Q_w increases at the onset of deglaciation and sediment from the upper valley is deposited on the piedmont (*1*), and Q_s/Q_w drops after the reservoir is emptied, leading to fan incision (*2*). D: Q_s/Q_w increases with deglaciation and evacuation of glacial sediments (*1*) but the gradient adjusts progressively along the entire reach, offsetting any incision to the upstream end of the system (*2*).

Finally, in the case of a fully glaciated catchment, the mountain valley is entirely lined with alluvium. When the glacier retreats, sediment flux increases slowly at the outlet as sediment starts to be evacuated (Figure 5.5 A & D *1*). But there is no abrupt transition to low sediment flux because the entire valley progressively adapts its longitudinal profile to climatic changes.

5.6 Conclusion

The amount of post Late Glacial Maximum entrenchment in the piedmonts of the Tian Shan is well correlated with the extent of maximum glacial overprint. The observed correlation can be reasonably explained to a first order by changing ratios of Q_s/Q_w whereby glaciated catchments primarily modulate Q_s and fluvial catchments modulate Q_w. Alluvial fans can also incise autogenically, without an external trigger (Nicholas, Clarke, and Quine, 2009; Reitz and Jerolmack, 2012). But there are no suggestions that it happened in the Eastern Tian Shan where neighboring rivers look alike. Autogenic dynamics do however play a role in enhancing vertical incision rates during river entrenchment (Chapter 3).

Sediment transport commonly results in damping of environmental signals by the buffering and delay of sediment pulses (Romans et al., 2015). Here, the contrast between the south and north piedmonts demonstrates that where alluvial reaches are discontinuous, an environmental signal that would otherwise have minor impacts can be amplified by a capacitor. The same climatic forcing can thus result in widely different morphological expressions. Strategies to study past climate can take advantage of non-linear responses and exacerbated signals to measure clearer trends.

Acknowledgment

This study is supported by a PRF New Direction grant of the American Chemical Society (grant number: PRF #53814-ND8) and a Doc.Mobility fellowship of the Swiss National Foundation (project number: P1SKP2_158716) for Malatesta.

References

Avouac, Jean-Philippe et al. (1993). "Active Thrusting and Folding Along the Northern Tien Shan and Late Cenozoic Rotation of the Tarim Relative to

Table 5.1: Names of the rivers numbered in Figure 5.1 and their incision at the apex of the Quaternary fan. For the smaller rivers unnamed on maps, we use the closest locality. The indices next to the river names refer to the geometry of the upper catchment: (a) fluvial; (b) semi-glacial; (c) glacial.

No.	**River**	**Incision, m**	**No.**	**River**	**Incision, m**
	North:		16.	Qunancun (a)	1
1.	Guertu (b)	102	17.	Tiemenguan (a)	11
2.	Sikeshu (b)	107	18.	Talikecun (a)	2
3.	Kuitun (b)	310	19.	Cedaya (a)	34
4.	Anji Hai (b)	119	20.	Keyin Like (a)	27
5.	Jingou (b)	104	21.	Yangxia (a)	8
6.	Manas (b)	135	22.	Tuduan (a)	1
7.	Tashi (b)	46	23.	Kaerta (b)	76
8.	Hutubi (b)	121	24.	Kuche (a)	7
9.	Sautun (b)	69	25.	Yatu (a)	10
10.	Toutun (b)	176	26.	Bozi (a)	19
11.	Urumqi (b)	72	27.	Kuoshi (a)	9
			28.	Kala Su (a)	5
	South:		29.	Tailweiqiuke (a)	3
12.	Toksun (a)	5	30.	Baicheng (a)	10
13.	Hoxud (a)	7	31.	Muzart (c)	16
14.	Hejing (a)	4	32.	Tailan (c)	14
15.	Kaidu (a)	68	33.	Kumerik (b)	26

Dzungaria and Kazakhstan". In: *Journal Of Geophysical Research* 98.B4, pp. 6755–6804.

Bufe, Aaron, Chris Paola, and Douglas West Burbank (2016). "Fluvial bevelling of topography controlled by lateral channel mobility and uplift rate". In: *Nature Geoscience* advance online publication SP - EP -.

Burchfiel, B C et al. (1999). "Crustal shortening on the margins of the Tien Shan, Xinjiang, China". In: *International Geology Review* 41.8, pp. 665–700.

Cai, Yanjun et al. (2017). "Holocene moisture changes in western China, Central Asia, inferred from stalagmites". In: *Quaternary Science Reviews* 158, pp. 15–28.

Cheng, Hai et al. (2016). "Climate variations of Central Asia on orbital to millennial timescales". In: *Scientific Reports*, pp. 1–11.

Gilbert, Grove Karl and Edward Charles Murphy (1914). "The Transportation of Debris by Running Water". In: *U. S. Geological Survey Professional Paper* 86, pp. 1–263.

Gong, Zhijun, Sheng-Hua Li, and Bo Li (2014). "The evolution of a terrace sequence along the Manas River in the northern foreland basin of Tian Shan,

China, as inferred from optical dating ". In: *Geomorphology* 213.C, pp. 201–212.

Heermance, Richard V et al. (2007). "Chronology and tectonic controls of Late Tertiary deposition in the southwestern Tian Shan foreland, NW china". In: *Basin Research* 19.4, pp. 599–632.

Jelinowska, A et al. (1995). "Mineral Magnetic Record of Environment in Late Pleistocene and Holocene Sediments, Lake Manas, Xinjiang, China". In: *Geophysical Research Letters* 22.8, pp. 953–956.

Koppes, Michéle et al. (2008). "Late Quaternary glaciation in the Kyrgyz Tien Shan". In: *Quaternary Science Reviews* 27.7-8, pp. 846–866.

Li, ChuanXin, ZhaoJie Guo, and Guillaume Dupont-Nivet (2010). "Late Cenozoic tectonic deformation across the northern foreland of the Chinese Tian Shan". In: *Journal of Asian Earth Sciences* 42.5, pp. 1–8.

Li, Yingkui et al. (2014). "Timing and extent of Quaternary glaciations in the Tianger Range, eastern Tian Shan, China, investigated using 10Be surface exposure dating". In: *Quaternary Science Reviews* 98.c, pp. 7–23.

Lifton, Nathaniel et al. (2014). "Constraints on the late Quaternary glacial history of the Inylchek and Sary-Dzaz valleys from in situ cosmogenic 10Be and 26Al, eastern Kyrgyz Tian Shan". In: *Quaternary Science Reviews* 101.C, pp. 77–90.

Lu, Honghua, Douglas West Burbank, and Youli Li (2010). "Alluvial sequence in the north piedmont of the Chinese Tian Shan over the past 550 kyr and its relationship to climate change". In: *Palaeogeography Palaeoclimatology Palaeoecology* 285.3-4, pp. 343–353.

Mackin, J H (1948). "Concept of the Graded River". In: *Geological Society of America Bulletin* 59.5, pp. 463–511.

Molnar, Peter et al. (1994). "Quaternary climate-change and the formation of river terraces across growing anticlines on the north flank of the Tien-Shan, China". In: *Journal of Geology* 102.5, pp. 583–602.

Nicholas, Andrew P., Lucy Clarke, and T A Quine (2009). "A numerical modelling and experimental study of flow width dynamics on alluvial fans". In: *Earth Surface Processes and Landforms* 34.15, pp. 1985–1993.

Poisson, Blanche and Jean-Philippe Avouac (2004). "Holocene hydrological changes inferred from alluvial stream entrenchment in North Tian Shan (Northwestern China)". In: *Journal of Geology* 112.2, pp. 231–249.

Qin, Boqiang, Yafeng Shi, and Ge Yu (1998). "The reconstruction and interpretations of lake status at 6 ka and 18 ka B.P. in inland mainland Asia". In: *Chinese Science Bulletin* 43.14, pp. 1145–1157.

Reitz, Meredith D and Douglas J Jerolmack (2012). "Experimental alluvial fan evolution: Channel dynamics, slope controls, and shoreline growth". In: *Journal Of Geophysical Research* 117.F2, F02021–19.

Rhodes, Thomas E et al. (1996). "A Late Pleistocene-Holocene lacustrine record from Lake Manas, Zunggar (northern Xinjiang, western China)". In: *Palaeogeography Palaeoclimatology Palaeoecology* 120.1-2, pp. 105–121.

Romans, B W et al. (2015). "Environmental signal propagation in sedimentary systems across timescales". In: *Earth-Science Reviews* 153, pp. 7–29.

Stroeven, Arjen P et al. (2013). "Glacial geomorphology of the Tian Shan". In: *Journal of Maps* 9.4, pp. 505–512.

Yang, Shaomin, Jie Li, and Qi Wang (2008). "The deformation pattern and fault rate in the Tianshan Mountains inferred from GPS observations". In: *Science in China Series D: Earth Sciences* 51.8, pp. 1064–1080.

Yin, An et al. (1998). "Late Cenozoic tectonic evolution of the southern Chinese Tian Shan". In: *Tectonics* 17.1, pp. 1–27.

Yu, G, S P Harrison, and B Xue (2001). *Lake status records from China: Data Base Documentation*. Tech. rep. 4. Jena, Germany: Max Planck Institute für Biogeochemie.

Zech, Roland (2012). "A late Pleistocene glacial chronology from the Kitschi-Kurumdu Valley, Tien Shan (Kyrgyzstan), based on 10Be surface exposure dating". In: *Quaternary Research* 77.2, pp. 281–288.

Chapter 6

MIXING AND BUFFERING OF ENVIRONMENTAL SIGNALS BY AGGRADATION-INCISION CYCLES ALONG THE ROUTING SYSTEM

with Quentin Berger[1] and Jean-Philippe Avouac[2]

To be submitted to Basin Research

6.1 Introduction

In this final chapter, we investigate the effect of remobilization of sediments deposited in previous cycles and their mixing in the modern sediment flux on the signal recorded in the foreland stratigraphy. The effect of alluvial landscapes on the sediment routing system has been mostly studied under the angle of the transfer of mass: defining the degree of buffering of the sediment flux Q_s when it moves from source to sink and is temporarily stored along the way (e.g. Métivier and Gaudemer, 1999; Castelltort and Van Den Driessche, 2003; Allen et al., 2013; P D Clift and Giosan, 2014). This approach helps to better interpret the meaning of sediment bodies in the stratigraphic record (e.g. Paola, Heller, and Angevine, 1992; Goodbred Jr. and Kuehl, 2000; Armitage et al., 2011; Braun et al., 2014; Schlunegger and Castelltort, 2016). Another aspect of the problem is that after a temporary deposition of sediments, the remobilized material of the following incision phase is rarely entirely the same as what was just deposited. A fraction of the material remobilized might have been stored for a significant period of time. This mixing changes the information held within the sediment flux (e.g. Dunne et al., 1998; Wittmann et al., 2011; Galy and Eglinton, 2011). The study of geochemical signals in the stratigraphic record to reconstruct climatic and tectonic histories is common (e.g. France-Lanord, L. Derry, and Michard, 1993; Burbank, L. A. Derry, and France-Lanord, 1993; Peter D Clift et al., 2008). As we are moving toward finer temporal resolutions, a good understanding of the mixing aspect of the 'mixing and buffering' problem is required. The recycling of sediments buried

[1]Laboratoire Probabilités et Modèles Aléatoires, Université Pierre et Marie Curie, 75005 Paris, France

[2]Division of Geological and Planetary Sciences, California Institute of Technology, Pasadena, CA 91125, USA

for a significant amount of time can be particularly problematic for the analysis and interpretation of radiogenic signals (e.g. Bierman and Steig, 1996) which can be used to estimate modern but also paleo-erosion rates (Charreau, Blard, et al., 2011). We investigate this issue here using a numerical model that describes the mixing of old sediments in the modern flux. The model was designed based on our understanding of the dynamics of the North piedmont of the Eastern Tian Shan described in previous chapters where vast amounts of Pleistocene deposits are remobilized in the modern sediment flux during stream incision (Figure 6.1).

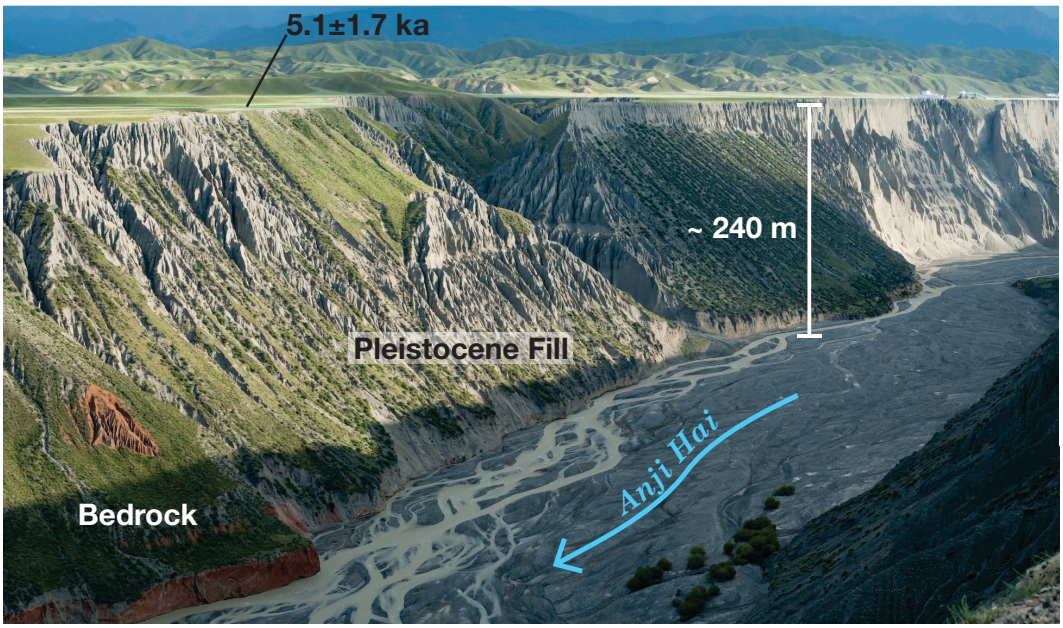

Figure 6.1: Field view of the Anjihai river illustrating how sediment remobilization during incision into previously aggraded fan strata results in sediment mixing.

The question of signal transfer along the sediment-routing system has been approached from different perspectives by many authors. Romans et al. (2015) review the different sedimentary systems that can affect the transmission of environmental signals from source to sink. They show that the keyfactor resides in the capacity of a fluvial sediment routing system to amplify or buffer signals. the climatic signals they discuss are changes in sediment fluxes driven by variations in precipitation and water discharge. In a companion review, Jaeger and Koppes (2016) explore the cryospheric source to sink systems. In these examples, the primary signal is production of sediment by glacial erosion

before its transport to the marine domain by subglacial water. Our contribution straddles the two reviews with a primary punctual sediment flux signal created by the mountain glaciers and then transported in the fluvial system. The dissociation of the two and the sudden delivery of a large sediment pulse to the fluvial system is key for the amplification of the environmental signals in the north Tian Shan. There are a number of studies in which the history of mountain building has been inferred from foreland sedimentary records (e.g. Mugnier and Huyghe, 2006; P. G. DeCelles and P. C. DeCelles, 2001; Simoes and Avouac, 2006; Horton and P. G. DeCelles, 1997; Alizai et al., 2011). In such studies it is assumed that the space available for sediment accumulation due to underthrusting of the foreland is filled up to constant base level and the buffering effect of the piedmont is ignored. The transient storage of sediment along this route modulates however the stratigraphic record by increasing the non-linearity of sediment transfer, adding complexity to the stratigraphic record, and delaying the downstream propagation of tectonic or climatic signals affecting the headwaters (Métivier, 2002; Jerolmack and Paola, 2010; Armitage et al., 2011). P D Clift and Giosan (2014), in a rare study, quantified the amount of sediment buffering in the entire Indus system since the LGM with volume balance calculations. They showed a lag of more than 10 kyr in the transmission of bedload across the system due to aggradation and incision of the foreland floodplains.They however only constrain the lag in delivery of the volumetric package and not necessarily the age of the remobilized sediments. The effect of transient storage has been studied in floodplains, which provide temporary accommodation and yet still transmit high-frequency climate cycles to the basins (Castelltort and Van Den Driessche, 2003; Allen, 2008; Simpson and Castelltort, 2012).

Sediment recycling has been studied in lowlands as a consequence of lateral migration and avulsion of river channels. In the Amazon basin, Wittmann et al. (2011) show that large avulsions can lead to recycling of sediments as old as 1-3 Ma. In the Ganges Brahmaputra, Galy and Eglinton (2011) measure an average sediment residence time of 15 kyr in the floodplain due to sediment exchanges between channel and banks. Lauer and Willenbring (2010) show that recycling of sediment in floodplains is largely anecdotic for nuclides decaying on a Myr timescale but can significantly affect the signal of short-lived nuclides such as ^{14}C. Sediment recycling in the upland and piedmont has been

recognized as a source of potential problems for cosmogenic nuclide studies in river bedload (Bierman and Steig, 1996) but there has been no studies we know of that sought to quantify the magnitude both buffering and recycling in a simple alluvial system.

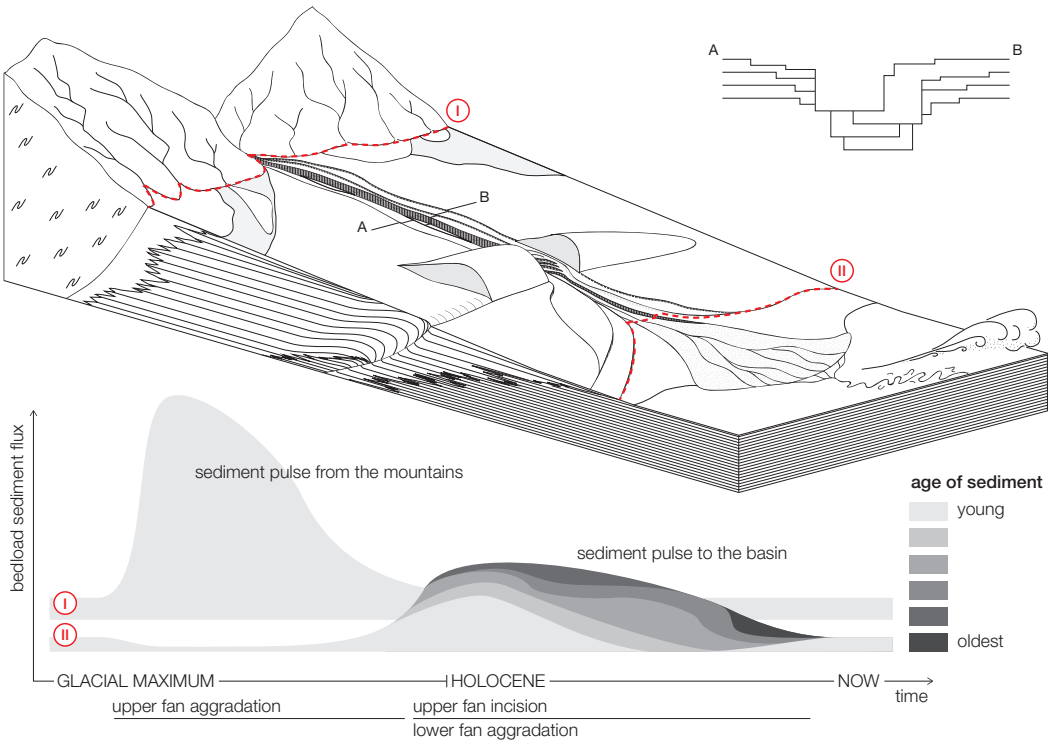

Figure 6.2: Conceptual model of the piedmont morpho-sedimentology inpired by the Kuitun River. The two boundaries (I) and (II) mark the position of sediment gauges that would record the flux coming out of the high range and into the piedmont (I) and out of the piedmont into the basin (II). The inset stratigraphy shows the complicated stratigraphy that aggradation-incision cycles and limited lateral movement of the channel would cause. The sediment fluxes through the two gauges are represented at the bottom with a gradient of gray symbolizing the age of the sediments remobilized..

6.2 Conceptual model

We cast the Tian Shan field sites in a conceptual model that captures the essential dynamics at play (Figure 6.2). In a piedmont with two telescoped fans like the North Tian Shan, this scenario can be described with the bedload sediment flux, Qs, through two boundaries (I) and (II) measuring the sediment flux from the mountain to the piedmont (I) and from the piedmont

to the basin (II). At equilibrium, the sediments that are not trapped by local subsidence bypass the alluvial fan, thus initially, the sediment fluxes at the apex (Q_s(I)) and at the toe of the fan (Q_s(II)) differ only by the amount of accommodation. When the ratio $Q_s(\mathrm{I})/Q_w$ of upstream sediment flux over water discharge increases, the fan aggrades and steepens, and Q_s(II) is greatly reduced, this is the onset of transient storage. As Q_s(I) decreases, or conversely Q_w increases, the fan incises and Q_s(II) picks up, delivering sediments to the lower fan and the proximal basin. The gradient of the stream shallows and the lower fan aggrades until the entire piedmont evolves back to the equilibrium geometry that sustains Q_s(I). This dynamic is illustrated in the time evolution of sediment fluxes through the two boundaries in Figure 6.2 (bottom) as an increase of $Q_s(\mathrm{I})/Q_w$ migrates through the piedmont in the post- and interglacial period. The flux plot characterizes the delay in sediment transfer and the difference in surface area represents the net flux loss across the fan, i.e. permanent sedimentation on the piedmont.

While aggradation-incision cycles eventually transfer a large fraction of the sediments produced in the mountain to the basin — Allen et al. (2013) measures between 5% and 15% of net loss in the sedimentary flux loss traversing the Pyrenean piedmont — the nature of these sediments can reflect several different past aggradation cycles recycled during river incision and piedmont deformation (Jolivet et al., 2014). Repeated river aggradation, lateral migration, and incision on the piedmont creates a complex stratigraphy illustrated by the cross section in the top right corner of Figure 6.2. Each time the river incises, it excavates older deposits and recycles them in the modern sediment-routing system (shades of gray in Figure 6.2). In this context, we define the age of sediment as the time when it leaves the high range. We ignore the sediment mixing occurring in the high range for the purpose of this plot. A quantitative understanding of the recycling process is important for the interpretation of the sedimentary and geomorphic record. It is also relevant for measurements in modern channels that can be biased by the recycling of older deposits. Additionally, the coupling between tectonics and sedimentation is another factor of buffering, for example the sediment accumulation in piggy-back basins, the effect of a fold-and-thrust belt on the drainage geometry or the modulation of lithological facies progradation by active thrusting (Flemings and Jordan, 1990; Tucker and Slingerland, 1996). Sediment storage can be transient on a

much longer timescale (Myr) when strata are thrusted or folded and eroded at the surface.

Observed recycling and mixing in the Kuitun River

In the previous chapters, we have established a sequence of repeated aggradation-incision cycles triggered by climatic changes and identified the age of sediment layers exposed in the Kuitun catchment by Holocene incision. The last important flux of sediment from the high range occurred from 25 to 15 ka and the coarse load was deposited on the alluvial piedmont as documented by the aggradation age at 18 ka followed by the fill terrace marking the onset of incision at 13.8 ka (samples #TS13_03 and #TS13_11, Chapter 4, Figure 4.9). Jolivet et al. (2014) calculate that the volume of material removed from the upper fan of the Kuitun as well as from the backfilled mountain valley is 2.7 ± 0.5 km^3. The samples of the Kuitun stratigraphy exposed in the valley walls give us a clue about the age composition of the sediment outflux. We do not have a complete overview of the stratigraphic age of the canyon wall, but the eight samples dating the stratigraphy at various heights and positions provide a reasonable overview of what was recycled since 13.4 ka (Figure 4.9).

Guerit et al. (2016) estimate that the volume of the lower fan which they call the 'Holocene fan' is equivalent to the excavated volume of the upper fan with 2.4 ± 0.7 km^3. The bulk if not all the recycled sediments have been transported to the lower fan and we can suppose that the finest fraction has been transported the farthest into the proximal basin. The fact that the volumes of incision and deposition are equivalent supports the framework of a very limited sediment flux coming from the mountain during upper fan incision and that the modern sediment flux in the river is almost entirely made of recycled sediments amalgamating upstream erosion since the Middle Pleistocene at least.

Field observations and dated surfaces allow us to constrain the geometric evolution of the Kuitun River in the last 100's kyr. The fact that the river maintained three gaps in the anticline over repeated aggradation-incision cycles indicates that its lateral mobility was limited to these piercing points. Furthermore, we dated a sample from the last aggradation phase downstream

of the anticline (18.4 ± 3 ka, TS13_45) and the fan surface (T11) on either side of the river were not reworked since at least 35 ka (sample KTN-01 from Poisson, 2002). It shows that the penultimate canyon carved by the river and filled between ca. 24 and 15 ka was crossing the anticline through the same gap. A large part of the recycled material must have been the young previous fill. The oldest stratum dated in the canyon walls of the Pleistocene fan, and thereby recycled in the modern flux is 402.7 ± 45.8 ka (TS13_10). This age corresponds to an aggradation period before or after MIS 11. The oldest sediments recycled in the modern stream are 10 Ma sandstones in the core of the anticline (Charreau, Chen, et al., 2005). But they represent a very small fraction of the total load given the narrow width of the anticline and its slow uplift rate. The environmental signal carried by the recycled fan sediments in significant quantities is therefor a 500 kyrs mixture of ages representing at least four to five glacial periods.

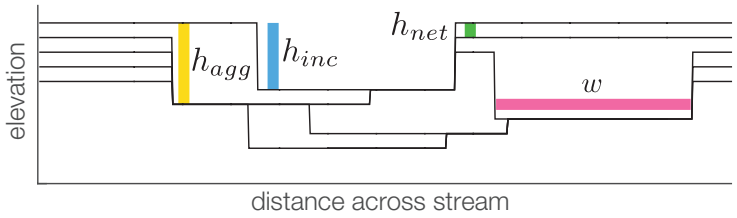

Figure 6.3: Definition of the vertical length-scales and the lateral migration from one timestep to the next entering the model.

6.3 Principles of the numerical model

In the previous chapters we have established that piedmonts can amplify climatic forcing by their strong morphological reaction to moderate climatic changes (Chapters 4 and 5). The critical aspect of a piedmont with regard to sediment mixing is its capacity to quickly incise deep in its stratigraphy when the transport capacity of the drainage exceeds the sediment flux provided by the upper catchment. Figure 6.1 shows over 200 m of Holocene incision in the Anji Hai River of the Eastern Tian Shan. A phase of aggradation of piedmont fans occurred after the LGM due to export of till from the glaciated upper portion of the catchment. It was followed by incision as the source of material got depleted while relatively wet conditions maintained a sustained transport capacity until the middle Holocene. As we discussed in chapter 4, the conse-

quence is the recycling of previously deposited clastic material in the modern sediment routing system (Figure 6.2).

If we step back and ignore entrenchment feedbacks, we can reduce a piedmont that repeatedly aggrades and incises to a system that oscillates between two geometries: 1) a flat surface and 2) a rectangular canyon. To identify the total mixing that occurs during one cycle, we do not need to resolve the syn-entrenchment evolution and we can simplify the incision as an instantaneous erosion phase. In the following pages, we present a simple numerical model that quantifies the effect of piedmont dynamics on the sediment routing. Not only can we derive a better understanding of sediment routing across piedmonts and how signals due to tectonics or climate are recorded in the foreland stratigraphy, but we can also issue simple sampling advices, based on piedmont geometries. We compare the model prediction for three different river geometries to illustrate the impact on sediment mixing. We discuss in the end the implications for the retrieving the impact of climate fluctuations from the stratigraphic records based on sedimentation rates or geochemical proxies.

We model the sediment mixing occurring across an alluvial piedmont that undergoes repeated phases of aggradation of the fan and incision of a canyon driven by climatic changes as we observed in the case of the northern piedmont of the Eastern Tian Shan. The model considers an alluvial river that aggrades and incises repeatedly. Aggradation heights are greater than incision depth to sustain long term aggradation of the model space (Figure 6.3).

The relevant lengthscales of the problem are the width and depth of the incised canyon w and h_{inc}, and the height of aggradation h_{agg}. Together they define the net aggradation of the system: $h_{net} = h_{agg} - h_{inc}$ (Figure 6.3). The oldest generation that can be remobilized by the incising canyon is given by the largest previous integer (floor function) of the division of the depth of the canyon by the net aggradation of the system: $n_{gen} = \lfloor h_{inc}/h_{net} \rfloor$. Generations are ordered from younger to older in the terminology we use here. Conversely the ratio h_{net}/h_{inc} gives the minimum fraction of last generation sediments in the output flux. When $h_{net}/h_{inc} > 1$, then there is no remobilization of sediments older than the latest phase of aggradation.

The relevant timescale in the system is the duration of a full cycle of incision and aggradation: t_{cycle}. For the sake of simplicity we consider only two timesteps: instantaneous aggradation and instantaneous incision. The material added to the cross-section during aggradation is tagged with an age of deposition. With t_{cycle}, we find the age of the oldest sediment that can be remobilized by incision: $T_{max} = n_{gen}\ t_{cycle}$. And the long term aggradation rate is $a = h_{net}/t_{cycle}$.

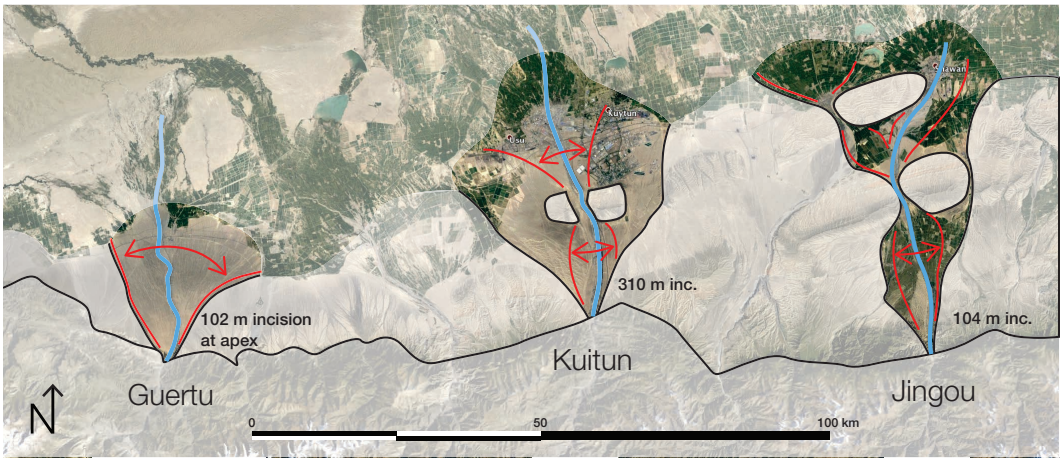

Figure 6.4: Alluvial fans in the north piedmonts of the Eastern Tian Shan. To the west: the Guertu has a large freedom of lateral movement. To the East: the Kuitun, and Jingou have lateral motion limited by the anticlines they must traverse at a few pinching points. At the fan apex, the Guertu, Kuitun, and Jingou are incised 102, 310, 104 m respectively.

The last important term that determine the routing process in this simplified model is the local lateral migration of the channel between each cycles: $L_x = f_{x_i} - f_{x_{i+1}}$. The lateral position of the canyon on the x-axis is picked randomly at each incision time step. The position of the canyon can be chosen from an arbitrary distribution: e.g. uniform distribution straddling the entire model width or normal and centred in the middle of the model space. L_x is not a fixed variable and changes from cycle to cycle. From one time step to the next, the river can follow divergent or convergent paths along stream Most of the values describing this system can be measured in the field if the fan is currently incised.

The output of the models is the average distribution of different generations present in the output flux over the run (Figure). The random pick of a river course makes that distribution differ significantly from one run to the other. If the river migrates further away than one channel width from its past course, the bulk of excavated sediment will be of older generations, but if the river occupies the exact same course, then the entire output flux will be of the youngest generation. A point that needs to be stressed here, is that the proportion of each individual generation in the output flux depends on the proportion of others. We cannot use the average distribution to predict the proportion p_i of sediments of generation i in the output flux individually, because the uncertainty on the presence of each generation depends on the amount the others. In other terms, the significant p_i's are *not* independent: indeed, the greater p_1 is, the smaller $p_2, p_3, \ldots$ will be; and conversely the smaller p_1 is, the greater $p_2, p_3, \ldots$ will be. Intuitively, we therefore have that the p_i's are negatively correlated. This is why we need to consider the complete joint distribution of $(p_1, \ldots, p_n)$. We therefore translate the output of the model in cumulative probabilities. The question that we try to answer is "how much sediments of generation n are present in the output flux?" In practice we assess "how much of the output flux can be described by generations 1 to n with a given confidence."

We develop the numerical model in two phases: first, we design a single 2D model for a valley cross-section and characterize its behavior; second, we assemble the cross-sections in series to expand the model along stream following the approach of introduced in chapter 3. We keep the model geometry simple to establish which patterns arises from the main parameters controlling a natural system without added complexity.

6.4 Application to the north Tian Shan

Modelling three rivers

We now use the model to simulate to first order the mixing expected for three different rivers on the north piedmont of the Eastern Tian Shan (Figure 6.4). 1) the Guertu river is incised by 100 m at its apex and flows on an alluvial fan without lateral constraints; 2) the Jingou River incises by the same depth, ca. 100 m at its apex, but its course is limited by an anticline that severely

Table 6.1: Key variables of the three example rivers used for the modelling presented here.

River	incision	migration
Guertu	102 m	unconstrained
Jingou	104 m	constrained
Kuitun	310 m	constrained

reduces its lateral mobility; and finally 3) the Kuitun River which, like the Jingou River has limited lateral migration because of an anticline but that is incised by 300 m. We assume that the aggradation rate is the same in the three rivers and use the value of 1.2 mm/yr at the apex to match the average aggradation rate of 0.7 mm/yr for the entire fan determined by Charreau, Chen, et al. (2005). We have established in previous chapters that the period of an aggradation-incision cycle is 21 kyr, that is, if the river recycles material deposited, for example, 5 generations ago, the age of that sediment will be ca. 105 ka.

Numerical setup

We translate the geometry of the field and satellite observations in the geometry of the model (Figure 6.5, Table 6.1). The parametrization means that from the Guertu to the Jingou, only the lateral migration is reduced, and from the Jingou to the Kuitun, only depth of incision is increased, all other parameters stay the same.

The model is made of 20 cross sections in series and we show the result of repeated cycles of aggradation and incision in Figure 6.6. There are 10 cycles for the Guertu and 20 cycles for both the Jingou and the Kuitun River. It is already noticeable from the stratigraphy of the models with a pinch point that there is significant overlap of successive channel courses. In that case the channel will primarily erode the fill of the previous canyon.

We can track the the distribution of the different generations of sediment present in the output flux of the model at each incision step (Figure 6.7 top row). The initial steps have only as many generations represented as time

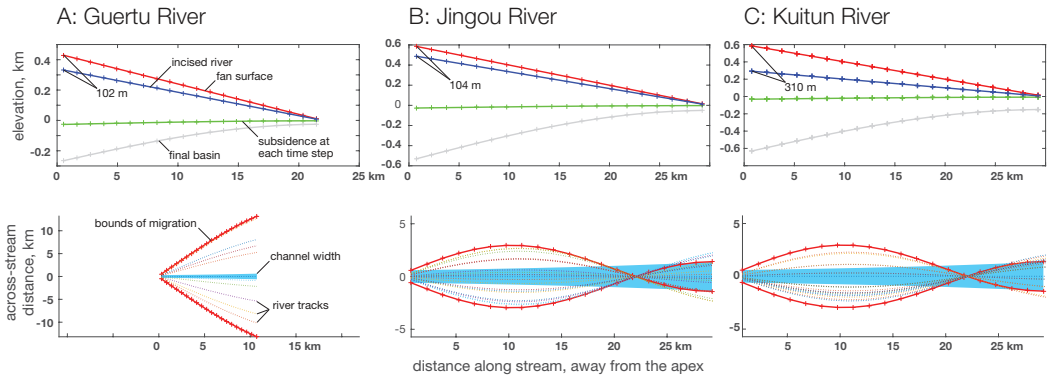

Figure 6.5: Parameters of the three runs describing sediment mixing across the alluvial fans of the Guertu, Jingou and Kuitun River. Top panels show the two geometries between which the model switches in red and blue. The Guertu and the Jingou Rivers are incised by about 100 m both, while the Kuitun is incised by three time as much. At each time step accommodation is created (green line) and accumulates during the model run time to reach the gray line that represents elevation of the oldest generation stratum. The bottom panels show the lateral mobility of the model. The Guertu is unconstrained, while both the Jingou and the Kuitun River have to pass through the pinch point of an anticline.

steps, but as soon as a stratigraphy deeper than the canyon is established, the mixture of sediment is relevant for the statistics ($n_{gen} = \lfloor h_{inc}/h_{net} \rfloor$). In the bottom row of Figure 6.7, we plot the total composition of the relative ages of the sediments in the output flux. However, as explained above, the probabilities, of the individual ages are negatively correlated with each other, and we cannot transform the lower row of Figure 6.7 into a probability density function. We need to use cumulative probabilities.

Figure 6.8 shows the cumulative distribution functions (cdf) of the distribution of sediment generation for routing along each of the three rivers. They are produced from runs with identical parameters as Figure 6.7 but where 60 cycles were accumulated to obtain an amount of data large enough to estimate statistics. The cdf indicates how many generations of sediments (contour lines) are necessary to account for different fractions of the total output flux (x-axis) with different probabilities (y-axis). The slope of the n^{th} contour line reflects the probability distribution function (pdf) of the accumulation of generations 1 to n. A steep slope indicates a narrow peak of distribution. This is the case of the Guertu example (Figure 6.8 A and top of figure 6.9) where the

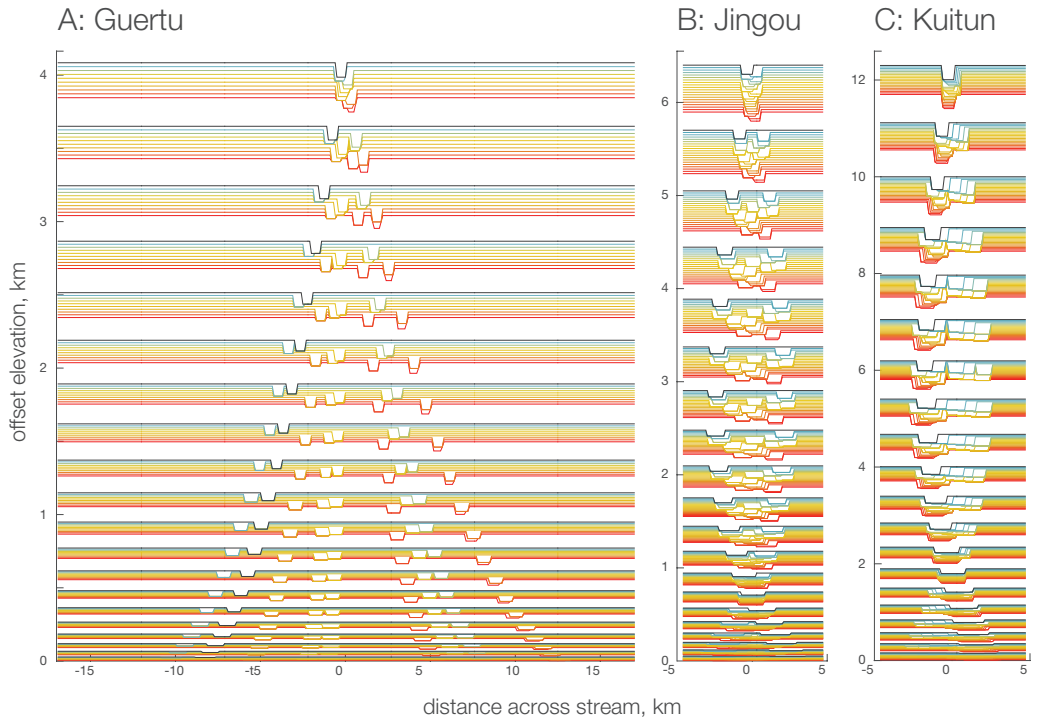

Figure 6.6: Offset cross sections of the runs reflecting the geometry of the Guertu (A), Jingou (B) and Kuitun (C) Rivers. The across stream dimension is at the same scale in the three plots. The y-axes with the elevation of the offset profiles are stretched for the comparison. The lengths of the rivers are 12, 30, and 30 km respectively.

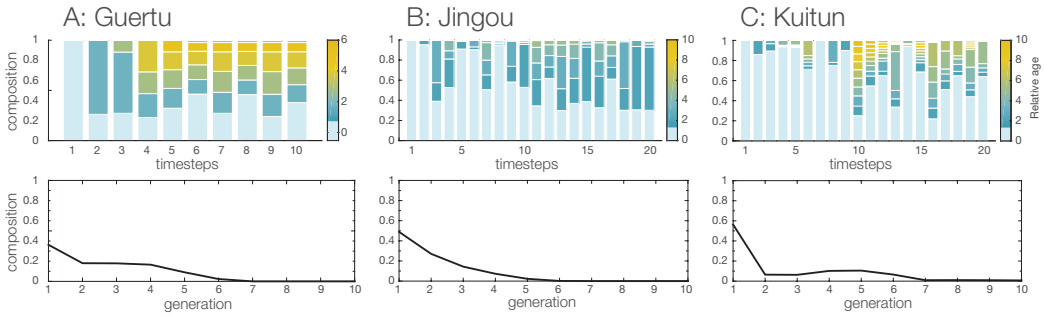

Figure 6.7: Distribution of sediment generations present in the output flux of the runs reflecting the geometry of the Guertu, Jingou and Kuitun Rivers. Generations are ordered from present to past. Top: histogram of the generations evacuated at each timestep. The initial incision episodes incise in a young stratigraphy and it is only after as many cycles as the oldest generation that the river recycle (n_{gen}) that the model output is relevant for statistics (e.g. 5 cycles in the Guertu). Bottom: Average distribution of sediments in the output flux of the short runs.

river mostly incises in a uniform stratigraphy made of horizons undisturbed by former canyons due to the wide lateral migration. The high output variability of the Kuitun configuration (Figure 6.8 and top of Figure 6.10) results in shallower slopes of the contour lines in the cdf, representing wide peaks in the respective pdfs of generations 1 to n.

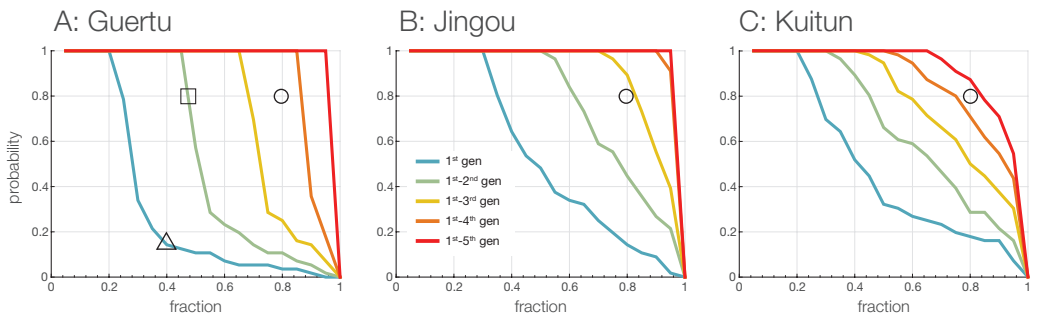

Figure 6.8: Complementary cumulative distribution plots of the runs reflecting the geometry of the Guertu (A), Jingou (B) and Kuitun (C) Rivers. For example in A, the triangle indicates that we have a probability of 0.15 that generation 1 sediments constitute at least 40% of the output flux. The square indicates that there is an 0.8 probability that at least half of the output flux is made of generation 1 and 2. The circle in each plot queries how many generations are necessary to account for 80% of the output flux with a probability of at least 0.8. In the Guertu, there is a probability of at least 0.8 that 4 generations account for 80% of the output flux. In the Jingou, it is 3 generations, and in the Kuitun 5 generations. By corollary, in the Guertu, there is a probability at least 0.8 that 20% of the output flux is made of generation 5 and/or older, in the Jingou, the same is true for generation 4 and/or older, and in the Kuitun it is the case for generations 6 and/or older.

Model results

The first order observation we can draw from this model is that the output flux of the Jingou River with constrained lateral migration and 100 m of incision is the one that requires the smallest number of generations to describe its content. Along the Kuitun river, the incision three time as deep but with a similar aggradation rate means that older generations are thrown in the mix, furthermore, the complex stratigraphy (Figure 6.6 C) of the piedmont means a large variability in the content and that is captured by the south east striking contour lines. An illustration of this effect is that the Guertu River (Figure

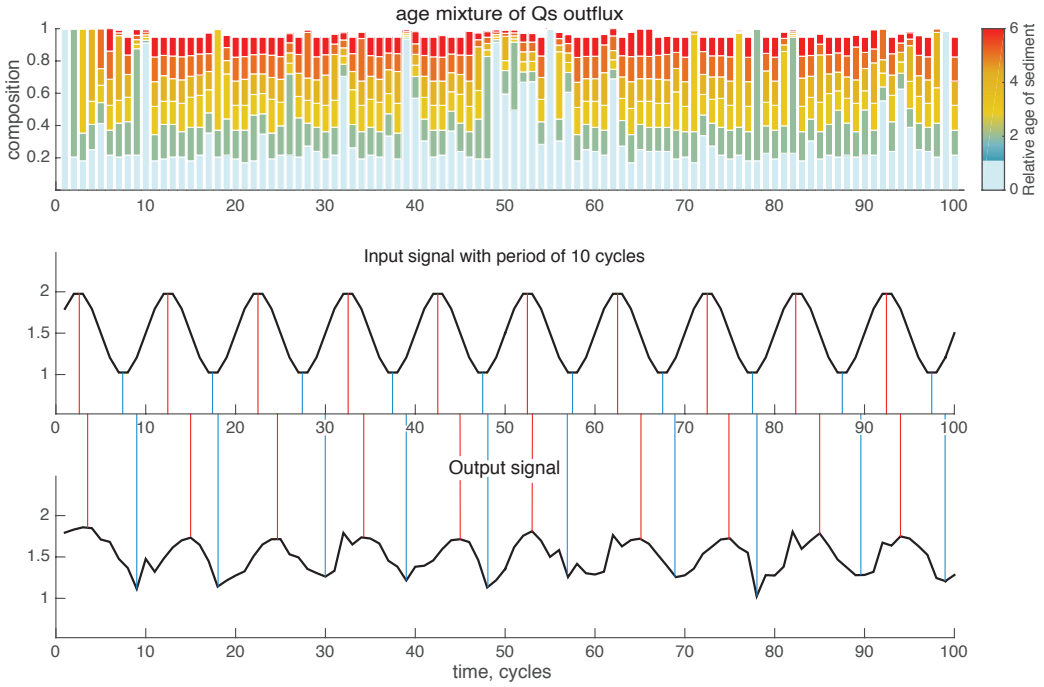

Figure 6.9: Result of a 100-cycle run with the geometry of the Guertu (low proportion of youngest generation and low variability in mixing). Top: distribution of sediment generations in the output flux ordered from young to old. Middle: input of a regular signal with a period of 10 cycles. Bottom: output of the signal after recycling of older sediments on the piedmont.

6.7 A) has almost a very similar composition at each time step, and the probability contour lines are steep (Figure 6.8 A), indicating clear transition: i.e. in the Guertu, 40% of the output flux is made of generation 1+2 with a probability of 1, but the probability drops to 0.2 for 60 % of the output flux made of generations 1+2.

This simplified routing model, thus shows that the degree of sediment mixing depend on local properties of the drainage system. The sediment record from a core sampled in front of the Kuitun River would not reproduce environmental signals the same way than a core sampled 50 km away in front of the Jingou.

- For the Kuitun there is a 0.8 probability that 20% of the output flux contains recycled sediments that are 126 ka and older (for t_{cycle} = 21 kyr)

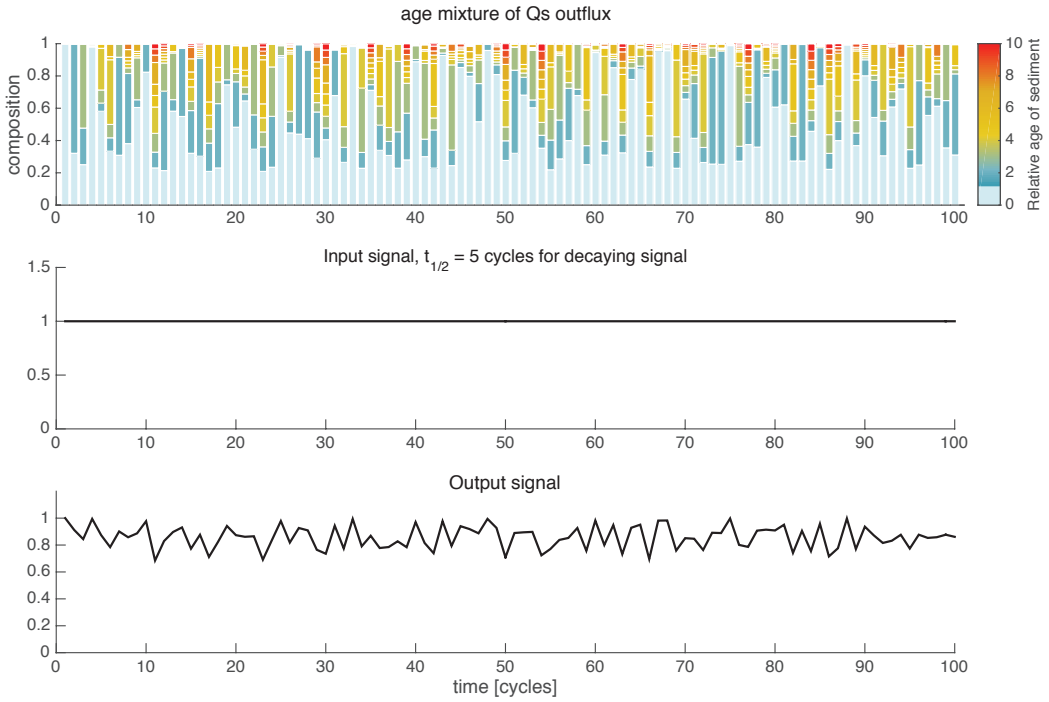

Figure 6.10: Result of a 100-cycle run with the geometry of the Kuitun (high proportion of youngest generation and high variability of mixing). Top: distribution of sediment generations in the output flux ordered from young to old. Middle: input of a steady signal with a half life equal to 5 cycles. Bottom: output of the signal after recycling of older sediments on the piedmont.

- Conversely, there is a 0.8 probability that that 80% of the output flux is a mixture of generation 1 (21 ka) to 5 (105 ka)
- For the Jingou there is a chance of 0.8 that 20% of the output flux is made of sediments between 84 ka and 105 ka.
- conversely, there is 0.8 probability that 80% of the output flux is a mixture of generations 1 (21 ka) to 3 (63 ka).

Transfer of geochemical signals across the routing system

We now estimate how a signal acquired in the sediment source area (for example denudation rates recorded by cosmogenic isotopes which might be stable or radiogenic, or a change in sediment provenance which might be tracked using some geochemical proxy or the mineral content) is transferred across the routing system and recorded in the stratigraphy.

We track the modification of an arbitrary signal across the piedmont in three examples: 1) the transfer of a step function across a piedmont; 2) a sinusoidal signal carried by a stable tracer with a 10-cycle period (Figure 6.9); 3) a steady signal carried by an unstable tracer with a half life of 5 cycles (Figure 6.10).

Transfer of a step function

In the first example (Figure 6.11), we follow the transfer of a sudden change in the input signal through the piedmont as it is filtered by geometries inspired by the Guertu, Jingou, and Kuitun Rivers (Figure 6.4 and 6.5). The input signal doubles at the 20^{th} cycle (Figure 6.11 D).

The regular mixing occurring across the Guertu geometry transforms the punctual change into a progressive transformation over n_{gen} cycles (Figure 6.11 A and E). In the Jingou-inspired geometry, the transformation occurs faster because of the larger proportion of the youngest generation in the output flux, but the transition is not smooth due to the variability of the output (Figure 6.11 B and E). The output generated by the geometry resembling that of the Kuitun River is a rough transition with several intermediary peaks. In this run, the bulk of the transition is finalized 6 cycles after the change in input signal. But we notice a slight dip in the signal at the cycle 29 when 25% of the output is made of generation 6 or older.

The transfer timescale for a step function that we observe in Figure 6.11 is already encapsulated in the cdfs presented in Figure 6.8. The number of generations necessary to describe 95% of the output flux with a high degree of confidence corresponds to the timescale of transfer. With the timescales of the north Tian Shan where 1 cycle is 21 kyr long, a instantaneous change recorded by a stable geochemical proxy would result in a ramp of duration of 21 to 84 kyrs, with more or less pronounced superimposed fluctuations at the time scale of the aggradation/incision cycles.

Sinusoidal signal

In the second example we assess the modification of a regular sinusoidal signal with a period of 10 cycles. We use the geometry of the Guertu as a filter:

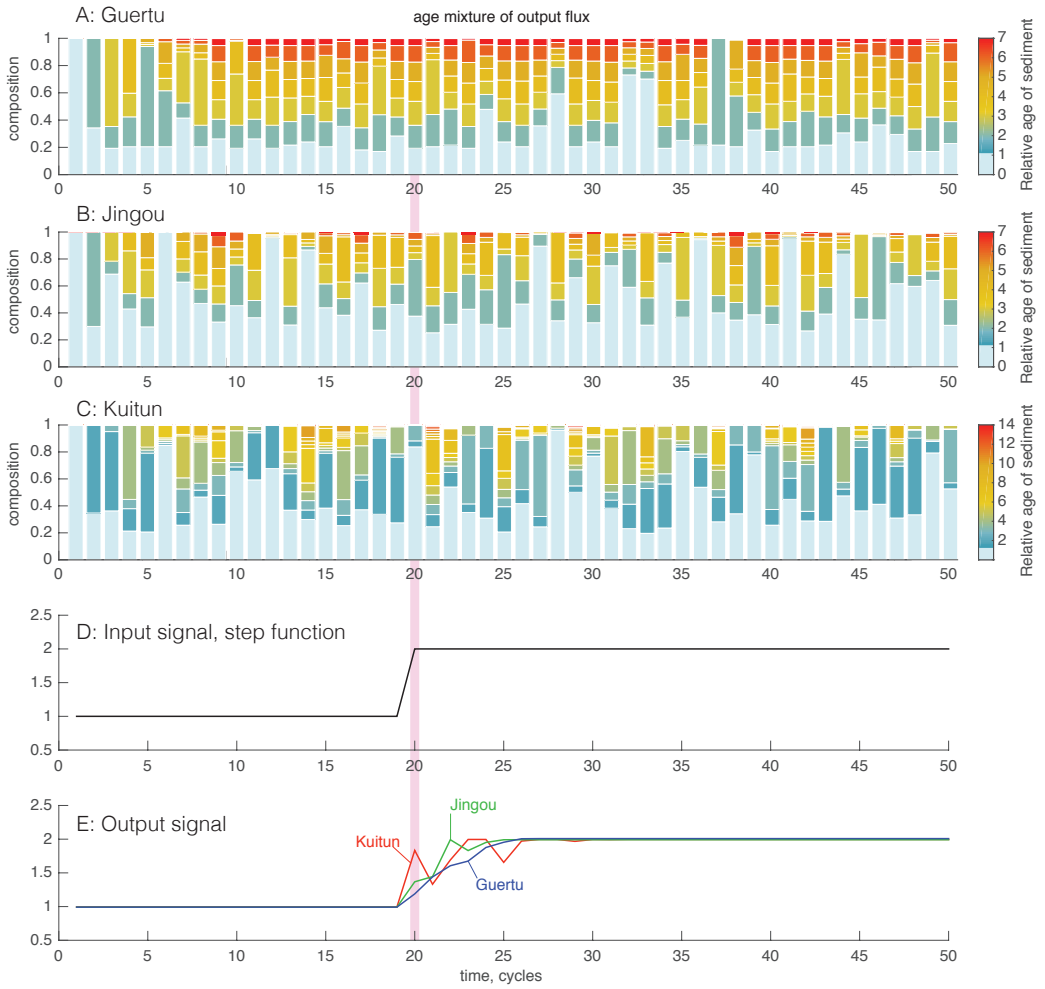

Figure 6.11: Result of a 50-cycle run illustrating the transfer of a single step function across the piedmont. A, B, and C: distribution of sediment generations in the output flux ordered from young to old in geometries inspired by the Guertu, Jingou and Kuitun Rivers. D: input of a signal that suddenly doubles at the 20^{th} cycle. E: output of the signal after recycling of older sediments on the piedmont in the three different geometries.

small fraction of the youngest generation is represented in the output flux but the age mixture has a low variability throughout the model run (Figure 6.8 A).

Each output flux usually contains the 6 latest generations with similar distribution throughout the run. As a consequence, the peaks of the signal are shifted by one to four cycles (vertical red and blue lines in middle and bottom plot of Figure 6.9). The variability in the amount of shift means that the symmetry of the signal is lost. The maximum and minimum values of the signal are mixed together with intermediate values and the amplitude of the output signal is all the more reduced.

With the timescales of the north Tian Shan where 1 cycle is 21 kyr long, the phase of the incoming signal is shifted by a very significant lag of 21 to 84 kyrs.

Constant signal recorded by a decaying isotope

In the third example we track how a constant signal carried by a decaying tracer is modified by mixing across the piedmont (e.g. denudation rate recorded by a radiogenic nuclide). The half-life of the tracer is 5 cycles, that is 105 kyrs for the north Tian Shan. We use the high variability example inspired by the Kuitun geometry as a filter.

The river can remobilize sediments deposited more than 10 cycles ago, thereby injecting flux significantly decayed tracers back in the modern sediment flux. The bounds of that mixing are nevertheless known thanks to the characterization of the cdf for this geometry (Figure 6.8 C): a minimum of 20% of the outflux is made of the youngest generation (teal contour line) and generations 5 and older have a probability of 0.5 to make less than 5% of the output flux, and a probability of 0.05 to represent 30% of the output flux (red contour line).

Beside the average decrease in its strength, the output signal inherits a noise with a frequency equal to that of the aggradation/incision cycles in the piedmont. The variability in the output signal at a period of one cycle is a pure artifact due to transfer along the routing system and is completely absent from

the original signal.

6.5 Discussion and Implications for large scale sediment routing

The probabilistic description of buffering and mixing across the north piedmont of the Eastern Tian Shan presented here, together with the field results reporting the remobilization of sediments deposited 400 kyrs ago in the modern sediment flux (Chapter 4), show that signals acquired in the sediment source area which could result from climate or tectonics can be significantly transformed as they are transferred across an alluvial piedmont. Alluvial piedmonts are however landforms built with the coarse bedload coming from the high range which is only a small fraction (estimated to between 20 and 50%) of the total sedimentary load (Turowski, Rickenmann, and Dadson, 2010; Liu et al., 2011). The majority of the sediment flux is indeed not temporarily trapped on alluvial piedmonts and moves to the lowland deposition areas. Here we have ignored the fraction of the sediment transferred directly as suspended load to the foreland. In reality this fraction mixes with the bedload and suspended load derived from remobilization of piedmont deposits. Some mixing model of these two terms would be needed to characterize fully the foreland stratigraphy. Although in a large system like the Indus drainage, the volume of sediment intermittently trapped on the piedmont is large and represents a notable fraction of the submarine stratigraphy (P D Clift and Giosan, 2014). In that case, the mixing and buffering described here has the potential to affect the sediment record at a large scale.

Exchange of material between river channel and banks during lateral migration has been well established (Dunne et al., 1998). Sea level fall has nevertheless the potential to result in the remobilization of very old sediments through the entrenchment of coastal rivers in passive margin deposits. Métivier and Gaudemer (1999) showed that low sea levels are very unlikely to significantly alter the volume balance of sediments because it would take too long to erode a sufficient portion of the costal sediments. However, even the narrow incision of an entrenched river in a coastal floodplain will remobilize sediments of older age that could carry geochemical tracers irrelevant to the contemporary state of the upstream drainage.

References

Alizai, Anwar et al. (2011). "Sediment provenance, reworking and transport processes in the Indus River by U–Pb dating of detrital zircon grains". In: *Global and Planetary Change* 76.1-2, pp. 33–55.

Allen, Philip A (2008). "From landscapes into geological history". In: *Nature* 451.7176, pp. 274–276.

Allen, Philip A et al. (2013). "The Qs problem: Sediment volumetric balance of proximal foreland basin systems - Allen - 2013 - Sedimentology - Wiley Online Library". In: *Sedimentology* 60, pp. 102–130.

Armitage, John J et al. (2011). "Transformation of tectonic and climatic signals from source to sedimentary archive". In: *Nature Geoscience* 4.4, pp. 231–235.

Bierman, Paul R and Eric J Steig (1996). "Estimating rates of denudation using cosmogenic isotope abundances in sediment". In: *Earth Surface Processes and Landforms* 21, pp. 125–139.

Braun, Jean et al. (2014). "Rapid erosion of the Southern African Plateau as it climbs over a mantle superswell". In: *Journal Of Geophysical Research* 119.7, pp. 6093–6112.

Burbank, Douglas West, L A Derry, and Christian France-Lanord (1993). "Reduced Himalayan Sediment Production 8 Myr Ago Despite an Intensified Monsoon". In: *Nature* 364.6432, pp. 48–50.

Castelltort, Sébastien and Jean Van Den Driessche (2003). "How plausible are high-frequency sediment supply-driven cycles in the stratigraphic record?" In: *Sedimentary Geology* 157, pp. 3–13.

Charreau, Julien, P H Blard, et al. (2011). "Paleo-erosion rates in Central Asia since 9Ma: A transient increase at the onset of Quaternary glaciations?" In: *Earth and Planetary Science Letters* 304.1-2, pp. 1–8.

Charreau, Julien, Yan Chen, et al. (2005). "Magnetostratigraphy and rock magnetism of the Neogene Kuitun He section (northwest China): implications for Late Cenozoic uplift of the Tianshan mountains". In: *Earth and Planetary Science Letters* 230.1-2, pp. 177–192.

Clift, P D and L Giosan (2014). "Sediment fluxes and buffering in the post-glacial Indus Basin". In: *Basin Research* 26.3, pp. 369–386.

Clift, Peter D et al. (2008). "Correlation of Himalayan exhumation rates and Asian monsoon intensity". In: *Nature Geoscience* 1.12, pp. 875–880.

DeCelles, P G and P C DeCelles (2001). "Rates of shortening, propagation, underthrusting, and flexural wave migration in continental orogenic systems". In: *Geology* 29.2, pp. 135–138.

Dunne, Thomas et al. (1998). "Exchanges of sediment between the flood plain and channel of the Amazon River in Brazil". In: *Geological Society of America Bulletin* 110.4, pp. 450–467.

Flemings, Peter B and Teresa E Jordan (1990). "Stratigraphic modeling of foreland basins: Interpreting thrust deformation and lithosphere rheology". In: *Geology* 18, pp. 430–434.

France-Lanord, Christian, L Derry, and A Michard (1993). "Evolution of the Himalaya since Miocene time: isotopic and sedimentological evidence from the Bengal Fan". In: *Geological Society, London, Special Publications* 74.1, pp. 603–621.

Galy, Valier and Timothy Eglinton (2011). "Protracted storage of biospheric carbon in the Ganges–Brahmaputra basin". In: *Nature Geoscience* 4.12, pp. 843–847.

Goodbred Jr., S L and Steven A Kuehl (2000). "The significance of large sediment supply, active tectonism, and eustasy on margin sequence development: Late Quaternary stratigraphy and evolution of the Ganges–Brahmaputra delta". In: *Sedimentary Geology* 133.3-4, pp. 227–248.

Guerit, Laure et al. (2016). "Denudation intensity and control in the Chinese Tian Shan: new constraints from mass balance on catchment-alluvial fan systems". In: *Earth Surface Processes and Landforms* 41.8, pp. 1088–1106.

Horton, Brian K and P G DeCelles (1997). "The modern foreland basin system adjacent to the Central Andes". In: *Geology* 25.10, pp. 895–898.

Jaeger, John M and Michele N Koppes (2016). "The role of the cryosphere in source-to-sink systems". In: *Earth-Science Reviews* 153, pp. 43–76.

Jerolmack, Douglas J and Chris Paola (2010). "Shredding of environmental signals by sediment transport". In: *Geophysical Research Letters* 37.19, pp. 1–5.

Jolivet, Marc et al. (2014). "Unbalanced sediment budgets in the catchment–alluvial fan system of the Kuitun River (northern Tian Shan, China): implications for mass-balance estimates, denudation and sedimentation rates in orogenic systems". In: *Geomorphology* 214, pp. 168–182.

Lauer, J Wesley and Jane K Willenbring (2010). "Steady state reach-scale theory for radioactive tracer concentration in a simple channel/floodplain system". In: 115.F4, F04018.

Liu, Y et al. (2011). "Erosion rates deduced from seasonal mass balance along the upper Urumqi River in Tianshan". In: *Solid Earth* 2.2, pp. 283–301.

Métivier, Francois (2002). "On the use of sedimentation rates in deciphering global change". In: *Geophysical Research Letters* 29.15.

Métivier, Francois and Yves Gaudemer (1999). "Stability of output fluxes of large rivers in South and East Asia during the last 2 million years: implications on floodplain processes". In: *Basin Research* 11.4, pp. 293–303.

Mugnier, Jean-Louis and Pascale Huyghe (2006). "Ganges basin geometry records a pre-15 Ma isostatic rebound of Himalaya". In: *Geology* 34.6, pp. 445–448.

Paola, Chris, Paul L Heller, and Charles L Angevine (1992). "The large-scale dynamics of grain-size variation in alluvial basins, 1: Theory". In: *Basin Research* 4.2, pp. 73–90.

Poisson, Blanche (2002). "Impact du climat et de la tectonique sur l'évolution géomorphologique d'un piémont: exemple du piémont Nord du Tian Shan depuis la fin du Pléistocène ". PhD thesis. Université Paris XI.

Romans, B W et al. (2015). "Environmental signal propagation in sedimentary systems across timescales". In: *Earth-Science Reviews* 153, pp. 7–29.

Schlunegger, Fritz and Sébastien Castelltort (2016). "Immediate and delayed signal of slab breakoff in Oligo/Miocene Molasse deposits from the European Alps". In: *Nature* 6, pp. 1–11.

Simoes, Martine and Jean-Philippe Avouac (2006). "Investigating the kinematics of mountain building in Taiwan from the spatiotemporal evolution of the foreland basin and western foothills". In: *Journal Of Geophysical Research* 111.B10.

Simpson, Guy and Sébastien Castelltort (2012). "Model shows that rivers transmit high-frequency climate cycles to the sedimentary record". In: *Geology* 40, pp. 1–4.

Tucker, Gregory E and R Slingerland (1996). "Predicting sediment flux from fold and thrust belts". In: *Basin Research* 8.3, pp. 329–349.

Turowski, Jens M., Dieter Rickenmann, and Simon J Dadson (2010). "The partitioning of the total sediment load of a river into suspended load and bedload: a review of empirical data". In: *Sedimentology* 57.4, pp. 1126–1146.

Wittmann, H et al. (2011). "Recycling of Amazon floodplain sediment quantified by cosmogenic 26Al and 10Be". In: *Geology* 39.5, pp. 467–470.

Appendix A

SUPPLEMENTARY FILES FOR CHAPTER 4

Details of the sampling and analytical methods are listed in the supplementary file. Most of it is a description of the 20 post-IR IRSL samples collected by the Caltech-CAGS field mission to the Chinese Tian Shan in June and July 2013 and analysed in the UCLA luminescence laboratory. The detailed method for cosmogenic nuclide analysis is in Section A.2. Information about the samples is listed in Section A.3. Each sample location is described in Figures A.3 to A.26 with a wide view of the outcrop and a close-up view of the deposits. The photos are embedded at high-resolution in the pdf. The analytical results are illustrated with a sensitivity plot and a radial plot of single-grain equivalent dose D_e values. The UCLA lab number is indicated in brackets after the field number. The final Figure A.12 shows the details of the cosmogenic profile samples collected by the 2012 CRPG Nancy mission on terrace T18 of the Anjihai River.

A.1 Method for luminescence dating

Sample preparation, instrumentation, and measurement protocol

K-feldspar grains of 175-200 μm were isolated from the sedimentary samples under dim amber LED light conditions. Subsamples were wet-sieved, treated with 3% HCl, separated by density with lithium metatungstate (ρ <2.565 g/cm^3; Rhodes, 2015), and treated with 10% HF for 10 minutes to remove the outer layer from the grains.

Luminescence measurements were carried out using a TL-DA-20 Risø automated reader equipped with a single-grain IR laser (830 nm, at 90% of 150 mW) and a ^{90}Sr/^{90}Y beta source. Measurements of scatter in D_e values for Risø calibration quartz suggest that source inhomogeneity causes 11% overdispersion. Emissions were detected through a Schott BG3-BG39 filter combination. Samples were mounted on aluminium single-grain discs with 100 holes.

The U and Th concentrations were measured with inductively-coupled plasma mass spectrometry (ICP-MS), and the K concentration (Table A.2) was measured using inductively-coupled plasma optical emission spectrometry (ICP-OES). These values were used to calculate the total beta dose-rate contribution using the conversion factors of Adamiec and Aitken, 1998. A value of 12.5 ± 0.12 wt. % K content was used in calculating the internal dose rate (Huntley and Baril, 1997). Sediment samples were collected within each sample hole for water content measurement, and cosmic dose-rates were estimated following Prescott and Hutton, 1994.

A post-IR IRSL single-grain protocol (Buylaert et al., 2009) was used to measure equivalent dose (D_e) values. Individual grains were stimulated first at 50 °C for 3 s, and then at 225 °C for 3 s to measure the more stable post-IR IRSL signal. Preheating at 250 °C for 60 s was used before natural and regenerative measurements, as well as a stimulation with the IR diodes at 290 °C for 40 s at the end of each single-aliquot regenerative-dose (SAR) cycle Wintle and Murray, 2006.

Fading correction

Faded and unfaded ages of the samples are listed in Table A.2. The stimulation temperature of 225 °C for the post-IR IRSL measurement was chosen to minimise athermal fading while maximizing the solar-bleaching rate (B. Li and S.-H. Li, 2011; Kars, Reimann, et al., 2014). Nevertheless, post-IR IRSL signals exhibit a range of fading values (Buylaert et al., 2009). To assess the stability of the measured signal at room temperature, we measured the sensitivity-corrected luminescence following a beta dose of 70.7 Gy, a preheat of 250 °C for 60 s and a pause ranging from 3270 s to 1.02 $\times 10^6$ s (Huntley and Lamothe, 2001). These measurements were performed for two aliquots each of samples J0654, J0656, J0658, and J0661. It has been shown that single aliquot fading measurements for density-separated K-feldspar sediments correspond to the fading values derived from the brightest individual grains of a population (N. D. Brown et al., 2015).

The measured g-values for these samples were 3.60 ± 0.69, 4.63 ± 0.94, 4.34 ± 0.70, and 4.95 ± 0.75, giving a weighted mean value of 4.32 ± 0.38 % signal loss per decade with a time constant of 3349 s (Aitken, 1985, Appendix F).

These values are abnormally high for a post-IR IRSL protocol measured in the blue wavelength (e.g., Thomsen et al., 2008), but also notably uniform. We applied this fading correction to the young samples using the 'Luminescence' package within **R** (Kreutzer et al., 2012).

For some of the older samples, the equivalent dose was beyond the linear portion of the dose-response curve, rendering the g-value correction of Huntley and Lamothe, 2001 inappropriate. In these cases, we followed the approach developed by Lamothe et al., 2003. A single, unfaded dose-response curve for each sample was constructed using the approach of Kars, Wallinga, and Cohen, 2008; the dimensionless recombination center density (ρ'; Huntley, 2006) was estimated from laboratory fading measurements as $2.98 \pm 0.38 \times 10^{-7}$. The summed luminescence intensities of each single-grain disc were used for the measured dose-response curves. The unfaded curve was then faded to its natural level using the same g-value used for the young samples (equation 6 of Lamothe et al., 2003) and the corrected equivalent dose was calculated by mapping the natural intensity to the approximated natural dose-response curve.

For Type C samples, two routines were used to determine ages: the Minimum Age model with three variables (MAM-3, Galbraith et al., 1999) and the Discrete Minimum Model (DMM, Fuchs and Lang, 2001; Rhodes, 2015). Both methods compare well with 1σ overlap in most cases (Figure A.1).

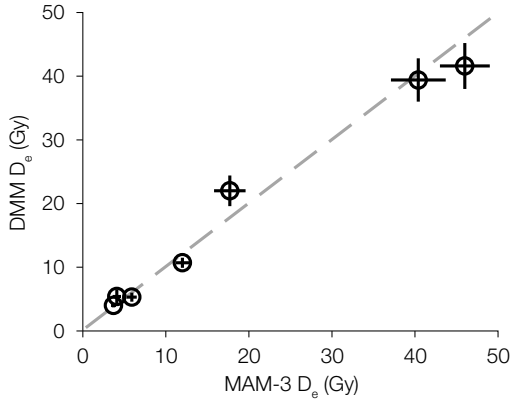

Figure A.1: Results obtained using the Discrete Minimum Model (DMM; as described within the text, assuming an overdispersion of 25%) are compared against the Minimum Age Model with 3 variables (MAM-3). Note correspondence over a wide range of equivalent dose values.

Table A.1: Post-IR IRSL protocol used for luminescence dating in this study. This single-aliquot regenerative cycle is repeated for the natural dose and all subsequent laboratory doses.

Step	Treatment	Description
1	Irradiation for t s	Natural dose (i.e., do nothing) for first cycle, laboratory dose for subsequent cycles
2	Heat to 250°C for 60 s	Preheat
3	IR laser stimulation at 50°C for 3 s per grain	IRSL
4	IR laser stimulation at 50°C for 3 s per grain	post-IR IRSL, Lx
5	Irradiation for t s	Test dose (same dose every cycle)
6	Heat to 250°C for 60 s	Preheat
7	IR laser stimulation at 50°C for 3 s per grain	Test dose IRSL
8	IR laser stimulation at 50°C for 3 s per grain	Test dose post-IR IRSL, Tx
9	IR diode stimulation at 290°C for 40 s	Hot bleach to empty all traps

A.2 Method for cosmogenic profile

Methods and parameters

Details of the sampling location and analytical results of sample TS12_ANJ_T1B are presented in Figure A.27. We infer the age of surface abandonment from the depth distribution of cosmogenic isotope concentration (Dunai, 2010; Gosse and Phillips, 2001). To better account for the potential deposit of loess and/or soil after terrace abandonment, we followed the approach of Braucher, Bourlès, et al. (2000) and Guralnik et al. (2011) and modified the general formulation of Lal (1991) as follow:

$$C(z,B) = -\overline{C_0}\mathrm{e}^{\lambda x/B} + \sum_{i=n,m_1,m_2} \frac{P_i}{\frac{\rho B}{\Delta_i} + \lambda}\, \mathrm{e}^{-\rho z/\Delta_i} \left(1 - \mathrm{e}^{\frac{\lambda}{B}+\frac{\rho}{\Delta_i}z}\right) \tag{A.1}$$

Where B is a 'negative' denudation rate (Braucher, Bourlès, et al., 2000) which represents the accumulation rate or burial rate since terrace abandon; t represents the time since initial exposure of the surface (in this case, the abandonment of the terrace surface); C_0 is the average cosmogenic inheritance (in atoms/g); λ is the decay constant of ^{10}Be equal to $\ln(2)/T_{1/2}$ where $T_{1/2}$ is the half-life of 1.387 Ma (Chmeleff et al., 2010; Korschinek et al., 2010); n, m_1, and m_2 refer to the neutrons, fast muons and slow muons, respectively; Δ is the respective attenuation length of neutrons, slow muons and fast muons ($\sim$160, $\sim$1500, $\sim$4320 g/cm^2 respectively) from Braucher, Merchel, et al. (2011) ; P is the respective local production rates (at g^{-1} yr^{-1}) for the neutrons, slow muons and fast muons; and ρ is the soil density (g/cm^3). This new formulation assumes that the few tens of centimeters of loess covering the terraces accumulated at a constant rate since the terraces abandonment. The exposure

Table A.2: Detailed results of post-IR IRSL luminescence dating. 'Depth' indicates the position of the sample below the surface. The unfaded age is the final calculated age for each sample. The river acronyms are KTN (Kuitun), AJH (Anjihai), and MNS (Manas). The distribution types are described in Section 4.1.2 of the main article.

Field code	**Lab code**	**% K**	**Th (ppm)**	**U (ppm)**	**Depth (m)**	**Total dose rate (Gy/ka)**	**Equivalent dose (Gy)**	**Dist. type**	**Faded age (ka)**	**Unfaded age (ka)**
TS13_37	J0645	2.4 ± 0.1	10.6±0.5	2.6±0.13	0.75	4.324±0.206	5.4±1.1	C	1.2±0.3	1.7±0.4
TS13_36	J0646	2.4 ± 0.1	10.3±0.5	2.85±0.14	3.0	4.398±0.212	9.7±0.8	B	2.2±0.2	3.3±0.3
TS13_45	J0647	2.4 ± 0.1	8.5±0.4	2.28±0.11	0.50	4.266±0.211	22±2.4	C	5.2±0.6	7.7±1.0
TS13_86	J0648	2.1 ± 0.1	8.6±0.4	2.61±0.13	3.0	3.897±0.184	22.1±1.3	B	5.7±0.4	8.4±0.7
TS13_11	J0650	2.3 ± 0.1	10±0.5	3.63±0.18	3.0	4.386±0.205	39.4±3.4	C	9.4±1.0	13.4±1.6
TS13_06	J0651	2.1 ± 0.1	9±0.5	2.67±0.13	1.32	4.109±0.193	41.6±3.6	C	9±0.9	15.1±1.7
TS13_01	J0652	2.2 ± 0.1	9.8±0.5	2.67±0.13	38.2	3.904±0.191	276.3±16.0	A	70.8±5.6	116.8±8.1
TS13_03	J0653	2.4 ± 0.1	9.6±0.5	2.65±0.13	7.5	4.242±0.210	51.4±6.1	B	12.1±1.6	18.3±2.6
TS13_12	J0654	2.4 ± 0.1	8.6±0.4	2.32±0.12	15	4.105±0.209	433.7±28.7	B	105.7±9.1	181±13.0
TS13_08	J0655	2.2 ± 0.1	10.1±0.5	2.73±0.14	100	3.956±0.194	124.8±17.5	A	31.3±1.7	48.9±3.6
TS13_07	J0656	2.6 ± 0.1	8.7±0.4	2.29±0.11	100	4.324±0.228	518.3±59.9	B	119.9±15.4	193.4±28.0
TS13_10	J0657	2.3 ± 0.1	4.8±0.2	1.37±0.07	200	3.479±0.191	846.7±83.2	B	243.4±27.8	396.5±36.7
TS13_09	J0658	2.5 ± 0.1	7.6±0.4	1.92±0.10	200	3.995±0.213	923.6±55.7	B	231.2±19.2	316.9±24.3
TS13_02	J0659	2.5 ± 0.1	8.4±0.4	2.11±0.11	200	4.160±0.219	839.2±134.9	B	201.8±34.4	286.1±40.9
TS13_19	J0661	2.4 ± 0.1	11.1±0.6	4.05±0.20	1.0	4.346±0.197	10.7±0.8	C	2.5±0.2	3.6±0.3
TS13_35	J0662	1.7 ± 0.1	7.5±0.4	1.91±0.10	10	2.177±0.094	53±8.0	A	24.3±3.9	37.4±6.4
TS13_14	J0663	2.3 ± 0.1	10±0.5	2.53±0.13	0.80	4.246±0.202	5.3±0.7	C	1.2±0.2	1.7±0.3
TS13_34	J0664	1.5 ± 0.1	5.7±0.3	1.68±0.08	4.0	3.017±0.137	489.2±58.9	B	162.2±21.1	236.1±26.3
TS13_32	J0665	2.2 ± 0.1	10.4±0.5	3.55±0.18	10	4.087±0.190	319.3±14.4	B	78.1±5.3	111±7.0
TS13_30	J0668	1.8 ± 0.1	5.2±0.3	3.51±0.18	4.0	3.642±0.168	188±15.0	B	51.6±4.9	81.3±9.0
TS13_33	J0669	2.2 ± 0.1	9.5±0.5	3.57±0.18	5.0	4.039±0.187	578.7±62.1	B	143.3±17.0	198.1±20.5

time of each sample is therefore dependent of its depth ($t = z/B$).

The local ^{10}Be production rates, P, for neutrons, fast muons and slow muons were scaled for local latitude and altitude according to Stone (2000) and the local atmospheric pressures were extracted from the ERA40 dataset (Uppala et al., 2005). In this study, we used the SLHL (see level high latitude) production rate of 3.9 ± 0.1 at g^{-1} yr^{-1} that was compiled by Balco et al. (2009) and revised by Braucher, Merchel, et al. (2011) to include the slow and fast muons contribution. The slow and fast muonic production rates (0.01 and 0.034 at g^{-1} yr^{-1} respectively) were derived from Braucher, Merchel, et al. (2011). Alluvium density was estimated by analyzing pictures of the outcrop in order to determine first the relative proportions of grains larger than medium gravel ($\varnothing > 1-2$ cm) and of sand-sized to medium gravel-sized grains. Bulk density was calculated by attributing densities of 2.7 ± 0.1 g/cm^3 to coarser grains and 1.9 ± 0.1 g/cm^3 to finer grains (Hancock et al., 1999).

Sample treatment

Quartz separation and isolation of pure beryllium oxide (BeO) was performed at CRPG (Nancy, France). Samples were first crushed and sieved. The 200-800 µm fraction was then processed by magnetic separation and the non-magnetic fraction was dissolved in a mixture of H_2SiF_6 and HCl. Quartz was then purified in three successive HF baths to remove atmospheric ^{10}Be from the quartz surfaces (E. T. Brown et al., 1991; Kohl and Nishiizumi, 1992). Next, the purified quartz was completely dissolved in HF after addition of 200 µl of an in-house 2.020 10^{-3} g/g ^{9}Be carrier solution. Purified BeO samples were obtained after subsequent purification by anion exchange, cation exchange and alkaline precipitation. The ^{10}Be/^{9}Be ratios of the BeO samples were measured at the ASTER (Accelerator for Earth Sciences, Environment and Risks) national AMS (Accelerator Mass Spectrometer) facility, located at CEREGE in Aix en Provence, France. These concentrations are normalized to the ^{10}Be/^{9}Be SRM 4325 NIST reference material using an assigned value of $2.79 \pm 0.03 \cdot 10^{-11}$ (Kunihiko Nishiizumi et al., 2007). This standardization is equivalent to 07KNSTD within rounding error. The mean ^{10}Be/^{9}Be ratio of 22 chemical blank samples is $1.7 \pm 0.7 \cdot 10^{-15}$. Blank corrections represent between 0.1% and 8% of the samples (average of 1.6%).

Table A.3: Sample data set and cosmogenic results

Sample name	**Depth (m)**	**Sampling thickness (cm)**	**Pure Qz weight (g)**	^{10}**Be**/^{9}**Be** 10^{-14}	^{10}**Be counts**	**[**^{10}**Be] 10**^{4} **(at/g)**	**error 10**^{4} **(at/g)**
TS12_ANJ_T1B_P0a	0	5	10	3.7	476	9.59	0.5
TS12_ANJ_T1B_P0d	0	5	9.7	3.8	381	10.11	0.61
TS12_ANJ_T1B_P0e	0	5	25	8.9	1145	9.58	0.33
TS12_ANJ_T1B_P1	-0.3	5	4.2	2.5	248	14.84	1.09
TS12_ANJ_T1B_P2	-0.75	5	2.6	1.3	155	12.29	1.27
TS12_ANJ_T1B_P3	-1.1	5	5.9	2.5	204	10.77	0.85
TS12_ANJ_T1B_P4	-2.5	5	2.2	1.1	113	11.42	1.43

A.3 Sample locations and results

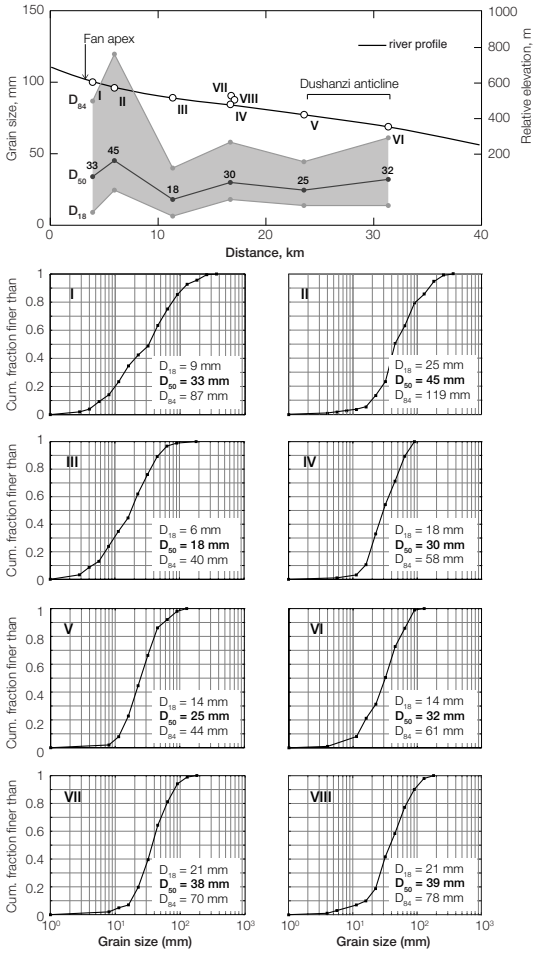

Figure A.2: Grain size survey of the Kuitun River. Top: along stream evolution of the grain sizes on active banks of the Kuitun River. Bottom: cumulative fractions of grain sizes for each survey. Location of the survey sites are shown in Figures 4 and 7 of the main article.

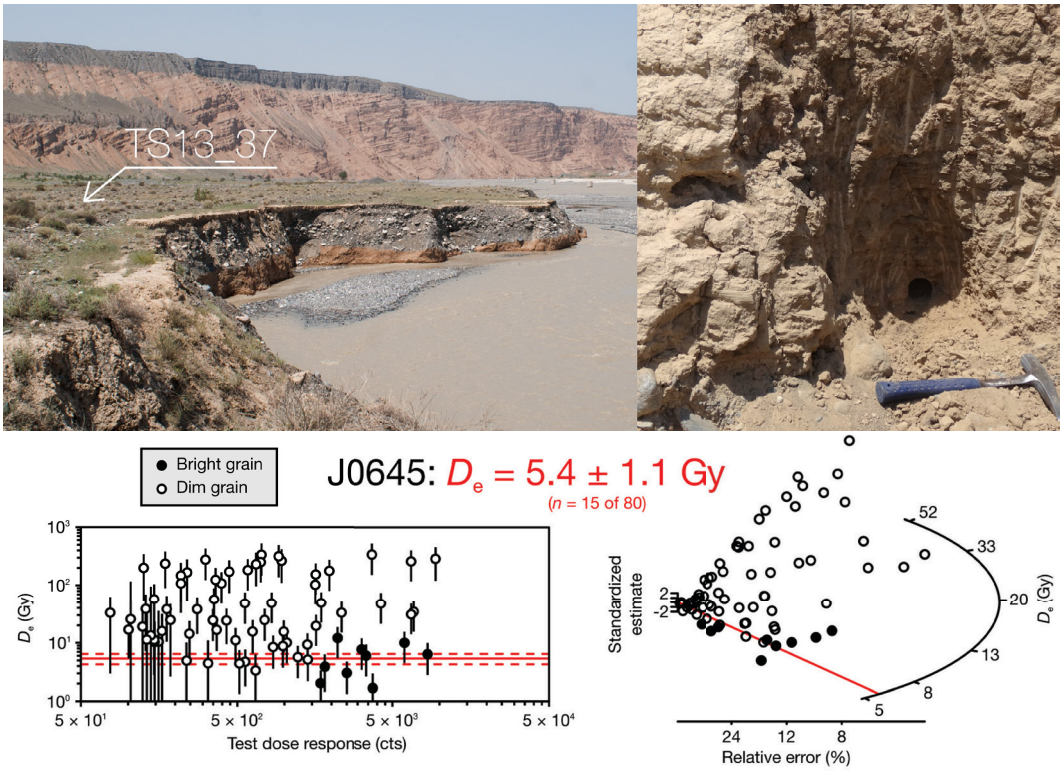

Figure A.3: Location and details of sample **TS13_37 (J0645) = 1.7 ± 0.4 ka**; Kuitun; abandonment. Sample taken in 0.8 m of fluvially reworked clayey fine sand to silt with few granules. The sample was collected 5 cm above the fluvial fill. The fluvial fill is 3.2 m thick and lies on a bedrock strath of T2. On 3.7.2013, the strath was 1.6 m above the water level. The general approach for analysis is to reject grains based on sensitivity and high outliers. The overdispersion is 0.54.

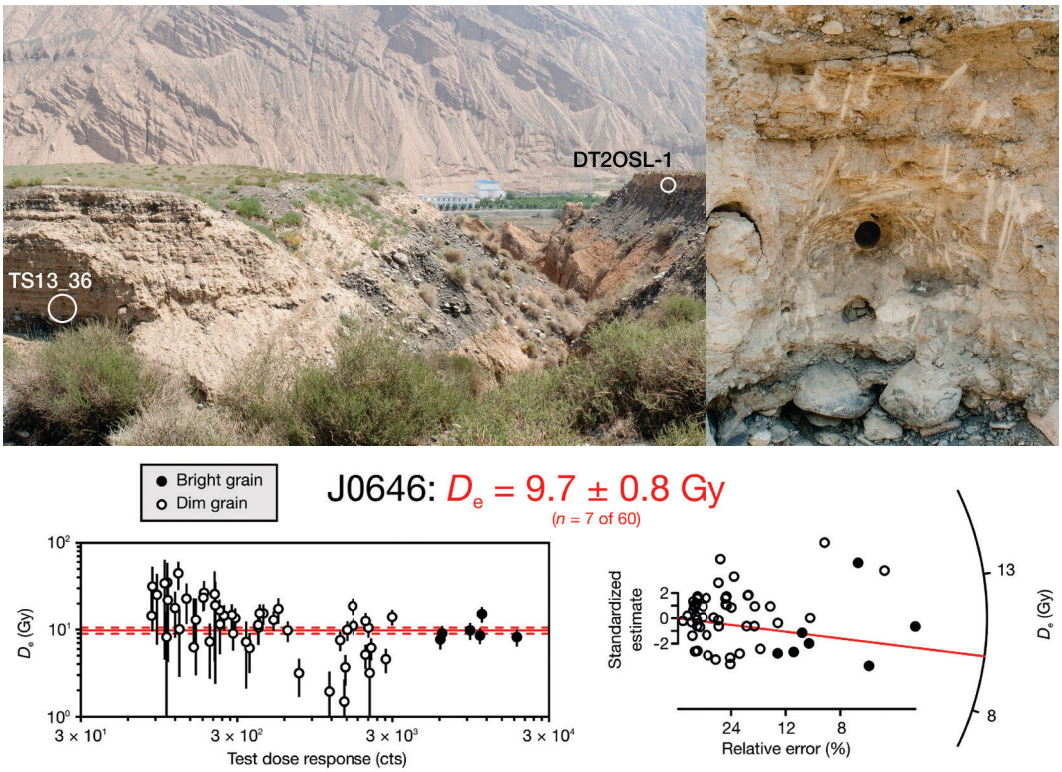

Figure A.4: Location and details of sample **TS13_36 (J0646) = 3.3 ± 0.3 ka**; Kuitun; abandonment. Sample taken in the silt of a fluvially reworked 3.2 m thick series of loess and cross-bedded medium grained sand 20 cm above the top of the alluvial cobble conglomerate. The alluvial cobble conglomerate lies on the terrace strath and the sample constrains abandonment age. The general approach for analysis is to reject grains based on sensitivity. The overdispersion is 0.2.

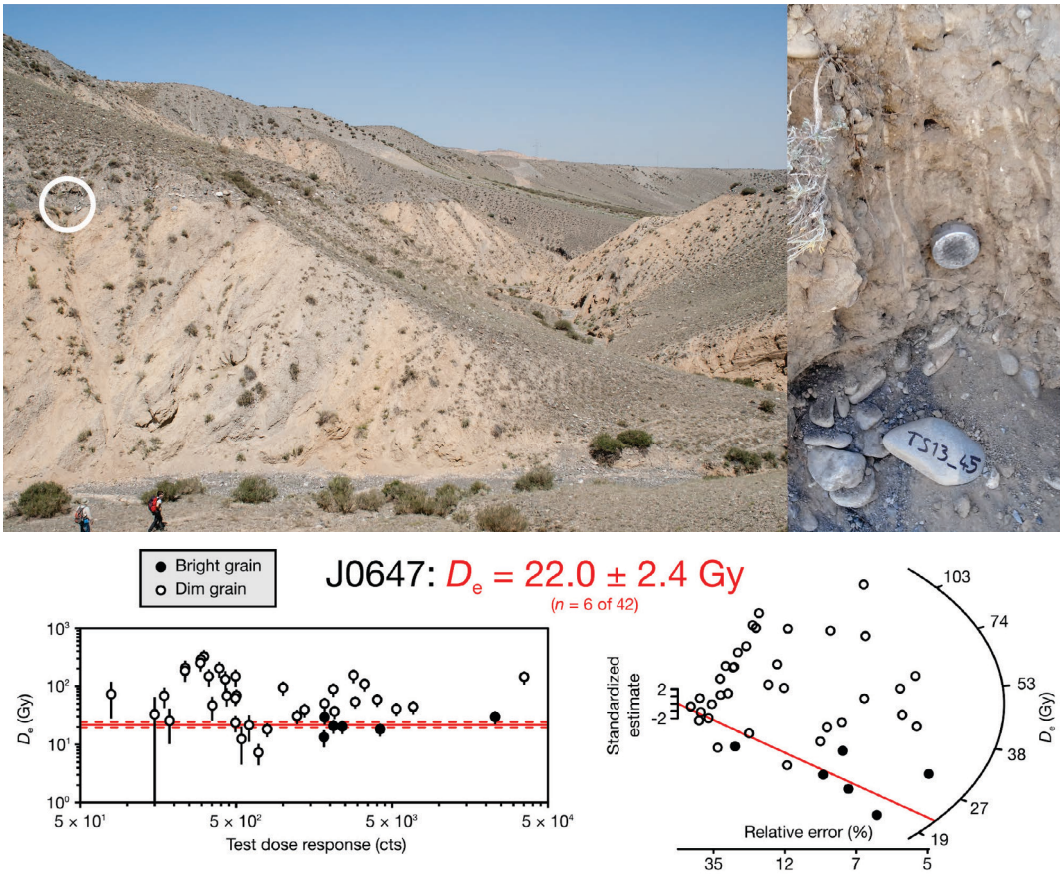

Figure A.5: Location and details of sample **TS13_45 (J0647) = 7.7 ± 1 ka**; Kuitun; abandonment. Sample taken in the middle of the 0.3 m thick silt horizon capping the 1.5 m thick cobble conglomerate that lies on the strath of T7. The silt horizon is covered by a layer of creeping colluvium. It was not possible to dissociate the colluvium from the capping silt unequivocally. But it is very likely that the silt constrains the abandonment age of terrace T7.

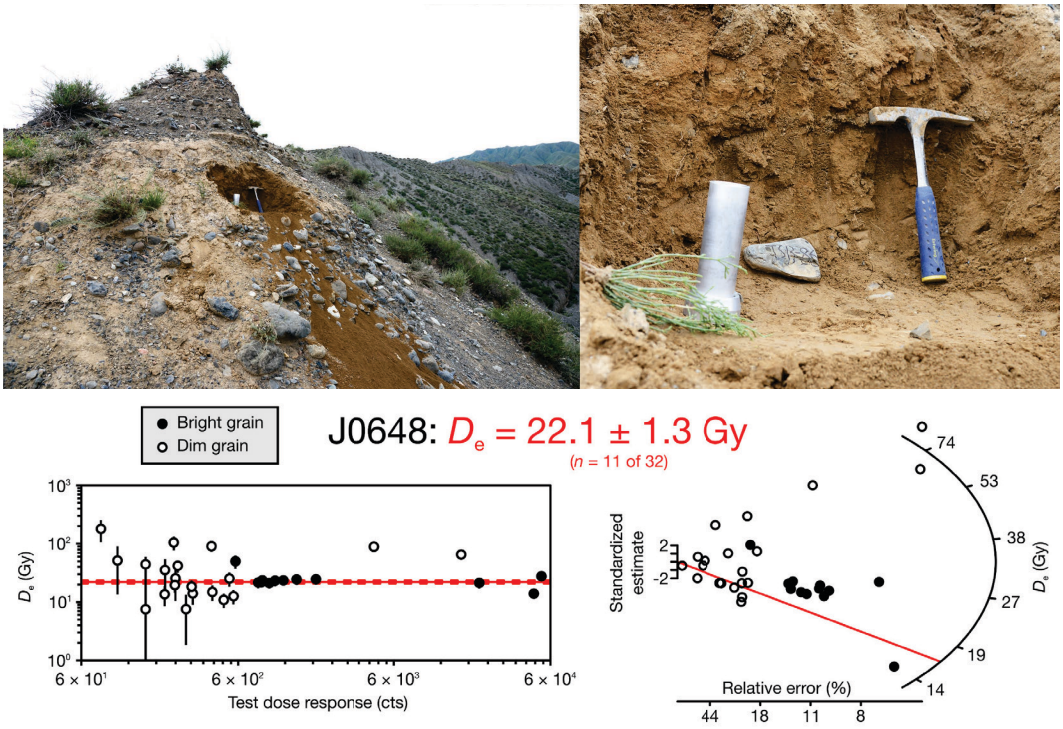

Figure A.6: Location and details of sample **TS13_86 (J0648) = 9.1 ± 1.3 ka**; Kuitun; abandonment. The sample was taken in a silt horizon 20 cm above the fluvial deposit of the terrace and below a colluvium wedge. Although it appears from the pictures that the overlying coarse deposit might be fluvial and not colluvial. The sample would then reflect an aggradation age, not an abandonment.

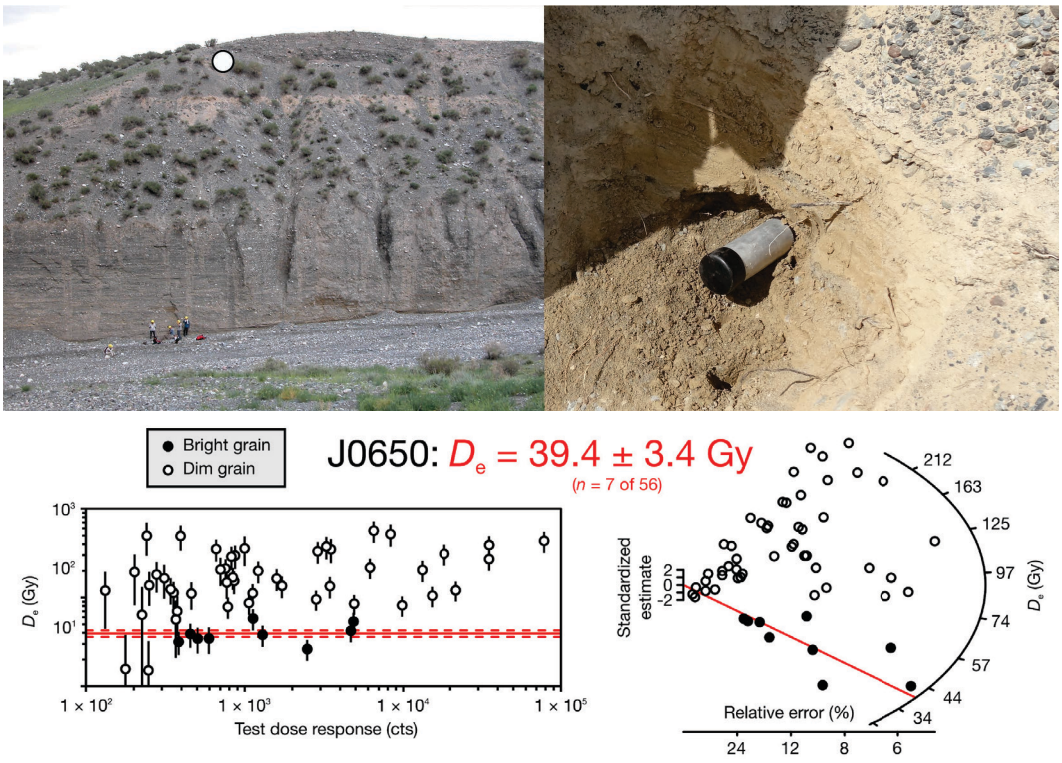

Figure A.7: Location and details of sample **TS13_11 (J0650) = 13.4 ± 1.6 ka**; Kuitun; abandonment. Sample taken in a silt lens at the base of the colluvium wedge covering the alluvial cover of the terrace T9. It constrains the abandonment of T9 and it is a repeat of sample KTN-09 (10±2 ka) of Poisson and Avouac, 2004.

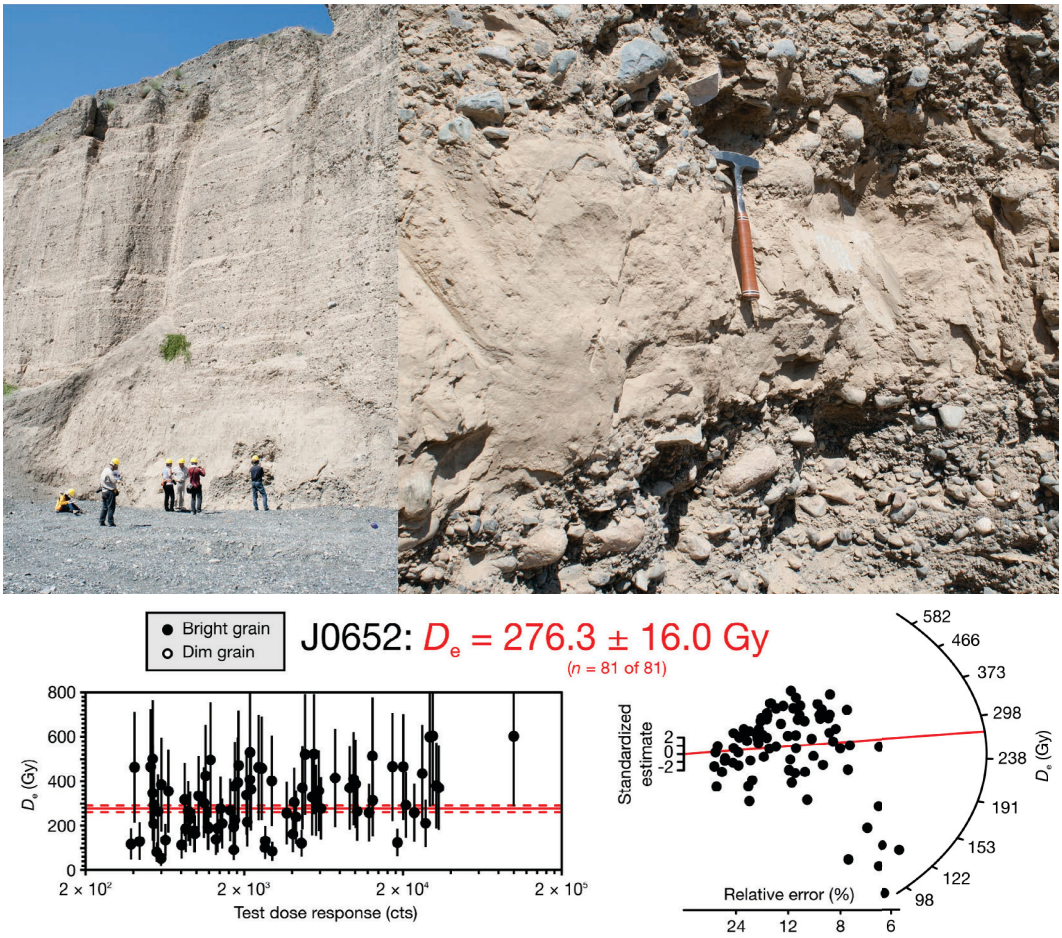

Figure A.8: Location and details of sample **TS13_01 (J0652)** = **112.4 ± 11.2 ka**; Kuitun; aggradation. Sample is collected at the base of the conglomerate cliff cut after abandonment of terrace T2. Material is a thick silt lens of reworked loess and very fine sand. The sample constrains a phase of aggradation of the alluvial fan. The overdispersion is 0.50.

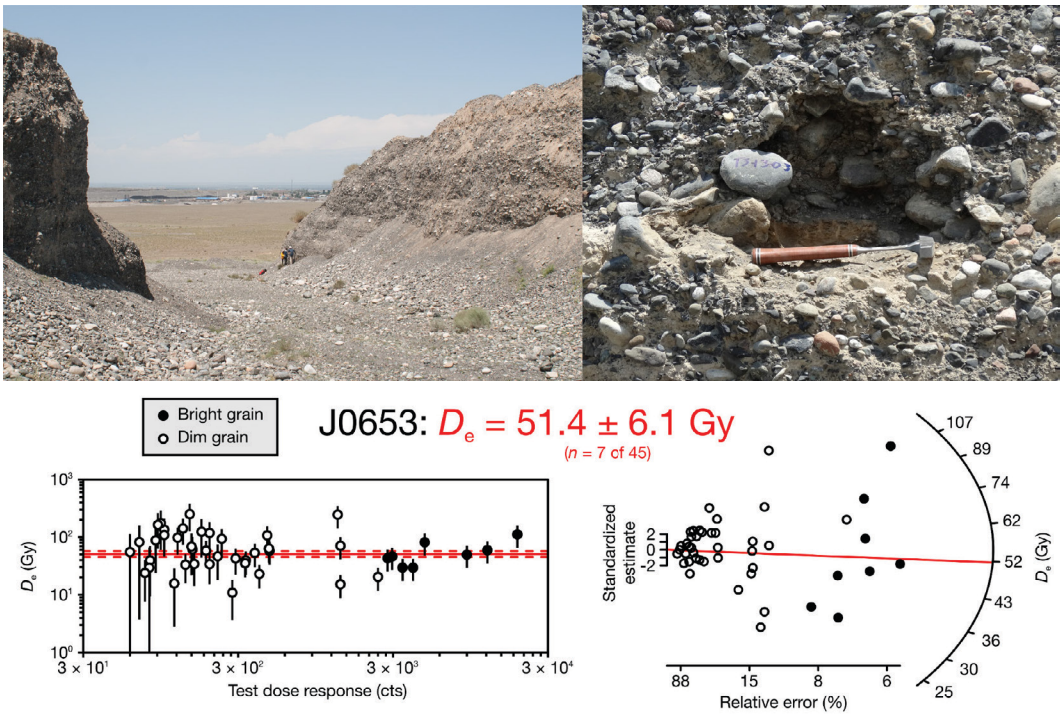

Figure A.9: Location and details of sample **TS13_03 (J0653) = 18.9 ± 3 ka**; Kuitun; aggradation. Sample is collected in the riser of T3 at the downstream end of the Kuitun. Material is taken from a thin lens of silt. The sample constrains a phase of aggradation of the alluvial fan. The overdispersion is 0.33.

Figure A.10: Picture looking down in the Swallow Canyon, the Kuitun Canyon is visible in the background.

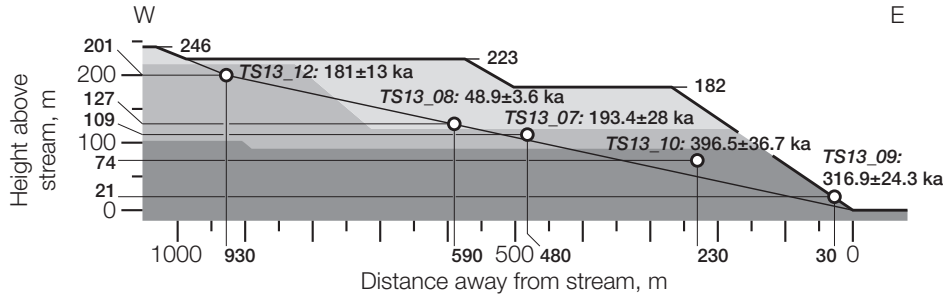

Figure A.11: Schematic profile of the tributary Swallow Canyon and location of the samples **TS13_12 (J0654) = 174.5 ± 20.4 ka**, **TS13_08 (J0655) = 48.9 ± 3.6 ka**, **TS13_07 (J0656) = 193.4 ± 28.0 ka**, **TS13_10 (J0657) = 402.7 ± 45.8 ka**, **TS13_09 (J0658) = 379.0 ± 39.6 ka**. The shading represent potential stratigraphy.

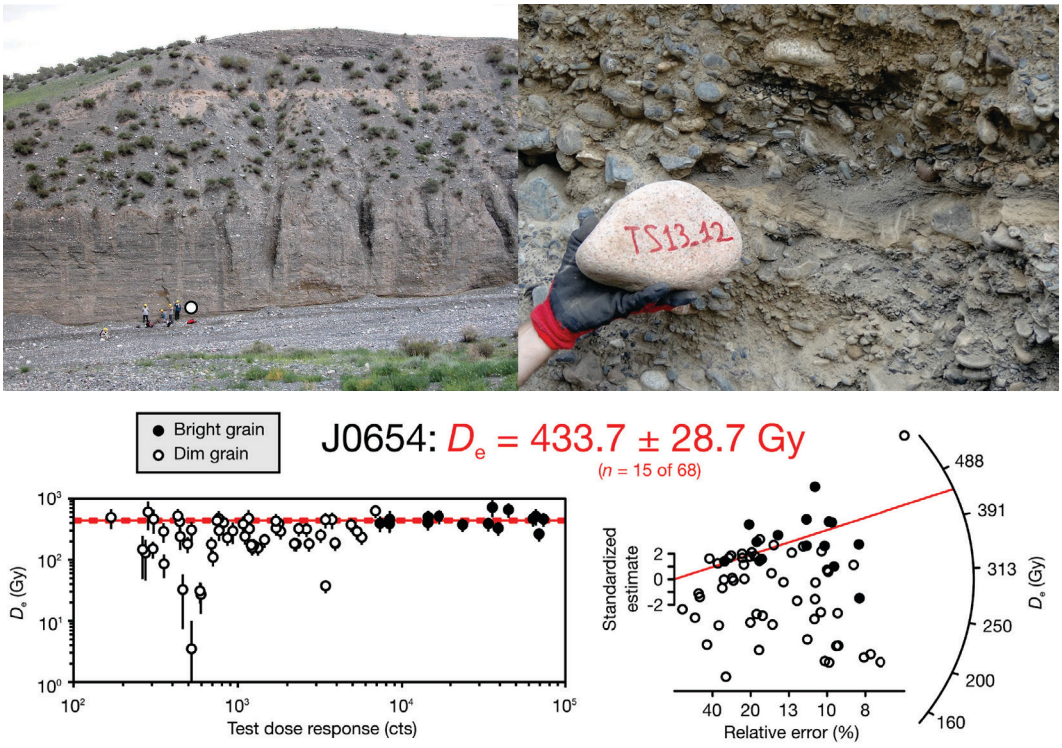

Figure A.12: Location and details of sample **TS13_12 (J0654) = 174.5 ± 20.4 ka**; Kuitun; aggradation. Sample taken in a 10-15 cm thick lens of reworked silt to medium sand 201 m above the river. The sample constrains a phase of aggradation of the alluvial fan. The overdispersion is 0.25.

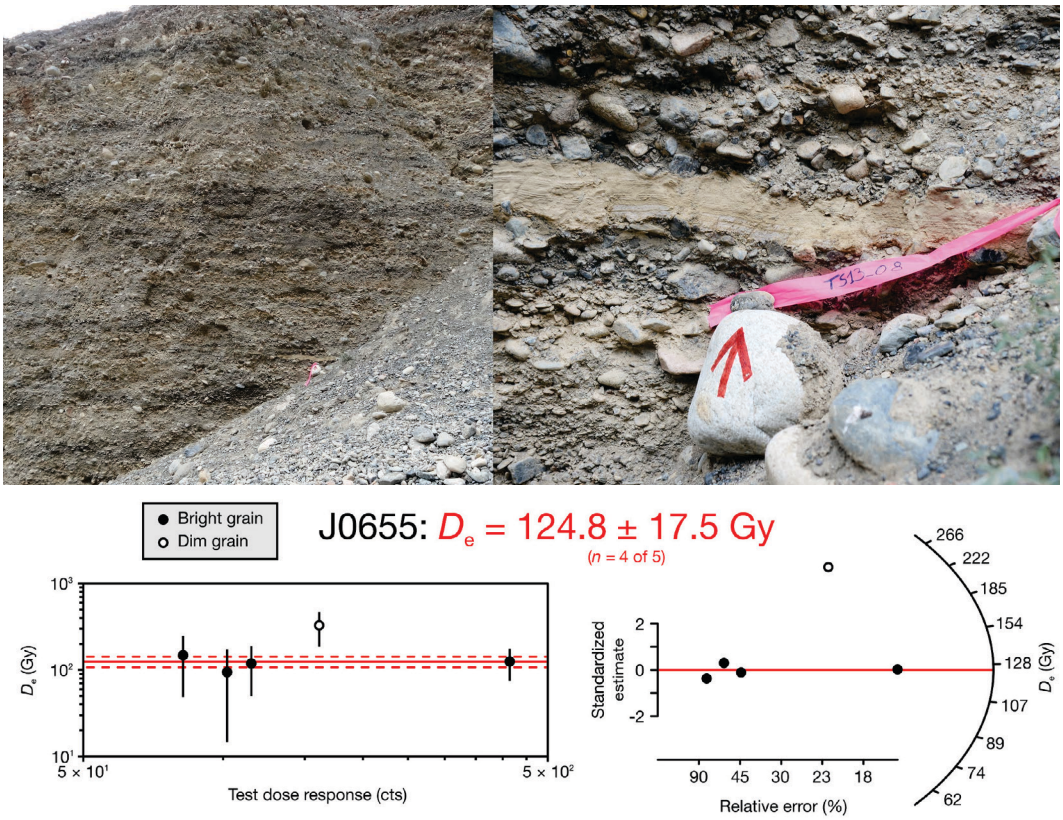

Figure A.13: Location and details of sample **TS13_08 (J0655) = 48.9 ± 3.6 ka**; Kuitun; aggradation. Sample taken in a thin lens of reworked silt 127 m above the river. The sample constrains a phase of aggradation of the alluvial fan. The overdispersion is 0.42.

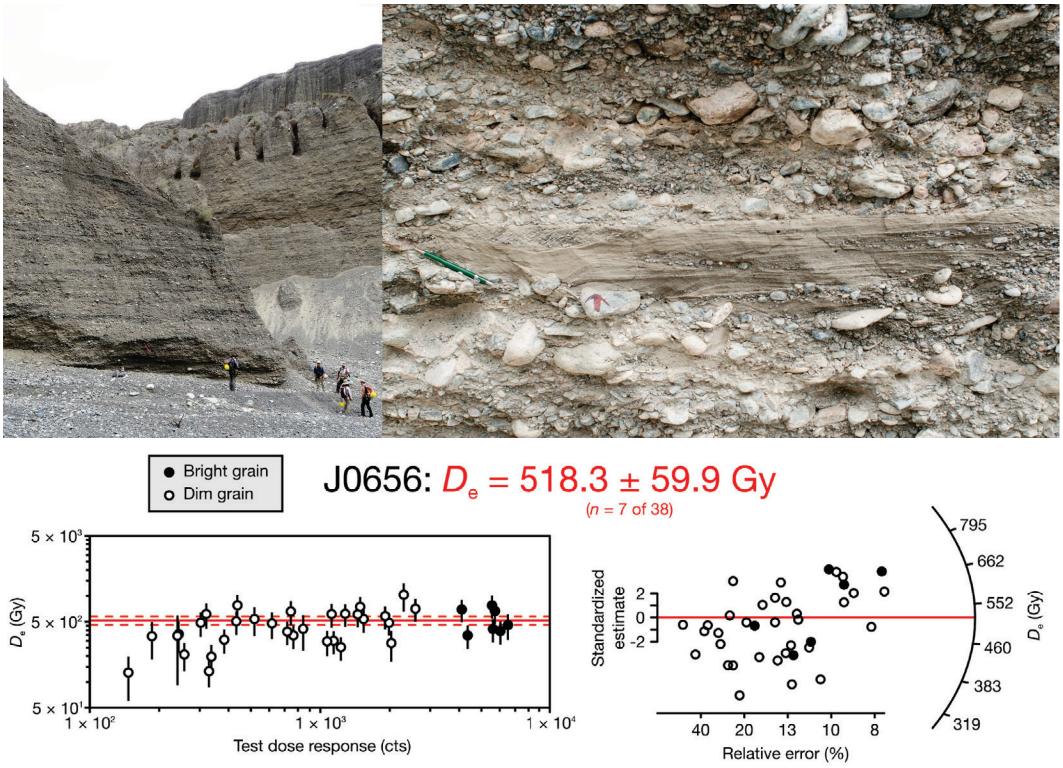

Figure A.14: Location and details of sample **TS13_07 (J0656) = 193.4 ± 28.0 ka**; Kuitun; aggradation. Sample taken in a lens of reworked silt to fine sand 109 m above the river. The sample constrains a phase of aggradation of the alluvial fan. The overdispersion is 0.28.

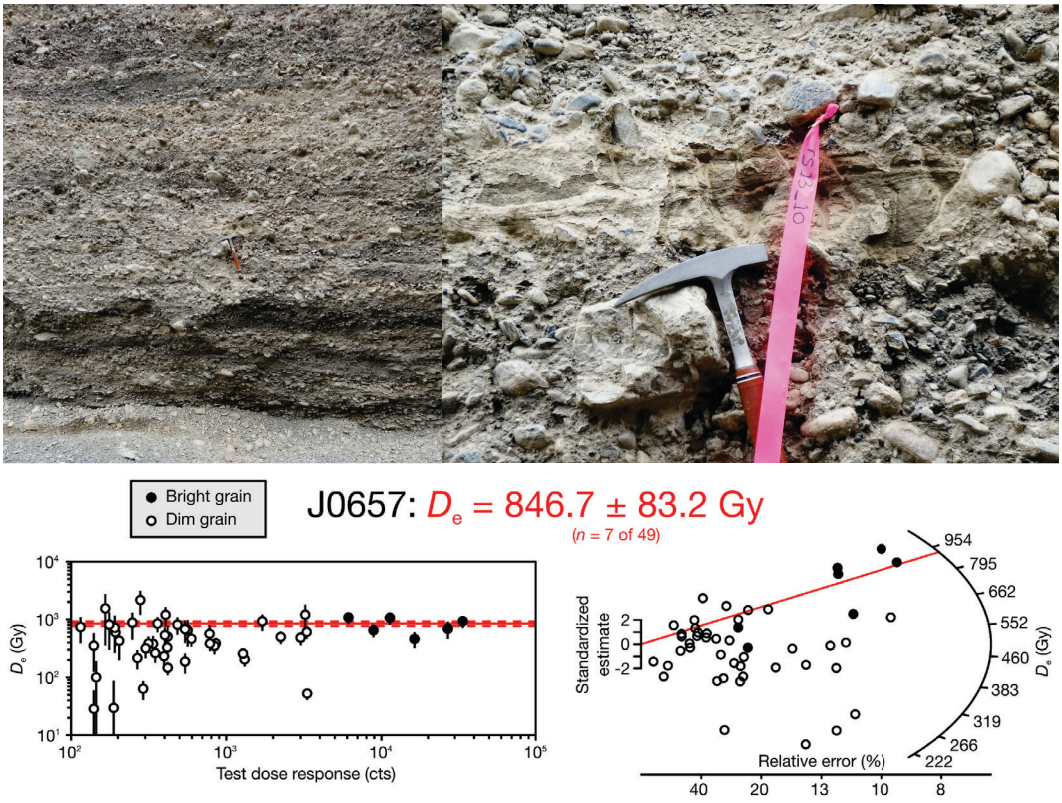

Figure A.15: Location and details of sample **TS13_10 (J0657)** = **402.7 ± 45.8 ka**; Kuitun; aggradation. Sample taken in a 10-15 cm thick lens of reworked silt to fine sand 74 m above the river. The sample constrains a phase of aggradation of the alluvial fan. The overdispersion is 0.22.

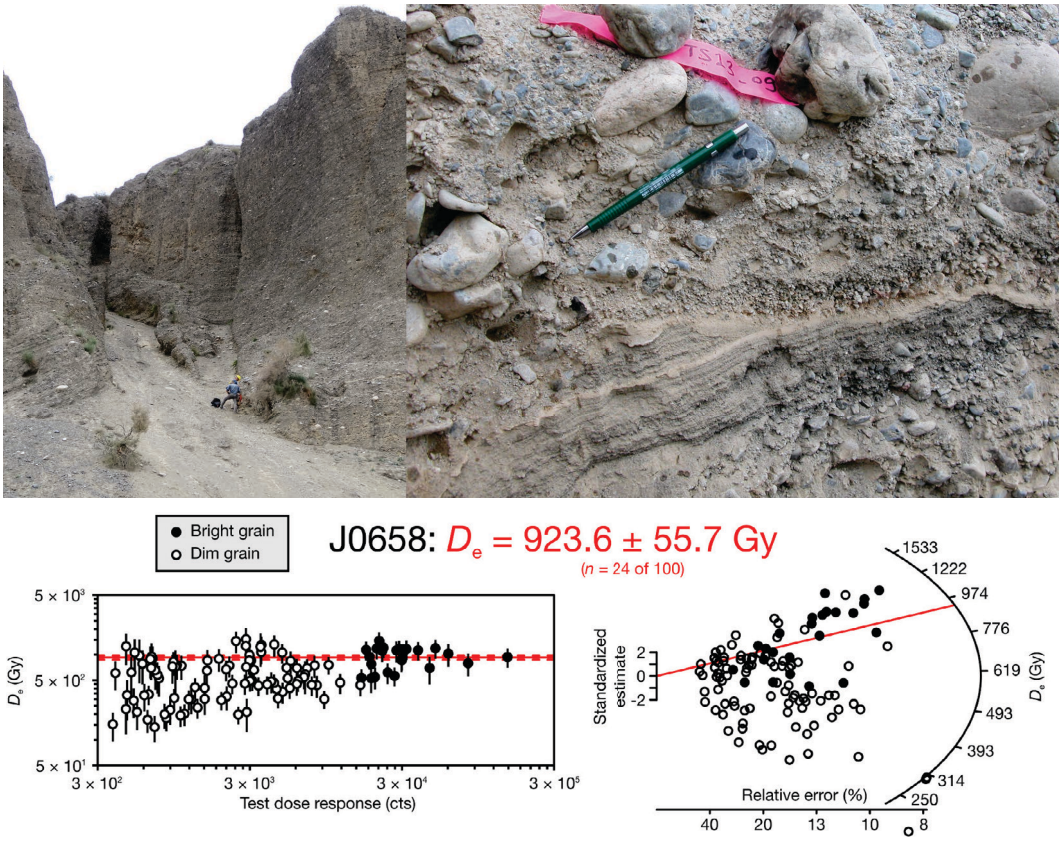

Figure A.16: Location and details of sample **TS13_09 (J0658)** = **379.0 ± 39.6 ka**; Kuitun; aggradation. Sample taken in a thin lens of reworked silt to medium sand 21 m above the river. The sample constrains a phase of aggradation of the alluvial fan. The overdispersion is 0.25.

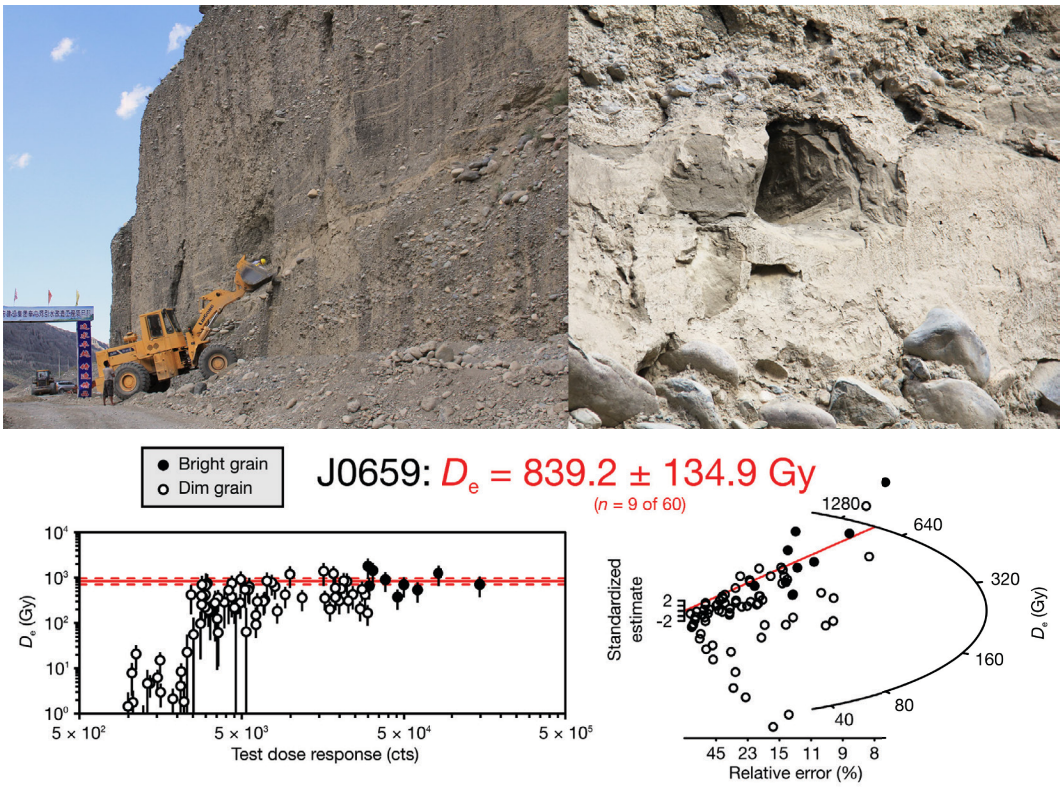

Figure A.17: Location and details of sample **TS13_02 (J0659)** = **330.8 ± 60.8 ka**; Kuitun; aggradation. Sample is collected at the base of the Kuitun main conglomerate cliff that is cut by Holocene incision, >250 m below the alluvial fan surface. Material is taken from a 1-1.5m thick loess horizon. The overdispersion is 0.46.

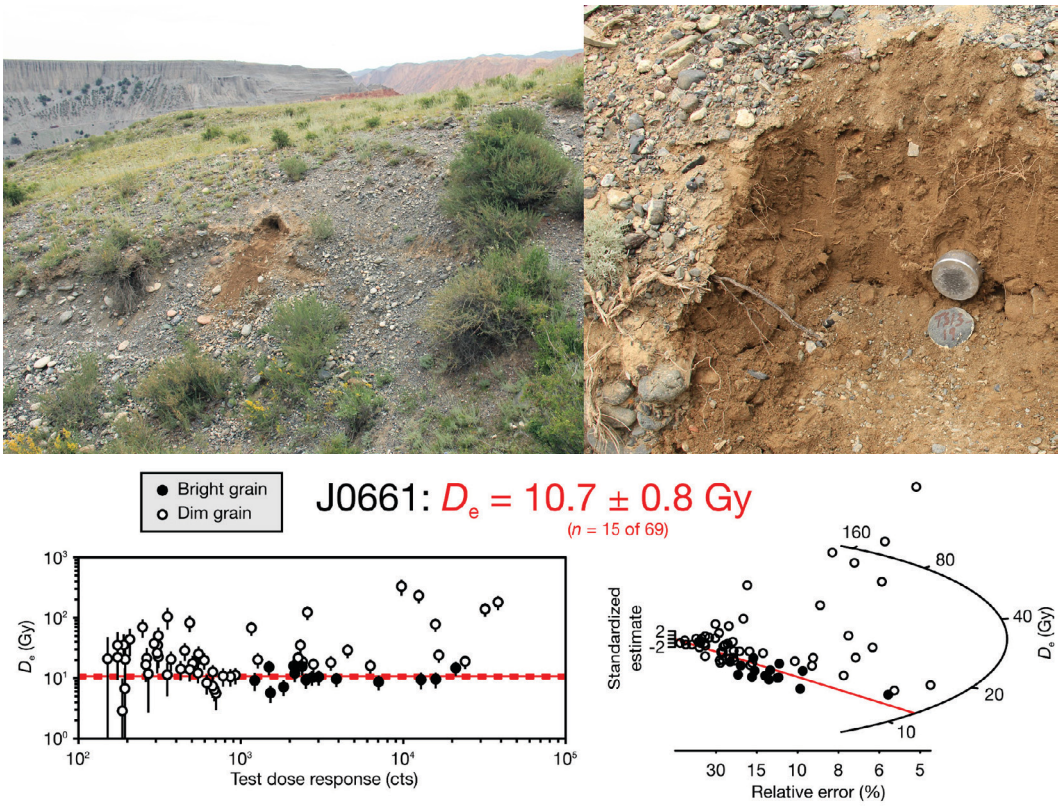

Figure A.18: Location and details of sample **TS13_19 (J0661) = 3.6 ± 0.3 ka**; Anji Hai; abandonment. Sample taken in a fine sand bed capping the fluvial deposits of terrace T13. The sample should constrain the abandonment of T13.

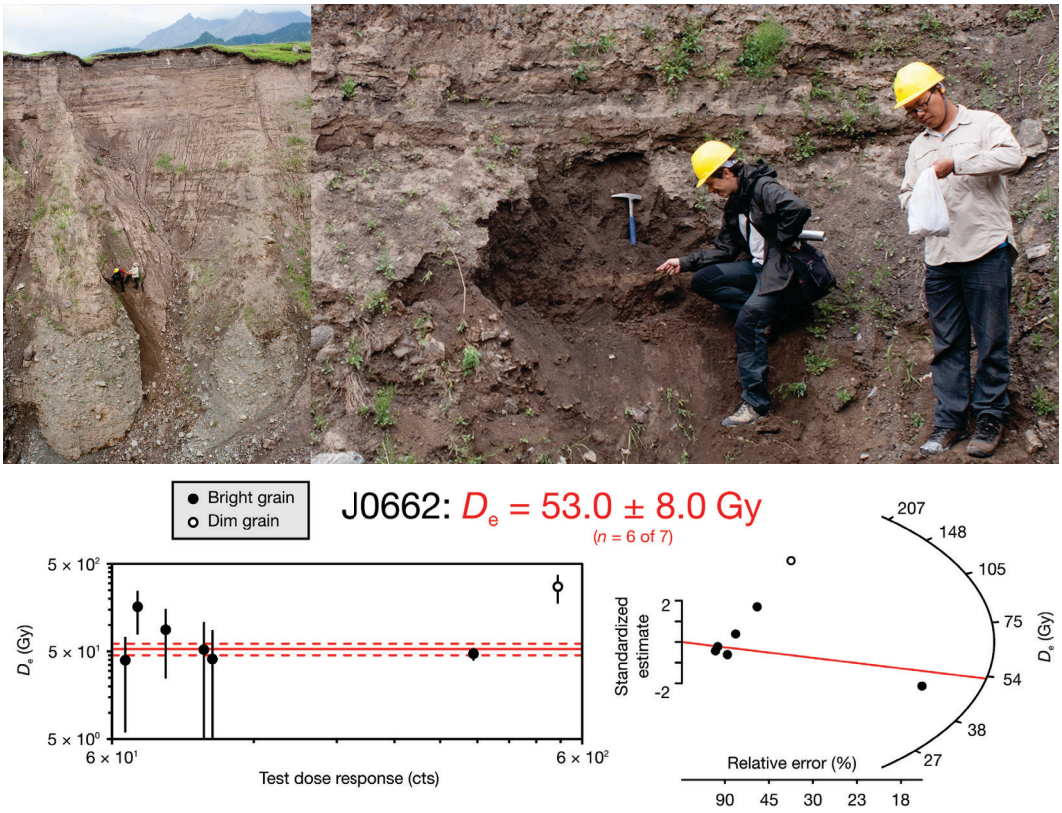

Figure A.19: Location and details of sample **TS13_35 (J0662) = 37.4 ± 6.4 ka**; Anji Hai; abandonment. Sample taken in a silt horizon at the base of a ca. 10 m thick colluvial wedge, 5-10 cm above the top of the cobble conglomerate fill that defines the main terrace of the Anji Hai Tributary. Sampling was done in a side wash cutting through the terrace. From this sample, we expect an abandonment constraint for the main terrace. The overdispersion is 0.

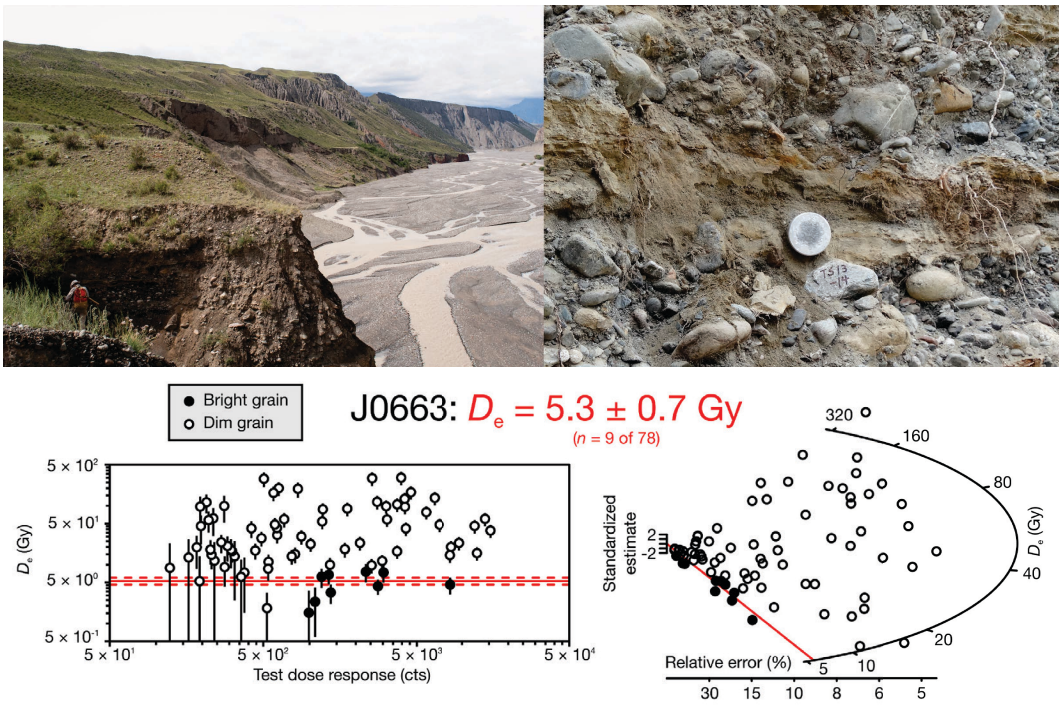

Figure A.20: Location and details of sample **TS13_14 (J0663) = 1.7 ± 0.3 ka**. Sample taken in a lens of reworked silt to fine sand at 0.8 m depth in the alluvial fill under terrace T2. The sample will provide an age constrain on the alluvial fan aggradation.

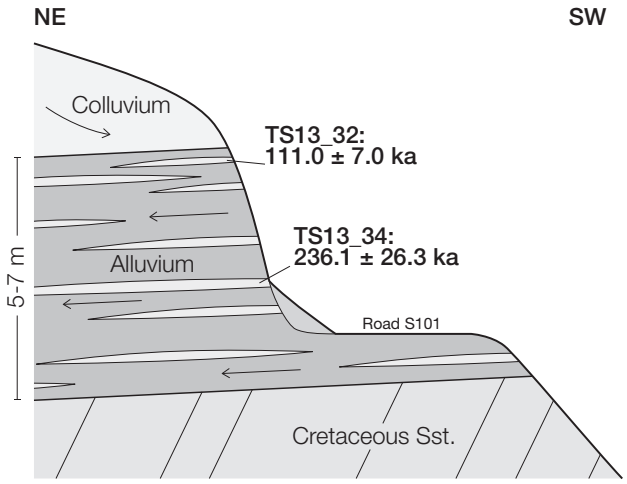

Figure A.21: Stratigraphic relationship between **TS13_32 (J0665)** and **TS13_34 (J0664)**; Toudao; the samples are collected from silt lenses in an alluvial conglomerate that lies unconformable on Jurassic sandstone and is capped by colluvium.

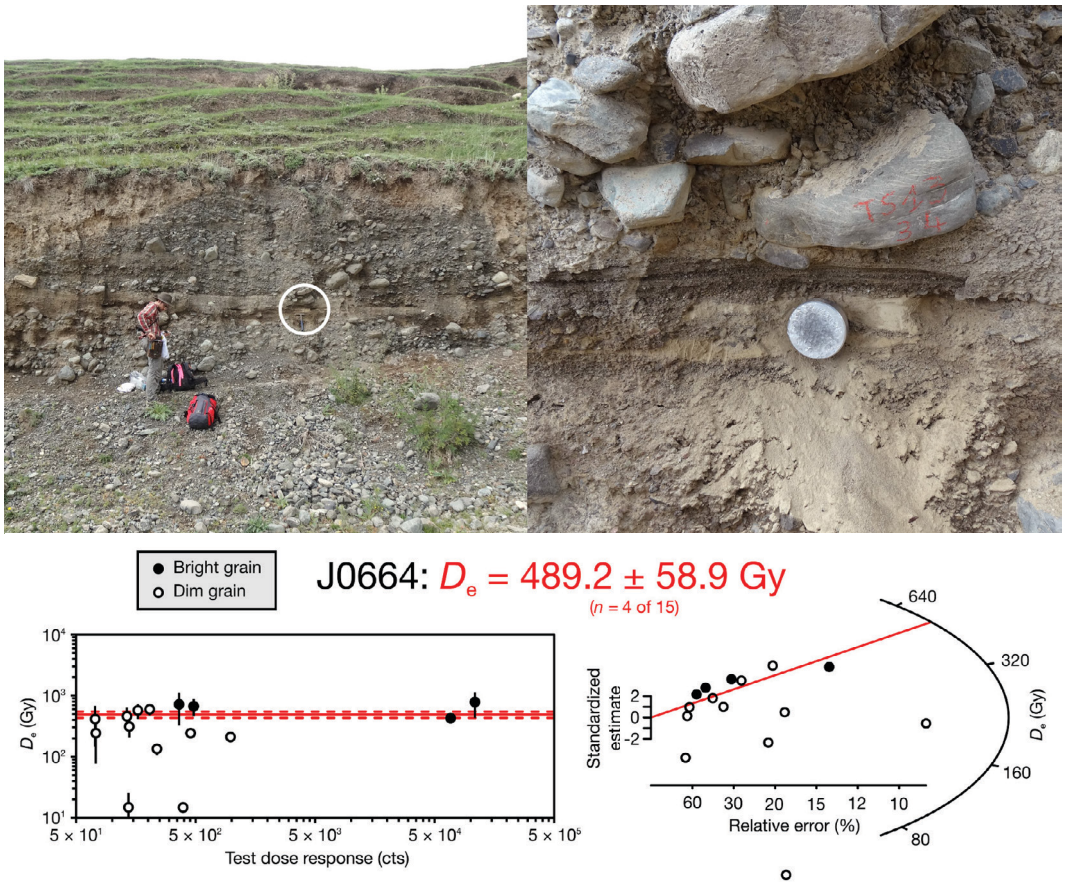

Figure A.22: Location and details of sample **TS13_34 (J0664) = 265.9 ± 40.7 ka**. Sample collected in a narrow silty sand lens less than 10 cm thick, with granules and then pebbles and cobbles conglomerates above and below. The sample lies 2-3 m above the bedrock and 3-4 m below sample TS13_33, the two constrain the age of the fluvial deposit on the strath. The overdispersion is 0.

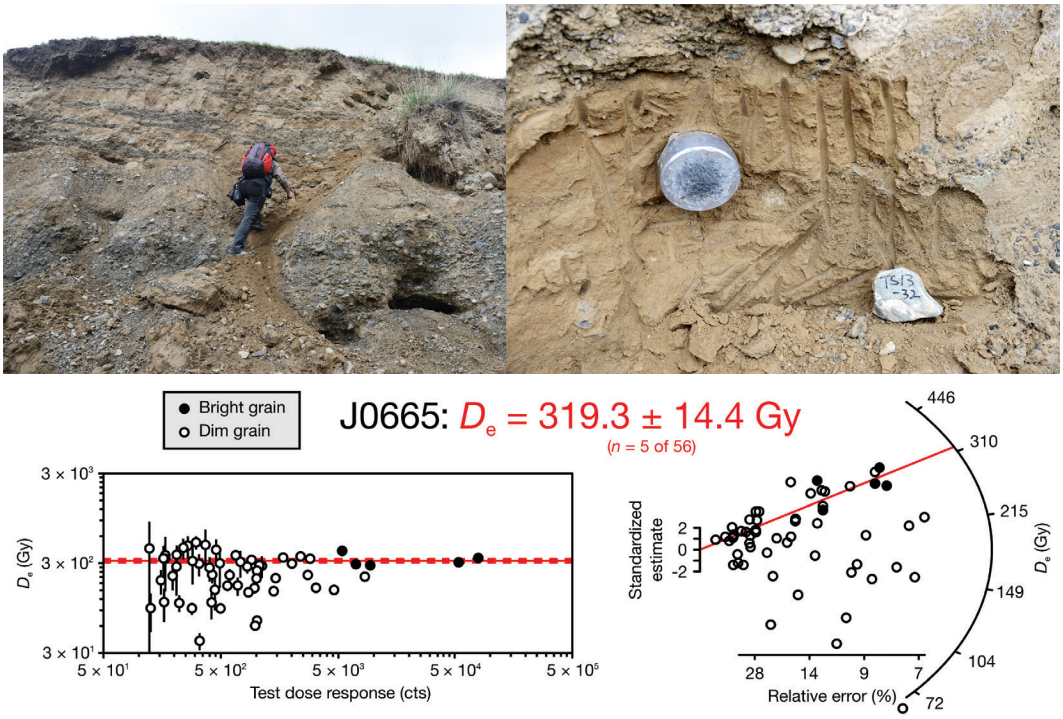

Figure A.23: Location and details of sample **TS13_32 (J0665)** = **124.0 ± 10.9 ka**; Anji-Hai tributary; abandonment. Sample taken in the first reworked silt lens above the massive fluvial cobble conglomerate and below a few thinner pebble conglomerate horizons. It represents the very last phase of aggradation that postdates the deposition of the main fill (cobble conglomerate) of this high terrace. The sample lies 3-4 m above TS13_32. The overdispersion is 0.03.

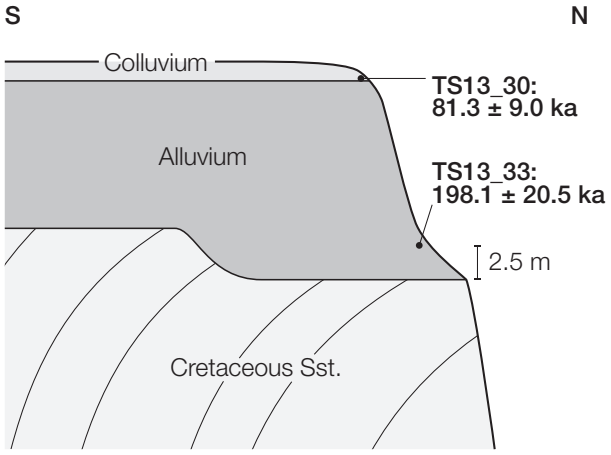

Figure A.24: Stratigraphic relationship between **TS13_30 (J0668)** and **TS13_33 (J0669)**. The samples are collected from silt lenses in a thick alluvial conglomerate that lies unconformable on Jurassic sandstone and is capped by colluvium.

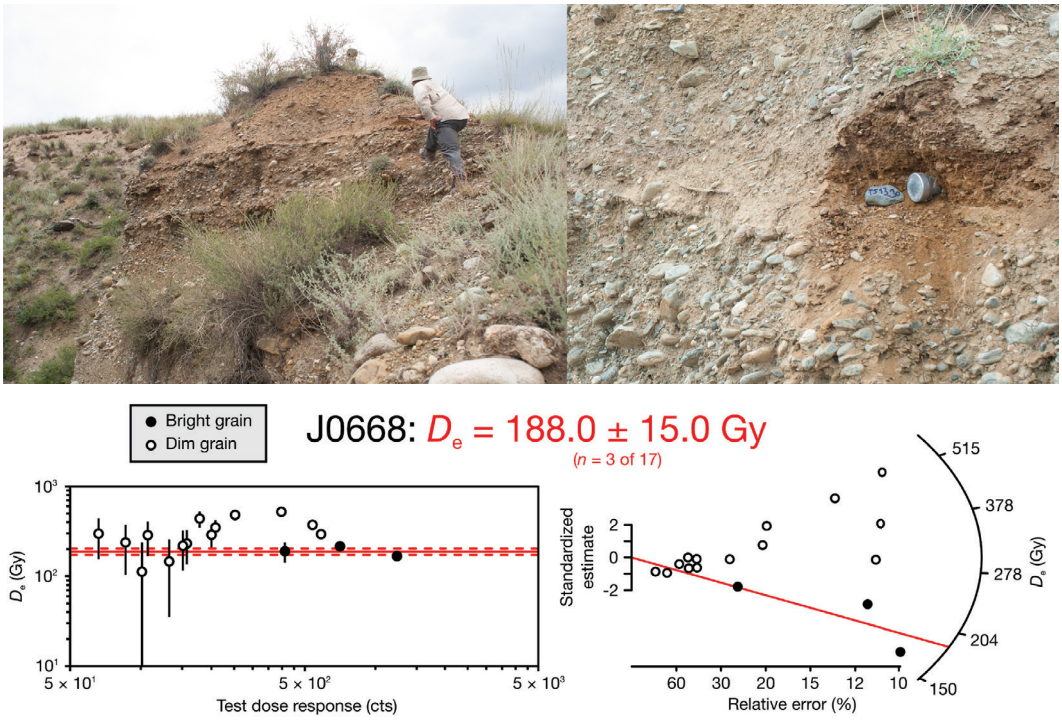

Figure A.25: Location and details Location and details of sample **TS13_30 (J0668) = 81.3 ± 9.4 ka**; Manas; abandonment. The sample is in front of Jiawei in the left picture. The sample was collected in the clay to fine sand capping the fluvial cobble-pebble deposits of the main strath terrace in the Upper Manas). This bed is covered by angular to subangular cobble-pebble colluvium and soil. The sample should constrain age of the Upper Manas strath terrace. The overdispersion is 0.05.

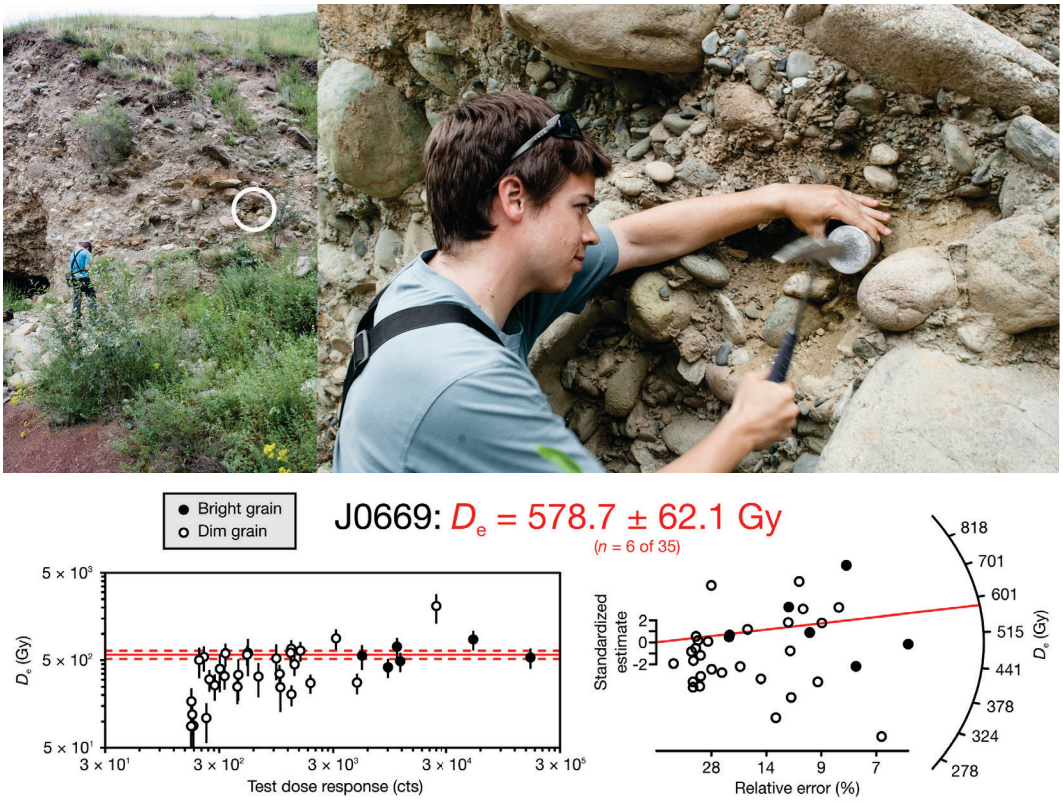

Figure A.26: Location and details of sample **TS13_33 (J0669)** = **231.7 ± 33.4 ka**. Sample taken in a very small clayey silt in the boulder conglomerate of the main strath terrace of the Upper Manas. The sample lies 2.5 m above the strath. It is a good constraint on the creation of the strath (assuming that the boulder conglomerate present today is the original cover of the strath). The overdispersion is 0.24.

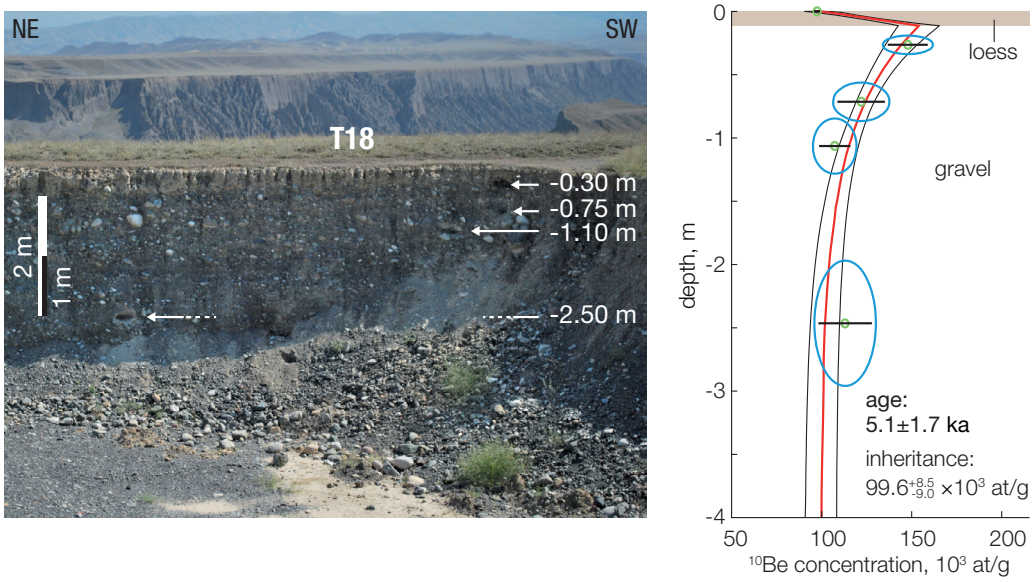

Figure A.27: Left: sampling site for the depth profile analysis of sample **TS12_ANJ_T1B = 5.1 ± 1.7 ka**. Right: ^{10}Be cosmogenic concentrations as a function of depth. The red line show the best fit model. Fine sediments (silt, loess, soil) are assumed to have a bulk density of 1.6±0.2 g/cm^3. The measured depths are converted to theoretical depths with the respective densities (blue ellipses).

Table A.4: Supplementary Table Compilation of all published ages dating surfaces of the north alluvial piedmont of the Eastern Tian Shan. The map no. column lists the numbering used in the maps ("e" for external source). The relative height* is the elevation of the sample above the river divided by the height of the fill terrace marking the incision onset. Easting and Northing are referenced in the UTM zone 45 T. The River acronyms are ANJ (Anjihai), ANJw (Anjihai windgap), HTB (Hutubi), JNG (Jingou), KTN (Kuitun), MNS (Manas), TDO (Toudao), TSH (Tashi), and URQ (Urumqi). The sources are 1: this study; 2: Poisson and Avouac (2004); 3: Poisson (2002); 4: Gong, S.-H. Li, and B. Li (2014); 5: Lu et al. (2014);6: Honghua Lu, Burbank, and Y. Li (2010); 7: Stockmeyer, *in review*; 8: Fu et al. (2017). * Combination of the surface F_2 samples following Honghua Lu, Burbank, and Y. Li (2010, p. 348). † These samples are not included in Figures 13 and 14 because they only border a small ephemeral stream that crosses the windgap after it was abandonment by the Anjihai River. The coordinates for Fu et al. (2017) listed here are the mean positions of the samples that contribute to each age.

River	**Map code**	**Sample no.**	**Age (ka)**	**Height***	**Lat. (°N)**	**Lon. (°E)**	**Method**
KTN	01	TS13_01[1]	116.8±8.1	0.10	44.3260	84.7793	p-IR IRSL
KTN	02	TS13_02[1]	286.1±40.9	0.05	44.1408	84.7354	p-IR IRSL
KTN	03	TS13_03[1]	18.3±2.6	0.67	44.3685	84.7927	p-IR IRSL
KTN	07	TS13_07[1]	193.4±28.0	0.44	44.2146	84.7740	p-IR IRSL
KTN	08	TS13_08[1]	48.9±3.6	0.52	44.2150	84.7729	p-IR IRSL
KTN	09	TS13_09[1]	316.9±24.3	0.09	44.2154	84.7806	p-IR IRSL
KTN	10	TS13_10[1]	396.5±36.7	0.30	44.2143	84.7771	p-IR IRSL
KTN	11	TS13_11[1]	13.4±1.6	1.00	44.2123	84.7672	p-IR IRSL
KTN	12	TS13_12[1]	181±13.0	0.82	44.2121	84.7669	p-IR IRSL
ANJ	14	TS13_14[1]	1.7±0.3	0.16	44.1008	85.0983	p-IR IRSL
ANJ	19	TS13_19[1]	3.6 ±0.3	0.88	44.0929	85.0986	p-IR IRSL
MNS	30	TS13_30[1]	81.3 ±9.0	0.95	43.8489	85.8011	p-IR IRSL
TDO	32	TS13_32[1]	111±7.0	1.00	43.9734	85.1261	p-IR IRSL
MNS	33	TS13_33[1]	198.1±20.5	0.80	43.8489	85.8013	p-IR IRSL
TDO	34	TS13_34[1]	236.1±26.3	1.00	43.9738	85.1255	p-IR IRSL
TDO	35	TS13_35[1]	37.4±6.4	1.00	43.9794	85.1071	p-IR IRSL
KTN	36	TS13_36[1]	3.3±0.3	0.32	44.2919	84.7873	p-IR IRSL
KTN	37	TS13_37[1]	1.7±0.4	0.02	44.2962	84.7885	p-IR IRSL
KTN	45	TS13_45[1]	7.7±1.0	0.76	44.2885	84.7819	p-IR IRSL
KTN	86	TS13_86[1]	8.4±0.7	0.65	44.2900	84.7900	p-IR IRSL
ANJ	1B	TS12-ANJ-T1B[1]	5.1 ±1.7	1.00	44.1052	85.0973	TCN
KTN	e1	OSL-T2-1[2]	10 ±1	0.92	44.2142	84.7725	OSL
KTN	e2	OSL-T2-2[2]	10.8 ±2	0.92	44.2142	84.7725	OSL
KTN	e3	OSL-T4-1[2]	7.3 ±1	0.65	44.3242	84.7728	OSL
KTN	e4	OSL-T4-2[2]	6.8 ±0.5	0.65	44.3223	84.7735	OSL
KTN	e5	OSL-T4-3[2]	7.5 ±1	0.65	44.3222	84.7738	OSL
KTN	e6	C-T5-1[2]	3.3 ±0.1	0.32	44.3213	84.7789	^{14}C
KTN	e7	C-T5-2[2]	3.4 ±0.2	0.32	44.2997	84.7811	^{14}C
KTN	e8	KTN_01[3]	35 ±10	1.00	44.2713	84.7625	OSL
KTN	e9	KTN_02[3]	86 ±10	1.00	44.2894	84.7600	OSL
MNS	e10	T-6-loess-bottom[4]	19.9 ±1.5	1.00	44.1786	86.1401	p-IR IRSL
MNS	e11	T-5-loess-bottom[4]	12.4 ±0.8	0.83	44.1284	86.1064	p-IR IRSL
MNS	e12	T-4-loess-bottom[4]	4 ±0.4	0.58	44.1659	86.1172	p-IR IRSL

MNS	e13	T-3-loess-bottom[4]	3.1 ±0.3	0.44	44.1673	86.1155	p-IR IRSL
MNS	e14	T-2-loess-bottom[4]	1.4 ±0.3	0.22	44.1677	86.1139	p-IR IRSL
MNS	e15	T-1-loess-bottom[4]	0.5 ±0.1	0.11	44.1685	86.1114	p-IR IRSL
URQ	e16	4 (T7)[5]	255 -25/+15	1.00	43.4043	87.2149	OSL
URQ	e17	2 (T5)[5]	142 ±14	1.00	43.4867	87.3060	OSL
URQ	e18	1 (T2)[5]	3.52 ±0.04	0.73	43.5314	87.3304	^{14}C
mix	e19	2-3-4-5 $(F_2(T_2))^{6*}$	295 ±25	1.00	—	—	ESR
TSH	e20	1 $(T_3(F_3))^6$	1.8 ±0.2	0.16	44.1576	86.3416	OSL
TSH	e21	1 $(T_3(F_3))^6$	26 ±2.7	0.16	44.0122	86.3360	OSL
JNG	e22	3a $(T_3(F_3))^6$	28.7 ±3	0.80	44.1814	85.4513	OSL
JNG	e23	3b $(T_3(F_3))^6$	12.6 ±1.3	0.97	44.1814	85.4513	OSL
JNG	e24	TGL-T4[7]	19.6 +14.5/-8.3	1.00	44.0649	86.3351	p-IR IRSL
TSH	e25	TGL-T3[7]	42.8 +18.2-12.7	1.00	44.0709	86.3280	p-IR IRSL
TSH	e26	TGL-T2[7]	75.2 +31.7/-17.6	1.00	44.0647	86.3280	p-IR IRSL
TSH	e27	TGL-T1[7]	188.8 +62.8/-47.1	1.00	44.0673	86.3138	p-IR IRSL
TSH	e28	TGL-T0[7]	245.6 +72.3/-55.9	1.00	44.0686	86.3094	p-IR IRSL
ANJw	e29	AJH-02-04[8†]	3.6±0.1	1.00	∼44.27	∼85.17	OSL & p-IR IRSL
ANJw	e30	AJH-06,07,08[8†]	9.0±0.6	1.00	∼44.27	∼85.18	OSL & p-IR IRSL
ANJw	e31	AJH-08,09,11,12[8]	53.3±2.2	1.00	∼44.26	∼85.19	OSL & p-IR IRSL

Appendix B

SUPPLEMENTARY FILES FOR CHAPTER 5

Map of the Eastern Tian. The depth of river incision at the apex of the Quaternary fan is marked by the width of the green outline. The width of the dark blue track in the mountain valleys scales inversely with the relief in a 300 m radius window centered along the rivers: the larger the circle, the wider the valley is (U-shaped). The pink shading in catchment 23 represents a recently captured branch. See Table S1 for river names. Hillshade is from ASTER GDEM V2.

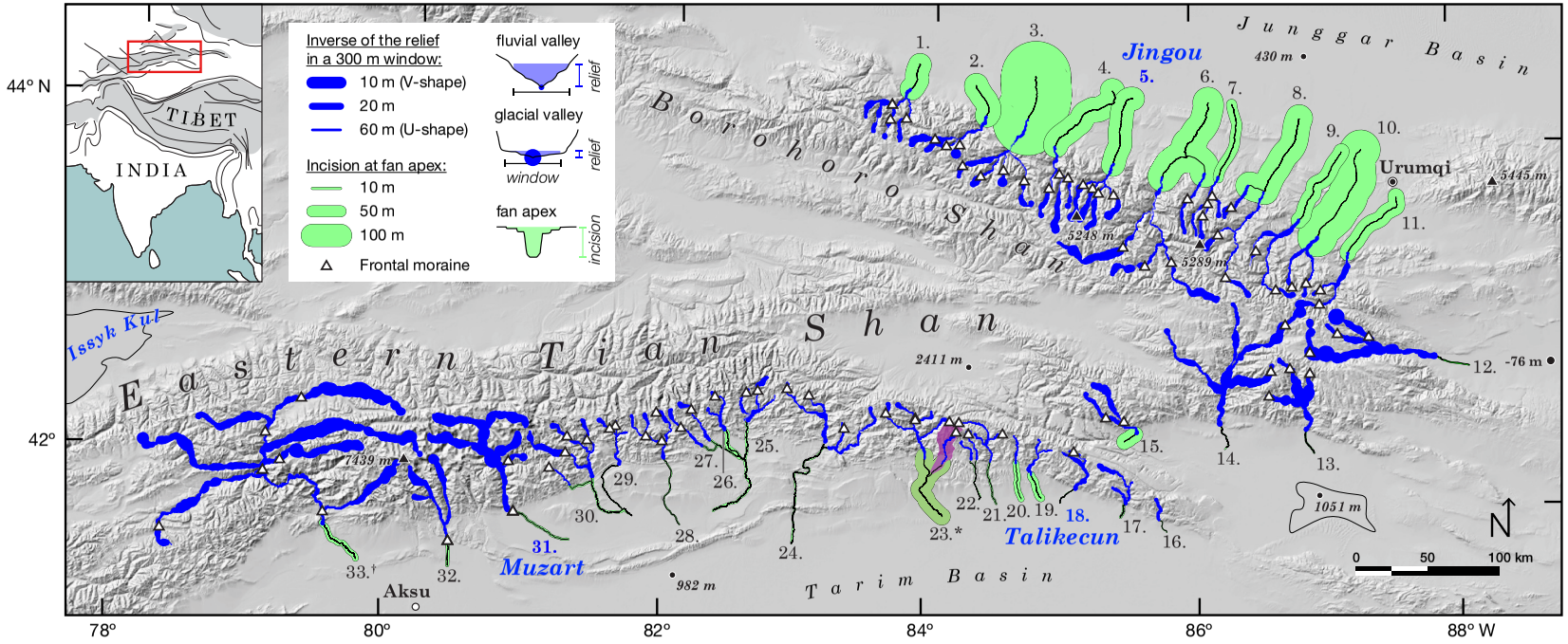

Figure B.1: Map of the Eastern Tian. The depth of river incision at the apex of the Quaternary fan is marked by the width of the green outline. The width of the dark blue track in the mountain valleys scales inversely with the relief in a 300 m radius window centered along the rivers: the larger the circle, the wider the valley is (U-shaped). The pink shading in catchment 23 represents a recently captured branch. See Table S1 for river names. Hillshade is from ASTER GDEM V2.

References

Adamiec, Grzegorz and M J Aitken (1998). "Dose-rate conversion factors: update". In: *Ancient TL*, pp. 37–50.

Aitken, M J (1985). *Thermoluminescence Dating*. London: Academic Press.

Balco, Greg et al. (2009). "Regional beryllium-10 production rate calibration for late-glacial northeastern North America". In: *Quaternary Geochronology* 4.2, pp. 93–107.

Braucher, R, Didier L Bourlès, et al. (2000). "Application of in situ-produced cosmogenic 10Be and 26Al to the study of lateritic soil development in tropical forest: theory and examples from Cameroon and Gabon". In: *Chemical Geology* 170.1-4, pp. 95–111.

Braucher, R, S Merchel, et al. (2011). "Production of cosmogenic radionuclides at great depth: A multi element approach". In: *Earth and Planetary Science Letters* 309.1–2, pp. 1–9.

Brown, Erik Thorson et al. (1991). "Examination of surface exposure ages of Antarctic moraines using in situ produced 10Be and 26Al". In: *Geochimica Et Cosmochimica Acta* 55.8, pp. 2269–2283.

Brown, Nathan D et al. (2015). "Single-grain post-IR IRSL signals of K-feldspars from alluvial fan deposits in Baja California Sur, Mexico". In: *Quaternary International* 362, pp. 132–138.

Buylaert, Jan-Pieter et al. (2009). "Testing the potential of an elevated temperature IRSL signal from K-feldspar". In: *Radiation Measurements* 44.5-6, pp. 560–565.

Chmeleff, Jérôme et al. (2010). "Determination of the 10Be half-life by multi-collector ICP-MS and liquid scintillation counting". In: *Nuclear Instruments & Methods In Physics Research Section B-Beam Interactions With Materials And Atoms* 268.2, pp. 192–199.

Dunai, Tibor J (2010). *Cosmogenic Nuclides*. principles, concepts and applications in the earth surface sciences. Cambridge University Press.

Fu, Xiao et al. (2017). "A fluvial terrace record of late Quaternary folding rate of the Anjihai anticline in the northern piedmont of Tian Shan, China". In: *Geomorphology* 278, pp. 91–104.

Fuchs, M and A Lang (2001). "OSL dating of coarse-grain fluvial quartz using single-aliquot protocols on sediments from NE Peloponnese, Greece". In: *Quaternary Science Reviews* 20.5-9, pp. 783–787.

Galbraith, R F et al. (1999). "Optical dating of single and multiple grains of quartz from Jinmium rock shelter, northern Australia: Part I, experimental design and statistical models". In: *Archaeometry* 41.2, pp. 339–364.

Gong, Zhijun, Sheng-Hua Li, and Bo Li (2014). "The evolution of a terrace sequence along the Manas River in the northern foreland basin of Tian Shan, China, as inferred from optical dating ". In: *Geomorphology* 213.C, pp. 201–212.

Gosse, John C and FM Phillips (2001). "Terrestrial in situ cosmogenic nuclides: theory and application". In: *Quaternary Science Reviews* 20.14, pp. 1475–1560.

Guralnik, Benny et al. (2011). "Constraining the evolution of river terraces with integrated OSL and cosmogenic nuclide data". In: *Quaternary Geochronology* 6.1, pp. 22–32.

Hancock, G S et al. (1999). "Dating fluvial terraces with Be-10 and Al-26 profiles: application to the Wind River, Wyoming". In: *Geomorphology* 27.1-2, pp. 41–60.

Huntley, D J (2006). "An explanation of the power-law decay of luminescence". In: *Journal of Physics: Condensed Matter* 18.4, pp. 1359–1365.

Huntley, D J and M R Baril (1997). "The K content of the K-feldspars being measured in optical dating or in thermoluminescence dating". In: *Ancient TL* 15.1, pp. 11–13.

Huntley, D J and M Lamothe (2001). "Ubiquity of anomalous fading in K-feldspars and the measurement and correction for it in optical dating". In: *Canadian Journal of Earth Sciences* 38.7, pp. 1093–1106.

Kars, Romée H, T Reimann, et al. (2014). "Bleaching of the post-IR IRSL signal: new insights for feldspar luminescence dating". In: *Boreas* 43.4, pp. 780–791.

Kars, Romée H, J Wallinga, and K M Cohen (2008). "A new approach towards anomalous fading correction for feldspar IRSL dating–tests on samples in field saturation". In: *Radiation Measurements* 43.2-6, pp. 786–790.

Kohl, C P and K Nishiizumi (1992). "Chemical isolation of quartz for measurement of in-situ-produced cosmogenic nuclides". In: *Geochimica Et Cosmochimica Acta*.

Korschinek, G et al. (2010). "A new value for the half-life of 10Be by Heavy-Ion Elastic Recoil Detection and liquid scintillation counting". In: *Nuclear Instruments & Methods In Physics Research Section B-Beam Interactions With Materials And Atoms* 268.2, pp. 187–191.

Kreutzer, S et al. (2012). "Introducing an R package for luminescence dating analysis". In: *Ancient TL* 30.1, pp. 1–8.

Lal, Devendra (1991). "Cosmic-Ray Labeling of Erosion Surfaces - Insitu Nuclide Production-Rates and Erosion Models". In: *Earth and Planetary Science Letters* 104, pp. 424–439.

Lamothe, M et al. (2003). "Towards a prediction of long-term anomalous fading of feldspar IRSL". In: *Radiation Measurements* 37.4-5, pp. 493–498.

Li, Bo and Sheng-Hua Li (2011). "Luminescence dating of K-feldspar from sediments: A protocol without anomalous fading correction". In: *Quaternary Geochronology* 6.5, pp. 468–479.

Lu, Honghua, Douglas West Burbank, and Youli Li (2010). "Alluvial sequence in the north piedmont of the Chinese Tian Shan over the past 550 kyr and its relationship to climate change". In: *Palaeogeography Palaeoclimatology Palaeoecology* 285.3-4, pp. 343–353.

Lu, H et al. (2014). "Late Quaternary alluvial sequence and uplift-driven incision of the Urumqi River in the north front of the Tian Shan, northwestern China". In: *Geomorphology* 219, pp. 141–151.

Nishiizumi, Kunihiko et al. (2007). "Absolute calibration of 10Be AMS standards". In: *Nuclear Instruments & Methods In Physics Research Section B-Beam Interactions With Materials And Atoms* 258.2, pp. 403–413.

Poisson, Blanche (2002). "Impact du climat et de la tectonique sur l'évolution géomorphologique d'un piémont: exemple du piémont Nord du Tian Shan depuis la fin du Pléistocène ". PhD thesis. Université Paris XI.

Poisson, Blanche and Jean-Philippe Avouac (2004). "Holocene hydrological changes inferred from alluvial stream entrenchment in North Tian Shan (Northwestern China)". In: *Journal of Geology* 112.2, pp. 231–249.

Prescott, J R and J T Hutton (1994). "Cosmic ray contributions to dose rates for luminescence and ESR dating: Large depths and long-term time variations". In: *Radiation Measurements* 23.2-3, pp. 497–500.

Rhodes, Edward J (2015). "Dating sediments using potassium feldspar single-grain IRSL: initial methodological considerations". In: *Quaternary International* 362, pp. 14–22.

Stone, John O. (2000). "Air pressure and cosmogenic isotope production". In: *Journal Of Geophysical Research* 105, pp. 23753–23759.

Thomsen, Kristina J et al. (2008). "Laboratory fading rates of various luminescence signals from feldspar-rich sediment extracts". In: *Radiation Measurements* 43.9–10, pp. 1474–1486.

Uppala, S M et al. (2005). "The ERA-40 re-analysis". In: *Quarterly Journal of the Royal Meteorological Society* 131.612, pp. 2961–3012.

Wintle, Ann G and A S Murray (2006). "A review of quartz optically stimulated luminescence characteristics and their relevance in single-aliquot regeneration dating protocols". In: *Radiation Measurements* 41, pp. 369–391.